QUEEN MARY AND WESTFIELD COLLEGE
DEPARTMENT OF MATERIALS
UNIVERSITY OF LONDON

A study of Carbon Fibre / Epoxy Interface using Remote Laser Raman Microscopy

by

Alkiviadis Paipetis

A thesis presented for the degree of Doctor of Philosophy in the Faculty of Engineering of the University of London

1997

to Elena

Abstract

The micromechanics of reinforcement of model carbon fibre / epoxy composites has been investigated using the technique of Remote Laser Raman Microscopy. The technique allows *in situ* axial stress monitoring in highly crystalline fibres, such as carbon.

For this purpose a remote fibre -optic probe was designed and tested. Tailor - made optics have been introduced at both input and output positions of each fibre - optic to provide laser collimation and maximum efficiency. The probe design takes advantage of the pinhole nature of the optical fibre to achieve depth discrimination.

A full characterisation of the high modulus M40 fibres using conventional testing and Raman Spectroscopy preceded the study of the stress transfer. The study was performed as a function of fibre sizing, coupon geometry and elevated temperature. Model composites were subjected to incremental tensile loading, while the stress in the fibre was monitored at each level of applied strain. The stress transfer regime was studied in the elastic domain using the short fibre coupon test and shear lag approach was employed to model the stress transfer efficiency of the interface through the use of the shear-lag parameter β. The study of the long fibre coupon test led to the identification of interfacial failure mechanisms which were also investigated by Scanning Electron Microscopy (SEM). Finally, the stress build-up in the fibre in the presence of energy dissipation mechanisms was modelled, and the stress-transfer efficiency was assessed at different levels of applied composite strain.

Acknowledgements

I would like to thank my supervisor Dr Costas Galiotis for his help and guidance throughout the course of this project.

Many thanks to Dr Nick Melanitis for initiating me to Raman Spectroscopy, and to Dr Cosmas Vlattas, Mr Fabrice Bollet, Dr Stelios Sapalidis, Dr Michalis Zervos, Dr Klisthenis Dimitriadis and all the members of the Raman Lab (Ms Yak-Nam Wang included) for their support and friendship.

Special thanks to Mr Varinder Chohan for the stress calibration experiment and Mr Fabrice Bollet for his assistance with the SEM.

I am indebted to the European Commission for providing financial support under the BRITE - EURAM project BREU/CT91-9503.

I am grateful to my parents Stephanos and Potoula for their constant encouragement and for discretely providing me with an invaluable feeling of security. Finally, I wish to express my gratitude to Ms Elena Zervou for her tireless help and support.

Contents

List of Tables

CHAPTER 4

CHAPTER 5

List of Figures

CHAPTER 2

CHAPTER 3

CHAPTER 4

CHAPTER 5

APPENDIX 1

APPENDIX 3

Nomenclature

A/D	analog to digital
$\boldsymbol{a}$	polarisability of a molecule
a_{ε}	Raman frequency - strain proportionality constant
α_L	Raman frequency - laser power proportionality constant
a_{σ}	Raman frequency - stress proportionality constant
α_T	Raman frequency - temperature proportionality constant
b	constant (Morse potential)
β	shear-lag parameter
BEA	Boundary Element Analysis
c	velocity of light
CCD	Charged Coupled Device
Ce-TZP	commercial ceria-stabilised zirconia
D	displacement discontinuity parameter for an imperfect interface
D_e	dissociation energy
$\Delta\nu$	frequency shift or *Raman Frequency*
$\Delta\tilde{\nu}$	Delta wavenumbers
δ_{max}	maximum deflection of the cantilever beam
$\mathbf{E_{2g}}$	the double degenerate graphitic Raman band
$\vec{E}$	electric field
$\mathcal{E}_{stored}$	measured stored energy
$\mathcal{E}_{elastic}$	predicted stored energy assuming an elastic stress state
E	Young's modulus
E_f	fibre modulus
E_m	matrix modulus
ε_z, ε_r, ε_θ, γ_{rz}	strain components in cylindrical coordinates r, θ, z
ε_∞	far field strain
F	restoring force

f	focal distance of a lens
***f* number**	ratio of the spectrometer focal length the collection mirror diameter
$\bar{f}(z)$	average functions for the fibre and the matrix cylinders, over their radii
FDA	Finite Difference Analysis
FEA	Finite Element Analysis
FGL	Fragmentation Gauge Length
$\Phi(r)$	confocal pupil function
GF	strain gauge factor
G_m	matrix shear modulus
$G_m^{R_\infty}$	shear modulus of a matrix cylinder of radius R_∞
γ_{LV}	solid - vapour surface energy
γ_{SL}	liquid - vapour surface energy
γ_{SV}	solid - vapour surface energy
H	proportionality constant for the shear-lag model
HM	High Modulus
HTT	High Temperature Treatment
HY-951	triethylene tetramine curing agent
h	extinction coefficient
$\hbar$	Plank's constant
I	total radiating energy from an oscillating dipole
IFSS	Interfacial Shear Strength
IM	Intermediate Modulus
ISS	Interfacial Shear Stress
k	force constant
l	finite length of a cylinder or fibre
l^*	equivalent elastic stress transfer fibre length
l_0	initial length of a cylinder or fibre
L_a	in-plane coherence length of the graphene layer
L_c	c-axis coherence length of the graphene layer
l_c	critical length
l_f	fragment length
λ	wavelength of the light

LM	Low Modulus
LRS	Laser Raman Spectroscopy
l_t	transfer or ineffective length
m	Weibull shape parameter
MEBS	M40 sized high modulus carbon fibre
MIT	Micro-Indentation Test
MUS	M40 unsized high modulus carbon fibre
μ	Coulomb friction coefficient
MY-750	unmodified liquid epoxy resin
N	number of atoms in a polyatomic molecule
n	refractive index
na	numerical aperture
ν	frequency
$\tilde{\nu}$	wavenumber
ν_0	frequency of the incident or excitation light
ν_m	matrix Poisson' s ratio
ν_r	frequency of a component of the scattered light
ν_{ref}	reference zero stress frequency values obtained for the E_{2g} band
OD	optical density
$\vec{P}$	electric dipole moment
P	axial force
P_{max}	maximum axial force
PAN	polyacrylonitrite
PBO	poly(p-phenylene benzobisoxazole) fibre
PBZT	poly(p-phenylene benzobisthiazole) fibre
PPTA	poly(p-phenylene terepthalamide) fibre; trade name Kevlar$^{\circledR}$49
q	thickness of the cantilever beam
θ	contact angle
$\mathbf{r}_{1,2}$	real levels
R	radius of the fibre
R'	interfibre distance
R_{ca}	confocal aperture radius

R_{fo}	fibre optic core radius
R_L	laser beam radius
R_s	laser spot radius
R_∞	radius of the shear perturbation cylinder
ReRaM	Remote Raman Microprobe
RT	Room Temperature
ρ	density
S	shear force
SEM	Scanning Electron Microscopy
s_i $(i=1,2)$	constants depending on the elastic properties of the material.
σ	normal stress
σ_{fu}	fibre axial strength
$\bar{\sigma}_{fu}$	mean fibre strength
σ_{max}	maximum axial stress
σ_{mu}	matrix tensile strength
σ_s	threshold stress
σ_u	tensile strength
σ_0	constant
σ_z, σ_r, σ_θ	normal stresses in cylindrical coordinates r, θ, z
$\bar{\sigma}_z$	average axial stress over the cross-sectional area of the fibre
σ_∞	far field stress
TEBS	sized intermediate modulus T800 fibre
TEM	Transmission Electron Microscopy
TUS	unsized intermediate modulus T800 fibre
τ	shear stress
τ_{mu}	matrix shear strength
τ_{rz} $\tau_{r\theta}$, $\tau_{\theta z}$	shear stresses in cylindrical coordinates r, θ, z
U_p	potential energy function
u, v, w	displacement components in cylindrical coordinates r, θ, z
$\mathbf{v}_{1,2}$	virtual levels
V_f *and* V_m	fibre and matrix volume fraction respectively
w_∞	far field axial displacement in the matrix

Ω_0	initial strain-gauge resistance
Ω_s	measured strain-gauge resistance after straining
x	displacement co-ordinate
ξ	displacement co-ordinate
y	penetration depth of an incident beam
Y-TZP	yttria-stabilised tetragonal phase zirconia
Ψ	stress function
ζ	index of stress transfer efficiency

Chapter 1: Introduction

Composite materials play a very important role in nature as well as engineering applications. Reinforcement in preferential directions allow for the tailoring of the composite according to the needs of specific applications, providing high specific strength and stiffness in comparison with monolithic materials. Central to an understanding of the mechanical behaviour of a composite is the concept of load sharing between the constituent phases. This requires the study of the *interface*, or the common boundary between the distinct phases.

The aim of this research was to investigate the adhesive properties of carbon fibre / epoxy interfaces with a view to identify and model the micromechanics of stress transfer. For this purpose, the technique of Laser Raman Spectroscopy (LRS) was used. LRS is by now a well established tool used to assess the level of interfacial adhesion in polymer based composites, as it can provide in situ stress measurements with a resolution of one micrometer.

In order to describe the necessary aspects of the technique used, chapter 2 is concerned with the fundamental principles related to LRS. The theory of Raman scattering is outlined, together with general considerations related to the properties of the scattered light. The fundamental theory regarding the stress dependence of the Raman frequencies is subsequently presented. It is this property of the Raman scattered light that provides the possibility of local stress monitoring. Thus, highly crystalline fibres can be used as internal strain gauges providing experimental information about the stress state in fibrous composites, as well as the mechanisms of load transfer between the fibre and the matrix.

With a view to exploiting fully the potential of stress monitoring with LRS, the realisation of a remote Raman microprobe based on flexible waveguides was undertaken as part of this work. The rationale, design and testing of this probe is given in detail in chapter 3. The remote Raman microprobe uses the versatility of optical fibres in order to enable the use of the unique properties of the Raman light away from the optical table. The design of the probe aims to the optimisation of the optical components used. Thus, through the use of interchangeable optics, the microprobe is capable of exploiting the maximum resolution offered by the objective lens. At the same time, using the confocal nature of the optical fibre endface, the user is capable of choosing the optimum combination for efficiency and depth discrimination. Various applications of the Remote Raman Microprobe prove its versatility as a complete alternative to conventional systems.

In chapter 4, an overview of carbon fibres and their properties is given. Aspects of their manufacturing processes, structure and morphology, as well as their Raman activity and its sensitivity to applied stress are covered. The experimental part of the chapter, deals with the characterisation of the high modulus carbon M40 fibres, which were used for the purposes of this investigation. This involved the measurement of the gauge length dependence of the strength of the fibres, microscopy studies and a full Raman characterisation of the fibres. Indications about the surface morphology of the fibres were obtained through the study of vibrational modes related to the structural disorder of graphite. Finally, the response of the Raman spectrum of the fibres to stress, strain and temperature was quantified.

Chapter 5 deals with the micromechanics of reinforcement in model composites. A detailed review of the literature concerning the fibre interface is presented, regarding the nature of the interface / interphase and the mechanisms of stress transfer. Existing models describing the behaviour of the interface and methods of interfacial testing are subsequently described, together with references regarding the use of LRS as a means of assessing the interface in fibrous composites.

The evaluation of interfacial adhesion in carbon fibre epoxy systems was performed by means of a single fibre composite coupon. The model composite incorporated either a short or a long carbon fibre. The coupon geometry and the temperature of the environment were studied as a function of the fibre sizing. Initially, modelling of the behaviour of the interface in the elastic domain was undertaken. This was performed by applying the shear lag theory [**Cox, 1952**] to data obtained using the short fibre coupon. The interface was successfully modelled through the use of a single parameter β. Theoretical evaluation of the local properties of the matrix attributed the higher efficiency of the sized fibre interface to local property variations leading to considerably higher 'interfacial' shear modulus.

Subsequent axial monitoring of the long fibre coupon led to the evaluation of the Interfacial Shear Strength (IFSS) in room temperature as well as in 60°C. The stress transfer characteristics provided information about the nature of interfacial damage mechanisms and distinct failure mechanisms were identified and verified with Scanning Electron Microscopy (SEM) observations. The final part involved the modelling of interfacial adhesion using an energy approach. The comparison of the measured energy values to those predicted by assuming an elastic stress state led to the quantification of interfacial efficiency as a function of applied strain.

The conclusions and final remarks of the performed research are summarised in chapter 6. The overall evaluations related to the parts of this study are independently outlined, together with suggestions for further work in fields covered throughout the course of this investigation.

Chapter 2: Laser Raman Spectroscopy

2.1. THE RAMAN EFFECT

Raman Spectroscopy is concerned with the phenomenon of a change in frequency when light is scattered by molecules. If the frequency of the incident light is ν_0 and that of a component of the scattered light is ν_r, then, the frequency shift $\Delta\nu = \nu_0 - \nu_r$ is referred to as a *Raman Frequency* and is considered to be a property of the scattering medium.

The Raman Effect was theoretically predicted by Smecal [**1923**] and experimentally verified by Raman and Krishnan [**1928**]. The phenomenon may be visualised by considering the incident light as photons with energy $\hbar\nu_0$, where $\hbar$ is Plank's constant. When the photons collide with molecules, the collision may be elastic i.e. no energy exchange takes place; this gives rise to the *Rayleigh* line. If however the collision is inelastic, the energy exchange causes a quantum transition of the molecule to a higher energy level, and the photon is scattered with a lower energy ($\Delta\nu$ negative), referred to as the *Stokes* line. If the molecule is at an energy level above its lowest, an encounter with a photon may cause it to undergo a transition to a lower energy, in which case the photon is scattered with higher frequency ($\Delta\nu$ positive) inducing the *anti-Stokes* line [**Szymanski, 1967**].

2.2. THEORY OF RAMAN SCATTERING

If a molecule is subjected to an electric field $\vec{E}$, an electric dipole moment $\vec{P}$ is induced [**Svanberg, 1992**]:

$$\vec{P} = \boldsymbol{a}\vec{E} \tag{2.1}$$

where $\boldsymbol{a}$ is the *polarisability* of the molecule.

For an oscillating field $\boldsymbol{E} = \boldsymbol{E}_0 \, \boldsymbol{sin}(2\pi\nu_0 t)$, the polarisation varies at a frequency ν_0 resulting in the emission of light of the same frequency, i.e. the *elastic* or *Raleigh scattering*. The polarisability α of a molecule may vary as the molecule vibrates, or as it rotates in relation to an electric field. We may in this case regard:

$$\boldsymbol{a} = \boldsymbol{a_0} + \boldsymbol{a}_{1\nu} \, \boldsymbol{sin}(2\pi\nu_{\text{vibr}} t) \qquad \boldsymbol{a}_{1\nu} \ll \boldsymbol{a_0} \tag{2.2a}$$

for a vibrating molecule and, similarly:

$$\boldsymbol{a} = \boldsymbol{a_0} + \boldsymbol{a}_{1r} \, \boldsymbol{sin}(2\pi\nu_{\text{rot}} \text{t}) \qquad \boldsymbol{a}_{1r} \ll \boldsymbol{a_0} \tag{2.2b}$$

for a rotating molecule where the variation occurs at twice the rotational frequency. Combining equations 2.2 with equation 2.1, we acquire **[Svanberg, 1992]**:

For vibration,

$$P = \boldsymbol{a_0 E_0} \, \boldsymbol{sin}(2\pi\nu_{\text{vibr}} \text{t}) + \frac{1}{2}\boldsymbol{a}_{1\nu}\boldsymbol{E_0}\boldsymbol{cos}\{2\pi(\nu_0 - \nu_{\text{vibr}})t - 2\pi(\nu_0 + \nu_{\text{vibr}})t\} \tag{2.3a}$$

and for rotation

$$P = \boldsymbol{a_0 E_0} \, \boldsymbol{sin}(2\pi\nu_{\text{rot}} \text{t}) + \frac{1}{2}\boldsymbol{a}_{1\nu}\boldsymbol{E_0}\boldsymbol{cos}\{2\pi(\nu_0 - \nu_{\text{rot}})t - 2\pi(\nu_0 + \nu_{\text{rot}})t\} \tag{2.3b}$$

The first term in equations 2.3 is the *Rayleigh scattering*, the second is the *Stokes scattering* and the third is the *anti-Stokes scattering*.

Obviously the molecule is Raman active when $\alpha_{1\nu} \neq 0$, which forms the selection rule in the classical theory of the Raman scattering. It should be noted that, in the general case, the polarisability α in equations 2.1-2.3 is replaced by the polarisation tensor and the electric dipole moment $\vec{P}$ is not parallel to the electric field $\vec{E}$.

A usual way to visualise the change in polarisability is with the use of a displacement coordinate ξ which is a measure of the bond extension [**Banwell, 1983**]. Thus, for a stretching motion, ξ is positive when the bond is extended and negative when the bond is compressed. The variation of $\boldsymbol{a}$ with ξ is shown in figure 2.1. For small displacements, the $(\frac{\partial \boldsymbol{a}}{\partial \xi})$ derivative defines whether the equilibrium position $\xi = 0$ is a stationary point for the function $\boldsymbol{a}$ (figure 2.1a) or not (figure 2.1b), defining, thus, if the vibration is Raman active.

However, a full explanation of the phenomenon can only be obtained in quantum mechanical terms. According to Plank's law, the energy $\mathcal{E}$ that is gained or lost during the scattering is :

$$\Delta\mathcal{E} = \hbar \nu_0 \tag{2.4}$$

In this way, transitions are allowed between distinct energy levels. A full quantum mechanical model for the Raman effect can be achieved with the introduction of *virtual levels*. In figure 2.2, the allowable Raman transitions are shown [**Svanberg, 1992**]. The interaction with light induces the transitions from the *real levels* $\mathbf{r}_{1,2}$ to the *virtual levels* $\mathbf{v}_{1,2}$. When the molecule returns to the real levels, it emits the respective line where $\Delta\nu < 0$ for Stokes, $\Delta\nu = 0$ for Rayleigh and $\Delta\nu > 0$ for anti-Stokes.

The usual representation of Raman frequencies is in wavenumbers. The wavenumber $\tilde{\nu}$ corresponds to the number of waves per centimetre and is:

$$\tilde{\nu} = \frac{\nu}{c} \tag{2.5}$$

where ν is the frequency and c the velocity of light. Delta wavenumbers $\Delta\tilde{\nu}$ correspond to the wavenumber shift and are therefore a material property regarded as generally independent of the excitation frequency ν_0.

2.3. GENERAL CONSIDERATIONS ABOUT THE RAMAN EFFECT

Taking into consideration equation 2.1 for an oscillating field $\boldsymbol{E} = \boldsymbol{E}_0 \, \boldsymbol{sin}(2\pi\nu_0 t)$, the total radiating energy $\boldsymbol{I}$ from the dipole is:

$$\boldsymbol{I} = \frac{2}{3c^3}\overline{\left(\frac{d^2\boldsymbol{P}}{dt^2}\right)} \qquad (2.6)$$

where c is the velocity of light. The bar denotes time averaging. Since $\overline{\boldsymbol{sin}^2(2\pi\nu_0 t)} = \frac{1}{2}$:

$$\boldsymbol{I} = \frac{16\pi^4 c}{3\lambda^4}a^2\boldsymbol{E}_0^2 \qquad (2.7)$$

Here the relation $\nu = \frac{c}{\lambda}$ is used, where λ is the wavelength of light. An examination of equation 2.7 shows the expected proportionality of the Raman bands to the intensity of the excitation line; they are both proportional to E_0^2, that is, to the square of the electric vector of light. An important factor that has to be taken into account is that there is an upper bound of the excitation source intensity, above which the sample will decompose faster than the time needed to record the spectrum [**Loader, 1970**].

The Raman scattering is also proportional to the fourth power of the inverse of the wavelength λ or the frequency ν_0 of the excitation line. Changing from excitation of the spectrum operating at 647.1 nm to an argon ion laser operating at 514.5 nm results to a 3.7 times increase of the intensity of the recorded spectrum [**Loader, 1970**].

The quantum theory of Raman Scattering gives information about the temperature dependence of the Raman Scattering. According to the Boltzmann distribution law, the relative population in the real levels depicted in figure 2.2 is a function of temperature [**Colthup, 1975**]. Increased temperature results to increased intensity of the anti-Stokes line, since the probability of the anti-Stokes transition event is higher. This is due to the increase in population at higher energy levels.

The quantum theory of the Raman scattering also predicts that the Rayleigh light is coherent, in contrast with the Raman light which is incoherent [**Szymanski, 1967**]. This observation is important since no interference is expected from Raman lines; the intensities of individual spectra are added to produce the composite spectrum.

As mentioned before, the Raman effect consists of a complex phenomenon if we consider the possible vibrations of a polyatomic molecule. If we regard a molecule of N atoms, there are $3N-6$ degrees of freedom excluding simple (in phase) translations and rotations. Therefore $3N-6$ possible vibrational modes exist. If, for reasons of symmetry, two or more vibrational modes coincide, they are called degenerate. Non-degenerate modes are designated by the letters **A** or **B**, doubly degenerate modes by **E**, and triply degenerate by **F**. By virtue of its set of symmetry properties, a molecule can be assigned to a so-called point-group. Point-group theory is beyond the scope of this study, but it should be noted that the number of independent possible vibrations is reduced by the existing symmetry operations to provide the minimum number of linearly independent vibrations that may fully describe the system. This is called an irreducible representation of the point-group. By assigning a molecule to a specific point-group, one may predict all its vibrational properties.

2.4. STRESS DEPENDENCE OF THE RAMAN SPECTRUM

2.4.1 The Harmonic Oscillator

As mentioned earlier, there are $3N-6$ possible vibrations in the general case of a polyatomic molecule. Each one corresponds to an internal displacement co-ordinate. In the purely linear elastic case, the displacement may be regarded as directly proportional to the restoring force. The $3N-6$ set of constants of proportionality are called the force constants. In this case, all vibrations are purely harmonic and the potential energy of the system is the sum of the quadratic terms whose coefficients are the force constants.

Let us regard one simple vibrational motion. According to the above,

$$F = k\,(x-x_0) \tag{2.8}$$

where F is the restoring force, k is the force constant, and $(x-x_0)$ is the distance from the equilibrium position x_0. Integrating equation 2.8 with respect to x provides the potential energy function U_p:

$$U_p = \frac{1}{2}k\,(x-x_0)^2 \tag{2.9}$$

which is the parabola shown in figure 2.3a. This oscillation is harmonic and its frequency ν is independent from the distance from the position of equilibrium x_0. The quantum theory of the harmonic oscillator only allows one transition from one energy state to another $\Delta\nu = \pm 1$. These energy states are shown as dotted lines in figure 2.3a and are equidistant.

It is, however, well known that phenomena like overtones, combination bands, or difference bands **[Colthup, 1975]** cannot be explained by the simplistic harmonic theory. In addition, concepts like bond breaking at high deformations demand a different approach to the potential energy function. Such an approximation is the *Morse function*, where the potential energy is a function of the dissociation energy D_e, or the energy required to break the bond:

$$U_p = D_e(1-\mathrm{e}^{-b(x-x_0)})^2 \tag{2.10}$$

where b is a constant.

In figure 2.3b, the potential energy of the anharmonic oscillator is depicted. The dotted lines represent the allowable energy levels. The quantum theory accounts for more than one transition between energy levels.

2.4.2 Stress dependence of the vibrational frequency

The second derivative of the Morse anharmonic potential energy function provides the equation for the force constant [**Tashiro, 1990**]:

$$k = 2b^2 D_e (2e^{-2b(x-x_0)} - e^{-b(x-x_0)}) \tag{2.11}$$

As can be seen, the force constant is no longer a constant in the anharmonic case. Moreover, it is a function of the internuclear displacement and its dependence is depicted in figure 2.4a. For small positive internuclear displacements, $x = x-x_0 > 0$, the force constant is monotonically decreasing. For positions near the equilibrium, the Morse function resembles the harmonic oscillator function, and the frequency ν can be regarded as proportional to $\sqrt{k}$ [**Colthup, 1975; Tashiro, 1990**]. This results to a low frequency shift $\Delta\nu$ of the vibration. On the other hand, when the bond is compressed, that is when $\Delta x < 0$, the force constant increases causing a high frequency shift $\Delta\nu$.

The above principle provides the theoretical background for the frequency shift of distinct Raman bands when the molecule is subjected to external load. Theoretical determination of the expected shift $\Delta\nu$ has been presented for simple molecules [**Wool, 1975; Tashiro, 1990**]. More complicated analyses include the lattice dynamical theory to predict stress induced shifts in polymer chains.

For small displacements (figure 2.4.b), the stress dependence may be regarded to a good approximation as proportional to the applied stress field σ. Bretzlaff and Wool [**1983**] propose the following:

$$\Delta\nu = a_\sigma \sigma \tag{2.12}$$

where a_σ is the proportionality constant.

The key feature that links the stress dependence of the molecule to any macroscopic deformation is whether this deformation affects the material to a molecular level. Whereas amorphous materials are not expected to show detectable stress sensitivity, highly crystalline materials, such as Kevlar® [**Galiotis, 1985**] or carbon

[**Robinson, 1987b**], are reported to exhibit measurable stress sensitivity. Provided that a suitable reference value is provided for the unstressed material, experimental calibration curves enable us to translate Raman frequency shifts to absolute strain. In most cases, a direct proportionality of the shift to the applied strain is adequate [**Galiotis, 1983**], although higher order dependence has been proposed in the literature to account for non-linear elastic behaviour [**Melanitis, 1994**].

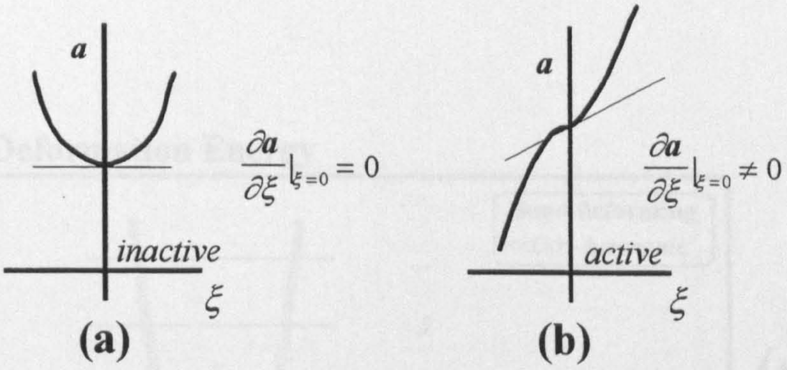

Figure 2.1: The variation of the polarisability ***a*** with the displacement coordinate ξ; (a) Raman active vibration; (b) Raman inactive vibration.

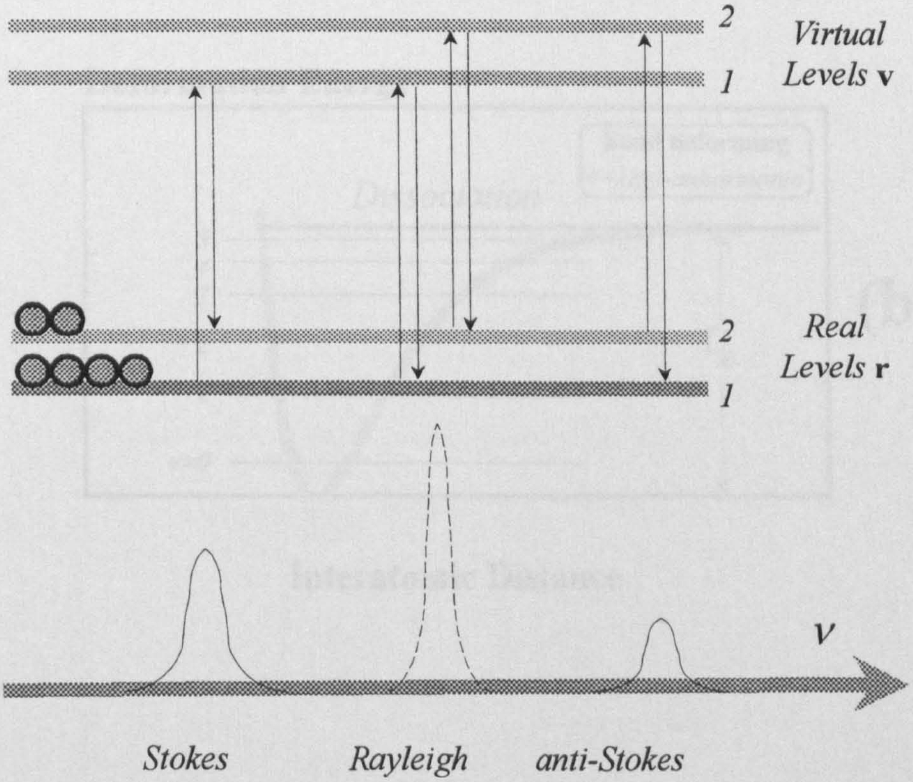

Figure 2.2: The Raman Effect: the marked transitions are responsible for the respective lines.

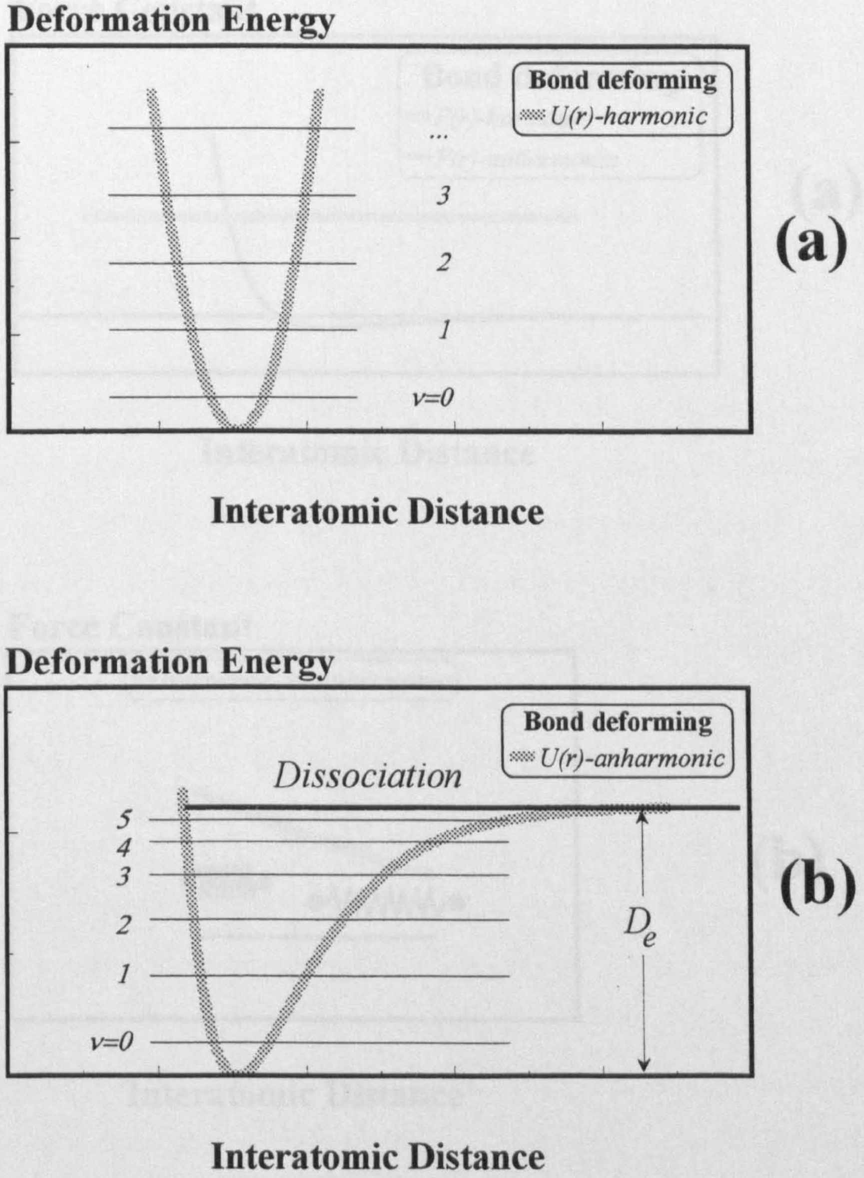

Figure 2.3 (a)The potential energy function U_p for the *Harmonic Oscillator*. The dotted lines mark the allowable energy levels and are equidistant. (b) The potential energy function U_p for the *Anharmonic Oscillator*. The dotted lines mark the allowable energy levels and are no longer equidistant.

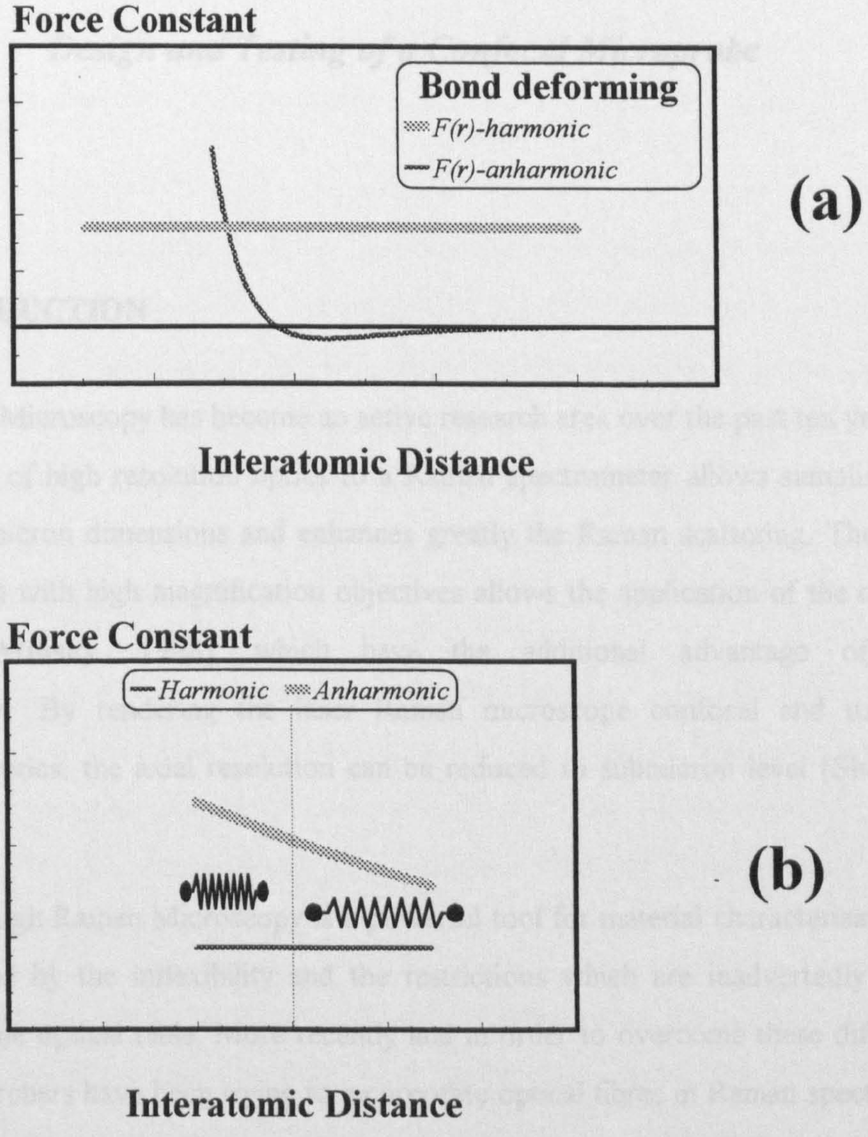

Figure 2.4 (a) the variation of the force constant as a function of interatomic distance; (b) for small displacements, the stress dependence may be regarded to a good approximation as proportional to the molecular deformation [**Vlattas, 1995**].

Chapter 3: Remote Raman Microscopy;

Design and Testing of a Confocal Microprobe

3.1. INTRODUCTION

Laser Raman Microscopy has become an active research area over the past ten years; the incorporation of high resolution optics to a Raman spectrometer allows sampling from areas of submicron dimensions and enhances greatly the Raman scattering. The use of lasers coupled with high magnification objectives allows the application of the *confocal principles* **[Minsky, 1988]**, which have the additional advantage of *depth discrimination*. By rendering the laser Raman microscope confocal and using the appropriate optics, the axial resolution can be reduced to submicron level **[Sharonov, 1994]**.

Although Raman Microscopy is a powerful tool for material characterisation, the user is limited by the inflexibility and the restrictions which are inadvertedly part of working on the optical table. More recently and in order to overcome these difficulties, various researchers have been trying to incorporate optical fibres in Raman spectroscopy set-ups. The advantages of the use of optical fibres are (a) flexibility and ease of alignment, and (b) decoupling of the Raman probe from the optical tables, which allow remote sampling in diverse (and occasionally hostile) environments. Various geometries are used such as fibre bundles, incorporating delivery and collection fibres (figure 3.1a) **[Dai, 1992; Williams, 1990; Schopp, 1990]**, or systems where the collection path is physically different from the delivery path (figure 3.1b, c, d) The optical paths may be either parallel to each other **[Carraba, 1992]** or at an angle up to 180° **[Myrrick, 1990]**. The efficiency of the fibre optic probes depends on the relative position of the laser delivery and collection fibres, and may be enhanced by the use of capillary tubes, which confine the laser illumination to a small volume [**Hendra, 1988**]. In the case of fibre fluorometric sensors, the effective depth and equivalent path length are both experimentally and theoretically assessed, both for a single [**Zhu, 1992a**] and for a double fibre configuration [**Zhu, 1992b**]. The angular dependence, as well as the optimum fibre geometry are theoretically simulated for maximum signal acquisition [**Plaza, 1986**].

However, when spatial resolution is important, as in the case of microprobing or Raman imaging [**Barbillat, 1994**], it is essential to focus the excitation beam to a finite size spot which limits the resolution of the system. In this case the delivery and collection paths are distinct [**Galiotis 1994**], and interchangeable microscope objectives may be used to account for sampling efficiency, resolution and working distance [**Da Silva, 1994**]. The efficiency of the remote probes is retained for more than 100 m away from the sampling area [**Everall, 1994**].

Attempts have also been made to apply the principles of confocality to set-ups incorporating fibre optics where the actual fibre-optic tip is used as the confocal aperture [**Gu, 1993**]. Appropriate matching of the optical components of the system can lead to high resolution set-ups, where the use of single mode fibres may even be beneficial due to increased coherence [**Gu, 1993**].

The combination of the aforementioned principles led to the in-house design and testing of a new fibre-optic confocal laser Raman microscope. This remote Raman Microprobe (ReRaM) has been designed so that specimens of any size and shape and under a variety of different environments can be interrogated. The incorporation of tailor-made optics at both input and output positions of each fibre, ensures laser collimation, maximum efficiency and enhancement of the Raman scattering. The purpose of the ReRaM is to combine the versatility of optical fibre Raman sensors with high resolution microprobing and depth discrimination, through the application of confocal principles. Finally, the incorporation of a CCTV camera may allow optical observations of the specimen during Raman data acquisition, rendering the system a fully functional optical microscope.

The system design primarily aims to obtain Raman spectra from polymer composite materials while they are subjected to various mechanical loading conditions. However, it can also be used for a whole variety of technological applications, such as, to conduct remote Raman measurements in chemically hostile environments or elevated temperatures, to monitor curing of polymer resins and the crystallisation of polymers during solidification, to provide non-destructive health monitoring of sections of large structures (e.g. aircrafts, ships, bridges, etc.) and to assess the quality of oil supplies or other chemical media.

3.2. THEORETICAL CONSIDERATIONS - DESIGN RATIONALE

3.2.1 The Raman System and its Basic Elements

A typical conventional Raman set-up is shown in figure 3.2a, where the distinct parts of the system are shown. These comprise the *excitation source*, the *microscope*, the *spectrometer* with the *data collection devices*, and, finally, the *data processing equipment*.

The excitation source is in most cases a *laser*. The laser is the acronym for *Light Amplification* by *Stimulated Emission* of *Radiation*. The development of lasers in the last decades has provided Raman spectroscopists with the perfect source for their studies. This is because lasers provide highly monochromatic coherent light of given frequency and polarisation. Lasers operating at *single mode* have the minimum bandwidth and, thus, provide the maximum resolution.

The *Raman microscope* is the key element of the system. As it comprises the excitation and collection optics, it is responsible for the efficiency and the resolution of the system. Since the development of the first practical systems in the early 1970s, the

Raman microscope has emerged as a powerful sampling system with applications in many different fields [**Andrews, 1992**]. A typical Raman Microscope is shown in figure 3.2b. The Raman Microscope combines spatial sensitivity with high local power densities, depending on the *spot size* of the focused laser beam. The *beamsplitter* is commonly a 50/50 white light beamsplitter, which automatically reduces the efficiency of the system by 50%. Other transmission to reflection ratios may also be used. However, the use of *dichroic* or *holographic* beamsplitters can enhance the efficiency of the Raman system dramatically [**Guenther, 1990**]. These beamsplitters exhibit preferential transmission / reflection ratio to the wavelength of the incident light, reflecting maximum laser light and, at the same time, allowing maximum transmission of the Raman light. An important feature of these beamsplitters is their *transmission edge*, which determines the efficiency near the laser frequency. Holographic beamsplitters achieve edges as near as 100 cm^{-1} from the laser line.

The *spectrometer* is responsible for the analysis of the spectrum. Its ability to analyse the frequency of the light depends on the entrance slit width, on its ***f number***, namely the ratio of its focal length to the first collection mirror diameter [**Young, 1993**], as well as on its *dispersive element*. In most cases, this is a *holographic grating*. The surface of the grating is etched with parallel grooves which diffract the incident beam. The number of grooves per mm (usually 300 to 1800) determine the *resolving ability* of the grating.

Since its introduction, the *Charged Coupled Device* (CCD) has replaced the *photomultiplier* as a photon counting device. The CCD has essentially zero dark current and better quantum efficiency than other devices. It is a two-dimensional / metal-oxide semiconductor device, which operates in a charge storage mode [**Andrews, 1992**]. The readout provides information of the stored charges in the CCD *pixels*. The main disadvantage of the CCD is that it is prone to *blooming*, which is caused by charge 'spilling' into adjacent pixels, if the potential well of a pixel fills. This is hardly a problem as far as Raman bands are concerned, but it does not allow observations near the intense laser line, in which case other filtration techniques are needed. Finally, the *data* *processing equipment* consists of the appropriate image analysis software, operating on dedicated hardware platforms.

All the distinct components described earlier play a key role to the requirements needed for the Raman set-up. The source is limited by the user requirements. Powerful lasers are usually bulky and, in most cases, constant cooling water supply is needed. The physical size of the spectrometer is directly related to its resolving ability. In order to avoid compromises regarding the efficiency of the set-up, the decoupling of the Raman Microscope from the optical table is needed. The use of flexible waveguides for the Laser-Microscope-Spectrometer coupling, is the obvious solution that provides the versatility of remote probing, without compromising in excitation or resolving power.

3.2.2 The Raman activity of Optical Fibres

The main problem associated with the use of optical fibres in Laser Raman Spectroscopy, is the high background noise generated by the optical fibre. Although it is perfectly feasible to detect the Raman Shift of strong scatterers, such as aramid **[Jahankhani, 1991]**, the Raman signal of weak scatterers, like that obtained from polycrystalline carbon fibres, is swamped by the background features of the optical fibre.

The main cause of background activity associated with the optical fibre is believed to be the Raman activity of pure silica. The Stokes Raman shift of silica extends over a large frequency range (up to 40 THz) with a broad peak near 13 THz or 440 cm^{-1} (figure 3.3). This behaviour is attributed to the non-crystalline nature of silica glass, where the molecular vibrational frequencies spread out and create a continuum **[Agrawal, 1989]**. The Raman activity scales inversely with excitation wavelength and depends on the specific laser power which is launched into the optical fibre. In this respect, optical fibres are known to act as broad band amplifiers. The background level and features may differ even by one order of magnitude, due to the presence of a variable amount of additives or impurities in them **[Williams, 1990]**.

The activity of the optical fibres may be blocked out by placing a narrow bandpass filter at the output of the delivery fibre to cut out any unwanted scattering. This eliminates the fibre-optic activity and only allows the excitation frequency to reach the sample. In order to eliminate completely the Rayleigh scattering which may be strong enough to excite traceable Raman activity from the collection fibre, a notch filter can be placed before the launching of the laser to the collection fibre. The bandpass and the notch filter act in a complementary fashion; the former 'cleans' the exciting light while the latter only permits the inelastically scattered light to enter the collection fibre-optic. The filter configuration is shown in figure 3.4.

The blocking efficiency of the bandpass filter must be sufficient to eliminate the activity of the laser delivery fibre. An Optical Density (OD) of the order of OD = 3 proved to be satisfactory (that is, allowing 10^{-3} of the intensity of the light of other than the bandpass frequency). It is, however, worth mentioning that the collection fibre-optic is extremely sensitive to the Raleigh backscattered light. Experimentation with filters of increasing optical density showed that the optical density of the notch filter has to be of the order of OD = 6. Otherwise, Raman activity from the optical fibre is still present when weak scatterers are interrogated. This is because the expected order of magnitude for the Raman shift of weak scatterers lies in this area. In the course of this study and for the chosen combination of filters, the bandpass filter was found to reduce the background level whereas the notch filter reduces the intensity of the recorded fibre-optic features (figure 3.5). The two filters reduced the background noise at least to the dark current noise level of the Charged Coupled Device (CCD). Thus, Raman spectrum acquisition even from weak scatterers was perfectly feasible and independent of laser power and/or exposure time (see § 3.4).

3.2.3 Optical Design of the ReRaM

Once the Raman activity of the optical fibres is eliminated, the efficiency of the remote probe depends solely on the careful coupling of the optical components of the system. A single mode polarisation preserving fibre laser may be used for laser beam delivery. In order for the laser beam to propagate efficiently in a single mode fibre, the beam must be focused onto the entrance face of the fibre with approximately the same numerical aperture and, therefore, spot size as the fibre. If the numerical aperture of the beam is too large, the spot size is smaller than that of the fibre and this results in efficiency loss. Similarly, if the numerical aperture of the beam is too small, the spot size is larger than that of the fibre and loss also results [**Young, 1993**]. Careful coupling of the launching optics may result in throughput efficiency higher than 70% [**Pointer, 1990**]. The output of the single mode optical fibre is coherent and can be very well approximated by a Gaussian profile. In addition, the launching of the laser into the single mode fibre leads to the creation of a plane wavefront at the exit point (figure 3.6). In this way, it provides spatial cleaning of the beam, as the optical fibre plays the equivalent role of a pinhole spatial filter [**Guenther, 1990**].

The optical fibre delivers a plane polarised beam at the entrance of the microscope, which is filtered by the bandpass filter and reflected by the beamsplitter to fill the objective. The choice of the beamsplitter should be made after taking into consideration the following parameters: available laser power, transmission of the backscattered Raman light, and operating requirements regarding detection close to the laser line. The use of holographic beamsplitters provides both high laser line reflection (90%) and Raman light transmission (90%).

The use of exchangeable collimating optics at the delivery fibre output, provides the desirable expansion of the beam, to fit the numerical aperture of the objective. This is particularly important in order to exploit fully the resolution capabilities of the given objective. The laser spot radius R_s, which is defines the lateral resolution of the system, can be calculated as:

$$R_s = \frac{f\lambda}{\pi R_L} \tag{3.1}$$

where λ is the incident wavelength, f is the focal distance of the objective, and $2R_L$ is the diameter of the beam. It is obvious that the spot is minimum $R_s = \frac{\lambda}{\pi\,(na)}$ where the numerical aperture of the beam *na* is identical to the numerical aperture of the objective. Overfilling the objective may cause power loss and vignetting [**Young, 1993**], due to diffraction of the incident laser beam by the pupil of the objective. Hence, the delivery single mode fibre serves the dual purpose of spatial filtering of the laser and expanding the beam so as to match the objective aperture.

The choice of the objective is the most important parameter, affecting the efficiency of any Raman microscope. In particular, the numerical aperture of the objective defines the spot size and, consequently, the spatial resolution of the system. A small spot delivers higher specific power of the sample and, thus, enhances the Raman scattering. Moreover, the numerical aperture of the objective defines the solid angle of the Raman light collection. Its magnitude defines the efficiency of the system as far as the collection of the backscattered radiation is concerned. For example, if ultra-long-working-distance lenses are to be used to avoid close contact with the specimen, then this can only be accomplished at large numerical apertures, and leads, therefore, to less efficient light collection.

Finally, in order to receive the total Raman signal collected by the objective, the numerical aperture of the collection fibre has to match or supersede the numerical aperture of the launching lens (figure 3.7). A single mode fibre cannot be used since the core size and the numerical aperture would reduce dramatically the efficiency of the system by reducing the collection solid angle.

3.2.4 The Confocal Principle

In figure 3.7, the solid collection angle is shown. In practice, the collection fibre is underfilled, and, in that sense, acts as a finite size aperture **[Gu, 1993]** rendering the system confocal, without dealing with the fibre profile dependent pupil function. The above is assumed to be true for a multimode fibre where, for bound rays, we regard the ideal case of a step pupil function $\Phi(r)$ **[Wilson, 1990]**:

$$\Phi(r) = \begin{cases} 1, r \leq 1 \\ 0, \text{otherwise} \end{cases} \tag{3.2}$$

A confocal arrangement used in reflection, is shown in figure 3.8. The pinhole is placed before the detector, providing depth discrimination. The idea consists of using a second microscope to image a pinhole aperture on a single point of the specimen [**Minsky, 1988**]. As has been proved both experimentally and theoretically, the application of the confocal principle improves the resolution at the expense of field of view. Stokes light is generally regarded as incoherent [**Szymanski, 1967**] and has a longer wavelength. However, the resolution results essentially from the primary incident radiation [**Wilson, 1990**]. Thus, although the numerical values are different and the sectioning strength is generally weaker, the principles of scanning and confocal imaging may be applied to Fluorescent and Raman Spectroscopy [**Wilson, 1990**].

For a given objective, the depth discrimination depends on the size of the pinhole aperture and the magnification of the system on the pinhole plane. Thus, spatial filtering at the collection fibre plane can be achieved by changing the focal length of the launching lens. This is understood as projecting the optical fibre tip with the proper magnification on the object plane. The magnification is dependent on the ratio of the launching lens focal length divided by the objective focal length and is proportional to the depth of focus (figure 3.9):

$$\frac{f_j}{f_{obj}} \propto \frac{R_{fo}}{R_{ca}} \tag{3.3}$$

where $2R_{fo}$ is the fibre optic core diameter, $2R_{ca}$ is the confocal aperture diameter, and f_j and f_{obj} are the focal lengths of the launching and objective lenses respectively.

The confocality of the system is demonstrated in figure 3.10, where the Raman spectrum of a carbon fibre embedded in an epoxy resin matrix, is obtained. As can be seen, a four-fold improvement in confocality is observed by reducing the confocal aperture from 2.8 μm to 1.8 μm. It is also important to note that the spatial filtering occurs before the actual launching in the multimode fibre and, as a result, the loss of coherence is not regarded as important. The collected light is subsequently launched via the delivery fibre optic to the single monochromator (figure 3.11). Matching the aperture of the optical fibre to the ***f number*** of the spectrometer has the additional advantage of making the output optics redundant.

3.3. EXPERIMENTAL SET-UP

The principles described in detail above, were used for the construction of the Remote Raman Microprobe (ReRaM) shown schematically in figure 3.11. The 514.5 line of a linearly polarised and operating at single mode argon ion laser (a) 1.3 mm in diameter, is directed through a 1/2 λ waveplate (b) and is focused onto a 10 μm single-mode polarisation-preserving optical fibre. The coupling between the incident laser beam and the fibre optic is achieved by the use of pre-focused fixed optics [**Pointer, 1990**]. The lens (c), with focal length f_c = 10 mm, focuses the beam down to a 2.5 μm spot, achieving a maximum throughput efficiency of 70%. The optimisation of the throughput efficiency is performed by using a four axis positioner. The same configuration at the output (d) produces a collimated beam of 3.0 mm in diameter, using a lens with focal length f_d = 20 mm. The beam passes through the bandpass filter (e), is reflected on a holographic beamsplitter (f) and fills the aperture of the objective (g). The latter is a 80x Olympus MS Plan ultra-long-working-distance (4.7 mm) objective of numerical aperture of 0.75, which has been corrected for infinity. This experimental set-up results to an optimum focal spot diameter of approximately 0.5 μm on the objective focal plane.

As far as collection is concerned, the 180° backscattered light goes through the holographic beamsplitter which attenuates the 514.5 line, and is then reflected by the mirror (h). The mirror (h) may be slid out for white light imaging. The longpass filter (i) (edge at the red side: 99 cm^{-1}) further blocks the remainder 514.5 nm light to avoid excitation of the collection fibre optic. The beam is then focused to a 50 μm multimode fibre (j). A selection of lenses may be used to provide the appropriate magnification of the sampling area and, at the same time, spatial filtering of the Raman signal (f_j = 30 ~ 63 mm; the equivalent confocal aperture is calculated from equation 3.3). The output of the fibre is collimated again (k) and is focused at the slit of a SPEX 1000M single Monochromator. Signal acquisition is performed with a Wright Instruments air-cooled CCD (300x1200 pixels) (l) and the spectral features are analysed by a Personal Computer.

3.4. APPLICATIONS

The confocality of the system has been demonstrated earlier (figure 3.10). Although the system was designed to monitor in situ stresses in composites, its versatility can be demonstrated in a variety of applications. Here the sensitivity and throughput of the ReRaM is shown by reference to the Raman spectra of a number of commercial materials.

Ceramics

The spectrum in figure 3.12a was acquired using the experimental parameters described earlier and 1 mW of laser (514.5 nm) power. The integration time was 5 s. The data of figure 3.12a illustrate the fundamental vibration at 520 cm^{-1} together with the first overtone at approximately 950 cm^{-1}. In figure 3.12b spectra from commercial ceria-stabilised (Ce-TZP) and yttria-stabilised (Y-TZP) tetragonal phase zirconia are shown. Again, 1 mW of laser power and 5 s of integration time were used.

Carbon Fibres

In figure 3.13, the Raman spectra of three different Courtaulds Graphil carbon fibres of low (LM), intermediate (IM) and high (HM) Young's moduli are demonstrated. The spectra were taken with 1 mW of laser power and 30 s of integration time. The main Raman peaks of the first order region at 1360 cm^{-1} and 1580 cm^{-1} are illustrated. In the case of the high modulus / high crystallinity carbon fibre, the second order overtone of the 1360 cm^{-1} at 2705 cm^{-}1 is also clearly obtained.

Commercial Polymers

In figure 3.14a, the spectra of commercial nylon 6,6 fibres used in carpets are illustrated within the 500-1700 cm^{-1} spectral window. This data were collected using the ReRaM with 1 mW laser power and an integration time of 30 s. All Raman features corresponding to amide, C-CO stretch, C-C stretch, N-H wagging, CH_2 bending vibrations are seen. Backbone vibrations are sensitive to the laser polarisation direction as shown in figure 3.14a. In figure 3.14b, the 1000-1400 cm^{-1} fingerprint spectral region of commercial polyethylene fibres taken with 1 mW of laser power and 10 s of integration time are shown. The C-C stretching (1000-1130 cm^{-1}), CH_2 rocking (1170 cm^{-1}), C-H twisting (1200 cm^{-1}), and CH_2 bending (1420 cm^{-1}) vibrations can be clearly seen in the spectra.

High Performance Polymer Fibres

Finally, in figure 3.15, the spectra of three different rigid and semi-rigid rod polymer fibres in their fingerprint spectral region of 1000-1700 cm^{-1}, are presented. The fibres are: (a) the poly(p-phenylene terepthalamide) (PPTA) fibre, known by the trade name of Kevlar®49, (b) the heat-treated poly(p-phenylene benzobisoxazole) fibre (PBO), and (c) the poly(p-phenylene benzobisthiazole) fibre (PBZT). The data were collected using a laser power of 0.3 mW and an integration time of only 0.5 s. The intensity of the Raman bands indicates that these polymer fibres are extremely strong Raman scatterers. However, as reported earlier **[Vlattas, 1994]**, both PBZT and PBO fibres exhibit considerable fluorescence which is particularly exarcebated at low excitation wavelengths, such as the 514.5 nm line employed in this work. The phenyl ring stretching vibrations of all three fibres within the frequency range 1600-1620 cm^{-1} are prominently featuring in figure 3.15. The very strong bands at 1474 cm^{-1} for the PBZT and 1559 cm^{-1} for the PBO fibres, correspond to heterocyclic ring and C=N stretching vibrations, respectively.

3.5. SUMMARY

A new remote Raman microprobe was designed and tested. Fibre-optics were used as flexible waveguides for transporting the incident laser beam and for collecting the inelastically scattered (Raman) light. The high background noise generated by the delivery optical fibre was successfully eliminated by the use of a narrow bandpass optical filter. A notch filter located at the entrance of the collection fibre optic was also employed to block the elastically scattered (Rayleigh) radiation. By careful selection of the optical density of the optical filters the background noise from the fibre optics was reduced to the dark current noise level of the CCD detector. The polarisation direction of the incident laser beam vis-à-vis a specimen reference axis was controlled by employing a polarisation preserving delivery fibre optic. The use of a single mode fibre had also added the advantage of delivering a plane wavefront at the delivery fibre optic exit point, providing spatial 'cleaning' of the incident beam. The use of interchangeable collimating optics provided the desirable expansion of the beam to fit the numerical aperture of the objective. The collection fibre optic was selected to match the numerical aperture of the objective for maximum efficiency. With the use of tailor made optics the collection fibre was underfilled, so as to exploit the confocal nature of the optical fibre endface. The confocal aperture was shown to be controlled by the ratio of the focal distance of the launching lens to that of the objective lens. Finally, the ability of the probe to provide high quality data from different classes of materials was demonstrated.

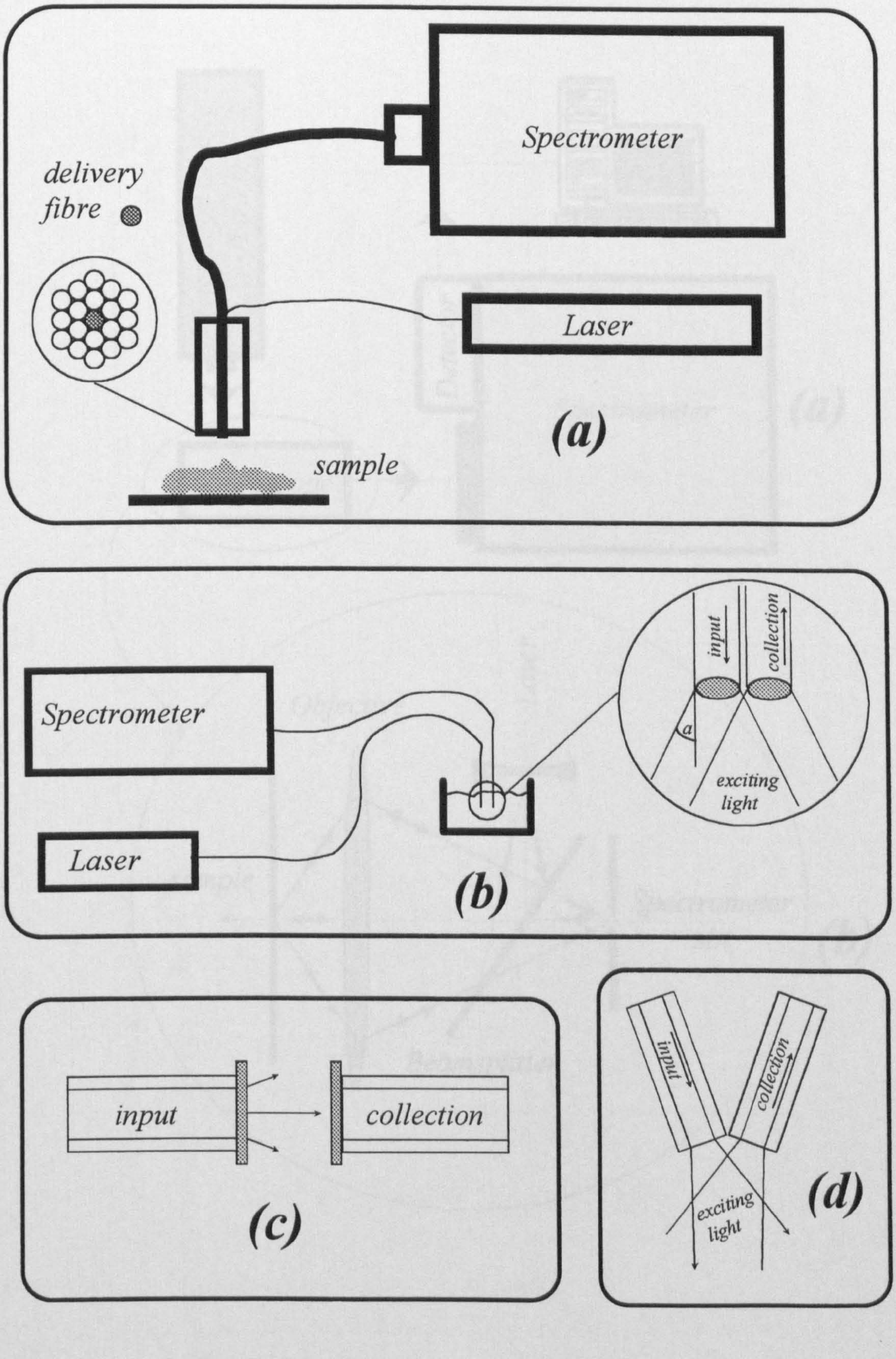

Figure 3.1 Optical fibre Raman probes; various geometries.

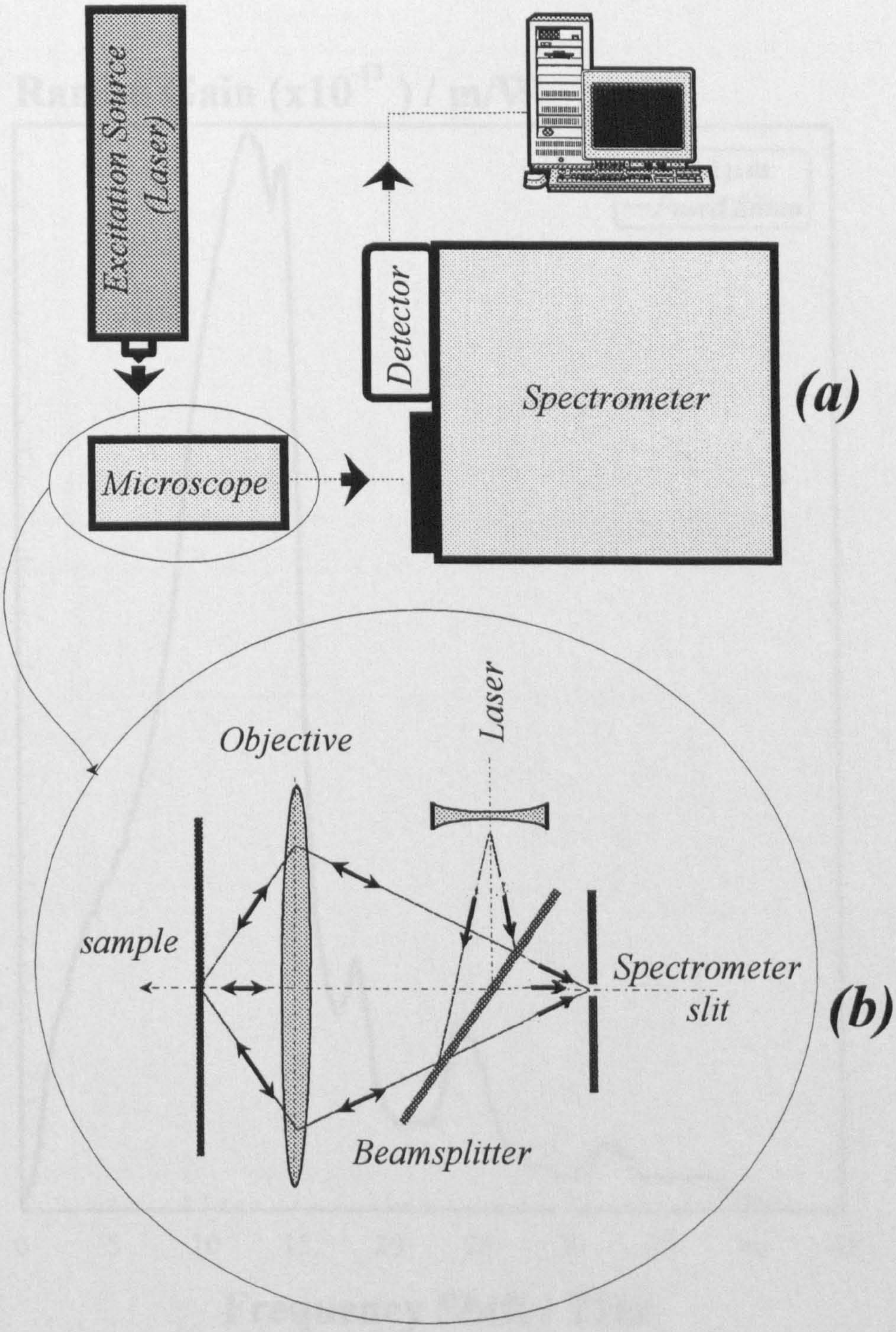

Figure 3.2 (a) Conventional Raman set-up; (b) the Raman microscope.

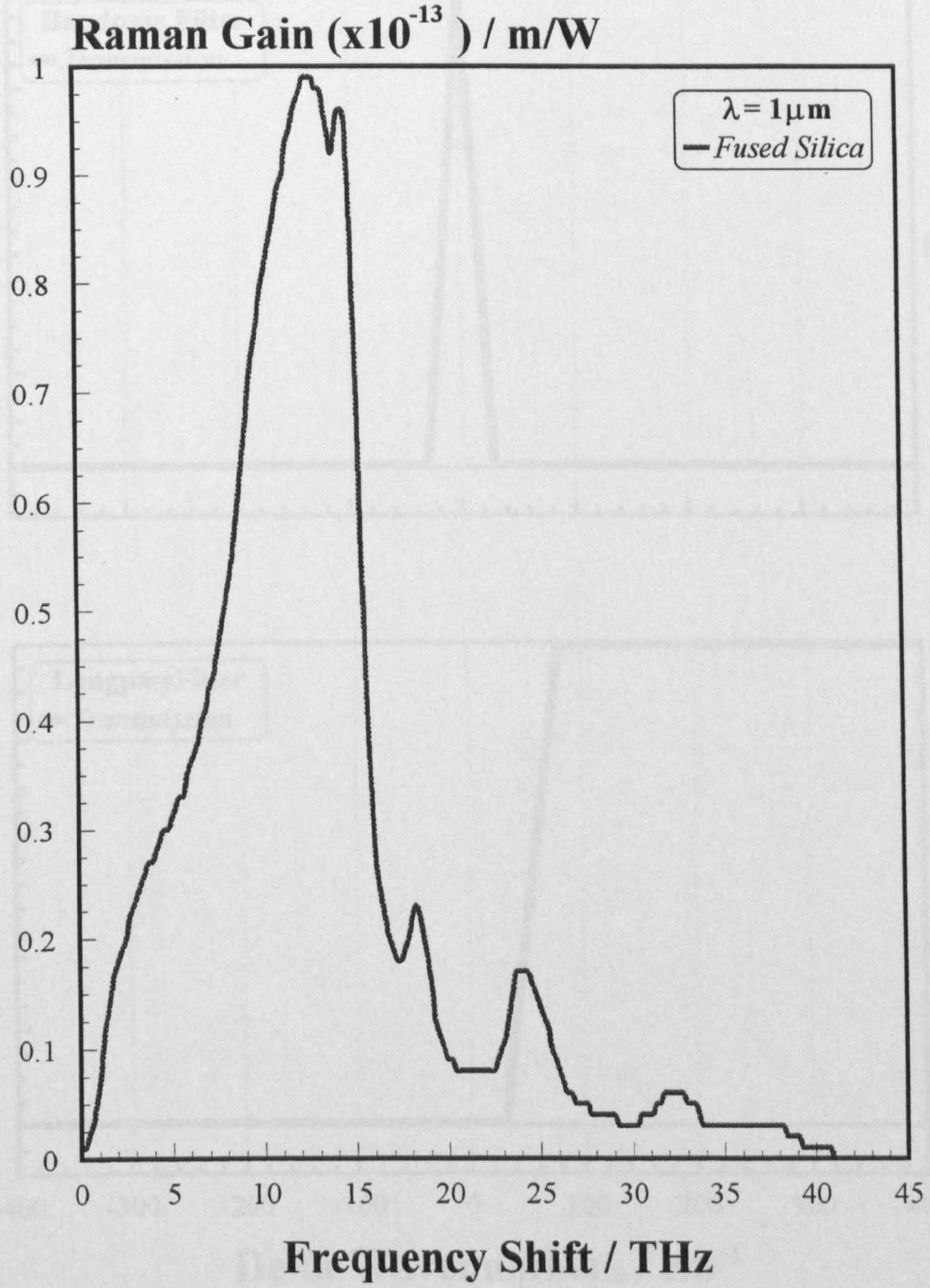

Figure 3.3 The Stokes Raman spectrum of Silica.

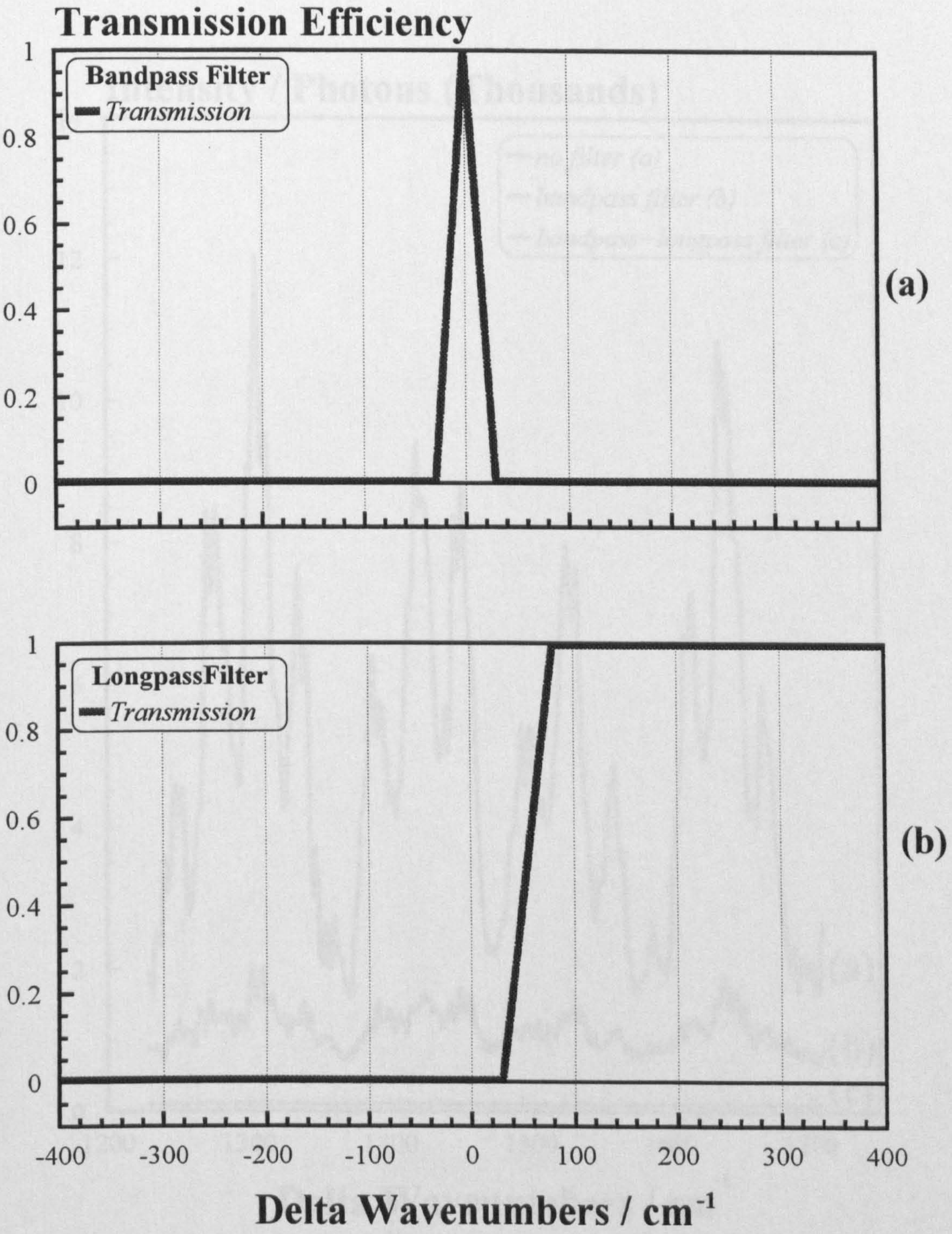

Figure 3.4 Schematic representation of the filtering requirements in order to discard the fibre-optic Raman activity.

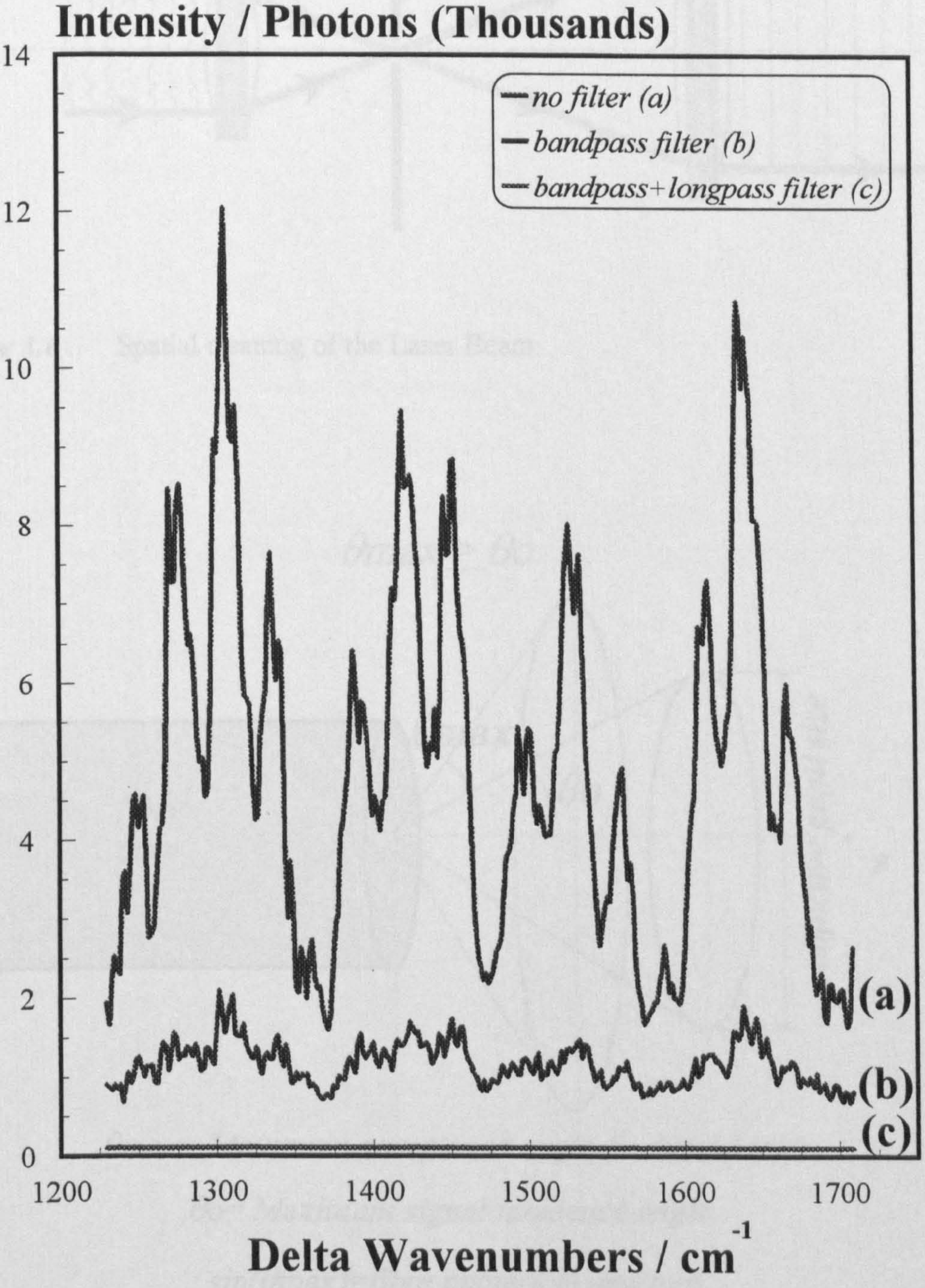

Figure 3.5 Observed features attributed to the Raman activity of the optical fibres. At prolonged exposure times, the features cover the Ráman signal from weak scatterers.

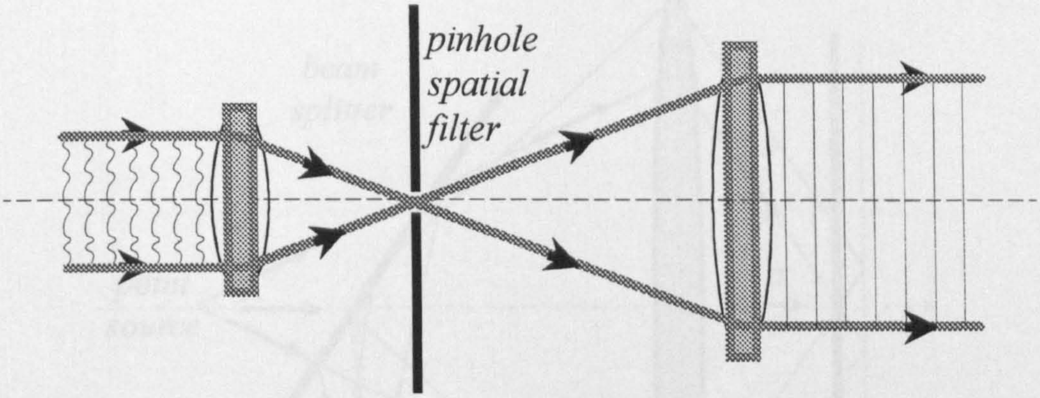

Figure 3.6 Spatial cleaning of the Laser Beam.

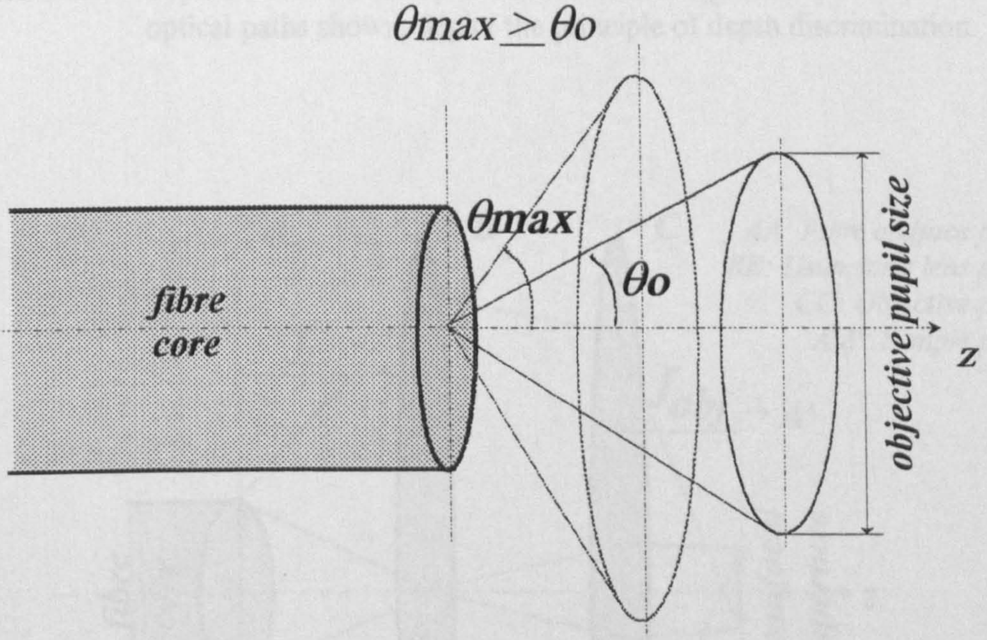

θmax= Maximum acceptance angle for bound rays

θo= Maximum signal incidence angle

sin(θmax)=fibre numerical aperture

Figure 3.7 The numerical aperture of the collection fibre should be more or equal to the numerical aperture defined by the objective aperture and the focal length of the launching lens.

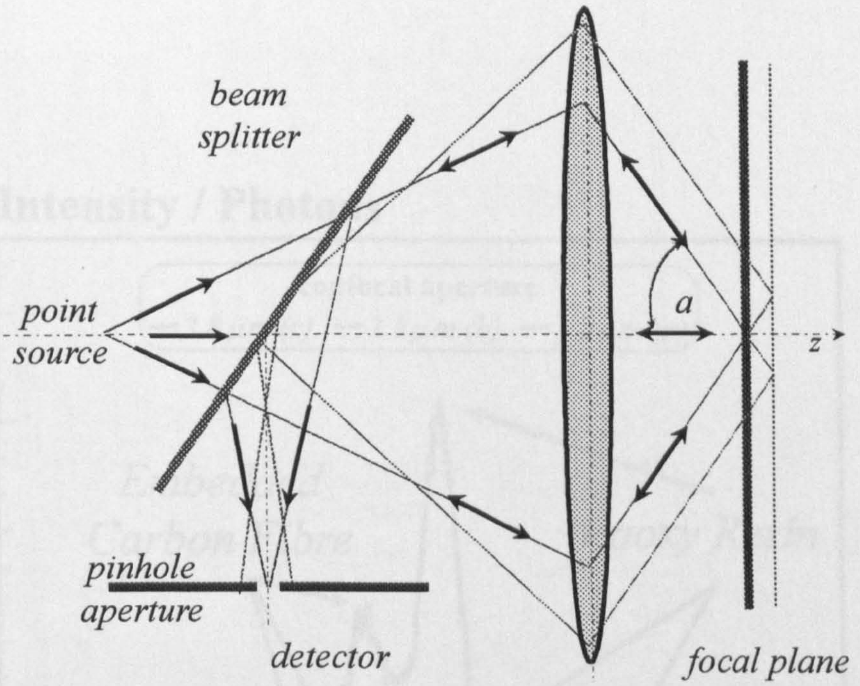

Figure 3.8 Typical confocal set-up in reflection mode [**Wilson, 1990**]. The different optical paths shown, depict the principle of depth discrimination.

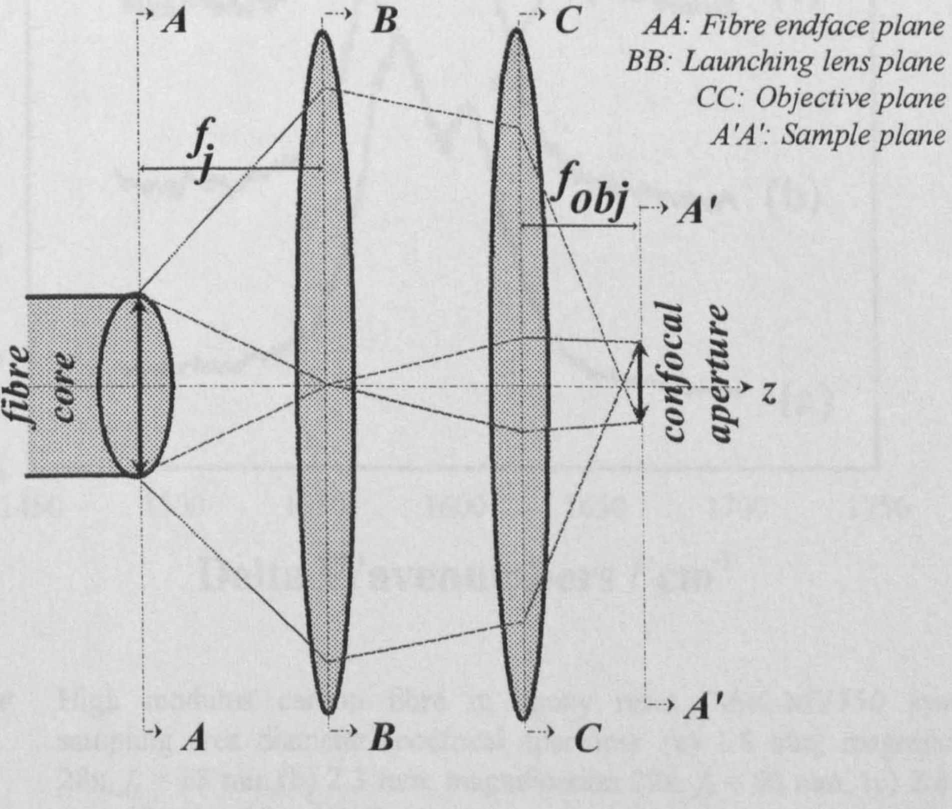

Figure 3.9 The confocal aperture is defined by the magnification of the launching lens.

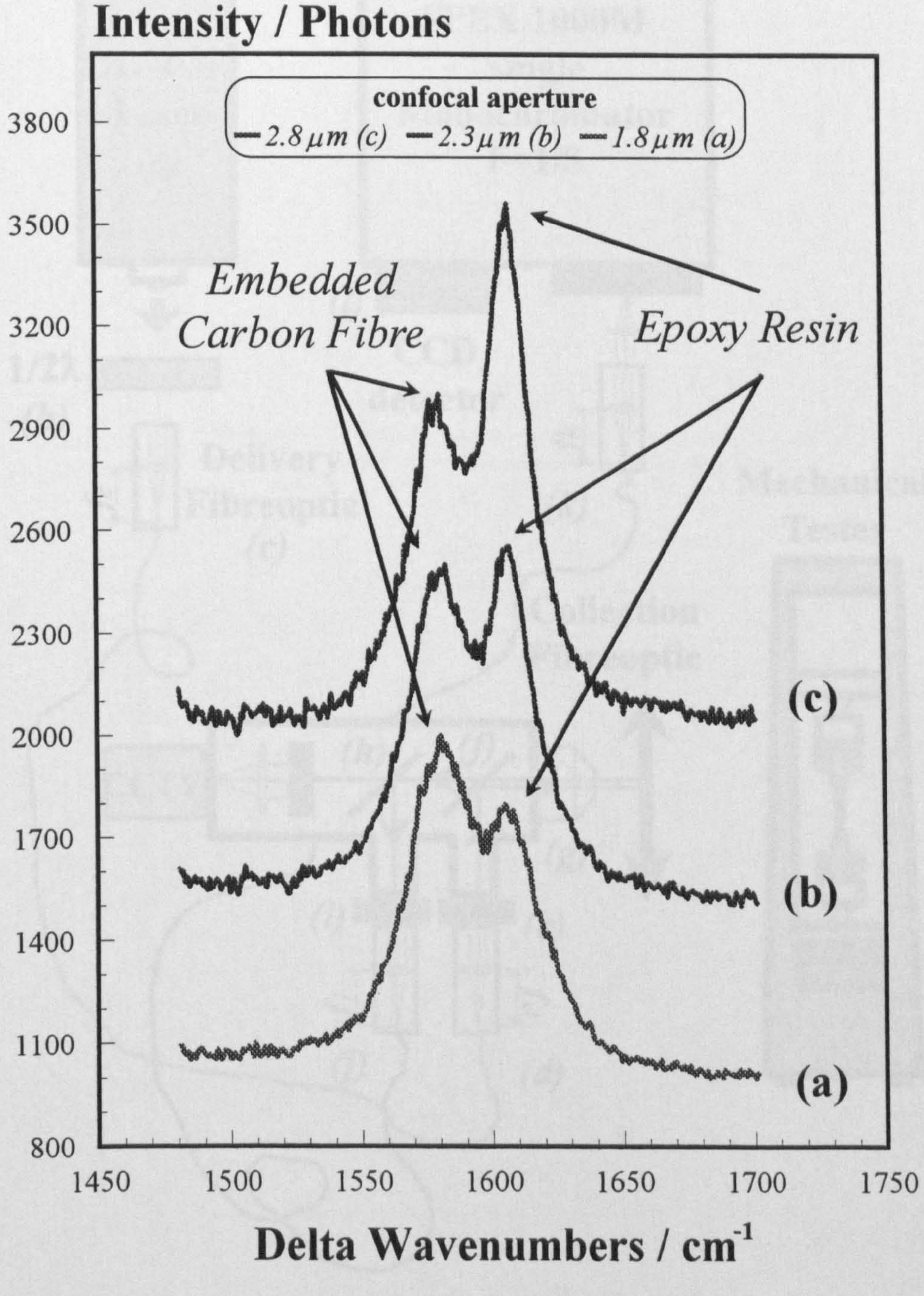

Figure 3.10 High modulus carbon fibre in epoxy resin (M40-MY750 system); sampling area diameter (confocal aperture): (a) 1.8 mm, magnification 28x, f_j = 63 mm,(b) 2.3 mm, magnification 22x, f_j = 50 mm, (c) 2.8 mm, magnification 18x, f_j = 40 mm.

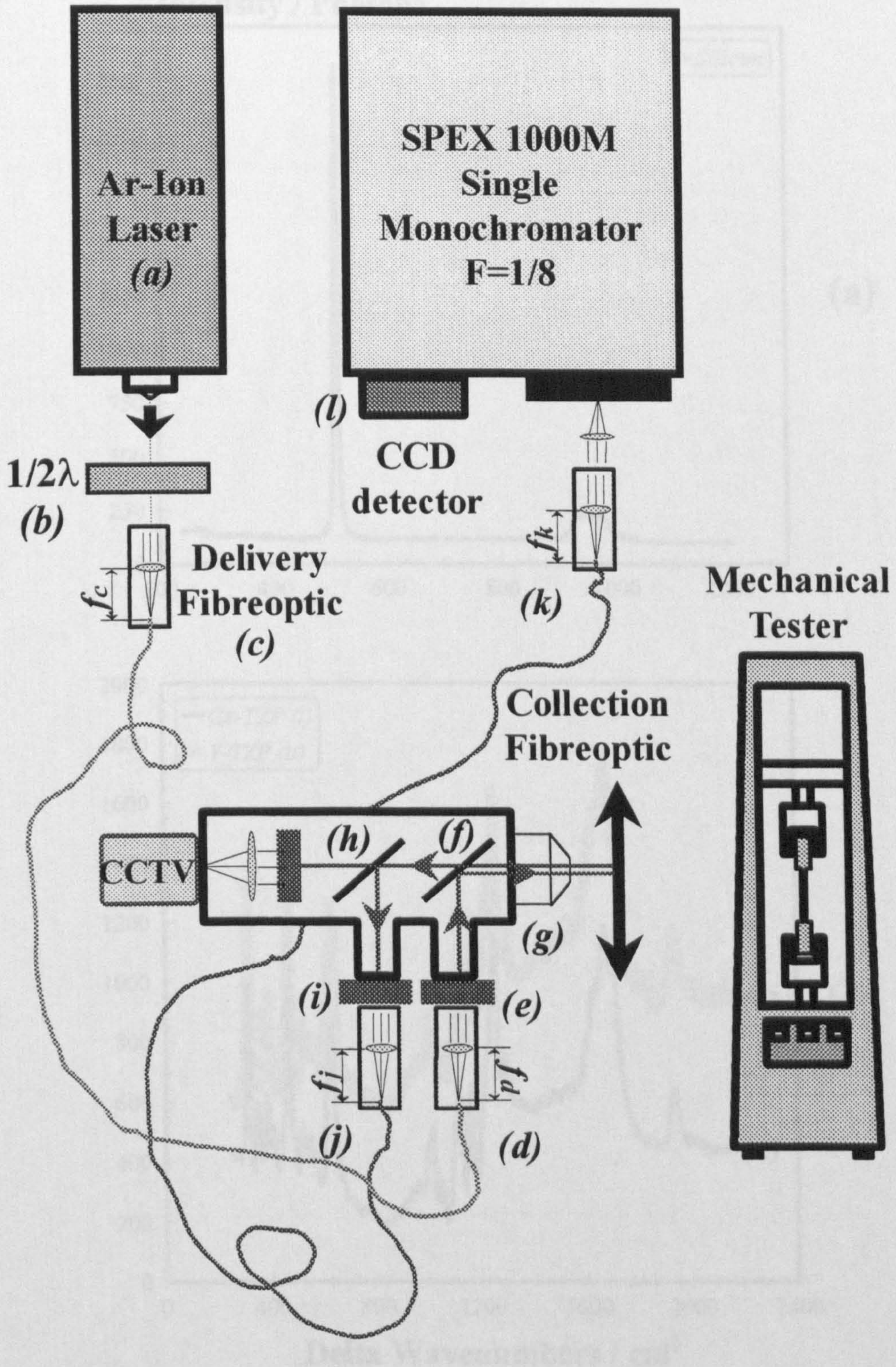

Figure 3.11 The experimental set-up, incorporating the Remote Raman Microprobe (ReRaM).

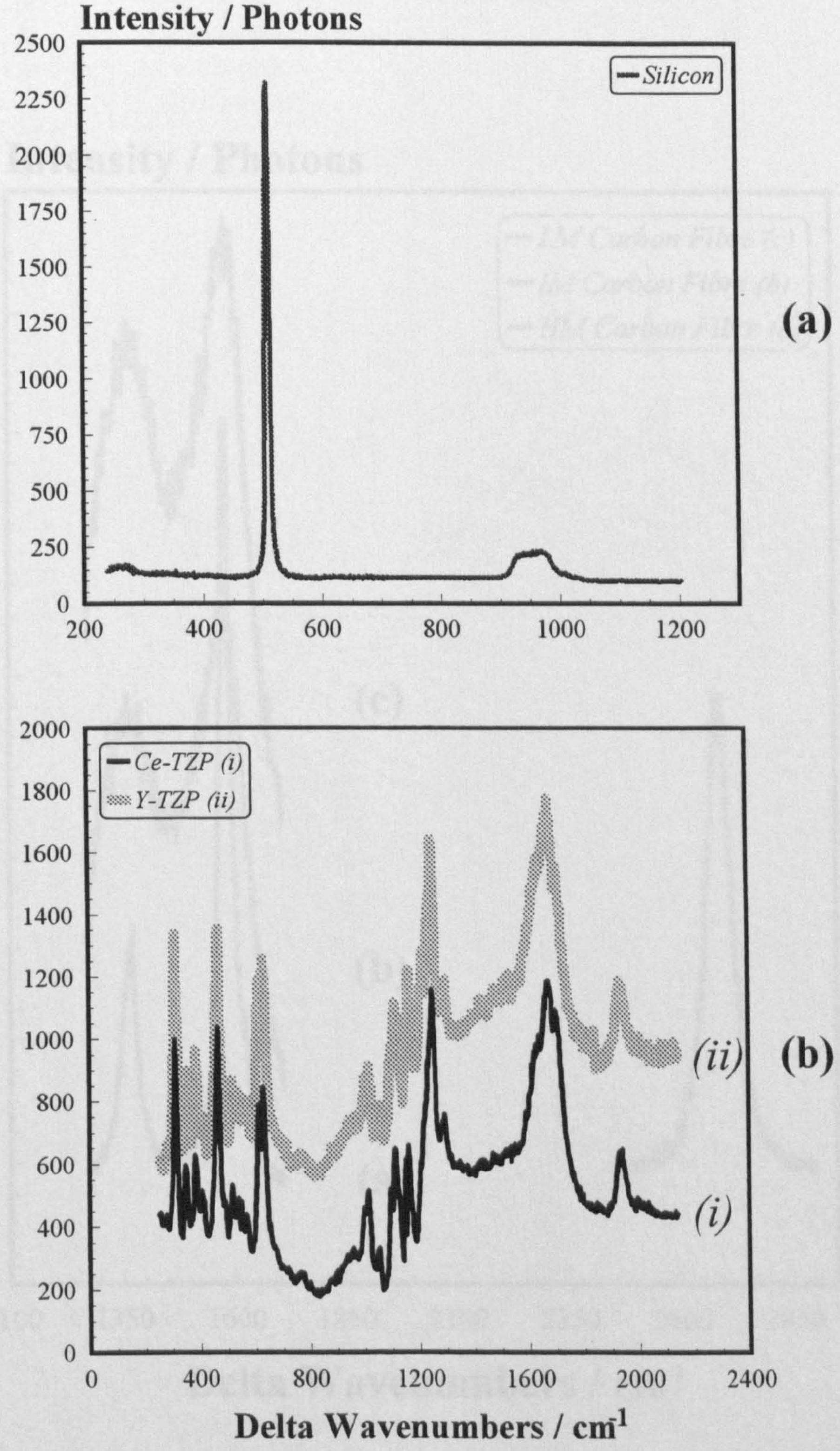

Figure 3.12 Laser Raman spectrum of (a) Silicon (exposure time 1 s, laser power 1 mW); (b) ceramics; tetragonal (Y-TZP) and monoclinic (Ce-TZP) phase zirconia spectra (exposure time 5 s, laser power 1 mW).

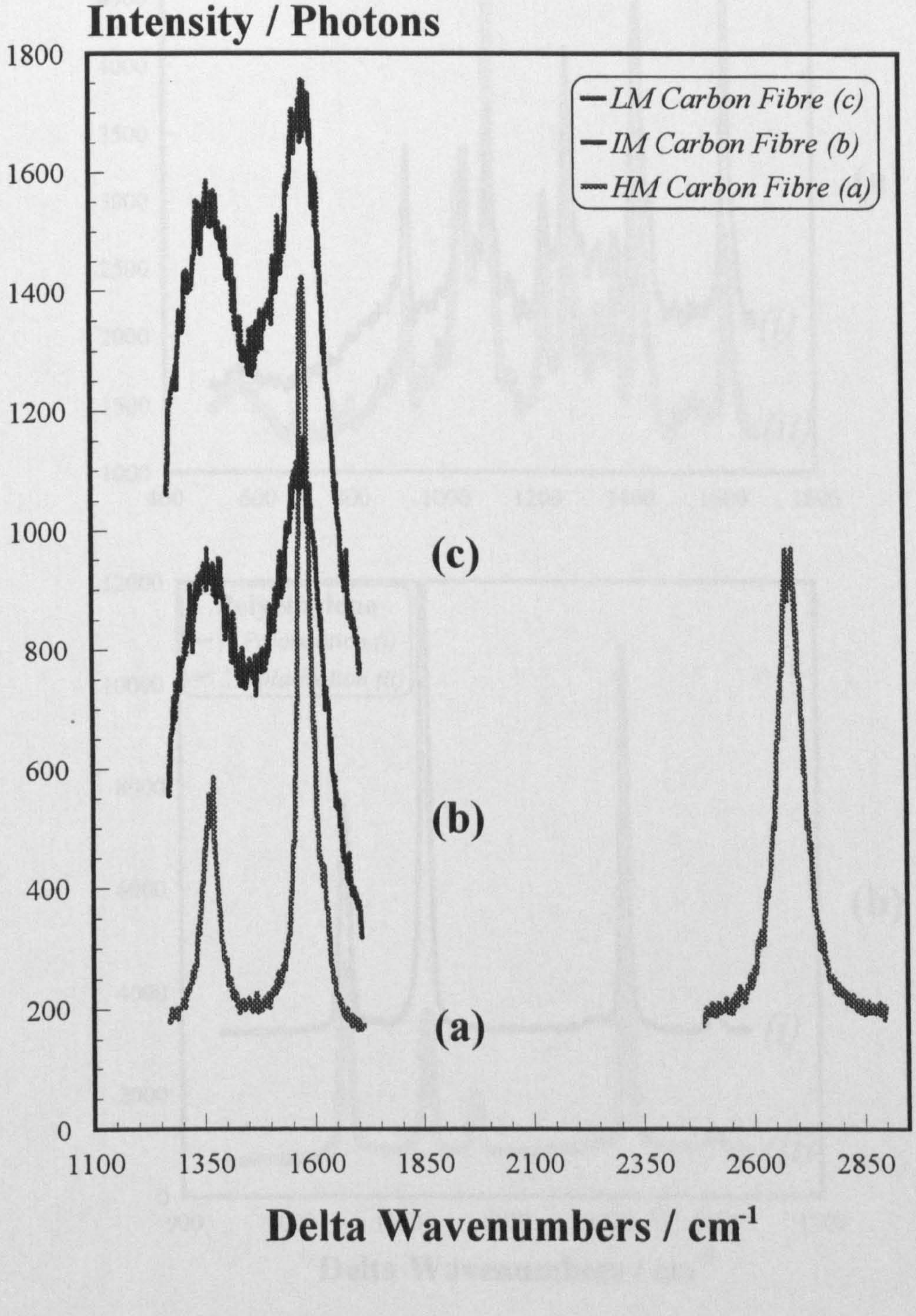

Figure 3.13 Laser Raman spectrum of Carbon Fibres (exposure time 30 s, laser power 1 mW).

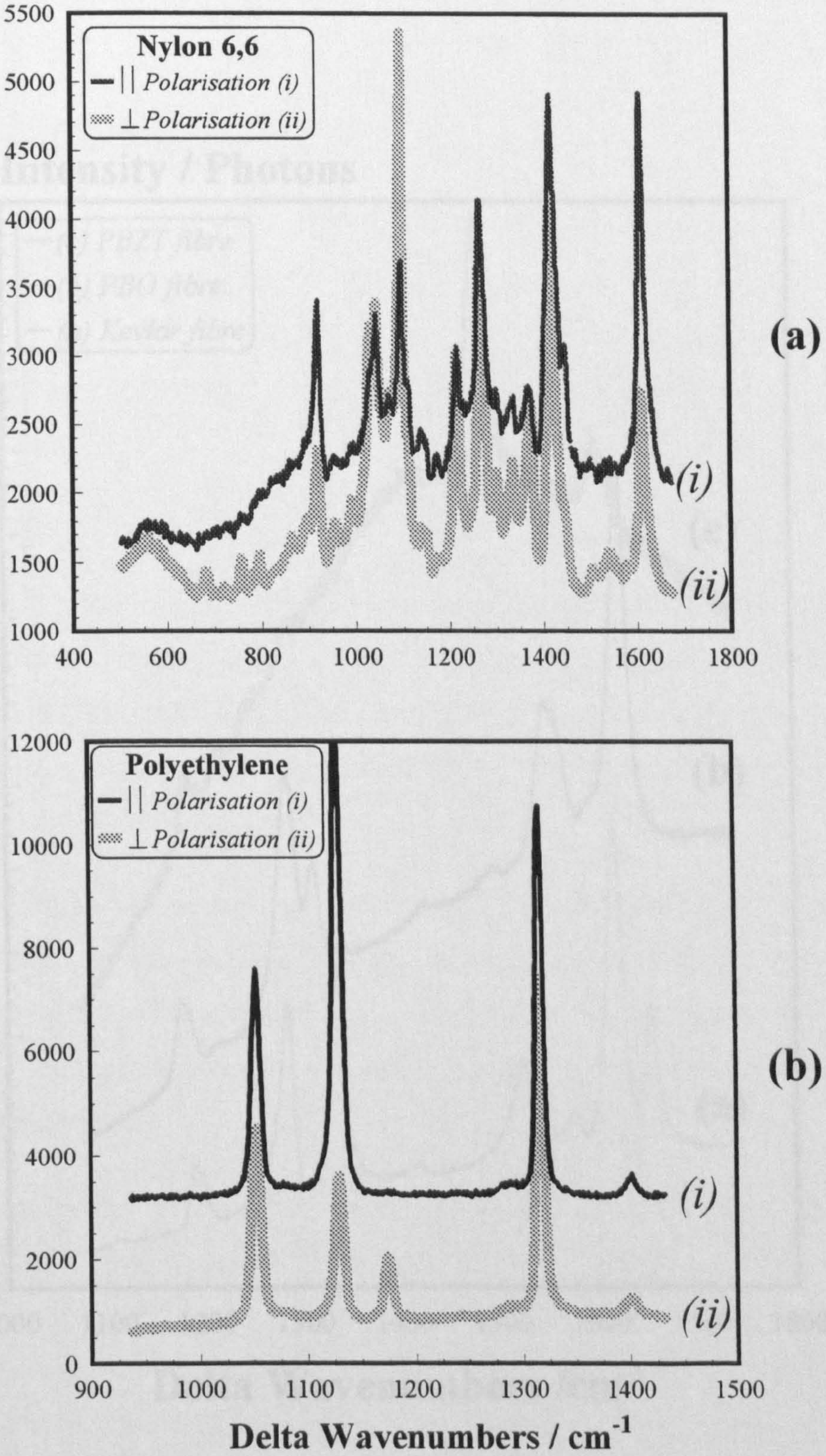

Figure 3.14 Laser Raman spectrum of (a) Nylon 6,6 in parallel and perpendicular polarisation (exposure time 30 s, laser power 1 mW); (b) Polyethylene fibres in parallel and perpendicular polarisation (exposure time 10 s, laser power 1 mW).

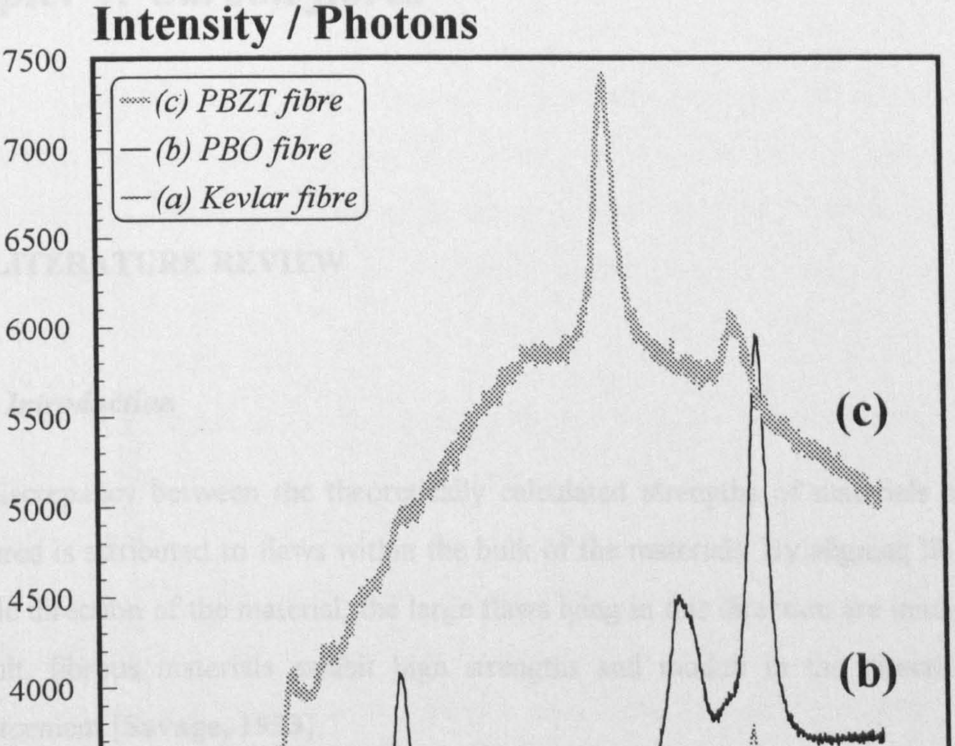

Figure 3.15 Laser Raman spectrum of high performance polymer fibres (exposure time 0.5 s, laser power 0.3 mW).

Chapter 4: Carbon fibres

4.1. LITERATURE REVIEW

4.1.1 Introduction

The discrepancy between the theoretically calculated strengths of materials and those measured is attributed to flaws within the bulk of the materials. By aligning fibres along specific direction of the material, the large flaws lying in this direction are minimised. As a result, fibrous materials exhibit high strengths and moduli in the direction of the reinforcement [**Savage, 1993**].

Carbon fibres provide an ideal candidate for fibrous composites, since they offer high specific strength and modulus. This has led to an increased use of carbon fibre composites in structures where weight saving is important, as in aerospace applications. Carbon fibre / resin composites offer strength to weight properties superior to those of any other material (table 4.1).

The exceptional properties of carbon fibres are attributed to the graphene hexagonal layer networks, present in natural graphite [**Fourdeux, 1973**]. In this hexagonal structure the strong sp^2 hybrid bonding within the hexagonal layer planes (figure 4.1) generates the highest absolute and specific moduli and theoretical tensile strength of all known materials (table 4.2). In the graphite crystal, the high value of the axial modulus (1020 GPa) is combined with very weak shear properties, due to the weak bonding between the neighbouring layers [**Kelly, 1982**]. These properties account for the excellent properties of graphite powder as a lubricant. The calculated modulus and strength of graphite is decreased by defects in the graphitic lattice, stacking faults and disclinations which simultaneously improve its shear properties **[Fitzer, 1985]**.

4.1.2 Processing of carbon fibres

Carbon fibres have been produced inadvertently from nodural cellulosic fibres, such as cotton or linen, for millennia. The first reported use of carbon filaments was by Edison who used them in incandescent electric lamps. After 1910, when the tungsten filaments started being used, the production of carbon fibres was terminated **[Savage, 1993]**.

The exceptional properties of graphite in laboratory experiments renewed the interest in carbon fibres. Today, all the continuous carbon fibres are produced from pyrolised organic precursors. Three precursors are currently used: rayon, polyacrylonitrite (PAN) fibres, and pitch, either isotropic or liquid crystalline (mesophase). Rayon and isotropic pitch are used to produce low modulus fibres. Mesophase pitch and PAN are used for the production of higher modulus fibres. The major manufacturing stages of the carbon fibre made from polymer precursors are shown in figure 4.2. In both cases, an oriented precursor is spun, stabilized by slight oxidation to thermoset the fibres, and, subsequently, carbonised at temperatures higher than 800°C. The High Temperature Treatment (HTT) that follows (1000° to 3000°C) increases the modulus of the fibre but after a stage has a detrimental effect on the strength of the fibres (figure 4.3).

The appropriate combination of processing parameters may provide a wide range of properties for the PAN fibres. They are generally divided in three categories:

1. Low modulus (LM) with a modulus of 90-120 GPa , which are commercial quality fibres.
2. Intermediate modulus (IM) with a modulus of 220-250 GPa, which offer in most cases the ideal material for advanced composite structures.
3. High modulus (HM) with a modulus of 360-400 GPa, which offer extraordinary stiffness at the expense of strain to failure which rarely exceeds 0.8%.

The variety of properties of PAN fibres is due to the processing parameters used in the conversion of polymer to carbon as well as to the high degree of orientation of C-C bonds present in the precursor fibre. Pretension during the high temperature treatment further enhances the orientation of crystallites. The Young's modulus of the fibre is directly related to the orientation of the graphene layers. This study is concerned with PAN fibres, and all references will be mostly confined to these fibres.

4.1.3 The structure of PAN fibres

The orientation of the graphene planes along the fibres axis is almost a linear function to the HTT of the fibre, as determined by X-ray diffraction [**Savage, 1993**]. As mentioned earlier, this is directly related to the fibre modulus. A high strength fibre has 66% of the graphene layers aligned within 15° of the fibre axis for a Young's modulus of 220 GPa. An increase of the modulus to 400 GPa would demand the same amount of crystallites to lie within 6°. The difficulty of obtaining preferred orientation, of less than 10° in the case of PAN fibres, limits the modulus obtained to approximately 400 GPa. The graphene layers alignment is shown in figure 4.4. The individual layers (figure 4.4a) are aligned along the axis of the fibre (figure 4.4b). The three-dimensional arrangement is shown in figure 4.4c [**Bennett, 1978**].

Transmission Electron Microscopy (TEM) and Scanning Electron Microscopy (SEM) studies of carbon fibres have provided an insight into the structure of PAN fibres. PAN fibres exhibit the skin-core effect, with the more oriented layers on the fibre surface [**Donnet, 1984**]. The in-plane and c-axis coherence lengths L_a at L_c, as defined in figure 4.5, as well as the curvature of the entangled planes create a three-dimensional structure. The degree of 'order' together with L_a and L_c in three dimensions defines a high modulus (figure 4.6a), or high strength(figure 4.6b) carbon fibre [**Guigon, 1984**].

4.1.4 Raman spectroscopy of carbon fibres

Apart from X-rays and Electron microscopy, Laser Raman Spectroscopy (LRS) has been a very important method for the characterisation of carbon fibres [**Tuinstra,**

1970a; Dresselhaus, 1988]. The major milestone was the invention of lasers, which allowed for the first time Raman spectrum acquisition from black materials, such as carbon [**Tuinstra, 1970a**].

4.1.4.1 The Raman spectrum of graphite

The Raman spectrum of graphite has been extensively studied. Pristine graphite crystallises according to the D_{6h} point group [**Dresselhaus, 1977**]. The irreducible representations for the optic modes of graphite have been previously determined and are given by [**Nemanich, 1977**]:

$$\Gamma_{opt} = 2E_{2g} + E_{1u} + 2B_{2g} + A_{2u} \tag{4.1}$$

The corresponding molecular vibrations are depicted in figure 4.7 [**Dresselhaus, 1977**]. The only Raman active modes are the E_{2g} modes. The Raman spectrum of graphite has been calculated theoretically [**Al-Jishi, 1982; Lespade, 1982**] and observed experimentally [**Tsu, 1978; Nakamizo, 1974; Tuinstra, 1970a**].

As shown in figure 4.7, one of the E_{2g} modes is a shear type rigid layer mode occurring at approximately 50 cm^{-1} [**Nemanich, 1977**]. The second one corresponds to the in-plane lattice vibrations [**Vidano, 1981**] and is observed at approximately 1580 cm^{-1}.

4.1.4.2 Raman spectra of carbon fibres

In figure 3.13, the Raman spectrum of PAN fibres is shown. The first order carbon fibre spectrum covers the area up to 2000 cm^{-1}, whereas the second order spectrum refers to higher wavenumbers.

The nature of the carbon fibre spectrum is evidently a function of the modulus of the fibre. The high modulus fibre exhibits the well-characterised graphitic E_{2g} band. The E_{2g} mode at 50 cm^{-1} is not shown, since spectral acquisition in the area within 100 cm^{-1} from the laser line requires special techniques. However, the first order spectrum exhibits two distinct bands at circa 1360 cm^{-1} and 1620 cm^{-1}. As the modulus decreases, these two bands tend to mask completely the graphitic band.

The two additional bands appear to be strongly interrelated and have been associated with the presence of crystalline disorder in graphitic materials [**Lespade, 1984**]. The disorder induced activity has been the most useful tool for the characterisation of carbon materials. Tuinstra and Koenig [**1970b**] have directly associated it to the amount of crystal boundary which is inversely proportional to the average crystal diameter in the graphite plane. However, Nakamizo et al. [**1974**] found that the intensity of the 1360 cm^{-1} band decreases and, consequently, disappears when the graphite is ground to a particle size less than one micron. Katagiri et al. [**1988**] directly relate the 1360 cm^{-1} band to the discontinuity of the graphite planes. The intensity of the 1360 cm^{-1} increases as the cross-section fibre is probed from the edge to the centre and this is attributed to graphite plane orientation since the degree of graphitisation is expected to be the same for a thin fibre [**Katagiri, 1988**]. This coincides with the remarks by Tuinstra and Koenig [**1970b**] that lattice orientation largely affects the ratio of the 1580 cm^{-1} to the 1360 cm^{-1} lines. The 1360 cm^{-1} can be attributed to the finite size graphite crystallites which are responsible for the change in the selection rules for Raman activity.

The 1620 cm^{-1} band present in the first order graphite spectrum has also been attributed to splitting of the graphitic band [**Tsu, 1978**] However, its close relation to the 1360 cm^{-1} line classifies it as another disorder induced feature [**Chieu, 1982**].

The second order Raman spectrum is dominated by an intense band at 2700 cm^{-1}. This band is considered as an overtone of the 1360 cm^{-1} line [**Chieu, 1982**] and is barely visible with decreasing modulus. Other reported bands include the 3250 cm^{-1} which is considered as an overtone of the 1620 cm^{-1} line [**Chieu, 1982**].

4.1.4.3 Wavenumber-environment response of the Raman spectrum of carbon fibres.

The anharmonicity of the molecular vibrations of graphite is regarded as the cause for the wavenumber shift of the Raman bands of carbon fibres [**Galiotis, 1988**].

All the Raman lines described in the previous section are reported to shift with applied stress [**Sakata, 1988**], temperature [**Fischbach, 1986**], laser power [**Ager, 1990**], and excitation frequency [**Vidano, 1981**].

As described in §2.4.2, the highly crystalline nature of carbon fibres is responsible for the imprint of any macroscopic change to the lattice vibrational level. The shift of the Raman bands has provided a unique tool for the study of the structural behaviour of carbon fibres in tension and compression [**Melanitis, 1994**] as well as for the study of the fibre matrix adhesion [**Melanitis, 1993a, b; Kim, 1986; Robinson, 1987a**].

Temperature is reported to have similar effects as strain, with the Raman lines shifting to lower wavenumbers. In the case of carbon fibres, the temperature dependence is studied in the literature indirectly, as the effect of laser induced heating on the spectrum [**Ager, 1990; Everall, 1991**], and is associated to the ability of the fibre to dissipate the incident laser power [**Melanitis, 1996**].

In the case of laser Raman microscopy, the temperature induced shift of the Raman bands is dependent on the power density of the excitation wavelength [**Andrews, 1992**]. Studies on the relative shift $\Delta\nu$ with applied stress σ and temperature T due to laser induced heating [**Melanitis, 1996**] show that it is acceptable to treat both effects as linearly independent. Bretzlaff and Wool [**1983**] proposed the following relationship:

$$\Delta\nu = a_\sigma \sigma + a_T T \tag{4.2}$$

where a_σ and a_T are the stress and temperature proportionality constants.

4.2. EXPERIMENTAL

4.2.1 Materials

The carbon fibres used in this study are the M40 fibres manufactured by Toray and supplied by Soficar. The fibres are high modulus PAN fibres. The M40B is the 'as received' unsized fibre with standard oxidative treatment, produced in 12K tows and code-named MUS (M40, Unsized, Standard Oxidative treatment). The M40-12K-40B fibre (MEBS) has additionally an epoxy-based sizing code-named 40B which consists of a blend of low molecular weight epoxies, a stabilizer and antioxidants. Propanol is used as a solvent, and no hardener is present. The quoted manufacturer's properties for the M40 fibre are shown in table 4.3.

4.2.2 Fibre mechanical characterisation

Although several methods have been used to define fibre diameter (shear image analyser, scanning electron microscope, laser diffraction [**Li, 1990**]) the irregularity of the fibre cross-section [**Hughes, 1986**] makes it difficult to define the diameter optically. For reasons of consistency, the fibre diameter was determined through density measurements and was found to be 6.6 μm [**BREU/ CT 91-9503, 1993**].

The received fibres were tested at 4 gauge lengths (more than 120 tests for each fibre type). The strength-to-length relationship is plotted in figures 4.8a and b in a logarithmic scale for the four gauge lengths [**BREU/ CT 91-9503, 1993**].

4.2.3 Scanning electron microscopy (SEM)

In figure 4.9, a scanning electron micrograph of the M40 fibre is shown. The fibre has failed in tension. The micrograph was taken with a JEOL field emission scanning electron microscope (kV=5eV, working distance 19 mm). No coating was used to prevent the presence of artefacts. Although the instrument provides very high resolution, no differences were detected between the sized (MEBS) and unsized fibres (MUS), due to the extremely thin layer of the fibre sizing, which does not exceed a few nanometers **[Savage, 1993]**.

4.2.4 Raman spectrum of the M40 fibres

The first order Raman spectrum of the MEBS and MUS fibres is shown in figure 4.10. Both spectra are recorded with 1 mW on the sample and 30 s acquisition time using the 50× Ultra Long Working Distance Olympus objective (numerical aperture 0.55).

There are three bands in the first order spectrum. The $\mathbf{E_{2g}}$ line at approximately 1580 cm^{-1} is the most prominent one, and is assigned to the in-plane vibration of the graphitic cell **[Tuinstra, 1970a; Tuinstra 1970b; Nemanich, 1979]**. This line is the only one predicted by assigning the graphite crystal to the D_{6H} point-group, and will be the reference line throughout this study.

The other two bands appear at 1360 cm^{-1} and at 1620 cm^{-1} respectively. These two bands are closely interrelated as they keep a constant intensity ratio **[Tuinstra, 1970b; Katagiri, 1988]**. Although the intensity ratio of the 1360 cm^{-1} to the 1580 cm^{-1} for the MEBS fibre is fairly constant and of the order of 0.3, this is not true for the MUS fibre. The 1360 cm^{-1} to 1580 cm^{-1} intensity ratio varies along the fibre length considerably from 0.3 to 1, depending on the focusing location.

4.2.5 Calibration of the E_{2g} graphitic mode of the M40 fibres

The Raman Spectra of the fibres were recorded as a function of stress, strain, temperature and laser power. The spectral window was defined by the size of the CCD camera and covers approximately 400 cm^{-1} in the first order spectral area of the carbon fibre spectrum which is enough to simultaneously record all three vibrational modes present. The position of the Raman modes was defined through a least square fitting routine (see appendix 1).

The E_{2g} graphitic mode was chosen throughout this study as the reference peak to monitor environment induced changes. Although all peaks do exhibit strain or stress sensitivity, the E_{2g} band has always been favoured among researchers for stress measurements [**Kim, 1986; Melanitis, 1994; Robinson, 1987b**]. This is due to the following: (i) it is the strongest feature of the carbon fibre spectrum [**Fitzer, 1987**], (ii) it is well defined theoretically and experimentally [**Lespade, 1982**], (iii) it is present on all graphitic structures [**Tuinstra, 1970a**], and (iv) although it is less sensitive to polarization [**Katagiri, 1988**] and excitation wavelength, it exhibits the maximum sensitivity to external stress from all first order high modulus carbon fibres Raman bands [**Galiotis, 1992**]. All calibration curves reported hereafter will refer to the E_{2g} mode.

4.2.5.1 Strain and stress calibration of the Raman spectrum

The wavenumber shift of the M40 fibres with strain was undertaken in two parts:

a) tensile testing by means of the microextensometer device,
b) tensile and compressive testing by means of the cantilever beam technique.

The stress calibration was performed via tensile testing on a Universal Testing Machine with simultaneous recording of the Raman spectrum with applied stress.

The microextensometer device is shown in figure 4.11. The fibre is attached on the jaws of the device using aluminium tabs and CN® adhesive. The initial gauge length used l_0 was 10 mm and mechanical strain was calculated as $\varepsilon = \Delta l/l_0$, where Δl is the applied elongation measured by the attached micrometer. The calibration curves for both MEBS and MUS are shown in figures 4.13 a and b respectively. The linear fit obtained from the spectroscopic data provides the strain dependence of the carbon fibre E_{2g} line α_{ε}, which is 11.1±0.4 for MEBS and 11.7±0.4 for MUS.

The cantilever beam geometry is shown in figure 4.12 [**De Teresa, 1988**]. The fibre is attached on the top of a perspex beam and flexed inducing a constant gradient of either tension or compression on the fibre [**Timoshenko, 1961**]. The exact local strain is a function of the position, provided that the fibre is well in contact with the beam, and the beam deformation is purely elastic. In this case, the strain in the fibre as a function of the position z ($0 \leq z \leq l$) along the beam is:

$$\varepsilon_f(z) = \frac{3q\delta_{max}}{2l^2}\left(1 - \frac{z}{l}\right) \tag{4.3}$$

where l is the cantilever beam span, δ_{max} is the maximum deflection of the beam (at the free end), and q is the beam thickness.

The cantilever beam technique has been used successfully in conjunction with LRS [**Melanitis, 1994**] to provide a continuum for the experimental shift from tension to compression as well as to characterise the structural behaviour and modes of failure of carbon or polymer fibres [**Vlattas, 1994**].

In figures 4.14a and b the calibration curves for MEBS and MUS fibres are respectively shown. Three fibres of each kind are tested both in tension and compression. All tensile and compressive data are merged in one graph for each fibre. The fibres fail at about 0.8%, both in tension and compression. All fibres failed in shear mode, that is, along a weak shear plane at approximately 60° to the fibre axis [**Melanitis, 1991**].

Both fibres exhibit non-linear behaviour particularly prior to compressive failure (~ -0.6 to 0.8%). This non-linearity is less apparent in the MUS calibration. However, the area between -0.5% and tensile failure is linear to a very good approximation (figure 4.14) and coincides with the wavenumber shift / strain calibration.

The Raman shift / stress calibration experiment was performed on a Hounsfield Universal testing machine. The gauge length of the fibres was 10 mm. As shown in figure 4.15, the fibres were mounted in carton tabs using CN® adhesive and aluminium foil. The tabs had standard holes punch with 10 mm of a gauge length. The fibres were mounted on the Hounsfield Universal Testing Machine on specially made grips, and subsequently cut on either side. The load was monitored using a 20 N load cell and Raman spectra were recorded at a function of load. No significant difference was observed between sized and unsized fibres. The master curves for the Raman shift / stress calibration of the

M40 fibre is showed in figure 4.16 for both MEBS (6 specimens) and MUS (5 specimens) fibres. The fibres are assumed to have a steady 6.6 μm diameter for stress calculations. The stress sensitivity of the fibres as calculated from the least square fitted line is 3.0 cm^{-1} / GPa.

4.2.5.2 Temperature sensitivity of the M40 fibres

The wavenumber shift of the E_{2g} line of M40 fibres was tested as a function of temperature and incident power.

The study of the temperature sensitivity of the M40 fibre was performed by using a specially designed environmental chamber. Data acquisition was performed through a glass window which was coated so as to allow maximum transmission of visible wavelength and block infra-red frequencies, allowing the chamber to reach temperatures up to 350°C. The fibres were mounted on a glass slide and monitored at a temperature range from room to 250°C, in discrete steps. The chamber temperature was allowed to stabilise for 30 min at each recording temperature prior to Raman spectrum acquisition. The laser power on the sample was kept constant at 1 mW. The least square fitted line indicated a temperature / Raman shift sensitivity of 0.025 cm^{-1} / °C (figure 4.17a).

The effect of laser power on the E_{2g} Raman line is shown in figure 4.17b. The fibres were tested over a power range from 0.5 to 10 mW. The fibre exhibits a laser power dependence of -0.35 cm^{-1} / mW, as indicated by the least square fitted line. In table 4.4, the Raman wavenumber shift rate of the E_{2g} line for all the parameters involved is shown. The temperature to power to stress sensitivity differ by an order of magnitude. All parameters were investigated using a 50× ultra long working distance objective, which resulted in a laser spot diameter of less than 1 μm.

4.3. DISCUSSION

4.3.1 Strength and morphology

As in all brittle materials, fracture in high modulus carbon fibres is associated with structural faults or flaws, which limit the theoretical strength of the material acting as stress concentrations [**Donnet, 1984**]. Voids, inclusions, or structural imperfections that occur through any stage of the fibre production, contribute to the strength loss.

The gauge length dependence of the M40 fibre strength exhibited in figures 4.8a and b reflects the distribution of flaws along the fibre [**Hughes, 1986**]. This suggests a volume dependence of fibre strength associated with the probability of a critical flaw present within that volume. In case of a fibre of constant diameter, this is only a function of length [**Hull, 1996**]. However, the high scatter demands a statistical treatment of the data. Assuming a two parameter Weibull distribution, if $\bar{\sigma}_{fu}$ is the mean of the distribution of the fibre strength at gauge length l, then [**Andersons, 1993; Bunsell, 1992**]:

$$ln(\bar{\sigma}_{fu} - \sigma_s) = -\frac{1}{m} ln l + ln \sigma_0 \tag{4.4}$$

where σ_s is a threshold value, and σ_0 is a constant (corresponding to the strength at 2.7 mm for $\sigma_s = 0$), and m is the Weibull shape parameter. The linear fit to the $ln(\bar{\sigma}_{fu} - \sigma_s)$ vs. $ln l$ data readily determines σ_0 and m and allows the extrapolation of the fibre strength to any gauge length. This is indispensable in order to model the failure of practical or model composites, a task which otherwise would require testing at gauge lengths of the order of 0.3 mm [**Hughes, 1986**].

In the case of the M40 fibre strength, σ_s is set to 0, since no strength threshold value is experimentally defined. The sized fibre exhibits within experimental error the same strength constant σ_0, and slightly higher dependence on gauge length. This is in agreement with strength data from intermediate modulus which where the presence of sizing caused the same effect [**BREU/ CT 91-9503, 1993**].

The sizing is reported to act as a protected sheath from abrasion during handling or composite manufacturing [**Savage, 1993**]. This would imply a higher concentration of surface flaws on the unsized fibre, which may affect the strength of the fibre.

Surface flaws play a critical role as stress raisers in untreated fibres [**Donnet, 1984**]. Initial oxidative treatment removes the weaker layers from the fibre surface, reducing the critical importance of surface flaws (figure 4.18). Thus, most commercially used fibres which have standard oxidative treatment mostly fail, due to the distribution of internal flaws, which seems to be the case with the M40 fibres. However, the absence of sizing may induce the shift of the surface flaw strength distribution to lower values for a given gauge length. In the case of the M40 fibres, the presence of sizing does not conclusively affect the strength of the fibres, but there is an indication of a trend which is more pronounced in the case of sized (TEBS) and unsized (TUS) intermediate modulus T800 fibres (table 4.5).

4.3.2 The first order Raman spectrum of M40 fibres

The first order Raman spectra of both fibres reveal important information about their morphology. The E_{2g} graphitic peak is present at both spectra (figure 4.10) and is not affected by the sizing. This is expectable since the graphitic E_{2g} line is a function of the graphitisation of the carbon fibre or of the final heat treatment temperature (HTT) [**Chieu, 1982**]. Both fibres are reported to be produced under identical conditions.

However, this is not the case with the disorder induced lines. The differences in the 1360 cm^{-1} to the 1580 cm^{-1} intensity ratio may can be attributed to the surface properties of the fibres. In figure 4.9, a high resolution SEM micrograph of the M40 fibre is shown. The higher axial orientation near the surface of the fibre is obvious, showing the sheath-core effect present for PAN fibres treated at high temperatures [**Donnet, 1984**]. The fibre structure consists of an outer zone surrounding the inner core.

The thickness of the outer zone is a function of the time of heat treatment in air during the pre-oxidation stage of carbon fibre preparation.

Therefore, the final surface of the HM carbon fibre is highly graphitic [**Donnet, 1984**]. Oxidative treatment of the fibre removes the outer graphitic planes and this results to an increase of the 1360 cm^{-1} to the 1580 cm^{-1} ratio [**Melanitis, 1991**]. Similar effects have been identified with polishing [**Katagiri, 1988; Fischbach, 1986; Lespade, 1984; Nemanich, 1979**], or ion bombardment [**Elman, 1981**] where the etching of the fibre surface resulted to an increase of the intensity of the 1360 cm^{-1} 'disorder' line.

Since both M40 fibres undergo identical treatment prior to sizing, then the local variation of the 1360 cm^{-1} line intensity can be attributed to abrasion due to the subsequent winding in spools or handling. These local variations take place within the radius of the laser spots which is in the order of a 1 μm and for an expected penetration depth of 100 nm [**Lespade, 1984**]. Thus, the surface variations which are present are of the order of magnitude of the fibre diameter but do not necessarily affect significantly the strength of the fibre, as postulated in the previous section. However, the 'amount of crystal boundary' is closely related to the stress transfer between the fibre and the matrix [**Tuinstra, 1970b**], and therefore is expected to play an important role in the interfacial properties of the composite.

4.3.3 Wavenumber shift of the E_{2g} graphitic band due to the environment

The E_{2g} band was found to be sensitive to environmental changes such as stress or strain, laser power and temperature. All these changes are theoretically explained by the anharmonicity of the vibrations inducing the Raman band.

As described in §2.4.2, the force constant is dependent on the bond deformation [**Tashiro, 1990**], and thus we can associate all wavenumber shifts to internal stresses developed due to environmental changes. Various researchers have used the linear approximation for the wavenumber shift / stress relationship [**Bretzlaff, 1983; Galiotis, 1985; Melanitis, 1993a, b**], which is adequate for the measured deformations. The shift of the Raman wavenumber for a given vibrational mode is due only to the stretching of the covalent bonds along the chain and is not affected by rotational or vibrational motions. If the fibre is considered as a aggregate of parallel arrays of identical fibrils arranged in series, then for a small deformation [**Melanitis, 1994**]:

$$\Delta v = a_\sigma \, \sigma \qquad (2.12)$$

Since $d\sigma = E\,d\varepsilon$ from equation 2.12:

$$a_\varepsilon = a_\sigma E \qquad (4.5)$$

The stress and strain sensitivity of both fibres tested was found to be -3.0 GPa % and -11.4 cm^{-1}/%, which confirms within experimental error the above equations for a fibre modulus of 390 GPa.

However, it is suggested that non-linearities in the stress-strain behaviour of both carbon and polymer fibres are present [**Melanitis, 1994; Vlattas, 1994**]. This is due to the fibre nature and may be explained if the crystallites within the fibre are normally distributed around the fibres axis. Redistribution of the crystallites during mechanical deformation would induce a modulus increase in tension, and modulus softening in compression.

The continuous curve that can be obtained through the cantilever beam experiment reveals all non-linearities in the strain / Raman wavenumber response of the fibres. In figures 4.14a and b the respective calibration curves are shown for both MUS and MEBS fibres. The non-linearities of the Δv / strain are more prominent near the fibre failure region, i.e. after -0.5%. However, the behaviour of both fibres is fairly linear up to -0.5%, indicating that, for relatively small compressive strain, one can assume linear shift with strain [**Melanitis, 1994**].

The induced shift through increasing laser power may also be associated with the increase of local stress within the probing area due to thermal expansion. Provided that a steady state is achieved, that is, the heating from the laser is efficiently dissipated, it is acceptable to assume a superposition of stress fields induced by either stress or localised heating. The same is valid for increasing temperature. The above argument is shown in the work by Melanitis et al. [**1996**], where no difference in the strain sensitivity is shown with increasing laser power. The increase in laser power only changes the offset of the $\mathbf{E_{2g}}$ line, shifting to lower wavenumbers.

Finally, it is interesting to comment that 1 GPa of applied stress is a shift equivalent to that of approximately a 10 mW laser power or 100°C temperature differential respectively (table 4.4). The effect of applied stress is much more prominent and, provided that the temperature and laser power are relatively constant, it will be the primary reason for the induced shift.

Material	*Density ρ / g cm^{-3}*	*Tensile strength σ_{fu} / GPa*	*Young's Modulus E_f / GPa*	σ_{fu} / ρ	E_f / ρ
		Composites (Parallel to reinforcement)			
E Glass	2.1	1.1	45	0.5	20
IM Carbon	1.5	2.6	170	1.7	113
HM Carbon	1.6	1.6	257	1.0	161
Aramid	1.4	1.4	75	1.0	50
		Metals			
Steel	7.8	1.3	1.3	0.2	26
Aluminium	2.8	0.3	0.3	0.1	26
Titaniun	4.0	0.4	0.4	0.1	25

Table 4.1 Strength to weight properties of various materials [**Savage, 1993**].

Material	*Density ρ / g cm^{-3}*	*Tensile strength σ_u / GPa*	*Young's Modulus E / GPa*	σ_u/ρ	E/ρ
Graphite	2.26	150	1020	66	451
Diamond	3.51	90	20	25	177

Table 4.2 Theoretical or measured properties of graphite and diamond [**Savage, 1993**].

Manufacturer	*Tensile strength σ_{fu} / GPa*	*Young's Modulus E_{fu} / GPa*	***Strain to Failure / %***	*Density ρ / $g\ cm^{-3}$*
TORRAY	245	392	0.6	1.78

Table 4.3 Properties of the M40 fibres, as quoted by the manufacturer [**Hughes, 1986**].

M40Fibre	*Stress* α_σ cm^{-1} / GPa	*Laser Power* α_L cm^{-1} / mW	*Temperature* α_T cm^{-1} / °C
Sensitivity	-3.0	-0.35	-0.025
R^2	0.959	0.981	0.955

Table 4.4 Wavenumber shift of the M40 fibres as a function of stress, laser power and temperature.

Fibre Type	***$\ln\sigma_0$***	***1/m***	***R***
MEBS	8.193	0.066	0.813
MUS	8.192	0.059	0.709
TEBS	3.807	0.117	0.962
TUS	3.749	0.084	0.952

Table 4.5 Mechanical properties of M40 and T800 fibres as a function of gauge length for both sized and unsized filaments [**BREU/ CT 91-9503, 1993**].

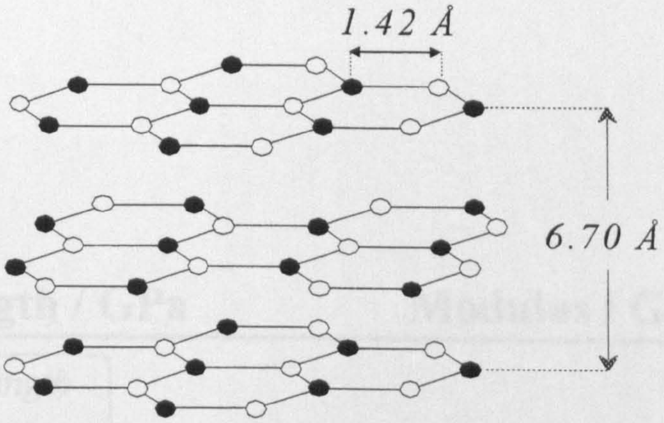

Figure 4.1 The structure of the graphite crystal [**Dresselhaus, 1988**].

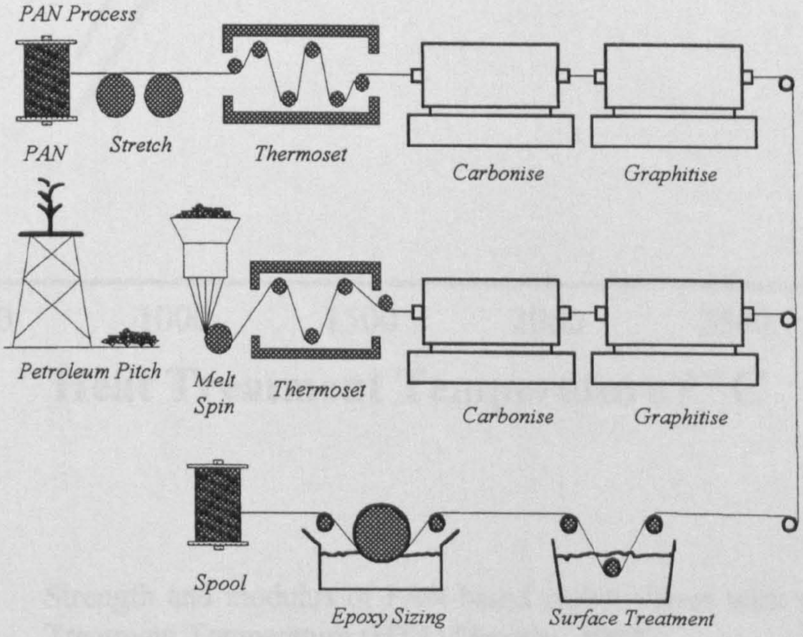

Figure 4.2 The processing sequence for PAN and mesophase pitch based precursor carbon fibres [**Savage, 1993**].

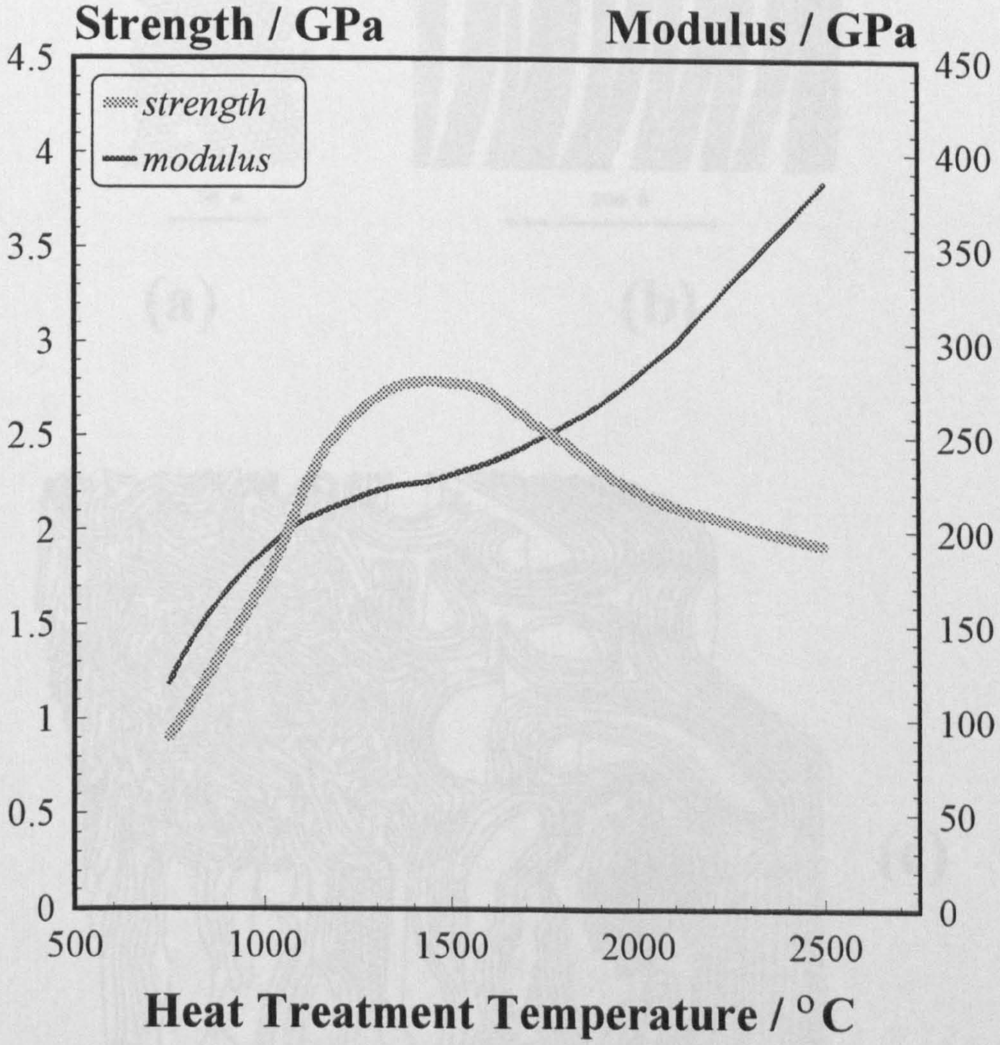

Figure 4.3 Strength and modulus of PAN-based carbon fibres with respect to Heat Treatment Temperature (HTT) **[Savage, 1993]**.

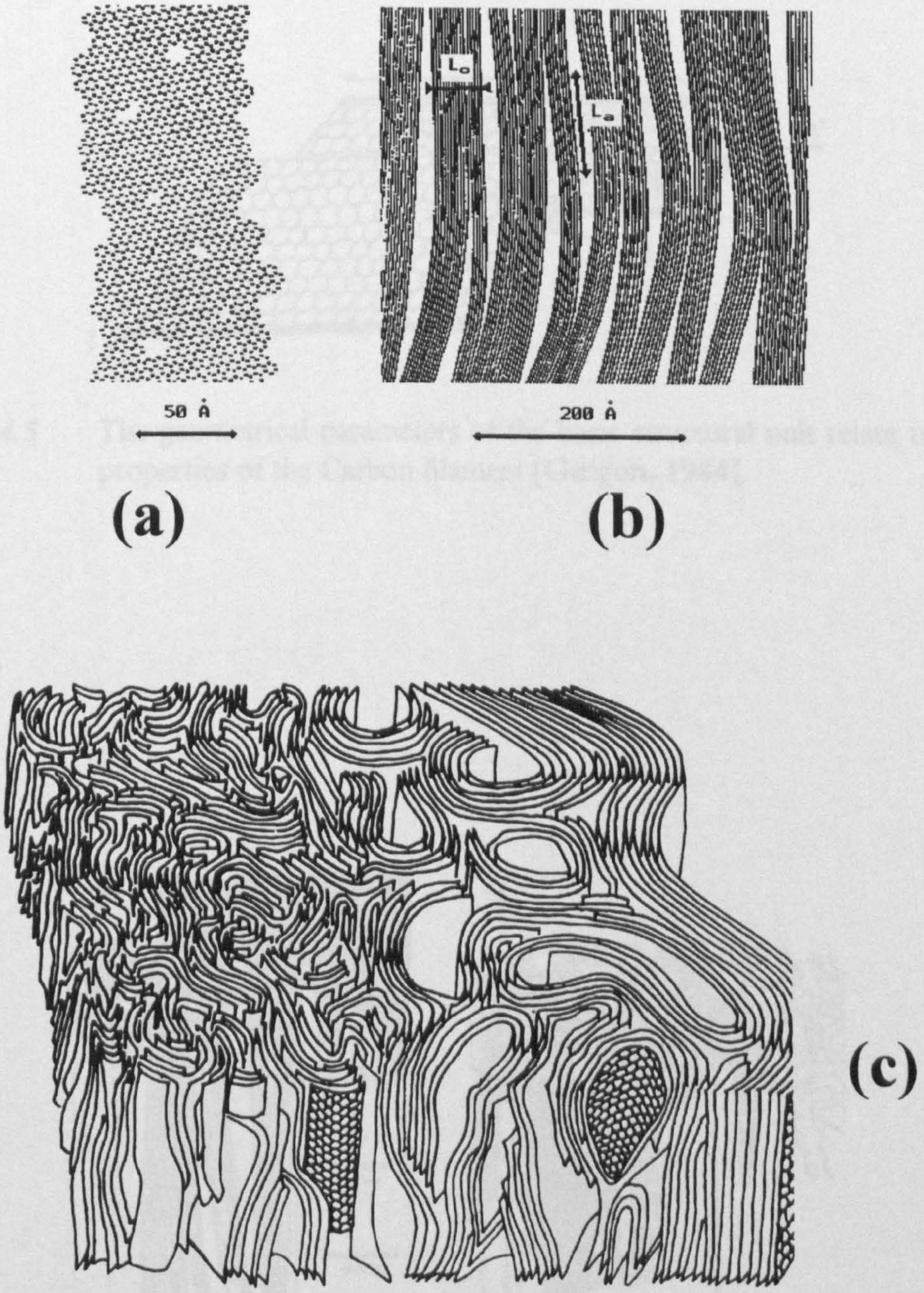

Figure 4.4 Structure of Carbon Fibres; (a) Sketch of a typical graphene plane in a carbon fibre. The cluster vacancies consist typical structural defects, (b) Axial arrangement and coherence lengths[**Fourdeux, 1973**] (c) Three dimensional order in carbon fibres [**Bennet, 1976**].

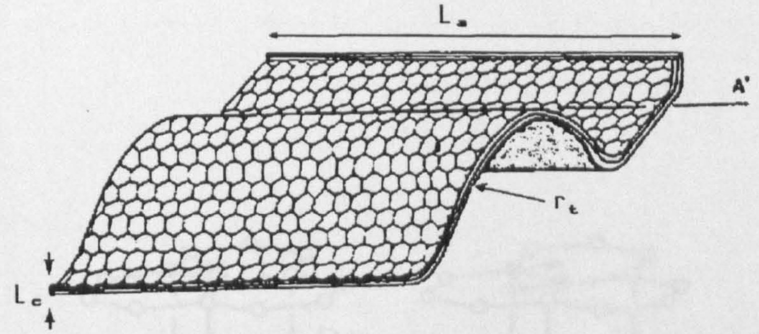

Figure 4.5 The geometrical parameters of the basic structural unit relate to the final properties of the Carbon filament [**Guigon, 1984**].

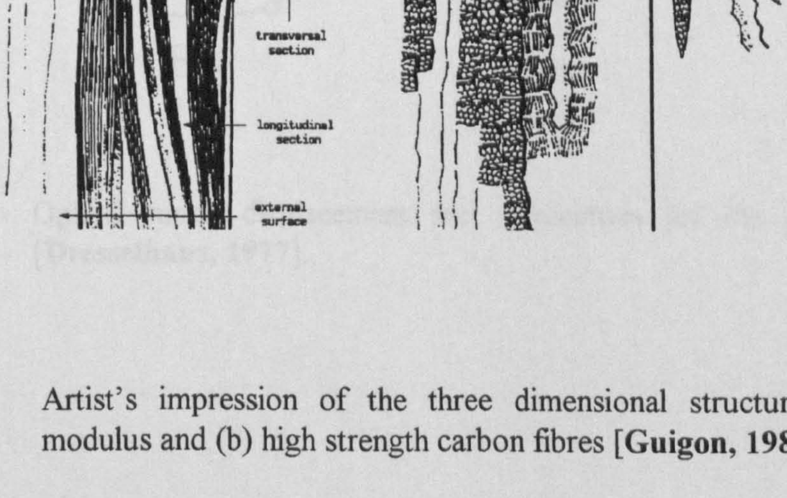

Figure 4.6 Artist's impression of the three dimensional structure for (a) high modulus and (b) high strength carbon fibres [**Guigon, 1984**].

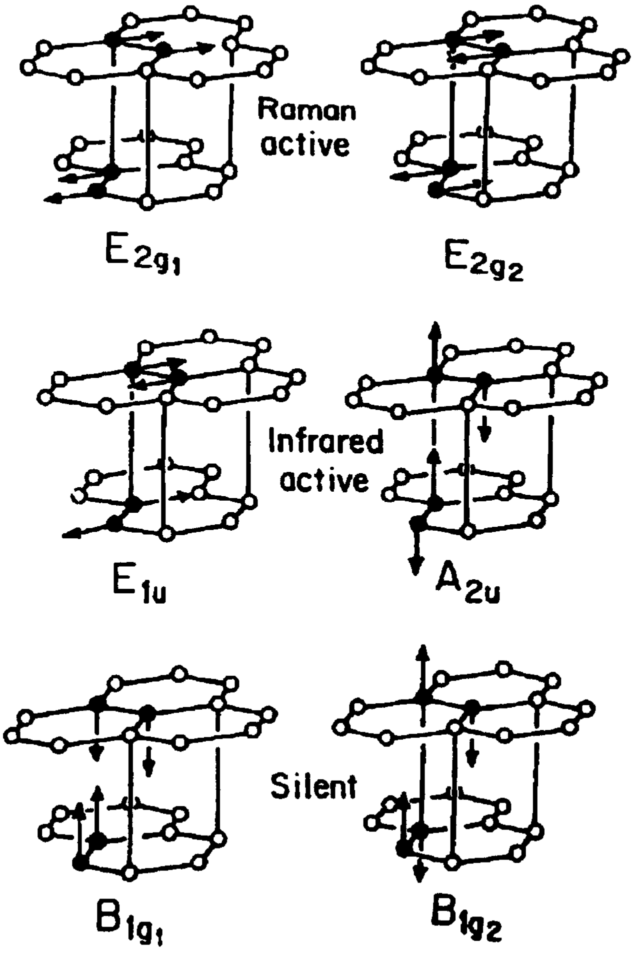

Figure 4.7 Optical mode displacement and symmetries for the graphite lattice [**Dresselhaus, 1977**].

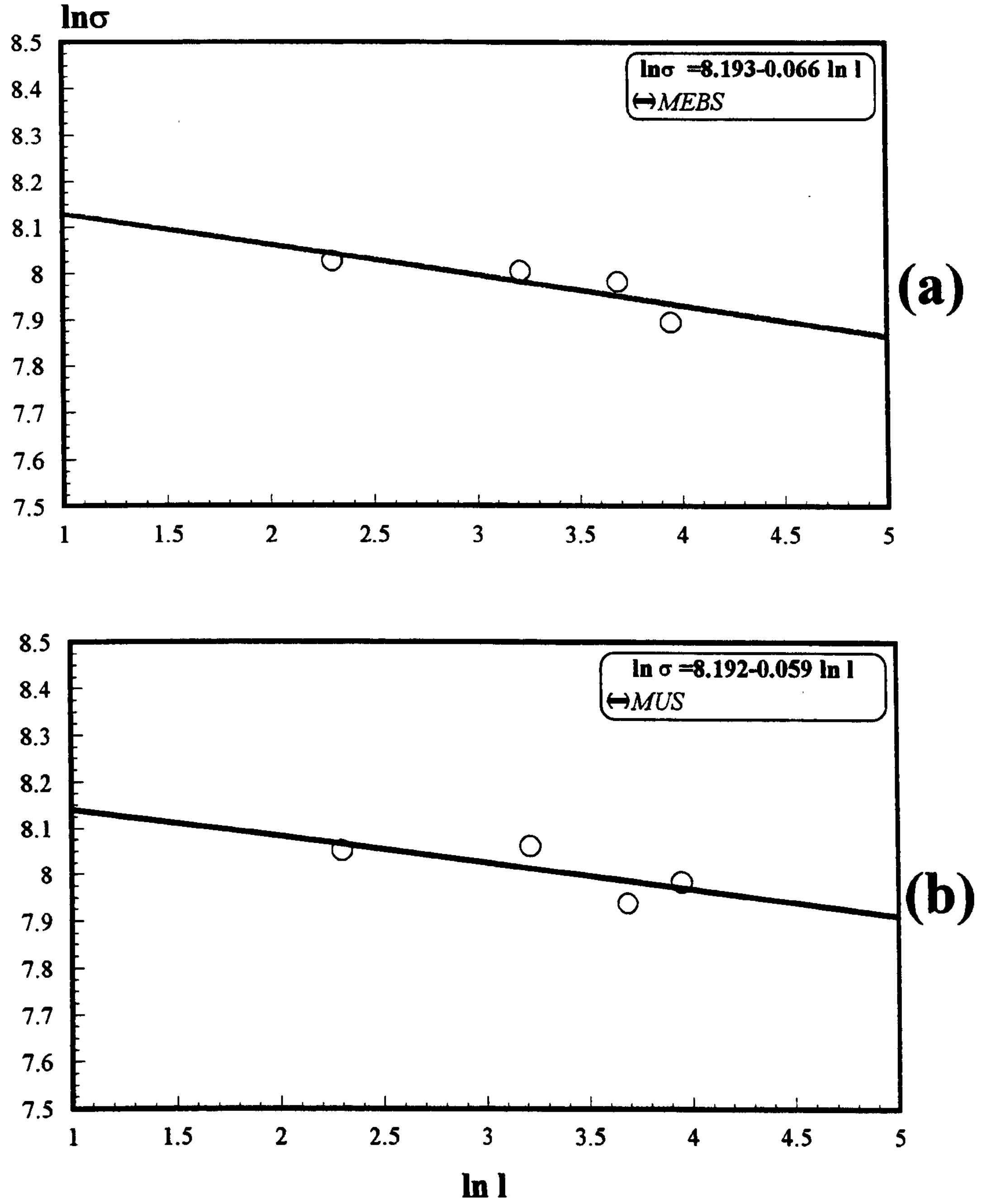

Figure 4.8 The gauge length dependence of the strength of the M40 fibres, (a) MEBS (sized fibre), (b) MUS (unsized fibre).

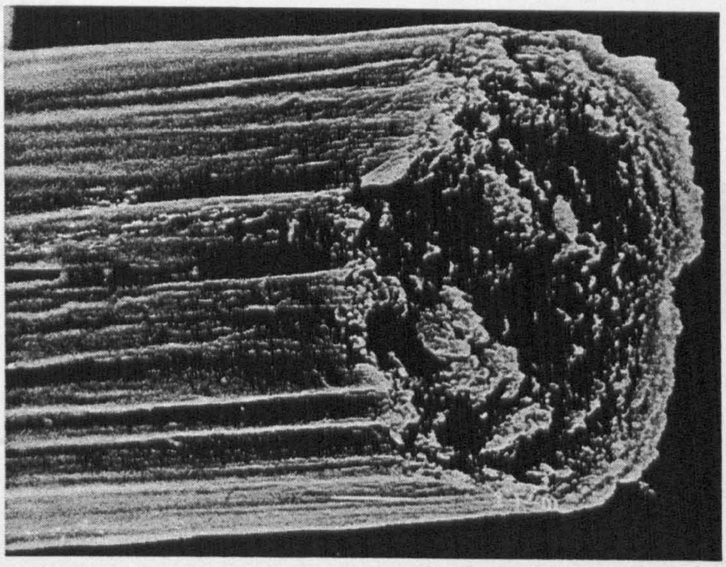

Figure 4.9 Scanning Electron Micrograph of the M40 fibre.

Figure 4.10 First order Raman spectrum of the M40 fibres.

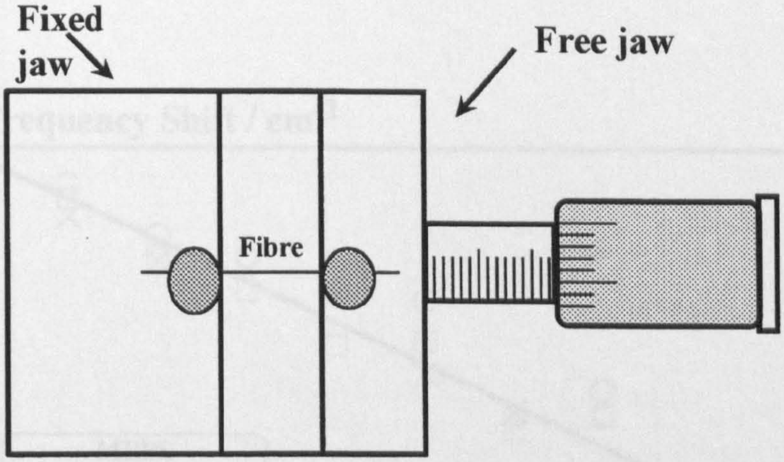

Figure 4.11 The microextensometer device for Raman shift measurements in tension.

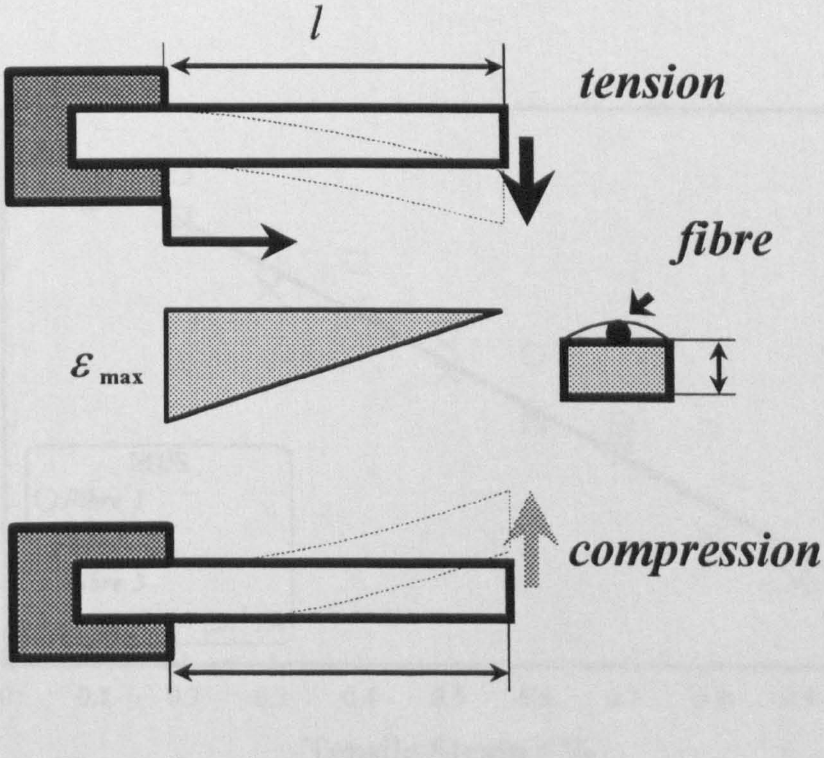

Figure 4.12 The cantilever beam device for Raman shift measurements in tension and compression.

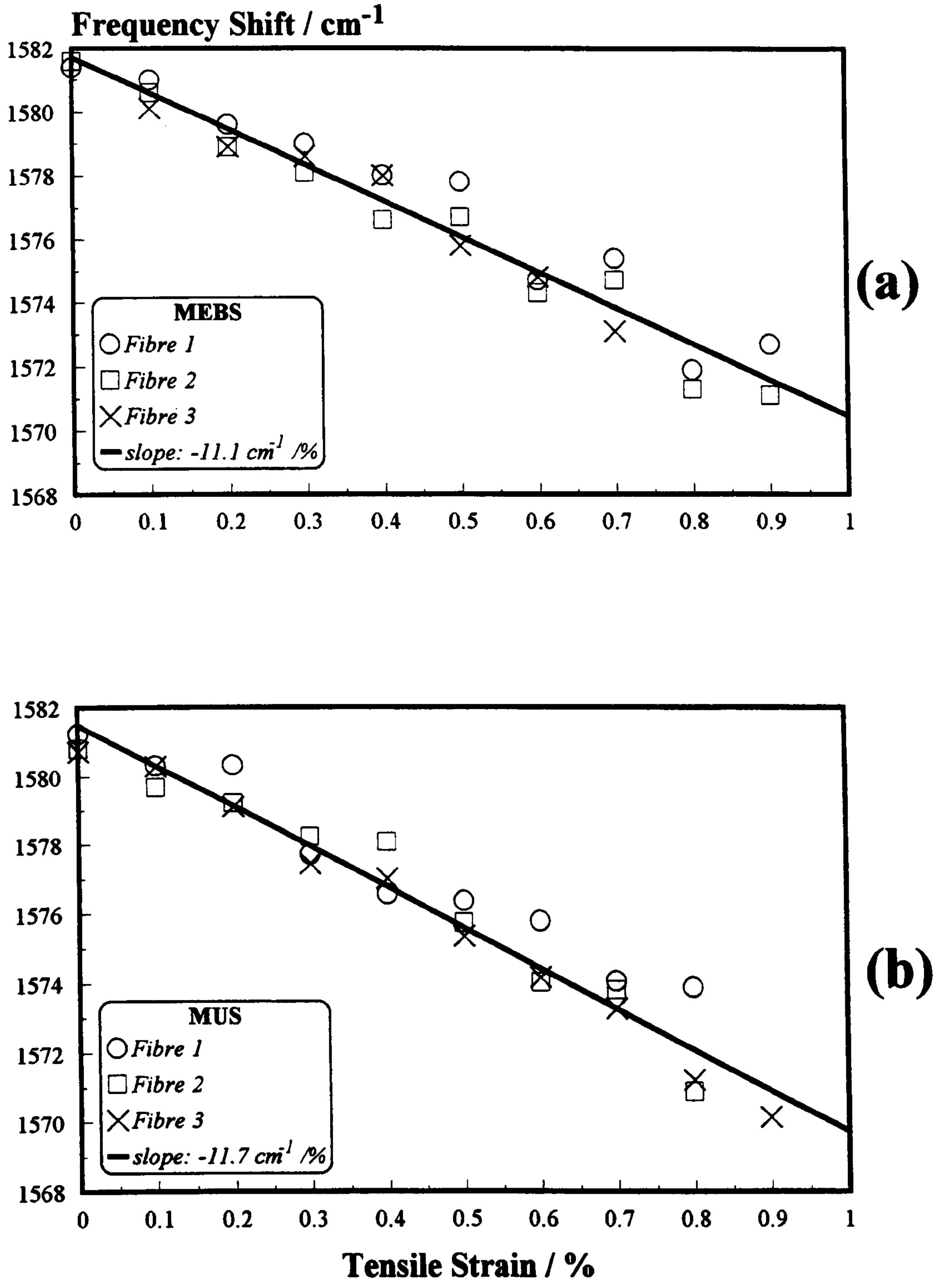

Figure 4.13 Raman shift / Strain calibration in tension for M40 fibres (a) MEBS (sized fibre) and (b) MUS (unsized fibre).

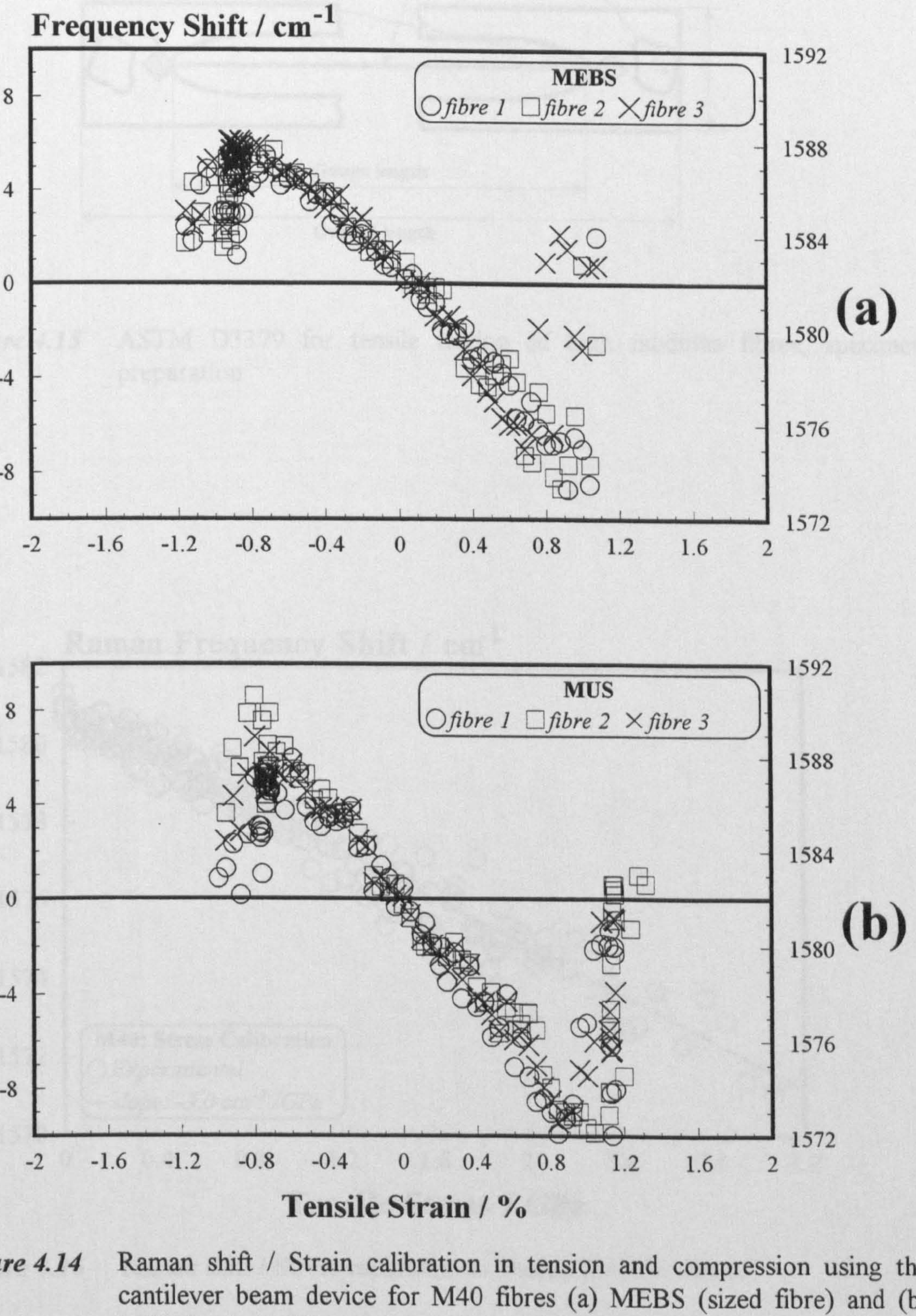

Figure 4.14 Raman shift / Strain calibration in tension and compression using the cantilever beam device for M40 fibres (a) MEBS (sized fibre) and (b) MUS (unsized fibre).

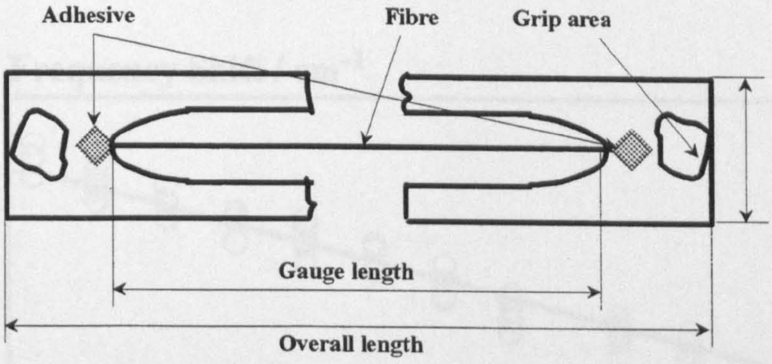

Figure 4.15 ASTM D3379 for tensile testing of high modulus fibres; specimen preparation.

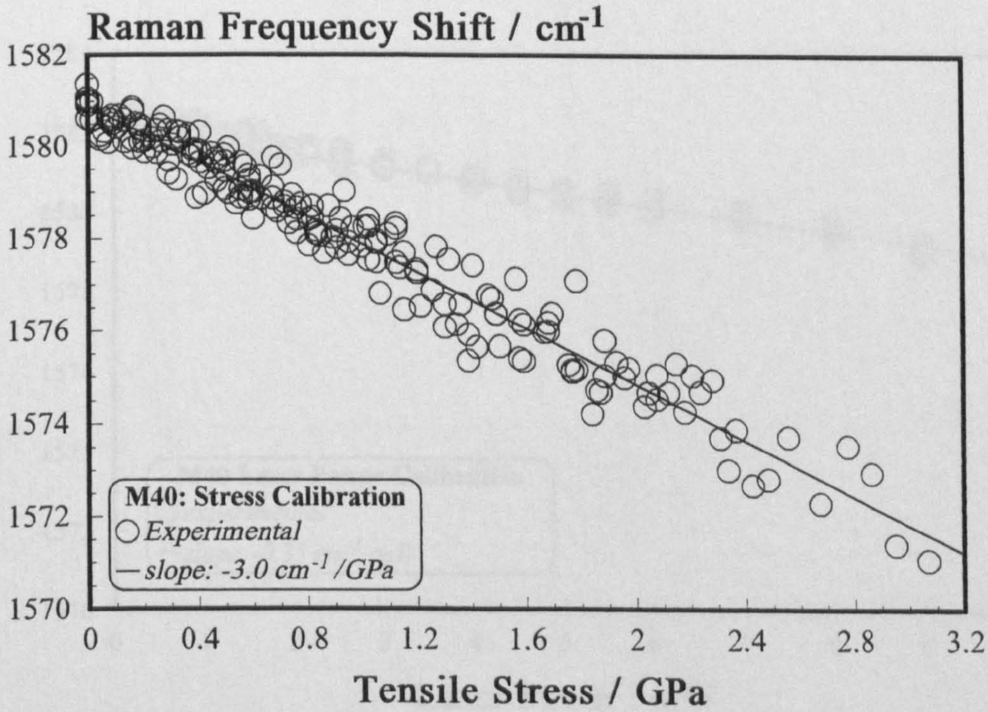

Figure 4.16 Raman shift / Stress calibration in tension for M40 fibres.

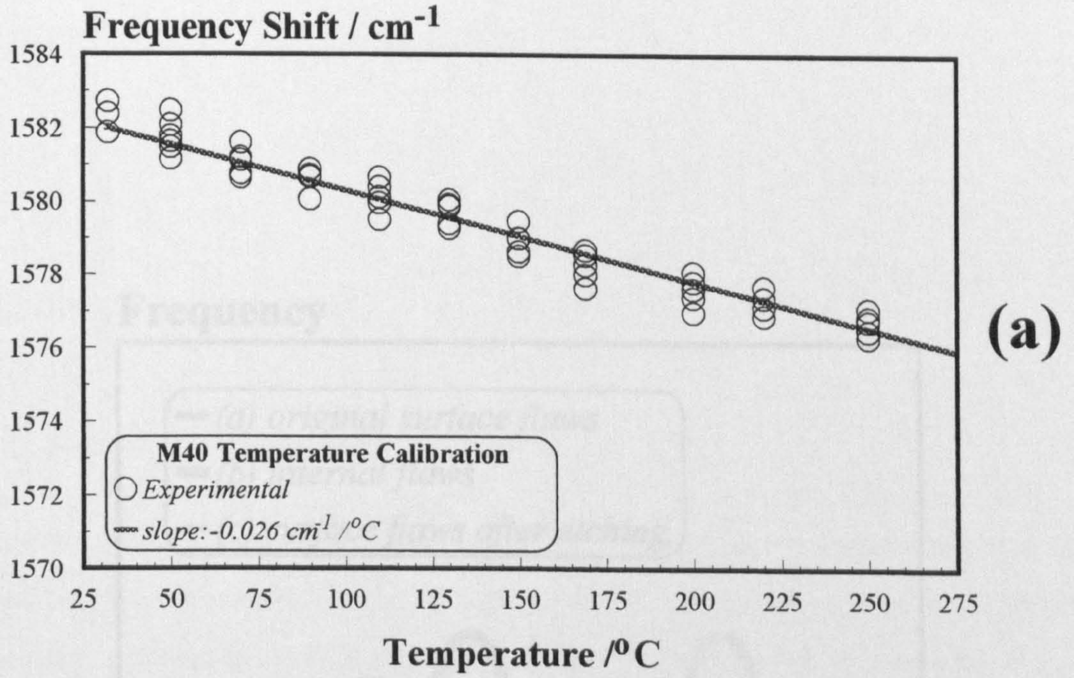

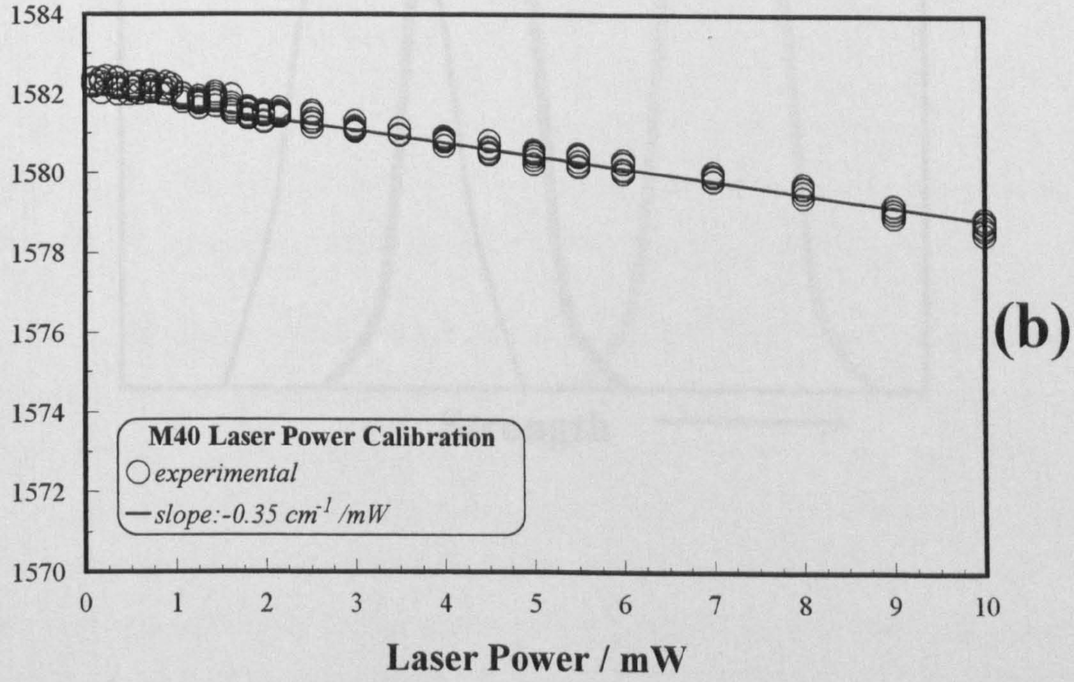

Figure 4.17 (a) Raman shift / Temperature calibration for M40 fibres.
(b) Raman shift / Laser power calibration for M40 fibres.

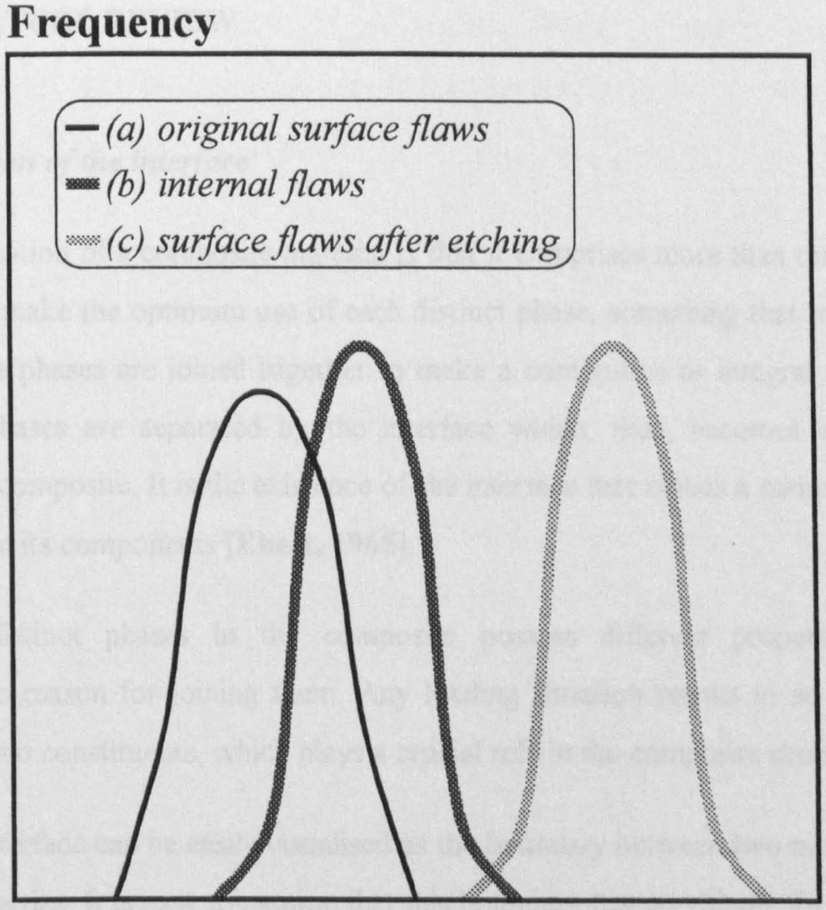

Figure 4.18 Strength distribution of different types of flaws. (a) original surface flaws, (b) internal flaws, (c) surface flaws after etching [**Donnet 1984**].

Chapter 5: Interfacial studies

5.1. LITERATURE REVIEW

5.1.1 Definition of the interface

The inherent notion of a composite material is that it comprises more than one phase. It is desirable to make the optimum use of each distinct phase, something that may only be achieved if the phases are joined together to make a contiguous or integral unit. Upon joining, the phases are separated by the interface which, thus, becomes a dominant feature of the composite. It is the existence of the interface that makes a composite differ physically from its components **[Ebert, 1965]**.

The distinct phases in the composite possess different properties, which constitutes the reason for joining them. Any loading situation results in an interaction between the two constituents, which plays a crucial role in the composite properties.

The interface can be easily visualised as the boundary between two materials with different properties. It is easy to assume that this boundary has no volume for calculation purposes. However, this is not the case on a smaller scale, where phenomena, such as surface roughness or chemical interaction, are of crucial importance. Moreover, it is much easier to attribute a physical meaning to a zone with a gradient of properties between the two constituents. In this case, the zone is termed the *interphase* and extends in three dimensions. If the mechanical characteristics of the interface in multi-phase materials are not affected by the typical length scale of the composite, two dimensional models can be applied **[Herrmann, 1996]**. However, if the bonding layer is of similar order of magnitude to that of a typical macroscopic size, like the reinforcement diameter, then the interphase has to be included in the mathematical modeling.

The scale of the interphase may differ dramatically in different composite materials. In the case of fibrous composites it may extend from a few nanometres to several fibre diameters. A typical unsized carbon fibre / epoxy interphase only extends for less than ~10 nm **[Guigon, 1994]**. The interphase of SiC fibres in Al matrix may extend to hundreds of nanometres **[Long, 1996]**. In thermoplastic matrices, the presence of transcrystallinity changes the matrix properties in the interphasial region totally. In this case the interphase may be more than one order of magnitude larger in diameter than the reinforcing fibre **[Heppenstall-Butler, 1996]**.

5.1.2 Mechanisms of interfacial adhesion

The concept of the interface requires that two surfaces come into intimate (atomic scale) contact **[Hull, 1996]**. When two rigid solids come into contact, the surface roughness confines the interface to the regions where asperities touch (figure 5.1a). In the case of a solid / liquid interface, wetting takes place. The extent of this wetting may be expressed in terms of the contact angle θ (figure 5.1b) and via the equilibrium of horizontal forces, the Young equation can be derived:

$$\gamma_{SV} = \gamma_{SL} + \gamma_{LV} \cos\theta \qquad (5.1)$$

Complete wetting takes place when $\theta = 0°$, which occurs when the surface energy of the solid is equal to or greater than the sum of the liquid surface energy and the interface surface energy. For example, graphite (γ_{SV} = 70 mJ m^{-2}) is readily wetted by epoxy resin (γ_{LV} = 43 mJ m^{-2}).

In the general case, interfacial adhesion may be attributed to distinct mechanisms **[Hull, 1996]**:

1) *interdiffusion and chemical reactions* (figure 5.2a); free chain ends between two polymers are entangled. Chemical reaction may also occur either deliberately

promoted or inadvertently caused (figure 5.2d). In the case of carbon fibres, adhesion depends on the angle of the surface basal plane relative to the axis of the fibre, as many reactions take place preferentially at the edges of these planes. Thus, higher surface orientation, as in the case of high modulus fibres, has a detrimental effect to adhesion. One of the mechanisms through which oxidative treatment of carbon fibres enhances adhesion, is by removing these surface layers [**Drzal, 1983a**].

2) *electrostatic attraction*; opposite electric charges make the two surfaces attract each other (figure 5.2b). This can be performed by the addition of functional groups on a surface which electrostatically attract functional groups of the opposite sign on the other surface. This is the case of the addition of silane coupling agents on glass fibres to promote adhesion to epoxy resin (figure 5.2c), or the addition of amine groups on carbon fibre surfaces to enhance their interface with bismalemide resins [**Favre, 1996**].

3) *mechanical keying*; the creation of fingerprint surfaces, due to good liquid solid wetting and subsequent solidification of the liquid, can substantially improve adhesion on a macro-scale (figure 5.2e). This type of adhesion is strongly influenced by residual stresses due to thermal mismatch of the two phases. This is mainly the 'frictional' type of adhesion and may be regarded as a sole function of the surface roughness resulting to a constant shear stress at the interface, or linearly dependent on the thermal stress field, the so called *Coulomb friction* [**McCartney, 1989**].

It is, however, obvious that explaining adhesion by means of isolating any of the aforementioned parameters is bound to be unsuccessful, since the interface or the 'interphase' is a complex region where all the above mechanisms are present. In figure 5.3 a proposed model for the interphase is shown [**Drzal, 1990**]. Apart from the two-dimensional region of contact, there is a region of finite thickness, where a bridging of the properties between the fibre and the matrix is achieved. Processing parameters may trigger further chemical reactions which are superimposed to create the final interphasial region.

When studying the interface, the fundamental problem lies in the extreme difficulty of measuring this gradient of properties in the fibre matrix interphase. In addition, it is the stress transfer from the matrix to the fibre that characterises the composite in a 'macro' scale. Thus, investigating the interface is a twofold process, that involves on one hand ascertaining the most efficient method to measure experimentally the stress transfer and on the other hand finding theoretical models that describe it accurately. An integral part of this process is to ensure that experimental variations and / or simplifying assumptions minimise systematic errors.

5.1.3 The interface and composite properties

The simplest assumption predicting composite properties is the rule of mixtures, where the properties of the constituent materials are added according to their respective volume fraction. In the case of a continuous fibre unidirectional composite loaded in the fibre direction, the rule of mixtures defines the stress σ sustained by the fibre and the matrix, through their respective volume fraction V **[Jones, 1975]**:

$$\sigma = \sigma_f V_f + \sigma_m V_m \tag{5.2}$$

where the subscripts f and m denote the fibre and the matrix, respectively.

The rule of mixtures is no longer macroscopically valid when shear forces are present due to the presence of local discontinuities, or if the material is not ***homogeneous***, that is, if the material properties change from point to point **[Halpin, 1992]**. Two simple cases for inhomogeneity may be regarded, where shear stresses are of primary importance: a) The short fibre composites, where the reinforcement is discontinuous, and b) the continuous fibre composites, where inhomogeneity is present at the locus of a discontinuity of the reinforcement.

The simplest case is the presence of a fracture in a unidirectional composite loaded in the fibre direction. In that situation, fracture of the fibres is regarded as the primary event which controls the local damage development and accumulation that will lead to the failure of the composite **[Reifsnider, 1994]**. In figure 5.4, such fractures within the composite zone are shown. The fracture of a fibre causes a local stress perturbation. The stress is redistributed to the neighbouring fibres through the interface. At some length from the fracture locus, the axial stress is restored on the broken fibre. This length is termed the *ineffective* **[Reifsneider, 1994]** or *transfer* **[Galiotis, 1993b]** length and is dependent on the stress transfer efficiency of the interface. The ineffective length defines the zone of influence of the fracture; small ineffective lengths create large stress concentrations in neighbouring fibres; large ineffective lengths increase the size of the 'flaw' within the composite, raising, thus, the possibility of cumulative flaws leading to fracture. For a single fibre embedded in an epoxy matrix, Drzal and Madhucar **[1993]** have identified the failure mechanisms with relation to various levels of interfacial adhesion (figure 5.5); as interfacial adhesion increases, the axis of failure propagation changes from a mode II crack which propagates along the fibre axis (figure 5.5a) to a mixed mode (figure 5.5b) and finally a mode I crack (figure 5.5c), which propagates transversely to the loading axis. It is worth noting that increased interfacial adhesion may improve on axis properties such as the tensile strength by 45% **[Drzal, 1993]**.

5.1.4 Analytical modelling of the shear transfer

The problem of the stress transfer at the locus of a discontinuity is a typical case of torsionless axisymmetric stress state **[Timoshenko, 1988]**. In cylindrical coordinates r, θ, z with corresponding displacements components u, v, w, the component θ vanishes and u, w, are independent of θ. The same is valid for the stress components with $\tau_{r\theta}$ and $\tau_{\theta z}$ being zero (figure 5.6). Thus, the strain components are reduced to:

$$\varepsilon_r = \frac{\partial u}{\partial r} \qquad \varepsilon_\theta = \frac{u}{r} \qquad \varepsilon_z = \frac{\partial w}{\partial z} \qquad \gamma_{rz} = \frac{\partial u}{\partial z} + \frac{\partial w}{\partial r} \tag{5.3}$$

and the equilibrium conditions are:

$$\frac{\partial \sigma_r}{\partial r} + \frac{\partial \tau_{rz}}{\partial z} + \frac{\sigma_r - \sigma_\theta}{r} = 0 \tag{5.4a}$$

$$\frac{\partial \tau_{rz}}{\partial r} + \frac{\partial \sigma_z}{\partial z} + \frac{\tau_{rz}}{r} = 0 \tag{5.4b}$$

The solution of the equations 5.4 and 5.5 with the appropriate boundary conditions provide the elastic stress-state. The boundary conditions for a cylinder of length *l* loaded in shear are **[Filon, 1902]**:

For $0 \leq z \leq l$:

$$\sigma_z(z) = \sigma_z(-z) \tag{5.5a}$$

$$\sigma_r(z) = \sigma_r(-z) \tag{5.5b}$$

$$\tau_{rz}(z) = -\tau_{rz}(-z) \tag{5.5c}$$

$$\sigma_z = 0, \text{ for } z = 0, l \tag{5.5d}$$

There is an additional boundary condition where:

$$\tau_{rz} = 0, \text{ for } z = 0, l \tag{5.5e}$$

that is, the shear stresses should be zero at the fibre break due to the symmetry of the stress tensor **[McCartney, 1989; Nairn, 1992; Nairn, 1996]**. However, the exact solution cannot provide finite stress values at the discontinuity, that is, at the end of the cylinder. Filon **[1902]** showed that, when there is a discontinuous transition from a stressed area to an unstressed one, stresses become infinite. The physical meaning of this finding is that at the discontinuity the stress-state cannot be elastic, and local yielding / damage are always present. The task of solving equations 5.4 involves defining the appropriate boundary conditions that will provide finite stress-values, and assuming that the effect of the discontinuity is highly localised and does not significantly affect the overall stress-state. It follows that condition 5.5e should be part of any elasticity analysis in order to provide finite stress values at the discontinuity **[Nairn, 1992]**.

5.1.4.1 One-dimensional models

The difficulty of providing a closed-form solution for the elastic equilibrium, as well as the statistical nature of interfacial and / or fibre failure, has led to a variety of analytical treatments. Through the appropriate assumptions, these lead to finite values of the stresses which can be used to model interfacial adhesion. The axial balance of forces at the interface for a cylinder of radius R yields (figure 5.7) [**Rosen, 1965**]:

$$\tau_{rz} = -\frac{R}{2}\frac{d\sigma_z(z)}{dz} \tag{5.6}$$

Kelly and Tyson [**1965**] made the simple assumption that τ_{rz} is constant, which yields:

$$\tau_{rz} = -\frac{R\sigma_{fu}}{l_c} \tag{5.7}$$

In this case, σ_f coincides with the fibre strength which is independent of z and the length l_c is the critical length, which is defined as the length where maximum axial stress is reached prior to the final fracture. In this approach, the fibre is perfectly elastic up to fracture, whereas the matrix (or the interface) is perfectly plastic. The stress-state, as postulated in the Kelly Tyson approach, is shown in figure 5.8a. Although its simplicity makes the constant shear stress approach extremely attractive, the elastoplastic behaviour of the matrix, as well as the lack of definition for radial or hoop stresses [**Nairn, 1992**] are obvious examples of its limitations.

Cox [**1952**] introduced the shear-lag theory, making the fundamental assumption that the shear force S is proportional to the difference between the axial displacement in the matrix w and the displacement in the matrix w_∞ that would exist if the fibre were absent:

$$S = H(w - w_\infty) \tag{5.8a}$$

where H is a proportionality constant which depends on geometrical and material parameters. Through the axial balance of forces (equation 5.6), the shear-lag assumption yields for the axial stress at the interface:

$$\sigma_z(z) = E_f \varepsilon_\infty \left[1 - \frac{\cosh\left(\beta\left(\frac{l}{2} - z\right)\right)}{\cosh\left(\beta \frac{l}{2}\right)} \right] \tag{5.8b}$$

where:

$$\beta = \sqrt{\frac{2G_m^{R_\infty}}{R^2 E_f \ln\left(\frac{R_\infty}{R}\right)}} \tag{5.8c}$$

ε_∞ is the far-field strain and $G_m^{R_\infty}$, defines the shear modulus of a matrix cylinder of radius R_∞ where there is shear perturbation. The interfacial shear stress is:

$$\tau_{rz}(z) = E_f \varepsilon_\infty \sqrt{\frac{G_m^{R_\infty}}{2E_f \ln\left(\frac{R_\infty}{R}\right)}} \frac{\sinh \beta\left(\frac{l}{2} - z\right)}{\cosh \beta \frac{l}{2}} \tag{5.8d}$$

The shear-lag equation has been derived by different authors and is based on the assumption that, for a given r, all stresses are only a function of z. It is worth mentioning that the shear stress τ_{rz} is not zero at the viscinity of the discontinuity, but has a finite value (figure 5.8b). Filon **[1902]** in a similar solution attributed this to the existence of a determinate system of radial shears over the flat end of the cylinder, which from symmetry must be self equilibrating. This, however, does not form part of the shear-lag solution, since radial shearing is ignored. The shear-lag solution **[Cox, 1952]** can be regarded as an upper bound to the elastic solution as the existence of radial shearing blunts the maximum axial shear. The constant shear model **[Kelly, 1965]** described previously is a lower bound where the matrix is assumed to be perfectly plastic and flowing freely. However, it should be noted that the constant shear model requires further assumptions for the fibre strength at the critical length, which may be additional sources of error.

Modifications to the above approaches were made, in order to account for matrix plasticity, interfacial debonding, as well as for damage, or frictional sliding at the interface. Dow **[1963]** introduced a modified shear-lag approach to account for the non-linear behaviour of the matrix. He introduced an incrementally changing matrix modulus at different levels of strain, simulating, thus, plasticity effects. Piggot **[1966; 1980]** combined the shear-lag and the constant shear approach to account for matrix yielding (figure 5.8c) and frictional sliding. Although these 'incremental' approaches are inherently flawed because they introduce unjustifiable discontinuities in the interfacial shear stress, they represent more closely 'real' conditions, where complex phenomena coexist and interact to produce a stress field which cannot be uniquely described through a single analysis.

5.1.4.2 Axisymmetric models

The solution of the equilibrium equation retaining all the components of stress has been attempted by various authors. These solutions aim to satisfy all boundary conditions related to the problem, through an admissible stress-state **[Nairn, 1996]**.

McCartney **[1989]** managed to provide closed-form solutions to various axisymmetric problems. In order to solve the equations of equilibrium, he introduced average functions $\bar{f}(z)$ for the fibre and the matrix cylinders, over their respective radii:

$$\bar{f}(z) = \frac{1}{\pi R^2}\int_0^R 2\pi r f(r,z)dr \qquad (5.9)$$

Thus, all the boundary conditions that he defined are satisfied, apart from two stress-strain-temperature conditions, which are satisfied only in an average sense. McCartney **[1989]** obtained closed-form solutions for all the stresses and extended his analysis to the frictionally bonded case, where Coulomb's law is valid:

$$\tau_{rz}(R,z) = \mu\sigma_r(R,z), \qquad (5.10)$$

Nairn [**1996**] managed to derive a stress function Ψ satisfying the equilibrium conditions for all stress components. The stress function has to satisfy [**Timoshenko, 1988**]:

$$\nabla_1^2 \nabla_2^2 \Psi = 0 \tag{5.11a}$$

where ∇^2 is:

$$\nabla_i^2 = \frac{\partial^2}{\partial r^2} + \frac{1}{r}\frac{\partial^2}{\partial r} + \frac{1}{s_i^2}\frac{\partial^2}{\partial z^2} \tag{5.11b}$$

and s_i $(i=1,2)$ are constants depending on the elastic properties of the material.

Through the stress function all components of stress may be defined either for isotropic (where $s_i = 1$ and ∇^2coincides with the Laplace's operator in cylindrical coordinates [**Timoshenko, 1988**]), or transversely isotropic materials [**Lekhnitski, 1963**]. The stress function satisfies all boundary conditions expect one: *the stress is zero in an average sense over the surface of the fibre*. Nairn et al. [**1996**] have extended this analysis to include an imperfect interface [**Hashin, 1990**], where the interphase is collapsed in two dimensions to allow for axial discontinuities. These are quantified through the use of a parameter *D*, by which any displacement discontinuities are proportional to the associated interfacial stress.

The above model provides an exact elasticity solution. The incorporation of the imperfect interface provides the flexibility needed to simulate any real conditions where local material variations are not measurable, or propagating interfacial damage creates differences along the axial direction.

5.1.5 Numerical Modelling

The difficulty to obtain closed-form solutions for the equilibrium equations (5.4), as well as to account for problems relating to local property variations, matrix plasticity and discontinuities created by crack formations, may be overcome with the use of numerical methods. Finite Element Analysis (FEA) [**Carrara, 1968; Fan, 1992; Guild, 1994**], Boundary Element Analysis (BEA) [**Selvadurai, 1995; Paris, 1996**], or Finite Difference Analysis (FDA) [**Zhang, 1983; Termonia, 1987**], have proved extremely useful in the fields of composite materials. The widespread use of numerical methods is facilitated by the explosive development of low cost and easily accessible computer power.

Termonia [**1987**] studied the locus of the discontinuity near the fibre end using Finite Differences Analysis (FDA) (figure 5.9). The study included the effect of stress transfer across the cross-section of the fibre. The build-up of stress along the fibre axis was found to be a unique function of the fibre to matrix elastic moduli ratio. The analysis was extended to predict the tensile strength of discontinuous fibre reinforced composites [**Termonia, 1990**].

Carrara and McGarry [**1968**] performed a detailed study on the effect of fibre end geometry to demonstrate that ellipsoidal ends minimise the maximum shear stress when the longitudinal axis of the ellipsoid is twice the fibre diameter. Fan and Hsu [**1992**] analysed the stress field for both isotropic and anisotropic fibres, the effect of modulus ratio, as well as the fibre end geometry, and compared the results to experimental data obtained with Laser Raman Spectroscopy.

The effect of matrix yielding and frictional bonding was studied in order to account for the discrepancies between theories of elastic stress transfer and experimental data [**Tripathi, 1996; van den Heuvel, 1997**]. The inclusion of an interphase with distinct properties has been extensively used as a method to account for local property variations [**Daoust, 1993**]. The use of a more compliant interphase was found to decrease the stresses at the fibre ends and, thus, more realistic stress values are obtained than those predicted by the shear-lag theory [**Cox, 1952**]. Agrarwal and Bansal [**1979**] related the modulus of the interfacial layer to the composite strength to find that a stiff interface has a beneficial effect on the tensile strength, without significantly affecting the modulus of the composite. Broutman [**1974**] proved through Finite Element Analysis that the toughness of the composite measured by the amount of strain energy absorbed can be maximised by controlling the interphase modulus.

Finally, the interfacial behaviour of composites has been modeled through the assumption of crack formation, either along the interface [**Gent, 1996**], or at an angle to the fibre axis [**Selvadurai, 1995**].

It is obvious that the numerical approaches can be enlightening in a variety of situations and provide considerable insight into composite micromechanics. The multiplicity of situations that can be modeled numerically have been successful in many cases to account for phenomena occurring in real composites. Not only do they provide interpretations to experimental observations, but they also have the potential to predict the behaviour of a composite under load.

5.1.6 Testing the interface

The role of the interface lies in transferring stresses between neighbouring fibres when shearing is present. This may happen at the locus of a discontinuity, such as a fibre fracture, or during off-axis and shear loading. The maximum value of shear stress that the interface can sustain is the interfacial shear strength of the system. However, the definition of interfacial failure is not a straightforward task. In most of the cases, interfacial failure involves debonding [**Netravali, 1989c**], shear failure [**Kelly, 1965**], or even a progression of damage parallel to the fibre axis which depends on applied strain and loading history [**Nairn, 1996**].

Although levels of interfacial adhesion can be directly linked to composite properties [**Drzal, 1993**], the outcome of full composite testing cannot be quantitatively associated to a measure equivalent to interfacial shear strength. Therefore, several micromechanical methods have been developed in order to provide a quantity, which ideally is a sole function of interfacial properties and is free of artefacts. Although there has been a wide variety of methods proposed in recent years, most can be reduced to three basic methods: the fibre pull-out test, the microindentation test and the fragmentation test.

5.1.6.1 The pull-out test

In the pull-out test [**Shiryaeva, 1962; Favre, 1972**], a length of the fibre l is embedded in a matrix block which is gripped (figure 5.10a). The free end of the fibre is gradually loaded until the fibre is pulled out from the matrix. The load displacement curve may be recorded. As the experiment starts, the load increases linearly with displacement up to a point where significant deviation from linearity occurs, probably due to plastic deformation of the matrix. The load reaches a maximum value and drops abruptly to a much smaller value controlled by friction [**Li, 1994**]. The interfacial shear strength may be derived through the maximum recorded load P_{max}.:

$$= \frac{P_{max}}{2\pi R\ell} \qquad (5.12a)$$

The necessary condition [**Broutman, 1969**] is that the maximum stress on the fibre σ_{max} does not exceed the fibre strength σ_{fu}:

$$\sigma_{max} = \frac{P_{max}}{\pi R^2} \leq \sigma_{fu} \qquad (5.12.b)$$

The pull-out test has the advantages that [**Drzal, 1993**]: (i) any reinforcing fibre may be used, (ii) any matrix may be used, and (iii) the load is directly measured.

The problems associated with the pull-out test are associated to artefacts due to the test geometry:

- The matrix is wetting the fibre creating a meniscus which complicates considerably the stress-state.

- Clamping of both the fibre and the resin block may be difficult, particularly when filaments with diameter of the order of 10 μm are used. The axial alignment of the fibre to the loading direction is reported to play a major role.
- The maximum recorded load P_{max} depends on the embedded length l. If constant shear is assumed as in equation 5.12a, the dependence is linear. However, various researchers have shown both theoretically [**Gray, 1984**] and experimentally [**Meretz, 1993**] that the shear stress is not constant.
- The pull-out test has been criticised because the state of stress at the juncture of the fibre and the matrix creates a normal tensile interfacial force which is not present in the actual composite [**Drzal, 1993**].
- Many tests are required to obtain a significant amount of data.

Apart from the simplistic analysis for the interfacial shear strength already presented, shear-lag [**Greszczuk, 1969**], and more complicated elastoplastic analyses [**Lu, 1995**] have been performed in order to estimate the complicated three-dimensional stress field for the pull-out test.

Modifications to the pull-out test have also been reported, such as the microbundle pull-out [**Qiu, 1993**]. In this case, the fibre is pulled out of a bundle of fibres tied together and wetted with a matrix drop (figure 5.10b). This technique offers the advantage of simulating a real composite with known volume fraction. Both the embedded length and volume fraction can be relatively controlled through sample preparation. Sastry et al. [**1993**] performed a complete analysis of the microbundle pull-out test. They assumed the existence of three zones near a fiber break, including elastic, plastic and frictional debond zones, which provided a reasonable fit to the experimental data under realistic assumptions.

Another variation of the pull-out test is the microbond test where, instead of embedding a fibre in the resin, a resin drop is applied to the fibre and cured in position (figure 5.10c) [**Pitkethly, 1996**]. More than one droplet may be placed on a single length of the fibre. The fibre is subsequently pulled through knife edges, which are close enough to restrain the resin droplet, while the load displacement curve is being recorded [**Penn,**

1989]. Although its simplicity makes the microbond test by far the quickest of micromechanical tests, there are many parameters that may affect its reliability. The most important of these are the size of the resin droplet, as well as the geometry of the knife-edges in relation to the droplet geometry, which may create stress concentrations or, generally, non-uniform loading [**Pitkethly, 1996**].

5.1.6.2 The microindentation test (MIT)

The MIT is one of the newest techniques developed to investigate the interface properties of composites [**Mandel, 1986**]. It is essentially a metallurgical hardness test applied to composite materials. A section of composite is carefully polished and placed in the test machine and a fibre that does not touch any neighbouring fibres is selected (figure 5.10d). The load is applied through an indentor which should be smaller that the diameter of the fibre and the load / displacement curve is recorded. Parameters, like polishing and the shape of the indentor, are of critical importance but are easily controlled. However, the technique involves the identification of the decohesion point, which in most cases is arbitrarily defined. In some cases it is defined as the point where the interfacial crack is more than a percentage of the circumference [**Desaeger, 1993**]. Other definitions involve a change of slope in the load displacement curve [**Netravali, 1989a**], or a load drop at a certain moment of the loading test [**Pitkethly, 1993**]. The interfacial shear strength values are subsequently derived through shear-lag [**Desaeger, 1993**] or Finite Element Analyses [**Tsai, 1990**].

The MIT involves real composite testing allowing a more realistic simulation of thermal stresses, polymer morphology, and the influence of neighbouring fibres and / or volume fraction. However, this is done at the expense of a unique failure criterion. Stress concentrations created by the indentor may cause fibre splitting during loading and this further complicates the detection of decohesion.

5.1.6.3 The fragmentation test

The fragmentation test is the oldest of the examined techniques [**Pitkethly, 1996**]. The test was first presented to model the behaviour of reinforced metal composites [**Kelly, 1965**]. The test consists of a single fibre embedded in a matrix, usually of a dogbone shape (figure 5.10e). The matrix is loaded in tension. When the strain to failure of the fibre is reached, the fibre fractures. The fragmentation process continues until saturation is reached; that is, when there are no more fracture events. If the test were governed by an elastic stress-state, saturation would never be achieved and the fragmentation process would continue until matrix failure. However, saturation is achieved and is attributed to interfacial failure.

The fragmentation test provides the possibility of recording the fragmentation process as a function of strain, either optically [**Waterbury, 1991**], or through acoustic emission techniques [**Favre, 1990**]. After saturation is reached, a distribution of fragment lengths is readily available. With the appropriate assumptions, it can be linked to the interfacial shear strength of the system.

While the coupon is being strained, the fibre fractures when its axial strength is reached. As a result, if l_c is the required length for the fibre to reach its strength value, then, the distribution of fragment lengths l_f will range from $l_c/2$ to l_c [**Narkis, 1988**]. In order to define l_c, the strength distribution of the fibre has to be known. Assuming a normal distribution of strength, the critical length l_c is straightforwardly defined as:

$$l_c = 4/3\, l_f \tag{5.13}$$

Netravali et al. [**1989c**] developed a relationship using the Weibull shape parameter for the fibre strength. Ling and Wagner [**1993**] developed a model where the strength and the spatial distribution of flaws governing the strength of the fibre, as well as the tensile strength variation along the fibre length, was incorporated. Baxevanakis et al. [**1993**] used other distributions than the Weibull distribution to describe the flaw distribution on the fibre so as to improve agreement with experimental data.

In order to derive interfacial shear strength values, a stress transfer model has to be assumed. The constant shear model is the most convenient to use and the interfacial shear stress is given by equation 5.7 [**Kelly, 1965**]. It is, however, obvious that any resultant value for interfacial shear strength depends on the stress transfer model that the experimentalist chooses.

Apart from the major problem associated with the interpretation of data, the fragmentation test has been criticised for a variety of drawbacks.

- The test is limited by the requirements of a tough matrix and a brittle fibre. The strain to failure of the matrix should be at least 3 times the fibre strength failure to achieve saturation [**Drzal, 1993**].
- The saturation stage is well above any service strain limit for the 'real' composite. Thus, interfacial failure mechanisms may be dominant that otherwise would not be important. These mechanisms may include debonding [**Wagner, 1995; DiBenendetto, 1996**], shear flow [**Nath, 1996**], or frictional sliding [**Piggot, 1980**], but are not readily identifiable through the test.
- The thermal expansion coefficient differential is inducing hydrostatic compressive stress field which otherwise would not be present [**Nairn, 1996**]. Most assumptions of frictional sliding would demand a direct dependence on radial stresses or the Coulomb friction law (equation 5.10). In addition, the compressive stress field is directly dependent on the specimen size and geometry, which further obstructs the standardisation of the procedure.
- Additional problems may arise from extensive fibre handling which contaminates its surface and consequently the interface.

The fragmentation test, although heavily criticised, remains still one of the most popular tests. This is due to the creation of a stress-state similar to that of the composite [**Drzal, 1990**]. The advantages that the fragmentation test offers are the following:

- many data points with one specimen,
- sensitivity to interfacial conditions,
- direct observation of interfacial events,
- qualitative assessment of stresses and failure modes.

The interrelation of interfacial shear transfer with fibre strength may also be regarded as an advantage, since it is clearly related to failure mechanisms in real composites. [**Gulino, 1991**].

The simplicity of the fragmentation test configuration provides the possibility of combining the test with existing techniques. The optical observations are in most cases performed using photoelastic techniques [**Tyson, 1965**]. The photoelastic principle is based on the birefringence, or optical anisotropy, created in an otherwise isotropic material, due to the presence of local stresses. The fragmentation process is optically enhanced and local discontinuities, such as fibre fractures, are much more easily spotted. [**Buxton, 1994**]. Polarisation studies in the fragmentation test may also provide qualitative information about the loci of stress concentrations. Thus, matrix failure or the interfacial debonding can be identified [**Detassis, 1995**]. More elaborate computerised optical equipment has also been used to monitor all stages of the experiment and information, such as the length distribution as a function of applied strain, can be obtained [**Waterbury, 1991**]. Simulations of the fragmentation process have also been performed in order to identify the mechanisms of stress transfer that provide best agreement to the experimental data [**Favre, 1991; Lacroix, 1995**].

The use of acoustic emission in combination with the fragmentation test provides the possibility of real time monitoring of the fragmentation process [**Favre, 1990**]. Thus, the laborious procedure of optical detection of cracks is eliminated, the use of non-transparent matrices is feasible, and more realistic loading conditions are provided, as the sample is continuously strained. As a result, unwanted effects such as matrix relaxation may be avoided [**Netravali, 1989b**].

Finally, the single fibre geometry such as the one used for the fragmentation test provides the ideal configuration for local stress monitoring using Laser Raman Spectroscopy (LRS) [**Galiotis, 1993b**]. The LRS application to interfacial monitoring will be extensively studied in the next section.

The overview of the most popular techniques to measure interfacial adhesion reveals that all techniques have inherent advantages and disadvantages. The lack of standardised procedures and the difficulty arising from the fibre dimensions and handling, makes all micromechanical tests extremely sensitive to conditions that cannot be controlled systematically. This is clearly depicted in the results of a round robin programme, where twelve laboratories used the aforementioned tests to evaluate adhesion [**Pitkethlky, 1993**]. The only parameters that were kept constant were the materials used. The study showed unacceptable interlaboratory differences (figure 5.11). Thus, the need for strict protocols in order to reduce interlaboratory scatter is outlined. It is also obvious that the interface is a complex system that can be dramatically affected by parameters which in most cases lead to systematic errors.

5.1.7 Interfacial studies using Laser Raman Spectroscopy

The ability of relating the shift of vibrational Raman frequencies to local strain values has rendered LRS a powerful tool for the micromechanical study of composites. [**Day, 1993; Galiotis, 1993a; Young, 1997**] Laser Raman Spectroscopy is to our knowledge the only reported technique to provide measurements relating directly to axial stress in the case of highly crystalline fibres. The fibres become embedded stress gauges along their axis direction [**Shadler, 1995**]. The only limitation is that the matrix must be reasonably transparent. Modified micromechanical tests have been used in conjunction with LRS to provide axial stress distributions along the fibre length. Galiotis et al. [**1984**] showed the axial stress distribution for an embedded polydiacetylene fibre in epoxy, to reveal a behaviour similar to that predicted by the shear-lag theory. The axial stress distribution during the fibre pull-out test have been analysed with LRS [**Boogh, 1992; Gu, 1995**]. Bannister et al. [**1995**] modeled the measured axial stress using a two zone model consisting of a constant shear zone and a shear-lag zone. The micromechanics of reinforcement of 2D model composites has been investigated and the fibre ineffective length has been related to stress concentrations as a function of interfibre distance in order to define the radius of the shear perturbation cylinder [**Atallah, 1993; Chohan, 1996**]. Three dimensional composites have also been studied and related to model composites [**Galiotis, 1996**]. Remote Laser Raman microscopy [**Paipetis, 1996**] also provided the possibility of in situ monitoring without the limitation imposed by rigid optical set-ups.

It is, however, worth noting that single fibre model composites have been the most extensively studied configuration by means of LRS in order to assess interfacial properties. The model coupons use the same geometry as the one used in the fragmentation test, where either long or short single filaments are aligned along the loading axis of the sample. After the initial work on polydiacetylene crystals by Galiotis et al. [**1984**], the single fibre coupon test has been used to study carbon [**Melanitis, 1993a**] and Kevlar® [**Galiotis, 1993b; Bannister, 1995**] interfacial properties, either in thermoset or thermoplastic matrices [**Schadler, 1992**].

The study of the stress transfer during the long fibre coupon test is performed after the sample is strained at distinct strain levels. [**Melanitis, 1992; Melanitis, 1993a**] The embedded fibre is then monitored at steps as small as one micron [**Paipetis, 1996**]. Experimental axial stress distributions are directly obtained via the frequency shift of well characterised Raman bands [**Robinson, 1987b**]. Experimental shear stress distributions are provided through the axial balance of forces [**Melanitis, 1993a**].

The possibility of measuring axial stress at the locus of a discontinuity led to a modification of the long fibre geometry, the short fibre coupon [**Melanitis, 1993b**]. The short fibre coupon test has an embedded fibre of finite length, where the fibre ends are within the gauge length of the sample. Thus, the discontinuity is already present and can be studied independently of fracture events. The short fibre coupon test has the distinct advantage that interfacial bonding may be monitored, before various complicated damage mechanisms are initiated by the massive energy locally released after the fibre breaks. In addition, the short fibre coupon test has been extensively used for fibres where the failure process is not easily traced optically, such as in the case of Kevlar® fibres [**Galiotis, 1993b**].

To summarise, the LRS study of single fibre model coupons either in short or long fibre configuration, makes up for all the inherent shortcomings of the 'classical' fragmentation test and provides unique advantages over conventional techniques as:

- The stress transfer is directly measured at the interface.
- The distribution of the axial strength of the fibre as a function of its gauge length is no longer needed, since local stress maxima are easily measured.
- The relative fibre to matrix strain to failure is not important since stress transfer at the discontinuity is measurable at any strain.
- No assumptions about the stress field need to be made; moreover, the validity of stress-transfer models may readily be tested.

5.1.8 A parametric study of the stress transfer in single fibre model composites

The study of the interface is not a straightforward task. However, the choice of controlled factors that play an important role to the interfacial properties of composites is very important in order to acquire further insight in the stress transfer mechanisms. The presence of a coupling agent between the fibre and the matrix, such as the fibre sizing, may promote the creation of an interphase. The sizing on carbon fibres consists of a thin layer of usually epoxy resin which serves a dual purpose: protect the carbon fibre surface and enhance the interfacial properties. Hence, the compatibility between the sizing and the matrix materials becomes a crucial parameter in composites. Guigon and Klinklin **[1994]** have shown that different sizings may improve the interfacial properties but, if the sizing is not compatible with the matrix, there is decohesion at the sizing-matrix interface. Cheng et al. **[1994]** conducted a detailed study of the sizing effect using both commercial and experimental sizings. They reported dependence of the stress transfer efficiency on molecular weight, deposition procedure, as well as, in some cases, on the presence of an interphase region as manifested by Scanning Electron Microscopy (SEM) studies. Yumitori et al. **[1994]** reported that the presence of a sizing resin improves the interface of a PES-thermoplastic matrix composite, but leads to the creation of a weak interphase in the case of epoxy matrix systems. In conclusion, it appears that the presence of sizing in carbon-fibre-polymer interfaces plays an important role in the properties of the interface but, as yet, its significance has not been adequately quantified.

In addition, the interfacial shear strength has been associated with the matrix dependent properties, such as the shear modulus **[Drzal, 1990]**, or the shear strength of the matrix [**Miwa, 1995**]. The onset of the fragmentation process has been reported to depend mainly on the fibre strength distribution, whereas the saturation level depends on the resin yield strength [**Andersons, 1993**]. The differential thermal expansion between fibre and matrix leads to the formation of a hydrostatic field on the fibre affecting the stress transfer and the Poisson ratio mismatch contributes to the stress field created during the fragmentation procedure [**Nairn, 1992**]. Finally, dynamic phenomena such as the viscoelastic behaviour of the polymer matrix [**Miwa, 1995; Detassis, 1995**] or the fibre fracture release energy [**Wagner, 1993**] may respectively affect the shear transfer or the interfacial failure mode.

In this study, Remote LRS and the single fibre model coupons in both short and long fibre configuration have been used in order to study the stress transfer efficiency of carbon fibre / epoxy interfaces. All studies were performed in relation to fibre sizing, specimen geometry and temperature of the environment. The chosen parameters are believed to provide important information regarding material properties because they are related to the local interfacial or interphasial chemistry, the temperature dependent stiffness of the matrix as well as to the resultant stress field and the possible mechanisms of interfacial damage.

5.2. EXPERIMENTAL

5.2.1 Materials

The performed study involved the investigation of parameters affecting the properties of the interface. As previously stated, the studied parameters were:

- the fibre sizing, or the interfacial chemistry,
- the coupon geometry, or the short fibre and the long fibre coupon test,
- the environment, or the temperature dependence.

The M40B-40B (sized) (MEBS) and M40B (unsized) (MUS) high modulus carbon fibres supplied by Soficar were used throughout this study. Both fibres were reported to have a standard level of oxidative treatment. The M40 fibres are extensively studied in chapter 4. The matrix used was the two part MY-750 / HY-951 epoxy system provided by Ciba Geigy (MY-750: unmodified liquid epoxy resin, and HY-951: triethylene tetramine curing agent). The following systems were studied:

- MEBS / MY-750 short fibre coupon at room temperature,
- MUS / MY-750 short fibre coupon at room temperature,
- MEBS / MY-750 long fibre coupon at room temperature,
- MUS / MY-750 long fibre coupon at room temperature,
- MEBS / MY-750 long fibre coupon at 60°C,
- MUS / MY-750 long fibre coupon at 60°C.

The manufacturer's quoted properties for the materials used are shown in table 4.3 for the fibres [**Hughes, 1986**], and in table 5.1 for the matrix [**Ciba-Geigy, 1979**].

5.2.2 Specimen preparation

The matrix for the model coupons was prepared as following: the epoxy resin (MY-750) was heated at 40^0C under vacuum for 30 min. This original conditioning of the epoxy resin was indispensable, in order to minimise the volume of trapped air in the viscous liquid, since after mixing with the curing agent, the limited pot-life of the mixture does not allow extensive degassing. The epoxy was subsequently mixed with the hardener (HY-951) at a ratio 4:1 and the mixture was degassed for 10 min under full vacuum before being used.

Specially designed silicon rubber moulds were used in order to manufacture the single fibre coupons. Two methods of specimen preparation were employed.

5.2.2.1 Short fibre coupons

In the short fibre configuration **[Vlattas, 1992]**, the coupons were prepared in three stages. A thin resin layer was initially applied at bottom of the silicon rubber mould (figure 5.12a). Single filaments of 1-4 mm length were carefully aligned on top along the axis of the mould (figure 5.12b). More than one filaments were aligned in the mould in order to provide the possibility of extensive monitoring and account for the possibility of destroying the fibre during polishing. Care was taken to place the single filaments away enough from each other so as not to have any interaction in the stress field. The mould was subsequently filled with the resin (figure 5.12c).

5.2.2.2 Long fibre coupons

In the long fibre configuration **[Melanitis, 1993a]**, individual fibres were carefully aligned along the full length of the silicon mould (figure 5.13a). The filaments were glued in position on the purposely made pins on the silicon rubber mould (figure 5.13b). Finally, the matrix was poured in the mould (figure 5.13c).

The single fibre composites were cured for 2 h at 60^0C. The cured coupons were removed from the moulds and left for a day at ambient temperature. They were subsequently post-cured at 120°C and allowed to cool down in the oven to room temperature, in order to avoid thermal shock effects. A substantial number of pure resin samples were also manufactured in order to be used for the matrix characterisation.

The cured dogbone samples were ground until the embedded fibre was approximately 100 μm away from the surface and subsequently polished. The pure resin samples were milled down using a milling machine and lightly ground using fine grinding paper to avoid stress concentration induced failures.. The final geometry of the samples is shown in figure 5.14.

5.2.3 Tensile testing and far field stress and strain measurements

All experiments were performed on a Hounsfield universal testing machine. The samples were loaded in tension and strained to failure. A 2000 N load-cell at full-scale was employed for load measurements, with simultaneous ±5V output.

The strain measurements were performed by means of electrical resistance strain-gauges. The strain-gauges (*resistance* 350.0±0.5Ω and *gauge factor* 2.09 manufactured by Techni Measure) were attached to the specimen using CN® adhesive. The future strain-gauge locations were ground locally to ensure optimum adhesion. Instant reading of the strain-gauges resistance was obtained by a Maplin M90205 digital multimeter. The strain-gauge resistance was converted to far field strain ε_∞, by applying the following equation:

$$\varepsilon_\infty = \frac{1}{GF}\left(\Omega_s - \Omega_0\right) \tag{5.14}$$

where GF is the gauge factor, Ω_0 is the resistance of the strain-free strain-gauge, and Ω_s is the resistance indicated at the multimeter during the experimental procedure.

It should be mentioned that above 3.0% applied strain, the strain-gauge reading is only an indicative measurement. This is due to the fact that the correlation between strain-gauge resistance and strain deviates from linearity at those levels and, as a result, a correction factor may be needed. At higher applied strain and when the strain-gauge output ceased to be reliable, the cross-head displacement of the testing machine was used to calculate strain values.

When real time monitoring of the strain was required, the strain-gauge was incorporated in a Wheatstone bridge under 5V in order to convert resistance to voltage measurements. Stress strain curves were subsequently produced by recording the respective stress and strain voltage through an analogue to digital (A/D) card manufactured by National Instruments to a personal computer.

5.2.4 High temperature testing

Testing at elevated temperatures was performed by using a specially designed environmental chamber fitted on the loading frame. The chamber allows temperature testing up to 200°C as well as controlled heating rate. The temperature is controlled through a single thermostat and steady state within the chamber is achieved through a fan operating at two speeds. Temperature control is accurate to ±0.1°C. The chamber is supported on special rubber mounts, so that the minimum amount of vibration from the operating fan is transmitted to the loading frame. This is indispensable when high resolution Raman monitoring (~ 1 μm) is required.

In order to allow for simultaneous Raman spectrum acquisition during real time testing, the chamber is designed with a glass window, tailor-made to allow visible radiation and block the infra-red frequencies. This design prevents heat loss through the glass surface, without inhibiting Raman Spectrum acquisition, if an appropriate long working distance objective is used.

5.2.5 Thermomechanical characterisation of the matrix

Pure resin samples prepared as described previously were tested in tension at room temperature, 40°C, 60°C, and 80°C. Five samples were tested per temperature. Rosette strain-gauges were attached to all specimens in order to obtain the Poisson's ratio values as a function of temperature.

The strain rate was 0.25x10^{-2} min^{-1}. The respective stress strain curves are shown in figure 5.15. The shear modulus values were calculated as a function of the measured modulus and Poisson's ratio. Shear strength values were calculated through the tensile strength values using the Von Mises criterion [**McCrum, 1990**]. The overall mechanical properties of the matrix for all studied temperatures are shown in table 5.2.

The glass transition temperature of the matrix was measured to be 88°C by means of a Perkin Elmer DSC 2C Differential Scanning Calorimeter (heating rate of 20° / min).

5.2.6 *Raman Studies*

5.2.6.1 Raman spectrum acquisition

Raman spectra were taken with a Remote Raman Microprobe (ReRaM). The ReRaM has been developed and tested in-house, and uses flexible waveguides for both the delivery and the collection of light. In addition, micrometer stages allow the translation of the ReRaM along all three axes down to an accuracy of 1 μm. The design of the ReRaM is extensively described in chapter 3 (figure 3.11).

In this work, the laser was focused to a submicron spot employing a laser power of approximately 1 mW on the specimen. The collected Raman light was guided through an optical fibre to a SPEX 1000M single monochromator. The Raman signal was collected via a Wright Instrument CCD and stored in a personal computer. Spatial discrimination was achieved by magnification of the focal spot to fill the optical fibre endface. A confocal aperture of 1.3 μm (§3.2.4) with the appropriate lens combination was used (figure 3.10). This configuration resulted in a 20 s typical spectrum acquisition time for the room temperature studies. The acquisition time was increased to 60 s for the studies at 60°C. This was due to signal loss occurring as the signal passed through the oven window.

As mentioned before (§4.2.5), the Raman band used for the purposes of this study is the 1580 cm^{-1} $\mathbf{E_{2g}}$ graphitic band. The epoxy resin does exhibit a considerable amount of Raman activity throughout the spectrum. In the spectral window of interest, the main feature that interferes with the carbon fibre Raman activity is the 1620 cm^{-1} line, which is attributed to a phenyl ring stretching vibration [**Chang, 1986**]. In order to further reduce the contribution of the resin Raman peak to the spectrum of carbon fibre, spectral deconvolution techniques were employed in this study. It should be noted at this stage that *the matrix Raman Spectrum does not exhibit wavenumber dependence*. This is because the matrix is not crystalline enough for the far field deformations to affect it at molecular level.

In order to obtain the maximum resolution from the Raman spectrum of the embedded fibre, the residual matrix contribution to the overall spectrum had to be eliminated. This was achieved by scaling the resin spectrum according to the intensity of a reference peak of the composite in a frequency region where the carbon fibre does not exhibit any Raman activity.

The deconvolution procedure is shown in figure 5.16. The frequency window is 1250 cm^{-1} to 1700 cm^{-1}. A typical composite spectrum consists of the sum of the carbon fibre and the matrix spectra (figure 5.6b). The matrix contribution can be completely eliminated by appropriately scaling a matrix reference spectrum (figure 5.16a) and subtracting it from the composite spectrum (figure 5.16b). Scaling may be performed by using a matrix Raman band in an area where the carbon fibre does not exhibit any activity. An appropriate band in this spectral window was the one appearing at approximately 1460 cm^{-1} (figure 5.16a). The scaled resin spectrum was then subtracted from the composite spectrum, leaving, thus, the pure Raman activity of the carbon fibre (figure 5.16c). The processed spectrum was subsequently fitted with a Lorentzian distribution function, which provided accurate estimates of peak position and bandwidth (see appendix 1).

5.2.6.2 Converting spectroscopic data to stress values

The conversion of spectroscopic data to stress values was performed by:

- obtaining frequent calibration values of unstressed fibres in the respective environment (room temperature or 60°C). The frequency values ν_{ref} obtained for the $\mathbf{E_{2g}}$ band were used as a reference for zero stress.
- converting the relative shift $(\nu - \nu_{ref})$ of the $\mathbf{E_{2g}}$ band to axial stress values σ_z through the use of the calibration curves obtained for the M40 fibres (figure 4.17):

$$\sigma_z = (\nu - \nu_{ref}) / \alpha_\sigma \tag{5.15}$$

Throughout this study the value of 3.0 cm^{-1} / GPa was used as the stress proportionality constant α_σ as calculated in §4.2.5.1.

5.2.6.3 Stress monitoring in model composites

(a) Residual stress distributions

Initial mapping of the fibre stress distribution in the unstressed coupons provided distributions of the residual stresses at room temperature for both long and short fibre configurations. A total of five samples were monitored in each configuration. In the case of the short fibre configuration, care was taken in order to acquire spectra sufficiently away from the fibre end. Thus, it was expected that the fibre had reached its far field stress value. Raman wavenumber distributions of free fibres in air were recorded throughout the four experiments, in order to acquire reference distributions for the unstressed fibre.

(b) Axial stress monitoring of the model composites

Raman data were collected by scanning the Raman microprobe point-by-point along the embedded fibre for each configuration studied (§5.1.7). The samples were mounted on the Universal Testing Machine, and strained at distinct strain levels.

The short fibre samples were monitored at applied far field strains of up to 0.6% at 0.2% increments. This was performed to assess interfacial adhesion at low far field strain values where the stress transfer may be regarded as elastic. The long fibre samples were monitored at applied far field strains of up to 5.00%.

In general, a section of the Fragmentation Gauge Length (FGL) of 2.5-3 mm in length, was scanned at different increments of externally applied far field strain. The strain rate was kept to minimum (i.e. $0.25\text{x}10^{-2}$ min^{-1}) in order to avoid relaxation effects during Raman spectrum acquisition. Within this 'window', measurements were taken at steps of 1 μm at the vicinity of a fibre break and, then, at steps of 2, 5 and 10 μm away from the locus of the fibre fracture.

5.2.6.4 Derivation of interfacial shear stress distributions

In order to derive interfacial shear stress values the axial balance of forces along the fibre has to be taken into account. Along a volume element of the fibre of infinitesimal width *dz*, the axial balance of forces yields (figure 5.7):

$$\left[\bar{\sigma}_z(z) + d\bar{\sigma}_z(z)\right]\pi R^2 - \bar{\sigma}_z(z)\pi R^2 - \tau_{rz}(z)2\pi R dz = 0 \qquad (5.16)$$

where $\bar{\sigma}_z$ is the axial stress acting on the cross-sectional area, τ_{rz} is the shear stress, and R the radius of the fibre. The bar denotes averaging over the cross-sectional area of the fibre.

Equation 5.16 is easily solved to yield the expression for the interfacial shear stress [**Cox, 1952; Rosen; 1965; Piggot, 1980**]:

$$\tau_{rz} = -\frac{R}{2}\frac{d\bar{\sigma}_z(z)}{dz} \qquad (5.17)$$

It is important to note that the above equation is valid for values of axial stress acting over the cross-sectional area of the fibre, or the integral of the axial forces over the cross-section. This is indicated by the bar on the axial stress that denotes averaging. The difference between equations 5.6 and 5.17 is the implication that the axial forces on the fibre cross section are not constant. The same conclusions may be derived through the axisymmetric elasticity equations (see appendix 2).

The Raman Technique yields axial stress values at the vicinity of the laser excitation beam. This provides the high axial resolution of the technique which makes the detection of local stress variations at sub-micron steps. Consequently, it is expected that the depth of focus of the beam, or the sampling area, is bound by the axial resolution which is of the order of magnitude of the spot size, that is, in the area of 1 μm (§3.3). Consequently, for non-absorbent or transparent materials this is the effective sampling volume of the Raman probe. In the case of highly absorbing materials, such as carbon fibres, the penetration depth y is linearly dependent on the *excitation wavelength* λ **[Guenther, 1990]**:

$$y=\frac{\lambda}{2\pi nh} \tag{5.18}$$

where n is the refractive index, and h the extinction coefficient of the material.

For a collimated beam, the penetration depth for graphite is of the order of 100 nm **[Lespade, 1984]**. Thus, it is obvious that axial stress measurements are confined to the above area which is defined by the optical properties of graphite and do not penetrate the fibre. In other words, there is at least one order of magnitude difference between the penetration depth and the fibre diameter.

Taking into account the above considerations, the sole assumption that is needed in order to calculate interfacial shear stress distributions through equation 5.17 is that *the measured axial stress for a penetration depth of 100 nm coincides with the average axial stress on the fibre.* In other words, the shearing in the fibre is not taken into account in the above model and the axial stress is regarded to be constant over the cross-sectional area of the fibre. It has been shown numerically **[Fan, 1992]** and analytically **[McCartney, 1989]** that the effect of shearing within the fibre is highly localised and is negligible within two fibre diameters. Where shearing within the fibre is not negligible, the measured $\bar{\sigma}_z$ is overestimated in equation 5.17, since the axial stress at the vicinity of the interface is expected to be higher than near the fibre axis **[Fan, 1992]**.

In general, the axial stress of the fibre within two fibre diameters is not expected to vary more than 10% of the maximum stress on the fibre. Variations of the axial stress over the cross-sectional area may be regarded as negligible as they lie well within the experimental error of the Raman measurements. As a result, equation 5.17 may be used for the experimental calculation of interfacial shear stresses.

5.2.6.5 Interpolation of the axial stress data

In order to derive experimental interfacial shear stress (ISS) values, the use of equation 5.17 presupposes the derivation of the axial stress data over the fibre axis z. This is done numerically by fitting a known function to the axial stress data and subsequently taking its derivative. Polynomials of 2nd to 5th degree have been used **[Melanitis, 1993a, b]** as well as locally weighted least square functions **[Schadler, 1992]**. In this study, cubic b-spline interpolation has been used **[Vlattas, 1992]**.

The b-splines allow for discontinuity of the derivatives of specific points, i.e. the fibre fracture and force continuity along the fibre length **[Hayes, 1974]**. Thus, they offer the following advantages:

- a continuous function may be obtained for both the axial and the interfacial shear stress,
- local discontinuities, such as fibre fractures, may be accounted for,
- the controlled use of interpolated third degree polynomials provides optimum fit without error induced oscillations present when higher (>4) degree polynomials are used as interpolating functions.

In this study, the experimental data of fibre stress versus distance-along-the-fibre were fitted with b-splines. By the use of equation 5.17 and differentiation of the fitted b-spline curve, the ISS profiles along individual fragments were derived. The interpolation process is discussed in appendix 3.

5.2.7 Additional studies

5.2.7.1 Optical microscopy

Conventional fragmentation studies were also performed. The long fibre model coupons were incrementally strained. Fracture events were recorded as a function of applied strain and the final length distribution of fragments at saturation was obtained for all studied systems.

Polarisation studies were also performed at room temperature using a Carl-Zeiss polarisation photomicroscope. The specimens were strained on the optical stage using a tensile device (figure 5.17). Characteristic optical micrographs were obtained at various levels of strain.

5.2.7.2 Scanning Electron Microscopy (SEM)

All samples studied using Laser Raman spectroscopy were subsequently strained to failure. At room temperature (RT), both sized and unsized specimens were tested to failure which occurred at approximately 8%. At 60°C, all samples failed at more than 10% applied strain. The fracture surfaces of the samples were gold-coated and, subsequently, examined in a JEOL 6300F field emission scanning electron microscope. An accelerating voltage of 15 kV was used with an 8 mm working distance objective lens. Characteristic micrographs of the fibre and the interface were taken at various magnifications.

5.3. RESULTS

5.3.1 Residual stress distribution at room temperature (RT)

As mentioned earlier, a systematic study of the residual axial stress, present in both long and short fibre coupons, was undertaken. In the long fibre case, the residual stresses, for both the sized and unsized systems, are 0.27±0.40 GPa and 0.04±0.40 GPa respectively (figures 5.18a and b). In the case of the short fibre, the residual stress distributions for both systems are much narrower. The measured values are -0.52±0.06 GPa and -0.43±0.06 GPa (figures 5.19a and b). Since no initial prestretching was present, the fibres are acting as internal strain-gauges and give an indication of the magnitude of the residual stresses due to the mismatch of the thermal expansion coefficients. Within experimental error, the distributions lie in the area of the maximum compression values observed in the long fibre coupons. The overall values obtained are shown in table 5.3.

5.3.2 Fibre axial stress and interfacial shear stress (ISS) distributions

5.3.2.1 Short fibre coupons (RT)

The length of the fibre in the two short fibre systems studied was 2-3 mm. For reasons of clarity the length of the fibre is presented in all graphs at a nominal 0.65 mm.

(a) MEBS / MY-750 (sized system) (RT)

The short fibre MEBS / MY-750 coupon was monitored at 2 μm steps for the first 150 μm from each fibre end and, subsequently, at 5 μm steps until 250 μm from the fibre end. The axial stress distribution prior to any load application is shown in figure 5.20a. The fibre axial stress built uniformly from the fibre ends and reached the maximum stress at less than 150 μm from the fibre end within experimental error. The maximum stress was of the order of -0.65 GPa. The compressive field is due to the difference in the thermal expansion coefficient between the matrix and the fibre. There was negligible load transfer from the fibre ends which, within experimental error, were at zero axial stress. The interfacial shear stress distribution was measured to be maximum at the fibre ends and decayed uniformly towards the middle of the fibre (figure 5.21a). The interfacial shear stress at this stage is measured to be approximately 21 MPa.

The axial stress at applied strain 0.1% is shown at figure 5.20b. The far field stress decayed to approximately -0.5 GPa. However, the axial stress built-up was not uniform any more. In particular, the right hand side fibre end exhibited an anomalous built-up at an area extending approximately 100 μm from the fibre end. Although the increase in far field strain was deducted from the rest of the fibre, the stress built-up area seemed to be 'frozen' in the initial stress field. This area is not uniformly responding to superimposed tensile stress, as can be seen in the interfacial shear stress distribution which exhibited two maxima on the right tip of the fibre (figure 5.21b). The first maximum was at the fibre tip and was approximately 23 MPa, which is believed to be within experimental error of the same magnitude as measured at 0.0% applied strain. The second maximum was much lower, at 8.25 MPa.

At 0.2% far field strain, the same observations are valid but are less apparent, due to smaller strain variations (figure 5.20c). The maximum interfacial shear stress is still at the fibre tips and retains the order of 10 MPa (figure 5.21c). At 0.3% applied strain the fibre axial stress can be regarded as uniformly zero within an error bar of 0.1 GPa (figure 5.20d). It should, however, be noted that appropriate magnification of the y axis would still reveal the existence of anomalous zones. Although it is still feasible to obtain interfacial shear stress distributions (figure 5.21d), the axial stress variations are well within the noise of the system and, thus, the derived values are prone to experimental error.

At applied strain 0.4%, the stress take-up from the fibre tips to the middle of the fibre becomes uniform again(figure 5.20e). All initial compression is at this point eliminated and the fibre far field axial stress is at the order of 0.5 GPa. The interfacial shear stress distribution is maximum at the fibre ends and decays smoothly towards the middle, reaching a maximum of approximately 21 MPa at the right fibre end (figure 5.21e).

Further load application increases the far field stress on the fibre (figure 5.20f) which reaches 0.9 GPa. Although the axial stress is not uniform after the stress build-up zone, uniform stress take-up from both fibre ends proves that the interface is still intact. The calculated maximum ISS reaches 31.35 MPa at the tip of the fibre (figure 5.21f).

The far field axial stress values and the maximum interfacial shear stress values, as calculated through the balance of forces model, are shown in table 5.4. The fibre far field stress as a function of applied strain is shown in figure 5.22a. The maximum ISS as a function of the fibre far field stress is shown in figure 5.22b.

(b) MUS / MY-750 (unsized system) (RT)

As in the previous case, the short fibre MUS / MY-750 coupon was monitored at 2 μm steps for the first 150 μm from each fibre end, and subsequently, at 5 μm steps until 250 μm from the fibre ends. The axial stress distribution prior to any load application is shown in figure 5.23a. The fibre axial stress built uniformly from the fibre ends. However, it did not reach its maximum value before 200 μm from the fibre end within experimental error. The maximum stress was of the order of -1 GPa which is considerably higher than the initial compression observed in the sized system. The difference is attributed to mainly to variations in the matrix curing conditions. As in the case of the sized coupon, there was negligible load transfer from the fibre ends. The interfacial shear stress is maximum at the discontinuity for both fibre tips (figure 5.24a).

The axial stress at applied strain 0.1% is shown in figure 5.23b. The far field stress decayed to approximately -0.6 GPa. The axial stress built-up was still uniform along the fibre. The interfacial shear stress exhibited two maxima, as previously noted for the sized fibre (figure 5.24b). However, this situation is not necessarily indicative of the creation of a similar anomalous zone as in the case of the sized coupon, since no obvious conclusions may be drawn from the axial stress profiles. At 0.2% far field strain, the far field stress is reduced to -0.3 GPa (figure 5.23c). The compressive field is finally eliminated, and, at 0.3% applied strain, the fibre axial stress can be regarded as negligible (-0.025 GPa) within an error bar of ±0.05 GPa (figure 5.23d). At applied strain 0.4%, the stress field becomes uniformly tensile and the fibre far field axial stress is of the order of 0.4 GPa (figure 5.23e). The interfacial shear stress distribution is maximum at the fibre ends and decays smoothly towards the middle (figure 5.24e). This is indicative of the elimination of anomalous zones along the stress transfer length. Thus, the two maxima previously observed are not present.

Further applied strain increase at 0.6%, raised the far field stress on the fibre to approximately 0.9 GPa (figure 5.23f). There is, however, an indication that the maximum far field stress would be of the order of 1 GPa, since the axial stress tends to decay after a maximum of 0.95 GPa at approximately 200 mm from the fibre ends. Uniform stress take-up from both fibre ends, as well as the fact that the maximum ISS is at the end of the fibre (figure 5.24f), prove that the interface is intact.

The far field axial stress observed on the fibre and the maximum interfacial shear stress values, as calculated through the balance of forces model, are shown in table 5.4. The far field stress as a function of applied strain is shown in figure 5.25a. The maximum ISS as a function of the fibre far field stress is shown in figure 5.25b.

5.3.2.2 Long fibre coupons (RT)

(a) MEBS / MY-750 (sized system) (RT)

Raman spectra were obtained at large intervals (200 μm) prior to fibre fracture to assess the stress transfer efficiency over the whole length of the embedded fibre. A residual tensile axial stress of the order of 0.2 GPa (figure 5.26a) was measured at the onset of the experiment, which is attributed to fibre prestretching during specimen preparation. The position in mm denotes the exact position within the Fragmentation Gauge Length (FGL), which is 40 mm for the specific specimen geometry (figure 5.14). The axial stress built uniformly along the fibre length with negligible local variations up to 1.0% (figure 5.26b). The axial stress variation was more significant at 1.0% and 1.2%, where indications of fibre failure initiation were detected (figure 5.26a). The applied far field strain increased the axial stress variation, without significantly affecting the mean axial stress, which at this point reaches approximately 2.2 GPa.

The first fibre fracture within the 'window' of Raman measurements was detected at 1.3% applied strain. Accurate stress mapping along 1 mm on either side of the fibre fracture point was undertaken. As can be seen (figure 5.27a), the axial stress near the fracture point was compressive and of the order of -0.5 GPa. As shown by Melanitis and Galiotis [**1993a**], the fibre recoils back after fracture and the trajectory of stress changes sign. Taking into account the residual tensile stress in the fibre at 0%, then the stored elastic energy was of high enough magnitude to subject that part of the fibre to a total compressive stress of approximately -0.7 GPa.

At an applied strain of 1.4%, four distinct fibre fractures were observed (figure 5.27b). The stress take-up along the fragments was smooth and the ISS profiles attained their maximum value at approximately 150 μm away from the fibre break (figure 5.28b). The maximum ISS value at this stage was 33.0±4.7 MPa. Further increase of the far field strain at 1.5 % did not lead to more fractures (figure 5.27c), and the ISS values remained the same within experimental error (figure 5.28c). At applied strain 1.7 %, a new fracture appeared within the monitored length at 26.7 mm (figure 5.27d). The new fracture seemed to have affected the stress built-up on either side of the newly created fragments at positions 26.3 mm and 27 mm, inducing more compressive stresses at the fibre tip and considerably high interfacial shear stresses at 26.3 mm (figure 5.28d). At this stage, saturation was achieved within the monitored length and the ISS reached a value of 38.5±13.7 MPa, which consisted the highest recorded variation in ISS values. At applied strain 1.9 %, the presence of a 'knee' in the ISS distribution at 26.3 mm indicated that the high shear stresses, which appeared in the previous strain level, resulted to local damage of the interface relieving the high shear stresses (figure 5.28e). The ISS retains the same values within experimental error but with considerably less standard deviation, that is 36.5±5.3 MPa.

At applied strain 2.1% (figure 5.28f), a maximum value of ISS of 41.9±3.5 MPa was measured. The ISS decays to zero at the fracture points with the exception of the fracture at 26.2 mm. The local ISS variations at this position are indicative of the damage initiation and propagation with applied strain. Thus, the maximum ISS value is falling as the far field strain is increased from 1.7 % to 1.9 % followed by a shift of the maximum towards the middle of the fragment at 2.1% (figure 5.28d-f).

The ISS decay to zero was indicative of some form of interfacial failure [**Melanitis, 1992**]. With further applied strain the locus of the maximum ISS is moving away from the fibre fracture. In terms of axial stress, this is indicated by an area of the fibre where the axial stress is oscillating around zero values, which clearly propagated further as the applied load increased. At applied strain 2.3 % (figure 5.27g), the initiation of the interfacial damage may be traced. The compressive stresses seem to be relieved within experimental error and the mean ISS values remain well within the previous recorded magnitude at 39.6±8.3 MPa (figure 5.28g). At 3.0 % applied strain, there are distinct areas of approximately 100 μm, where the fibre axial stress is reduced to zero (figure 5.27h). This became even more apparent at 3.8% applied strain (figure 5.27i). Finally, at 4.8% applied strain (figure 5.27j), the fibre length where the axial stress is efficiently transferred, is dramatically reduced with interfacial damage areas extending to more than half the length of individual fragments. The reduction in efficient stress transfer length is accompanied by a 22 % decrease of the interfacial shear stress values to 32.7±6.4 MPa (figure 5.28j). The individual maximum interfacial shear stress values and the average maximum ISS values are shown in table 5.6 and table 5.7 respectively.

(b) MUS / MY-750 (unsized system) (RT)

As in the case of the sized system, Raman spectra were obtained at large intervals (200 μm) prior to fibre fracture to assess the integrity and stress transfer efficiency of the whole coupon. A residual compressive axial stress of the order of -0.3 GPa (figure 5.29a), was measured at the onset of the experiment. This is attributed to thermal shrinkage of the resin during curing, which has not been offset in the axial direction by fibre prestretching during specimen preparation (as in the case of the sized system). The stress built-up is linear up to 1 % (figure 5.29b).

At 1.2 %, initiation of fibre failure may be traced at 21.4 mm (figure 5.29a). The first fibre fracture within the 'window' of Raman measurements was detected at 1.3% applied strain. Again, accurate stress mapping along 1 mm on either side of the fibre fracture point was undertaken. As can be seen (figure 5.30a), the axial stress near the fracture point was compressive and of the order of -1 GPa. Taking into account the residual tensile stress in the fibre at 0%, then the release of the stored elastic energy during fibre fracture and recoil, subjected the fibre to a total compressive stress of approximately -0.7 GPa, exactly as in the case of the sized fibre. A mean value of 27.9 MPa is calculated for the ISS, which is maximum at the fragment tip (figure 5.31a). At 1.4%, there were three distinct fractures within the window of measurements (figure 5.30b). The maximum ISS value up to this point was 28.9±5.7 MPa (figure 5.31b).

The fragmentation process continues at 1.5 % with a fourth fracture appearing at approximately 20.3 mm (figure 5.30c). At 1.6 % a new fracture appears at 20.9 mm (figure 5.30d). The axial stress at the fracture location is consistently compressive for all fragments. The interfacial shear stress remains relatively constant within experimental error at 32.6±8.1 MPa. At 1.6%, a new fracture appears at 20.9 mm (figure 5.31d).

At 1.7%, no new fractures are observed (figure 5.30e). The shape of the individual fragment profiles did not change as in the case of the sized system, and the ISS values remained the same within the standard deviation, that is 31±6.5 MPa (figure 5.31e). Further applied strain 1.9 % and 2.1% neither led to further fractures of the fibre (figure 5.30f, g) nor to significant changes in the shape and magnitude of the ISS (figure 5.31f, g). More fractures appeared at 2.6 % (figure 5.30h) and 2.9 % (figure 5.30i), where saturation within the preselected 'window' of measurements was achieved. Raman monitoring of the fibre was at this stage confined to the new fragments. At 3.4% applied strain, the fibre was fractured in very small fragments but the interface retained its initial efficiency (figure 5.30j). Even at 4.4%, the ISS values were as high as 31.9±8.6 MPa (figure 5.31k). It is interesting to note that a considerable proportion of the length of individual fragments is under axial compression.

The individual maximum interfacial shear stress values and the average maximum ISS values are shown in table 5.8 and table 5.9, respectively.

(c) Scanning Electron Microscopy (SEM) studies (RT)

Representative electron micrographs for the MEBS / MY-750 and MUS / MY-750 systems are presented in figure 5.32. The sized fractured fibre is shown in figure 5.32a for the sized system. There is a bright layer of resinous material (figure 5.32a), which remains on the fibre surface after fracture. A closer inspection of that region (figure 5.32b) at higher magnification reveals the characteristic ripples of polymeric material normal to the fibre axis. However, there is also indication of crack propagation between the fibre and this bright layer of resinous material, as seen in figure 5.32c. On the contrary, the MUS / MY-750 shows clear fibre / matrix debonding along the whole circumference of the fibre (figure 5.32d). The clean fibre surface, as well as its imprint on the resin reveal, clear failure at the interface.

(d) Additional optical fragmentation studies (RT)

Complementary conventional fragmentation studies on the sized and the unsized system at room temperature were performed in order to compare the Raman studies to the results obtained by the fragmentation test.

Long fibre model coupons were incrementally strained to saturation and the fracture events were recorded as a function of applied strain. In figure 5.33 the break density, or the number of fractures per unit length, are recorded as a function of applied strain. The two systems do not exhibit considerable differences up to break density of 1 mm^{-1}. The MUS / MY-750 system exhibits a slight offset to the fragmentation process of the order of 0.1% applied strain, when compared with the sized system. This may be attributed to different prestretching during the specimen preparation process. At break densities higher than 1.5 mm^{-1} the slope of the fragmentation process changes for the unsized system, and consequently, the fragmentation process slows down.

The initial part of the fragmentation process is related to the strength of the fibre [**Waterbury, 1991**]. Since the variation in strength for the two fibres is not significant, the fragmentation process is similar. However, this is not the case for higher break densities, where the fragmentation process is 'interface-dominated' [**Andersons, 1993**]. The interfacial failure of the unsized system is more obvious.

The distribution of the critical length values are shown in figure 5.34. The critical length is defined as the 4/3 of the fragment length [**Ohsawa, 1978; Netravali, 1989c**]. The difference between the two systems is clear, with the critical length of the unsized system shifted to higher values. Using the interpolation of the axial strength values to the critical length (§4.3.1) and the constant shear assumption [**Kelly, 1966**], the interfacial shear strength values for the sized and the unsized system at room temperature are calculated to be 30.1±6.1 MPa and 25.9±5.5 MPa respectively. These values are smaller than those derived by LRS by approximately 40% (table 5.14).

Optical micrographs of the sized and the unsized system taken under cross polars at 3.0% applied strain are shown in figure 5.35a and b, respectively (magnification 80x). The birefringent patterns are different for the two systems. For the sized system relatively stress-free zones may be observed near cracks (figure 5.35a). On the other hand, the birefringent patterns for the unsized system exhibit uniform stress transfer along the whole length of the fibre (figure 5.34b). This is in agreement with the observations made by LRS, whereby at room temperature interfacial damage was reducing the effective length for stress transfer for the sized system and stress was efficiently transferred along the whole fragment length for the unsized system, even at high applied strains.

5.3.2.3 Long fibre coupons (60°C)

(a) MEBS / MY-750 (sized system) (60°C)

Raman spectra were obtained at large intervals (200 mm) before the sample was heated in the environmental chamber. A residual tensile axial stress of the order of 1.0 GPa was measured (figure 5.36a), which is attributed to fibre prestretching during specimen preparation. Subsequently, the sample was heated and the Raman monitoring revealed a slight decrease in the residual stress field (0.8 GPa). As previously, Raman spectra were obtained at large intervals (200 mm) prior to fibre fracture to assess the integrity and stress transfer efficiency of the whole coupon (figure 5.36a). The axial stress take-up of the fibre was smooth up to 0.4% (figure 5.36b).

Two fibre fractures within the 'window' of Raman measurements were detected at 0.6% applied strain (figure 5.37a). The fractures occurred at an early stage, because of the considerable residual tensile field, and detailed stress mapping was carried out. The axial stress near the fracture points is compressive and of the order of -0.5 GPa. If the compressive stress at the fibre tip is added to the residual tensile field prior to fracture, a total stress of 1.3 GPa was estimated, which was considerably higher than the total stress of 0.7 GPa calculated in the same manner for both room temperature systems. At 0.8%, the window of measurements was confined to two individual fragments (figure 5.37b). The maximum ISS value up to this point was 14.3±5.6 MPa (figure 5.38b). At 1%, the ISS values remained the same within the standard deviation (figure 5.38c). The axial stress was transferred smoothly along the length of the fragments (figure 5.37c). Although the ISS values reached zero at the fibre tip in three out of four cases, the compressive stresses at the fibre tips were adequately bridging the fibre fractures.

At 1.4%, the ISS values indicated a slight increase and reached 19.7±4.8 MPa (figure 5.38d). The onset of interfacial damage was observed with the presence of a 'knee' on all ISS profiles, indicating a shift of the maximum ISS towards the middle of the fragment. At applied strain 2.0%, another fracture appeared (figure 5.37e). The ISS values remained at the same level within standard deviation (figure 5.38e). It should be noted that, unlike in the case of the sized system at RT, the axial stress values were consistently compressive at the fibre tip, and of the order of 0.5 GPa. Saturation within the preselected window of measurements was achieved at 3.0% with the appearance of a new fracture (figure 5.37f). Stress monitoring was subsequently confined to the area between 22.4 and 23.6 mm. The maximum ISS was reduced slightly at 16.6±2.4 MPa (figure 5.38f).

The individual maximum interfacial shear stress values and the average maximum ISS values are shown in tables 5.10 and 5.11, respectively.

(b) MUS / MY-750 (unsized system) (60°C)

The unsized system exhibited similar behaviour to that of the sized system at 60°C. A slight tensile axial stress of 0.45±0.09 GPa was monitored at room temperature, which relaxed marginally to 0.43±0.24 when the sample was heated to 60°C (figure 5.39a). The stress take-up was smooth up to 0.4% (figure 5.39b) and indications of forthcoming fractures were observed at 0.6% (figure 5.39a). At 0.8%, two fractures were detected (figure 5.40a). The axial stress at the fibre tip was slightly compressive and of the order of 0.3 GPa or less. According to the previous estimates, the 'recoil' stress in the case of the unsized system at 60°C was considerably less than the one observed in the sized system. If the original tension of 0.45 GPa is added to the recoil induced maximum compression at the fracture tip, then the total recoil stress was approximately 0.75 GPa. At this stage, the ISS was 8.9+3.6 MPa (figure 5.41a). It is interesting to note that the ISS profiles exhibit two distinct zones: a 'high ISS' one, where the maximum values reached more than 10 MPa, and a 'low ISS', where the ISS was practically constant for a length exceeding 1 mm. The 'low ISS' zone is characteristic of either frictional bonding [**Piggot, 1980**] or perfectly plastic [**Kelly, 1966**] interface.

At applied strain 1.0%, the ISS increased and reached a maximum of 11.8±5.0 MPa (figure 5.41b). At 1.2%, there were not considerable differences detected in the behaviour of the system (figure 5.40c). The maximum ISS retained the same magnitude within experimental error (figure 5.41c).

At 1.4%, saturation was reached within the window of measurements with the appearance of two additional fractures (figure 5.40d). The new fractures appeared approximately in the middle of the previously monitored fragments (figures 5.40a-c). The maximum ISS was calculated to be 8.7±2.4 MPa (figure 5.41d). At applied strain 1.6%, a further decrease of the ISS at 5.2±1.6 was observed (figure 5.41e). After this stage, the maximum ISS values were oscillating around 6 MPa to reach 5.3 MPa at 3.0% (figure 5.41h). It is interesting to note that the maximum axial stress of the fragments was dramatically reduced with applied strain. After saturation was reached at 1.4%, the maximum axial stress fell from approximately 1 GPa at 1.4% (figure 5.40d) to 0.5 GPa at 3.0% (figure 5.40a).

The individual maximum interfacial shear stress values and the average maximum ISS values are shown in tables 5.12 and 5.13, respectively.

(c) Scanning Electron Microscopy (SEM) studies

Representative electron micrographs for the MEBS / MY-750 and MUS / MY-750 systems are presented in figures 5.42a and b, respectively. Both systems exhibited clear fibre / matrix debonding along the whole circumference of the fibre, similar to that observed in the case of the MUS/ MY-750 at room temperature. Thus, in elevated temperatures there was no indication of damage propagating in the resin and the failure was clearly at the interface.

(d) Additional optical fragmentation studies (60°C)

Additional long fibre model coupons were incrementally strained to saturation at 60°C. The fracture events were recorded as a function of applied strain. In figure 5.43, the break density or the number of fractures per unit length are recorded as a function of applied strain. The MUS / MY-750 system exhibited a slight offset to the fragmentation process of the order of 0.15% applied strain when compared with the sized system. This is again attributed to different prestretching during the specimen preparation process. The onset of the 'interface dominated' fragmentation as defined in §5.3.2.2 can be traced at approximately 0.5% for the unsized system and at 0.65% for the sized system. Until this point the fragmentation process is parallel for both systems, since it is dominated by the fibre strength. The observed offset is eliminated at approximately 1.5% applied strain, where the unsized system is 'catching up' with the sized system. At higher strains the fragmentation process was, within experimental error, the same for the two systems.

The distribution of the critical length values are shown in figure 5.44. The observed differences are well within experimental variation. Using the Kelly-Tyson model [**Kelly, 1965**] the interfacial shear strength values (IFSS) for the sized and the unsized system at 60°C are calculated to be 19.1±4.4 MPa and 19.1±4.0 MPa respectively (table 5.14). The conventional fragmentation studies did not reveal any significant difference between the two systems at 60°C. It is interesting to note that, although for the MEBS / MY-750 the calculated values coincide with the LRS measured values, in the case of the MUS / MY-750 the calculated interfacial shear strength is overestimated. Even though this may be attributed to experimental variation, it is obvious that the assumptions made regarding the conventional fragmentation test may be a source of error. This is due to the inability of the constant shear model to describe variation in the shape of the stress transfer profiles. In the case of the MUS / MY-750, the stress transfer characteristics are indicative of a frictionally bonded interface which degrades rapidly, at higher applied strains after frictional slipping occurs. This mechanism is distinctly different from the 'shear flow' assumed in the Kelly-Tyson model.

5.4. DISCUSSION

As has already been mentioned, the measurement of the interfacial shear strength is a complicated task. It involves simulating the stress state in real composites and defining interfacial failure, as this would be expected to appear in service conditions. In the case of the single fibre coupon test, artefacts are created because (i) of the geometry of the test, where the fibre is embedded in a practically infinite matrix, and (ii) of the strain required to obtain experimental data, which exceeds the service strains of the composite by almost an order of magnitude.

In this study, the LRS technique has been used to identify and measure the parameters related to interfacial adhesion using single fibre model composites. In addition, the validity of the data obtained by the conventional fragmentation test is evaluated. As previously postulated, the tensile strength of unidirectional composites is controlled by the size of the flaw created around local discontinuities that accumulate to lead to failure [**Reifsnider, 1994**]. This size is directly controlled by the ineffective length which is related to the level of interfacial adhesion.

In the case of the fragmentation test, the stress transfer length has been related to the critical length [**Ohsawa, 1978; Netravali, 1989c**] or the fragment length. It is, however, arguable whether the distribution of lengths measured at saturation coincides (if the fragment length is considered), or is a linear function of the double of the ineffective length (if a critical length approach is adopted). This approach has been criticised [**Drzal, 1993**] since the failure mechanisms present in the classical fragmentation test dominate the saturation stage, without necessarily being part of the failure mechanisms dominating real composites. This postulation has led to the assumption of different 'zones' of interfacial adhesion [**Piggot, 1980; Melanitis 1993a; Nairn, 1996**]. These zones are usually of twin nature; zones of 'intact' interface whose properties consist a material property, and 'damaged' zones, where various mechanisms have led to a decreased level of adhesion. The latter zones have been modelled by means of elastoplastic approaches [**Piggot, 1980**], or by assuming an imperfect interface

[**Hashin, 1990; Nairn, 1996**] which scales the values of the stress field according to interface parameters corresponding to 'displacement jumps'. The 'damaged' zones extend normally from the fibre fracture towards the middle of the fragment. Initially, damage may occur due to the dynamic nature of the fibre fracture process. As the far field strain increases, the 'damage' zone is expected to increase towards the middle of the fragment. The mechanisms inducing the damage consist of local matrix failure, such as yielding or cracking, due to stress concentrations. The only necessary condition for the damage zone is that the maximum shear stress within the zone does not exceed the shear stress of the intact zone. Thus, the stress transfer at the interfacial damage zone may extend from the efficient intact interface to a plastic or frictional interface, and / or to a totally debonded interface [**Hashin, 1990**]. Consequently, the length at which stress is adequately transferred may be dramatically reduced at saturation.

LRS can be used to identify the mechanisms described above accurately, since it has been proven to be a very accurate tool to measure absolute stress values at resolutions of the order of a micrometer. Thus, accurate axial stress distributions may provide qualitative and quantitative information about (a) the stress field governing the fragmentation test geometry even prior to externally applied far field strain, (b) the regime of stress transfer in the intact interfacial zone, which can be achieved by the short fibre fragmentation coupon at low applied strain, (c) the nature and propagation of damage at high applied strains, and (d) the response of the interface at different environments. Thus, information about the validity of the data that the fragmentation test provides can be tested.

5.4.1 Residual stress field in single fibre model composites

The presence of the hydrostatic stress field in the single fibre fragmentation test is one of the reasons for the lack of reliability of the test. As can be seen in figure 5.18, the residual field on the fibre covers a wide range of values for the long fibre configuration. In general, a single fibre is subjected to a 3D compressive field, resulting from resin shrinkage during curing and from the mismatch of the fibre and resin thermal expansion coefficients upon cooling to room temperature. As shown schematically in figure 5.45, the prior application of an axial tensile stress during alignment of the fibre in the mould offsets the development of the thermal axial compressive stress in the fibre direction, without significantly affecting the magnitude of the radial or hoop stresses at the interface. The distributions of the short fibre configuration (figure 5.19) give a clear indication of the maximum residual stress field, since the only cause of the compressive stress measured on the fibre is the thermal shrinkage of the matrix. The maximum compression is of the order of -0.75 GPa for both systems.

A closer examination of the residual stress distribution of the long fibre configuration, reveals that the existing distribution is clearly a superposition of more than one different distributions, exhibiting the statistical nature of prestretching (figure 5.18). This effect is by far less prominent in the short fibre configuration. In this case, the distribution is much narrower, without indications that the measurements come from distinct distributions. The sized system is slightly more shifted towards compression, indicating that additional mechanisms such as curing / gelation time of the matrix may induce differences in the distribution of residual stresses. These differences, however, are negligible compared to those induced by the fibre prestretching (figure 5.45).

5.4.2 Short fibre coupons

5.4.2.1 Stress transfer characteristics

As can be seen in figures 5.20a and 5.23a respectively, prior to the application of tensile stress, both MEBS and MUS fibres are subjected to axial compression due to the thermal mismatch between the fibre and the matrix [**Chamis, 1972**]. Since there is no initial stress field on the fibre, the overall axial compressive strain in the fibre reflects the amount of one-dimensional shrinkage in the resin. Thus, the fibre acts as an internal gauge of the axial shrinkage of the matrix. Since the matrix is isotropic, one can easily calculate its volumetric shrinkage, which is 0.5% and 0.7% for the sized (figure 5.20a) and unsized (figure 5.23a) systems, respectively [**Robinson, 1987a**]. The obtained values are well within the limits of the residual stresses measured for the short fibre coupons and reflect the variability of the residual stress field which is operator dependent.

The most striking result, however, is that the stress built-up in the short fibre is also shear-dominated; the axial stress is zero at the end of the fibre and reaches its far field value at some distance away from it. Therefore, it is safe to assume that in the case of short fibre model composites, the load is transferred almost exclusively by shear and the effect of axial load transfer through the fibre ends is negligible.

Both systems are subjected to increments of applied tensile strain and, at 0.3% (figures 5.20d and 5.23d) strain, the compressive stresses have now been removed and the fibre stress distributions fluctuate around zero. At an applied strain of 0.6%, the fibre stress distributions are now purely tensile and the fibre stress is zero at the fibre end and reaches its maximum value at some distance away from it (figures 5.20f and 5.23f).

It is interesting to note that in the case of the MEBS / MY-750 system, the axial fibre stress distribution is not uniform, exhibiting secondary axial stress maxima. Schadler et al. [1992] have described a similar behaviour for a carbon fibre / polycarbonate matrix as the result of the superposition of an axial tensile stress upon a fibre which is in a three-dimensional state of compressive stress. The fibre exhibits zones where shear stresses do not readily respond to the superimposed axial field. In particular, the change of sign of interfacial shear, required for the transition from axial compression to axial tension, is gradual and, therefore, certain hysteresis can be observed near the middle of the fibre. The proposed model for this behaviour is shown in figure 5.46. For simplicity reasons constant shear is assumed. At 0.0%, the fibre is in axial compression building up from the fibre ends (figure 5.46a). The interfacial shear stress is negative and falls to zero values where the fibre reaches a constant strain value. As the far field strain is increased, the interfacial shear stress value changes sign at the fibre ends, but towards the middle of the fragment, the far field axial stress is clearly superimposed to the residual field, creating a discontinuous shear stress distribution (figure 5.46b). The effect is gradually eliminated after a threshold value, and the interfacial shear stress is homogeneous along the built up length (figure 5.46c). This behaviour is clearly non linear and cannot be explained through current stress transfer models. The MUS / MY-750 system does not exhibit similar effects and the transition from compression to tension is smooth throughout the experiment (figure 5.23a-f). This is indicative of the different nature of the interface in the case of the unsized system and requires further investigation as far as the nature of the phenomenon is concerned.

The maximum axial stress on the fibre of the two systems as a function of applied far field strain is shown in figures 5.22a and 5.25a, respectively. Both systems exhibit less sensitivity than the one-to-one line, with the sized system being clearly less responsive to externally applied strain. There is no clear indication that the 'frozen shear stress zones' (figure 5.46) are directly related to the response of the coupons to applied far field strain. However, this behaviour may be attributed to the existence of local variations of properties in the region of the interphase, with a much more pronounced effect in the case of the sized system.

5.4.2.2 Modelling the elastic stress transfer

(a) Measurement of the shear-lag parameter β

In fibre-reinforced composites the stress transfer process is activated at a discontinuity, such as a fibre break or a fibre end. There have been a number of analytical models that attempt to derive analytical expressions for the fibre stress distribution over a given fibre length as a function of the applied stress, the fibre and matrix moduli and the type of geometry and / or testing configuration. As described in §5.1.4.1, the most commonly used method for the prediction of the stress transfer characteristics in composites is the so-called *shear-lag* method, which was proposed originally by Cox [1952]. There are two sets of assumptions employed by Cox for the derivation of the axial stress in the fibre. The first set is concerned with the material parameters that are used for the formulation of the problem. These are:

1-the fibre and matrix behave as linear elastic solids,
2-the interface between the two components is perfect, and

3-there is no load transfer through the fibre ends.

The second set of assumptions is concerned with the mathematical formulation of the problem. The most fundamental of these assumptions require that the radial displacement, u, with respect to z and the transverse normal stresses, $\sigma_r + \sigma_\theta$, are either zero or negligible **[Cox, 1952; Nayfeh, 1977; Nairn, 1997]**:

$$\frac{\partial u}{\partial z} \approx 0 \tag{5.19a}$$

and

$$\sigma_r + \sigma_\theta \approx 0 \tag{5.19b}$$

Cox **[1952]** set out the whole problem by assuming that, if P is the load in the fibre at a fibre distance, z, then the rate of load transfer (or, in other words, the produced shear stress) at an applied far field strain, ε_∞, is proportional to the difference between the axial displacement of the fibre, w, and the corresponding displacement, w_∞, that the matrix would undergo if the fibre were absent. The latter is in effect the axial displacement in the middle of a short fibre - for which its length is longer than the critical length - or the axial displacement of a continuous fibre. The shear force S becomes thus the gradient of the axial force P. Hence, from equation 5.8a:

$$\frac{dP}{dz} = H(w - w_\infty) \tag{5.19c}$$

where H is a proportionality constant which depends on geometrical and material parameters. In order to derive the constant, H, Cox **[1952]** assumed that at a distance from the fibre axis equal to R_∞ the displacement of the matrix is, in fact, the unperturbed displacement w. As stated by Nayfeh **[1977]**, Galiotis **[1991]** and, more recently, Nairn **[1997]**, for single fibre model composites, the parameter R_∞ can be defined as the radius of a matrix cylinder beyond which there is no influence of the fibre upon the deformation of the matrix.

The final one-dimensional equation derived by Cox **[1952]** for the axial fibre stress, $\sigma_z(z)$ can be written as:

$$\frac{\partial^2\sigma_z(z)}{\partial z^2} - \beta^2\sigma_z(z) = -\beta^2 E_f \varepsilon_\infty \tag{5.20}$$

In fact, even more rigorous shear-lag analyses **[Nayfeh, 1977; Nairn, 1997]** based on axisymmetric elasticity equations for two concentric cylinders (e.g. single fibre model composites), rather than equation 5.19, can also be shown to lead to equation 5.20 **[Nairn, 1997]**. For a cylindrical fibre of length, l, radius, r, and modulus E_f equation 5.20 can be easily solved to yield:

$$\sigma_z(z) = E_f \varepsilon_\infty \left[1 - \frac{\cosh\left(\beta\left(\frac{l}{2} - z\right)\right)}{\cosh\left(\beta\frac{l}{2}\right)} \right] \tag{5.8b}$$

where ε_∞ is the far-field strain, and β is the shear-lag parameter which has units of inverse length and depends on the material properties and the geometrical foundation of the problem.

Equation (5.8b) can be simplified to:

$$\sigma_z(z) = E_f \varepsilon_\infty \left[1 - \cosh(\beta z) + \tanh\left(\frac{1}{2}\beta l\right)\sinh(\beta z) \right] \tag{5.21}$$

The function $\tanh\left(\frac{1}{2}\beta l\right)$ takes the value of unity for any value of $\beta l \geq 10$. For all short fibre composites for which $l \geq 2000$ μm and $\beta \geq 0.005$, then, from equation 5.8.b:

$$\sigma_z(z) = \sigma_\infty\left[1 - \cosh(\beta z) + \sinh(\beta z)\right] \tag{5.22a}$$

or

$$\sigma_z(z) = \sigma_\infty\left[1 - e^{-\beta z}\right] \tag{5.22b}$$

where $\sigma_\infty = E_f \varepsilon_\infty$ is the corresponding axial stress in the middle of the fibre.

In terms of strain values, equation (5.22b) can be written as:

$$\varepsilon_z(z) = \varepsilon_\infty\left[1 - e^{-\beta z}\right] \tag{5.22c}$$

The significance of equations 5.22b and c is that, for short fibres, the stress or strain distributions in the elastic region can be adequately predicted for a number of fibre / matrix combinations by just treating β as an *inverse length* fitting parameter rather than attempting to define it analytically. However, it is worth reiterating here that the best results are obtained only if $\beta l \geq 10$.

From equations 5.22b and c, it is evident that since laser Raman spectroscopy can provide $\sigma_z(z)$ and $\varepsilon_z(z)$ for any z (as well as, σ_∞ and ε_∞), the value of transfer length, l_t, for which $z = l_t = 1/\beta$ can be found from the experimental axial stress or strain profiles at corresponding values of $0.63\ \sigma_\infty$ or $0.63\,\varepsilon_\infty$. Alternatively the shear-lag parameter β can be obtained by fitting an exponential curve of the form of equations 5.22b and c to the experimental fibre stress or strain data, respectively.

The short fibre coupon geometry is ideal for the determination of β because at low applied strains both fibre and matrix behave elastically and the interface is intact **[Galiotis, 1993b]**, hence, the first two shear-lag assumptions are satisfied. In addition, as has been found experimentally in this study, as well as in other cases of carbon fibre / composites **[Schadler, 1992; Melanitis, 1993b]**, there is no measurable transmission of normal stresses through the ends of the fibre (3rd assumption).

Regardless of the complexity of the stress transfer profiles (§5.3.2.1), the methodology proposed in this study for the determination of β is relatively simple. For any given fibre stress distribution within the elastic region, the value of β is derived by (a) measurement of σ_∞ or ε_∞, and (b) fitting an exponential curve of the form of equations 5.22b or 5.22c to the raw data. The values σ_∞ or ε_∞ have to be determined from the fibre stress or strain distributions, by averaging the fibre stress or strain values at the middle of the fibre or at a distance well over the transfer length (see Tables 5.4 and 5.5). This way, any hysteresis between applied composite strain (measured by strain-gauges) and actual fibre stress or strain in the fibre does not affect the value of β.

The solid lines in figures 5.47a and b for the sized and the unsized systems respectively correspond to fits based on equation 5.22b. The values of β derived this way are given in table 5.15. Since for the MEBS / MY-750 and MUS / MY-750 systems the results obey the assumption $\beta l \geq 10$, then equation 5.22b is valid. The average β values are of the order of 0.02 μm^{-1} and 0.009 μm^{-1} for the sized system and unsized systems, respectively. It is interesting to note that, within experimental error, the value of β does not change significantly with strain level (table 5.15) and is, therefore, considered to be a true reflection of the elastic response of each system. The fitted curves represent very well the data points at 0% applied strain (fibre in compression), whereas in the case of 0.6% strain, deviations are observed particularly at the middle of the MEBS fibre (figure 5.47a). The reason for this discrepancy is the complexity of the stress field as the system is forced to undergo a shear generated compression-to-tension transition [**Schadler, 1992**]. However, the overall picture is satisfactory and in systems where the residual fibre compression is minimal or non-existent (e.g. high volume fraction composites, cold cured single fibre composites, etc.), the proposed method should yield excellent fits. In conclusion, the shear-lag parameter β can be used as an index of the stress transfer efficiency of the system as it is extremely sensitive to the conditions prevailing at the interface. In the case examined here, the addition of epoxide sizing to an identical M40B fibre has brought about an increase of β by a factor of 2.2.

(b) Interfacial Shear Stress (ISS) distributions

The exact equilibrium relationship between axial fibre stress, $\sigma_z(z)$, and interfacial shear stress, τ_{rz}, is given by:

$$\tau_{rz} = -\frac{R}{2}\frac{d\sigma_z(z)}{dz} \tag{5.6}$$

An interfacial shear stress distribution for the fitted axial stress profiles of figures 5.47a and b, can be obtained by combining equations 5.22c and d, provided that $\beta l \geq 10$:

$$\tau_{rz} = -\frac{R\sigma_{\infty}\beta}{2}e^{-\beta z} \tag{5.23}$$

The results for the two systems normalised by the far field stress, σ_{∞}, are given in figure 5.48. As can be seen, the stress transfer response of the two systems is considerably different: (a) the sized system indicates a considerably higher ISS value at the discontinuity ($z = 0$), (b) the decay of the interfacial shear stress is more pronounced in the case of the sized system. Evidently, at the location of the fibre end (z = 0) the maximum ISS attained by the two systems differs by a factor equal to β, which is 2.2 in the case examined here.

Finally, it is worth mentioning that an alternative approach to the estimation of the β parameter is obtained from equation 5.23 for the estimated maximum ISS values at the fibre tip or for $z = 0$:

$$\tau_{max} = -\frac{R\beta}{2}\sigma_{\infty} \tag{5.24}$$

The linear fit to the experimentally derived ISS values as a function of the applied stress provides the value of the β parameter for both ends of the fibre (figure 5.22b and 5.25b). The estimated mean values for β from the left and right profiles are 0.0201 and 0.0099 for the sized and the unsized systems respectively. These values are well in agreement with those obtained through equation 5.22b, with the β of the unsized system being more than double the respective value for the sized system. Thus, it is proved that the stress state can be regarded as elastic and, as extensively described in the previous section, radial shearing can be ignored without any significant effect in the modelling of the stress transfer.

As previous researchers have indicated, the symmetry of the stress tensor demands the value of interfacial shear stress to be zero at the discontinuity [**McCatrney, 1989**; **Nairn, 1992**]. However, the finite values of interfacial shear stress measured through the cubic spline fit (table 5.4 and 5.5) or calculated through equation 5.23 prove that at the elastic stress state, the effect of the discontinuity is highly localised in an area within less than a fibre diameter [**Nairn, 1992**] and may be ignored, without significant effect on the adhesion parameters.

As a result, the β parameter can be used to model the interfacial behaviour as inversely proportional to the ineffective length. The maximum interfacial shear stresses derived at the discontinuity coincide with the real values that are directly measured with LRS. In addition, possible deviations from the described model are within experimental error due to divergence from the elastic stress state and not to the inaccuracy of the model.

(c) Matrix shear modulus, $G_m^{R_\infty}$, and effective volume fraction, R_∞/R

As mentioned earlier, the shear-lag parameter, β, can be treated as an *inverse length* fitting parameter that satisfies the differential equation 5.20. It is worth examining now why β is such a sensitive index of the stress transfer efficiency. The simplest expression for β has been derived by Cox [**1952**] based on the assumptions mentioned earlier and, in particular, equation 5.8c:

$$\beta = \sqrt{\frac{2G_m^{R_\infty}}{R^2 E_f \ln\left(\frac{R_\infty}{R}\right)}} \qquad (5.8c)$$

For single fibre model composites, the parameter $G_m^{R_\infty}$, defines the shear modulus of the matrix cylinder of radius R_∞. The value of $G_m^{R_\infty}$ is undoubtedly affected by the interphase chemistry (fibre surface treatment, fibre sizing, presence of matrix oligomers, etc.) which, in turn, affects the value of β. Furthermore, the extent of the matrix cylinder, R_∞, beyond which the matrix flows as if the fibre were absent, is also affected by the induced shear perturbation and therefore cannot be considered as a constant. Therefore, in equation 5.8c, there are two unknown parameters which affect the value of β.

An independent method to estimate the ratio R_∞/R has appeared recently through the work on two-dimensional composites [**Chohan, 1996**]. By placing the individual fibres far apart, a critical distance *R'* has been defined over which there is no fibre-fibre interaction or, in other words, shear field perturbation. The value of R'/R for a similar sized M40B fibre / epoxy system was found to be equal to about 9 [**Chohan, 1997**]. Since *R'* in that case corresponds to the centre-to-centre interfibre distance, then it follows that for the sized system:

$$\frac{R_\infty}{R} = \frac{1}{2}\frac{R'}{R} = 4.5 \qquad (5.25)$$

In figure 5.49, the interfacial modulus $G_m^{R_\infty}$ is plotted as a function of β for 3 different values of R_∞/R of 5, 7 and 10. The dashed line corresponds to the matrix shear modulus (table 5.2). As can be seen, the presence of sizing at the interface appears to increase somewhat the matrix shear modulus (of radius R_∞), yielding a more efficient system. For the unsized system and for all values of R_∞/R, the matrix shear modulus appears considerably lower than its bulk value (figure 5.24). Lack of efficient cross-linking and / or precipitation of epoxide oligomers at the vicinity of the interface can account for the observed effect.

For the sized system, the higher predicted shear modulus is indicative of the presence of a variation in local properties, which may result in an increase in the local matrix stiffness by 40% for a matrix cylinder of five fibre radii (R_∞/R = 5). This indicates the existence of an interphase of considerable size compared to the fibre that plays an important role in the stress field. Assuming an equivalent increase in the local matrix shear strength, then, one should expect a higher ISS for that system, which is in agreement with the relatively high ISS values reported in the previous section.

It is, thus, obvious that through a simple shear-lag approach the axial stress data provided by LRS may give information about the stress transfer. Through this approach, the interface is characterised by a single parameter β that provides all the information for the stress state in the elastic region.

5.4.3 Long fibre coupons

5.4.3.1 Interfacial shear strength (IFSS) of model coupons

The average maximum interfacial shear strength (IFSS) of the three systems is plotted as a function of applied strain in figure 5.50. Overall, the maximum IFSS values for the sized fibre system are slightly higher than those of the unsized system. At the point of saturation, the IFSS of the sized and unsized systems at RT and at 60°C, are 41.9±3.5 MPa, 36.8±5.7 MPa , 18.9±7.1 MPa, and 11.8±5 MPa, respectively (table 5.14).

The average maximum values for the MEBS / MY-750 system at RT and at 60°C are approximately 30% higher than the estimate of the shear strength of the resin at the respective temperatures (table 5.2). The presence of sizing is beneficiary to the stress transfer both at room and high temperatures, by locally improving the shear properties at the interface. This is in accordance with the observations made in the previous section, where the properties of the *interphase* in the case of the sized system are predicted to be of much higher value than the properties of the bulk matrix (figure 5.49). Detassis et al. [**1995**], found that the presence of sizing may provide a twofold increase of the interfacial shear strength of carbon fibre reinforced composites as compared with the shear strength of the matrix as well as the IFSS of unsized fibres. Moreover, the IFSS of the unsized system coincided with the shear strength of the matrix.

This observation about the unsized system compares well with the findings of this study at room temperature. The measured IFSS is more comparable to the shear strength of the bulk matrix (table 5.2), although the measured values are still marginally higher. The striking difference occurs at 60°C, where the shear transfer efficiency seems to decrease dramatically. The maximum IFSS is recorded at 1.0% applied strain and is still comparable within the standard deviation to the shear strength of the matrix but, in this case, lies at the low end of the error bar (figure 5.50). It is worth noting that the stress transfer efficiency also decreases dramatically with applied strain falling to 50% of its maximum value at 3.0% (table 5.14). The difference of the IFSS measured cannot be solely attributed to the softening of the matrix. It can be postulated that the interfacial shear stress reaches a maximum at the area of 1.0% and at this stage slipping at the interface occurs. Under the assumption that the stress transfer is then dominated by frictional forces, the dramatically reduced values of the shear stresses may be attributed to the relief of the hydrostatic thermal stress field at elevated temperatures. Netravali et al. [**1989c**] confirmed through photoelastic studies similar observations for a carbon epoxy system; interfacial failure appears to initiate at the same time as a fibre fracture, but the existence of thermal stresses in the matrix sustains a frictional stress field which still transfers stresses but with less efficiency.

In general, shear stress transfer at the interface decreases with the increase of temperature [**Buxton, 1995; Detassis, 1995**]. Ohsawa et al. [**1978**] reported a linear dependence of IFSS with increasing temperature. The mechanism of shear transfer is simultaneously dependent on the shear strength at the interface / interphase and the residual stress field, which both depend on the temperature of the environment [**Ohsawa, 1978**]. It is therefore obvious that the IFSS depends on the maximum shear value that any of the two competing mechanisms are able to sustain.

Assuming the twin nature of stress transfer, at room temperature, frictional stresses at the interface are still a dominant mechanism of stress transfer and no considerable difference with regard to IFSS can be recorded with applied strain. However, at 60°C and after the interface fails, the frictional restriction sustains contact between the two surfaces but the IFSS falls to a much smaller value.

The corresponding IFSS values, as predicted from the Kelly-Tyson model [**Kelly, 1965**] (conventional fragmentation), are 30.1±6.1 MPa, 26.1±5.5 MPa, 19.1±4.4 MPa, and 19.1±4.0 MPa, respectively (Table 5.14). Although the Kelly-Tyson values at RT and 60°C compare well with the calculated shear strength of the resin (Table 5.2), they do not account for the differences observed between the sized and the unsized system. The inadequacy of the Kelly-Tyson model becomes more obvious in the case of the unsized system at 60°C. This can be attributed to the inability of the constant shear hypothesis to account for distinct failure mechanisms and / or a frictionally bonded interface which is very much dependent on the thermal stress field.

Overall, the sizing improves interfacial adhesion both at room and high temperatures, possibly by locally improving the shear properties of the matrix. At room temperature, the shear strength of interface of the unsized fibre is marginally better than the bulk matrix properties. The situation inverses at high temperature, where the interface fails at low shear values. In addition, it is obvious that the Kelly-Tyson model is not adequate to describe the stress transfer in all environments where mechanisms other than plastic flow, are present.

5.4.3.2 Modes of interfacial failure

(a) The elastic recoil mechanism

At room temperature, the presence of the residual stress field in the systems that were studied in detail, did not seem to affect the stress transfer after the fibre fractured. A 'recoil compressive stress' of the order of -0.7 GPa can be calculated, by adding the measured residual stress prior to testing to the compressive stress at the fracture tip, when there is little or no interfacial damage. The sized system at RT indicates 0.2 GPa residual stress prior to stretching (figure 5.26) plus -0.5 GPa when the first fracture appears (figure 5.27a). The unsized system at RT indicates -0.3 GPa residual stress prior to stretching (figure 5.9) and -1.0 GPa when the first fracture appears (figure 5.30a). This indicates that the fibre recoils to a stress value that depends on the initial stress field resulting from the superposition of the initial prestretching and the thermal stress field of the matrix (figure 5.45).

However, in the case of the sized system at 60°C, the residual stress prior to stretching is 0.8 GPa (figure 5.37) and, when the first fracture appears, it is -0.5 GPa (figure 5.37a). This corresponds to a 'recoil compressive stress' of the order of -1.1 GPa. The respective recoil stress for the unsized system (figures 5.39 and 5.40a) is of the order of -0.7 GPa, which is considerably less than the one recorded for the sized system.

The recoil principle is based on the assumption that the fibre recoils due to its elastic stored energy, and freezes in compression due to the existing hydrostatic thermal stress field created by the matrix. The energy is dissipated in the matrix. At higher temperatures, the initial hydrostatic thermal stress field is partially relieved and less energy is dissipated in the matrix. The reduction in the hydrostatic stress field will allow more frictional sliding of the fibre leading to higher compression stresses at the vicinity of the fibre fracture up to the point that the local interfacial properties will not be able to sustain any stress transfer. This is the case of the unsized system, where, the expected compressive field is partially relieved.

The recoil mechanism proves the existence of the frictional forces at the interface as postulated by Netravali et al. [**1989c**]. In the same study, birefringence patterns suggested the existence of a compressive field on the fibre after the fragmentation sample had fully relaxed, which proved that a slip did occur at the interface but at the same time the stress was still transferred. Thus, the recoil mechanism is clearly associated with interfacial failure, since the presence of compressive stresses in the otherwise tensile field can only be explained through a mechanism of interfacial slip of the fibre or a mode II crack propagating along the fibre axis. The stress field that forces the fibre into compression can only be governed by Coulomb frictional forces [**McCartney, 1989**]. It should be noted, however, that the transition from the frictional to the well-bonded area is not readily identified at low applied strains, since the compressive stress field extends for lengths extending from one to few fibre diameters and the axial stress is uniformly continuous. However, all studied systems exhibited elastic fibre recoil, indicating that the appearance of interfacial damage at the locus of the fibre fracture is inherent in the long fibre fragmentation test.

(b) Axial interfacial damage propagation

The energy dissipation mechanism is the parameter that defines the mode of interfacial failure. A very important parameter is the fracture toughness of the interface and/or the interphase, in relation to the achieved values of interfacial shear stress. By assessing the exact nature of the stress transfer profiles obtained using LRS at each level of applied strain, useful conclusions can be drawn as to the possible modes of failure at the interface level. This has already been confirmed by comparing stress transfer data in aramid / epoxy and carbon / epoxy with finite element analysis (FEA) predictions [**Guild, 1994; Nath, 1996**].

Inspection of the stress transfer profiles (figures 5.27a and 5.28a) and the corresponding ISS curves when the first fibre fractures appear at low applied strains, for the two systems at room temperature (figures 5.30a and 5.31a), shows that in all but one case, the ISS is maximum at the point of fracture and decays exponentially to zero at some distance away from the point of fibre fracture. Although the recoil mechanism is present with compressive stresses at the locus of the fracture, the induced damage is still highly localised to affect the shape of the ISS distribution which exhibits a Cox type behaviour. The 'knee' in the ISS curve observed on the left-hand side of the fragment for the sized system (figure 5.28a) is indicative of the onset of localised interfacial damage in this case. The onset of interfacial damage is more obvious for both systems at 60°C, where, in all cases, the locus of maximum ISS shifts from the fracture tip (figures 5.38a and 5.41a). Within experimental error, all systems indicate this shift of the locus of the maximum ISS away from the fracture tip with applied strain.

In the case of the sized system at room temperature, the propagation of damage can be clearly traced with applied strain. Indeed the ISS curve at 1.4% applied strain, reaches zero at 25.5 mm, whereas the onset of damage of the initial fracture at 26 mm has propagated further (figure 5.28b). However, this is not true for the fracture at 26.4 mm, where the ISS is discontinuous and the corresponding axial stress profiles indicate that the axial stress at the fibre tip is compressive. Melanitis et al. [**1992**] showed for a similar carbon / epoxy system that, when the ISS reaches zero or fluctuates around zero, then there is no adequate bridging between fibre and matrix. This situation does not necessarily arise as a result of mode-II debonding, because the high radial compressive stresses present at the interface and the compressive differential Poisson's ratio developed during tensile loading, ensure adequate bridging between the two surfaces by friction. It is concluded, therefore, that the type of stress transfer observed in the sized system corresponds to matrix or mixed-mode cracking as has been successfully modelled recently by FEA [**Nath, 1996**]. As shown in figure 5.51, this area of damage where no axial stress is transferred, increases with applied strain. The interfacial damage zone propagation is also responsible for the gradual elimination of any axial compression observed initially at the tip of the fibre fracture (figures 5.27a-d), as the additional damage mechanism is superimposed. The average value of mixed mode cracking at 4.8% applied strain is of the order of 125 μm (figure 5.51).

The absence of the fibre sizing, as well as elevated temperature, prevent the initiation of a mixed mode crack. Indeed, as shown in figures 5.30a-k (unsized system at RT), 5.37a-f (sized system at 60°C) and 5.40a-h (unsized system at 60°C), the axial stress is adequately transferred along the whole length of the fragments irrespective of the applied far field strain. The compressive stresses at the fibre tip bridge the fibre fractures providing adequate stress transfer.

The propagation of damage at the interface can be clearly identified by closely examining the individual axial stress profiles as the far field strain is increased. In figures 5.52 and 5.53 individual expanded profiles for the room temperature and high temperature systems are shown. At room temperature and low applied far field strain (figure 5.52a), the sized system exhibits efficient stress transfer along the entire length of the fragment, with a slight compression at the fibre tips. At higher applied strains, the situation changes; the stress is efficiently transferred only in the middle area of the fragment, whereas, for a considerable length on either side, it fluctuates around zero values indicating the propagation of a damage zone. Photoelastic observations of the sized system at room temperature and at applied strain 3.5% (figure 5.35a) confirm the existence of the damage zone with only a fraction of the fragment length exhibiting intense birefringence.

In the case of the unsized system at room temperature even at high applied strain (figure 5.52b), there is still a considerable amount of compressive stresses at the vicinity of the fibre breaks, but most importantly there are no areas in the fibre where the fibre axial stress is zero. This clearly indicates that the stress is transferred efficiently along the whole fragment and therefore the interfacial damage zone is adequately bridged. This behaviour is verified in figure 5.35b, where intense birefringent patterns extend along the entire length of the fragment. Similar behaviour is exhibited by both systems at high temperatures, with adequate stress bridging at the locus of the fibre failure (figure 5.53a and b), although in the case of the unsized system at high temperature, the efficiency of stress transfer is dramatically reduced. At this point, it is interesting to note that although a tensile axial stress field is superimposed on the fibre axis, the parts of the fibre which are in compression are not affected. On the contrary, as in the case of the unsized system at RT (figure 5.52b), a large proportion of the fibre may be 'frozen' in compression after the fragmentation process has reached saturation. This behaviour is similar to the 'frozen shear zones' observed in the short fibre coupons (§5.3.2.1). However, in the case of the long fragmentation coupon it may be suggested that the fragmentation process and the interfacial damage propagation make it impossible for the fibre to gradually perform a transition towards a tensile stress field.

The SEM micrographs of the fractured surfaces of the tested coupons provide further evidence for the nature of interfacial / intephasial damage. The fracture surface of the MEBS / MY-750 at room temperature (figures 5.32a-c) is indicative of damage extending in the matrix area. A clear indication of a residual matrix film on the fibre can be seen in figure 5.32c, which shows a crack propagating in the matrix, not necessarily along the fibre axis. The distinct failure of the interphase not only suggests the different failure mode but also gives strong indication for local property variations as predicted in the previous sections (figure 5.32a).

The presence of sizing is responsible for improved adhesive properties. The adhesion enhancement phenomenon can be explained on the basis that the sizing, being a low viscosity fluid, enhances wetting and simultaneously minimises trapped air pockets at the interface between fibres, reducing, thus, the flaw concentration at the interface [**Ying, 1983**]. During the curing of the matrix, the sizing layer interacts with the bulk matrix. The properties of this in situ sizing layer are, thus, imparted to the interphase [**Drzal, 1983b**]. In addition, the co-curing of the sizing and the matrix, causes the curing agent to diffuse in the sizing layer producing an interphase where the percentage of sizing is likely to be less than stoichiometric [**Netravali, 1989c**]. In this case, the properties of the interphase are likely to be stiffer but at the same time more brittle [**Mullin, 1968**]. Thus, the sizing is responsible for increased IFSS values but, at the same time, its reduced fracture toughness instigates crack formation in the matrix. Consequently, sized systems may display radically different post-fibre fracture processes [**ten Busschen, 1995**]. Drzal et al. [**1983b**] confirmed this behaviour by studying microtomed samples in the Transmission Electron Microscope; the microtomed flakes revealed a well bonded interphase in the case of a 'finished' carbon fibre epoxy system with cracks clearly propagating in the matrix.

The unsized system at room temperature exhibits a clean fibre surface as well as a distinct imprint of the fibre surface patterns on the surrounding matrix (figure 5.39d). This is also the case for both systems at high temperature (figure 5.42). It should be noted that no distinct differences in the interphase were noted in the case of the sized system at 60°C, proving, thus, that the interfacial damage mechanisms triggered at room temperature were not present. This is obviously due to the tougher nature of the interphase because of the increased temperature. In this case, the prevailing failure mechanism remains the mode II crack which is instigated by the fibre failure.

The proposed model for the two types of interfacial damage initiation and propagation is presented schematically in figures 5.54a and b. All systems exhibit the elastic fibre recoil at the onset of the fragmentation process where the radial compression developed during the curing of the matrix successfully bridges the fibre / matrix interface (figure 5.54a). As far as the sized system at room temperature is concerned, a mixed mode crack is relieving all stresses at the interface and propagates with applied strain (figure 5.54b) [**Mullin, 1968; ten Busschen, 1995**].

5.4.3.3 Modelling the stress transfer efficiency

As has been extensively described, during the fragmentation test there are several mechanisms that result to the reduction of the stress transfer efficiency of the interface. These mechanisms include matrix yielding [**Vlattas, 1992**] and cracking [**ten Busschen, 1995**]. Using LRS, Melanitis et al. [**1992**] identified the existence of such mechanisms by observing the existence of 'zones' of stress transfer along the fibre length. Thus, moving on the axis of the fragment from the fracture towards its middle, we can identify in sequence a region of 'damaged interface', where the stress transfer is poor, an intermediate region, where there is gradual improvement of the axial stress transfer, and the 'well bonded' region, where stress is transferred efficiently. With applied far field strain, the damaged zone increases to the detriment of the well bonded zone, whereas the intermediate zone remains constant.

Nairn et al. **[1996]** modelled the data obtained by LRS assuming the existence of only the efficient and the damaged zone. The respective zones may be characterised though single interface parameters that correspond to axial displacements **[Hashin, 1990]** relative to the elastic solution of the problem. The propagation of interfacial damage is associated to the failure of the interface when the interfacial shear strength is reached **[Galiotis, 1993b]**. It is, however, obvious that the damage mechanisms, no matter when and how they are triggered, act as energy dissipation mechanisms.

The energy released during the fragmentation test is primarily due to the fibre fractures. After the fracture events, secondary mechanisms contribute to further energy dissipation. This has been verified by the propagation of axial damage in the studied systems with applied strain which did not necessarily involve further fracture events (figure 5.51). Thus, it is expected that, with applied strain, the elastic stored energy in the fibre is reduced, and therefore, the resulting stress field constantly diverges from the equivalent stress field if the stress transfer continues to be elastic.

As has been shown in this study, LRS can be used to measure the elastic properties of the interface when the stress transfer is elastic. This can be performed by using the short fibre fragmentation test at low applied strains when the system is still within the elastic area. Thus, a single interface parameter may be obtained as an index of the elastic domain of the interface. However, even at the very onset of the fragmentation process, the stress field already diverges from its elastic equivalent. This can be seen in figure 5.55, where, if the stress transfer were elastic, the predicted axial stress distribution is superimposed to the axial stress field measured by LRS for relatively low applied strains and at the beginning of the fragmentation process. This difference can be visualised through the elastic stored energy in the fibre which corresponds to the area under the axial stress profile per unit fibre cross-sectional area.

In the case of the elastic stress transfer, this stored energy $\varepsilon_{elastic}$ can be calculated by integrating equation 5.8b along the whole of the fragment:

$$\varepsilon_{elastic} = \int_{z=0}^{l} E_f \varepsilon_\infty \left[1 - \frac{\cosh\left(\beta\left(\frac{l}{2} - z\right)\right)}{\cosh\left(\beta \frac{l}{2}\right)} \right] dz = E_f \varepsilon_\infty \left[1 - \frac{2}{\beta l} \tanh \beta \frac{l}{2} \right] \qquad (5.25)$$

In the case of the measured axial stress profiles, the stored energy on the fibre can be calculated by integrating numerically the measured axial stress values along the fragment length:

$$\varepsilon_{stored} = \int_{z=0}^{l} \sigma_z(z) dz \qquad (5.26)$$

Through equations 5.25 and 5.26, the equivalent elastic fibre length l^* may be defined, such as:

$$\varepsilon_{stored} = E_f \varepsilon_\infty \left[1 - \frac{2}{\beta l^*} \tanh \beta \frac{l^*}{2} \right] \qquad (5.27)$$

where l^* corresponds to the length that would be required for the fibre in order to store the same amount of energy if the stress state were elastic, for the same applied far field strain ε_∞. By dividing equations 5.25 and 5.27 the following is obtained for l^*:

$$\frac{\varepsilon_{stored}}{\varepsilon_{elastic}} l \left[1 - \frac{2}{\beta l} \tanh \beta \frac{l}{2} \right] = l^* \left[1 - \frac{2}{\beta l^*} \tanh \beta \frac{l^*}{2} \right] \qquad (5.28)$$

In equation 5.28, β can be defined by fitting the axial stress or the ISS data obtained from the short fibre coupon test (§5.4.2.2). l coincides with the length of individual fragments in the Raman Gauge Length and is measured optically. $\varepsilon_{elastric}$ is subsequently calculated through equation 5.25 using the maximum axial stress σ_{max} on the fibre, as measured though LRS. It should be noted that, in this case, σ_{max} does not coincide with the far field stress σ_∞, due to the small length of the fragments. Thus, the only unknown parameter is the equivalent elastic fibre length l^*, which can be derived by solving equation 5.28 numerically. Knowing the individual values of l^*, allows the definition of the index of stress transfer efficiency ζ:

$$\zeta = \frac{l^*}{l} \tag{5.29}$$

The index of stress transfer efficiency ζ takes values from 0 to 1 and describes the interface relative to an equivalent elastic domain. The value of ζ can provide a quantitative description of the state of the interface as a function of applied strain. In tables 5.16 and 5.17, the calculated values for ζ and all parameters used are shown for the MEBS / MY-750 and MUS / MY-750 at room temperature respectively. The respective mean values are shown in tables 5.18 and 5.19. For the value of the maximum axial stress and for the numerical integration the spline fitted data are used. It should be noted that the calculated energies correspond to energy per unit cross-sectional area. In figures 5.56a and b, ζ is plotted as a function of applied strain for the sized and the unsized systems, respectively.

The response of the sized system to applied strain shows that the efficiency of the interface falls immediately to 0.76±0.03 as compared with the elastic stress state immediately after the fragmentation process initiates (figure 5.56a). This energy loss is due to the change of the matrix properties at different increments of applied strain, as well as interfacial damage mechanisms, such as frictional sliding when the fibre recoil is present. Energy dissipation is inherent in the long fibre fragmentation and any elastic analysis of the fragmentation process is bound to provide an overestimation of the stress transfer efficiency of the interface. With further applied strain, the efficiency of the interface remains practically constant up to 2.3% applied strain. Thus, it is shown that the secondary damage mechanisms, are still negligible compared to the initial energy loss after the first fibre fractures.

However, the situation changes dramatically with further applied strain. At 3% the efficiency of the interface has fallen by approximately 20% to a mean value of 0.61±0.09. As postulated in the previous section this can be attributed to the initiation of additional failure mechanisms, such as matrix cracking. The reduction of ζ is accompanied by a considerable increase in the scatter of experimental data, indicating the statistical nature of interfacial damage. With further applied strain, ζ is reduced to reach a final value of 0.56±0.04. Thus, the efficiency of stress transfer is reduced to half its equivalent elastic value at high strains.

The unsized system exhibits a considerably higher index of stress transfer efficiency at 0.87±0.02 at the onset of fragmentation (figure 5.56b). This is expected due to the reduced adhesion properties of this system that are less likely to induce considerable damage to the interface. The system retains the high integrity of the interface until 2.1%. At further applied strains, the index is reduced to reach a minimum of 0.65±0.09 at 4.4% applied strain. The relative decrease in stress transfer efficiency is 25%, that is, half the respective decrease in the sized system. This occurs in spite of the fact that additional fracture events were recorded after 2.65%. This is in accordance with the previous findings (§5.4.3.2); that is, there are additional stress relieving mechanisms that become active in the case of the sized system, whereas the unsized system retains considerable stress transfer efficiency throughout the fragmentation process.

It is interesting to note that the energy approach to the long fibre coupon test takes into account the residual compressive field created due to the recoil mechanism. In this respect, the stored energy of the fibre which is in compression, is deducted from the stored energy of the part of the fibre which is still in tension. As previously described (§5.4.3.2), the recoil mechanism is a damage process that involves frictional sliding at the interface. This frictional sliding occurs immediately after the fracture event and the fibre is frozen in position due to the thermal stress field. It is, however, probable that the frictional damage extends to the positively stressed part of the fibre, in the form of a mode II crack at the interface. In order to evaluate the extend of this zone, the exact thermal stress state around the fibre has to be evaluated. The physical meaning of this approach is that, in the absence of the superimposed thermal stress field, the respective lengths on either side of the zero stress point would not be able to sustain any axial stress. This is the case of the unsized system at 60°C where the axial stress distribution at 3.0% indicates that the energy sustained by the fibre is considerably reduced (figure 5.53b) due to the relief of the thermal stress field. Moreover, the negative stored energy in the fibre has an adverse effect to the further loading of the specimen and, thus, has to be deducted from the total energy of the fibre.

It is, thus, demonstrated that the energy approach to the interpretation of the long fibre coupon data can provide quantitative information about the efficiency of the interface. The versatility of this approach lies with the fact that all energy dissipation mechanisms are accounted for. In this way, a universal approach is used to account for the properties of the matrix, frictional sliding,and matrix cracking. Thus, the interpolation of the single fibre data to 'practical' composites where artefacts, due to the residual stress field, are not present is feasible. The index of stress transfer efficiency ζ provides the information needed in order to scale the stresses developed in the elastic stress state and model adhesion in the locus of the discontinuity of a fracture. In terms of interfacial efficiency, the fracture event can be expected to increase the ineffective length and, as a result, the flaw size in the composite. This increase was found to be 33% and 12% for the sized and the unsized fibres respectively.

Summarising, although it was demonstrated that the interface in the elastic stress state can be solely described through the use of the single parameter β, the efficiency of the stress transfer depends on the amount of dissipated energy after fracture events start to appear and the far field strain is increased. Throughout this process, the interface is bound to lose in stress transfer efficiency. In addition, although the β parameter was measured to be constant in low applied strains, this is not necessarily the case at higher applied strains, where the matrix is plasticised. The index of stress transfer efficiency can successfully describe the extend of divergence from the elastic stress state, through a universal energy approach.

Specific Gravity	-	1.17
Tensile Strength *ISO/R 527*	/ MPa	75-85
Elongation at Break *ISO/R 527*	/ %	3.5-4.5
Modulus of Elasticity (tension) *ISO/R 507*	/ GPa	2.9-3.3
Flexural strength *BS 2782 (304C)*	/ MPa	105-120
Modulus of Elasticity (flexure) *ISO 178*	/ GPa	3.3-3.7
Compressive strength (Yield) *BS 2782 (303C)*	/ MPa	100-110
Deflection Temperature *BS2782 (102G)*	/ °C	85-90
Coefficient of Expansion *ASTM D 696-70*	/ (Linear/ °C)	$65\text{-}70\times10^{-6}$
Thermal Conductivity *BS 874 section 4.2.3*	/ (W/m °C)	0.21-0.23

Table 5.1 Manufacturer's quoted physical and mechanical properties for the MY-750 resin.

MY-750/°C	E_m / *GPa*[1]	ν_m [2]	G_m / *GPa*[3]	σ_{mu} / *MPa*[4]	τ_{mu} / *MPa*[5]
20	3.0±0.2	0.34	1.1±0.1	52.4±5.3	30.3±3.0
40	2.5±0.2	0.37	0.9±0.1	39.1±4.0	22.6±2.3
60	1.8±0.1	0.41	0.64±0.0	26.0±4.1	15.0±2.3
80	0.5±0.0	0.48	0.2±0.0	5.2±0.2	3.3±0.1

[1,2,4] Directly measured quantities

[3] Calculated as $G_m = E_m / 2(1 + \nu_m)$ for elastic isotropic materials **[Timoshenko, 1988]**

[5] Calculated as $\tau_{mu} = \sigma_{mu} / 1.73$ from the Von Mises criterion **[McCrum, 1990]**

Table 5.2 Mechanical properties of the MY-750 resin.

Specimen Configuration	***Short Fibre Coupon / GPa***	***Long Fibre coupon / GPa***
MEBS/MY-750	-0.52±0.06	0.27±0.40
MUS/MY-750	-0.43±0.06	0.04±0.40

Table 5.3 Residual stress distributions for the long and short fibre configuration at room temperature.

MEBS / MY-750 (short fibre coupon)						
Applied Strain / %	***0.0***	***0.1***	***0.2***	***0.3***	***0.4***	***0.6***
Axial Stress (GPa)[1]	-0.65	-0.51	-0.16	0.05	0.53	0.90[2]
ISS / MPa (Left)	-21.0	-9.4	-14.9	12.4	15.4	25.6
ISS / MPa (Right)	21.8	22.9(8.3)[3]	9.4	-6.8	-21.0	-31.4

[1]The axial stress values correspond to the maximum axial stress measured on the fibre and are calculated through linear fitting of the area 200 μm to 450 μm and calculating the middle value at 325 μm.

[2]This value is the average maximum of the maximum axial stress of the two profiles, at 0.6% (figure 5.20f).

[3]The first value corresponds to the measured maximum and the second value to the secondary maximum or the 'Knee' of the ISS distribution.

Table 5.4 MEBS / MY-750 (short fibre): measured axial far field stresses and calculated maximum ISS values for all strain levels.

MUS / MY-750 (short fibre coupon)						
Applied Strain / %	***0.0***	***0.1***	***0.2***	***0.3***	***0.4***	***0.6***
Axial Stress (GPa)[1]	-1.02	-0.59	-0.30	0.06	0.40	1.0[2]
ISS / MPa (Left)	-18.7	-5.5	-3.5	-4.0	10.1	16.7
ISS / MPa (Right)	14.19	8.7	42.9	8.4	-8.6	-18.3

[1]The axial stress values correspond to the maximum axial stress measured on the fibre and are calculated through linear fitting of the area 200 μm to 450 μm and calculating the middle value at 325 μm.

[2]This value is approximate since the far field stress value is not necessarily reached (figure 5.23f).

Table 5.5 MUS / MY-750 (short fibre): measured axial far field stresses and calculated maximum ISS values for all strain levels.

strain / %	***Maximum ISS / MPa (MEBS / MY-750, long fibre coupon at room temperature)***							
1.3	48.0	29.1						
1.4	33.6	32.9	25.8	37.6	31.2	36.5		
1.5	28.0	31.3	26.9	36.9	32.9	36.5		
1.7	28.8	42.1	22.8	57.6	57.0	40.9	29.8	29.1
1.9	34.1	45.0	34.0	37.7	31.1	42.5	35.6	31.7
2.1	38.5	45.1	43.3	43.4	43.0	46.6	37.5	37.6
2.3	36.4	53.6	41.2	34.0	29.1	47.3	36.2	39.1
3.1	41.8	38.3	46.3	35.8	42.3	39.6	35.2	32.6
3.8	37.0	31.4	34.9	28.1	38.2	37.9	31.2	32.0
4.8	24.4	24.1	38.1	31.9	43.5	37.3	33.3	29.4

Table 5.6 Maximum ISS values for the MEBS / MY-750 long fibre coupon at room temperature.

Average Maximum ISS (MEBS / MY-750, long fibre coupon at room temperature)			
strain/ %	*ISS / MPa*	***strain/ %***	*ISS / MPa*
1.3	38.5	*2.1*	41.9±3.5
1.4	33.0±4.7	*2.3*	39.6±8.3
1.5	32.1±4.1	*3.1*	39.0±4.6
1.7	38.5±13.7	*3.8*	33.8±3.7
1.9	36.5±5.3	*4.8*	32.7±6.4

Table 5.7 Average maximum ISS values for the MEBS / MY-750 long fibre coupon at room temperature.

strain / %	***Maximum ISS / MPa (MUS / MY-750, long fibre coupon at room temperature)***									
1.3	24.3	31.4								
1.4	24.0	27.5	26.8	37.1						
1.5	23.4	26.8	28.3	31.8	25.4	38.1	25.4	38.1	46.7	42.0
1.6	30.0	35.4	33.5	31.1	26.3	35.1	22.6	34.0	24.0	51.2
1.7	26.6	30.0	27.1	33.4	25.1	39.4	39.9	35.4	19.7	33.3
1.9	31.7	33.9	39.2	30.3	26.5	40.4	32.9	41.6	26.2	35.8
2.1	31.9	34.2	29.7	39.4	30.0	41.9	31.7	35.8	30.6	42.7
2.7	35.4	47.5	31.1	34.4	34.0	38.2				
2.9	29.4	39.4	40.7	16.4	50.0					
3.4	37.5	36.2	44.0	11.6	30.4	40.3	39.9	48.8		
4.4	29.4	36.3	20.2	23.9	24.5	39.1	37.0	44.7		

Table 5.8 Maximum ISS values for the MUS / MY-750 long fibre coupon at room temperature.

Average Maximum ISS

(MUS / MY-750, long fibre coupon at room temperature)

strain/ %	***ISS / MPa***	***strain/ %***	***ISS / MPa***
1.3	27.9	***2.1***	34.8±4.9
1.4	28.9±5.7	***2.7***	36.8±5.7
1.5	32.6±8.1	***2.9***	35.2±12.8
1.6	32.3±8.1	***3.4***	36.1±11.3
1.7	31.0±6.5	***4.4***	31.9±8.6
1.9	33.9±5.4		

Table 5.9 Average maximum ISS values for the MUS / MY-750 long fibre coupon at room temperature.

strain / %	***Maximum ISS / MPa (MEBS / MY-750, long fibre coupon at 60°C)***					
0.6	22.4	10	17.5			13.36
0.8	10	15.1	10.27			22
1.0	11.8	18.6	11.8			15.7
1.4	22.9	16	15.2			24.7
2.0	25.3	29.8	12.3	17.94	10.8	17.1
3.0	17.688	13.07	17.2	18.48		

Table 5.10 Maximum ISS values for the MEBS / MY-750 long fibre coupon at 60°C.

Average Maximum ISS

(MEBS / MY-750, long fibre coupon at 60°C)

strain/ %	***ISS / MPa***	***strain/ %***	***ISS / MPa***
0.6	15.8±5.4	***1.4***	19.7±4.8
0.8	14.3±5.6	***2.0***	18.9±7.4
1.0	14.5±3.3	***3.0***	16.6±2.4

Table 5.11 Average maximum ISS values for the MEBS / MY-750, long fibre coupon at 60°C.

strain / %	*Maximum ISS / MPa (MUS / MY-750, long fibre coupon at 60°C)*							
0.8	9.7	4.6	13.4	8.2				
1.0	7.5	11.0	9.8	19.0				
1.2	5.9	11.5	11.0	14.4				
1.4	7.1	8.8	6.8	6.8	9.6	13.1		
1.6	7.9	4.5	4.9	3.5	4.0	6.3		
1.8	7.9	6.0	5.1	7.5	5.9	6.8	7.3	8.3
2.0	4.6	4.7	5.1	6.3	6.2	9.2		
3.0	5.5	7.1	2.3	3.6	5.8	7.6		

Table 5.12 Maximum ISS values for the MUS / MY-750 long fibre coupon at 60°C.

Average Maximum ISS

(MUS / MY-750, long fibre coupon at 60°C)

strain/ %	*ISS / MPa*	*strain/ %*	*ISS / MPa*
0.8	8.9±3.6	***1.6***	5.2±1.6
1.0	11.8±5.0	***1.8***	6.9±1.1
1.2	10.7±3.5	***2.0***	6.0±1.7
1.4	8.7±2.4	***3.0***	5.3±2.0

Table 5.13 Average maximum ISS values for the MUS / MY-750, long fibre coupon at 60°C.

System		*Critical Length / mm*[1]	*Axial Strength / GPa*[2]	*ISS (classical) / MPa*[3]	*ISS (Raman) / MPa*[4]
MEBS/MY-750	***(RT)***	0.42±0.10	3.83±0.05	30.1±6.1	41.9±3.5
MUS/MY-750	***(RT)***	0.48±0.12	3.77±0.06	26.1±5.5	36.8±5.7
MEBS/MY-750	***(60°C)***	0.64±0.18	3.37±0.05	19.1±4.4	18.9±7.1
MUS/MY-750	***(60°C)***	0.64±0.16	3.37±0.05	19.1±4.0	11.8±5.0

---

[1] The Critical Length is 4/3 of the measured fragment length

[2] The Axial Strength is calculated by interpolating the fibre Weibull strength distribution to the Critical Length.

[3] The IFSS (classical) is calculated at saturation(Gauge length 40 mm) using the Kelly-Tyson Formula (equation 5.7) for individual fragments.

[4] The IFSS (Raman) is defined experimentally as the maximum average from all applied strain levels.

Table 5.14 Interfacial shear strength values as calculated through the constant shear stress model **[Kelly, 1965]** and as measured with LRS for all studied long fibre coupons.

System	*Applied Strain / %*	*β(Left)/ μm^{-1}*	*β(Right)/ μm^{-1}*	*Far-Field Fibre Stress / GPa*
MEBS / MY-750	0	0.0235	0.0192	-0.65
	0.6	0.0213	0.0191	0.90
MUS / MY-750	0	0.0095	0.0094	-1.0
	0.6	0.0082	0.0099	1.0

Table 5.15 Estimated *β* parameter for the short fibre coupons.

MEBS / MY-750 (long Fibre at RT) : $\beta = 0.021$						
Applied Strain / %	***l / mm***	***$\sigma_{z,max}$ / GPa***	***$\varepsilon_{elastic}$ / $MN\,m^{-1}$***	***ε_{stored} / $MN\,m^{-1}$***	***l^* / mm***	***ζ***
1.4	484	3.40	1.338	0.883	352	0.73
1.4	402	2.59	0.818	0.592	318	0.79
1.4	698	3.97	2.390	1.779	541	0.78
1.5	484	3.23	1.268	0.870	362	0.75
1.5	424	2.52	0.846	0.615	334	0.79
1.5	698	4.16	2.504	1.787	526	0.75
1.7	484	3.50	1.376	0.915	354	0.73
1.7	424	2.89	0.970	0.661	319	0.75
1.7	383	2.42	0.722	0.461	279	0.73
1.7	302	1.35	0.306	0.195	226	0.75
1.9	484	3.89	1.529	1.008	352	0.73
1.9	424	3.22	1.082	0.772	330	0.78
1.9	383	2.80	0.833	0.632	313	0.82
1.9	302	1.84	0.415	0.331	258	0.85
2.1	484	4.17	1.638	1.057	347	0.72
2.1	424	3.53	1.186	0.842	329	0.78
2.1	383	3.13	0.931	0.679	305	0.80
2.1	302	1.78	0.402	0.295	247	0.82
2.3	484	4.13	1.623	1.012	338	0.70
2.3	424	3.56	1.197	0.819	321	0.76
2.3	383	3.01	0.898	0.649	303	0.79
2.3	302	2.06	0.464	0.351	251	0.83
3.0	484	2.76	1.084	0.480	267	0.55
3.0	424	2.48	0.834	0.354	233	0.55
3.0	383	2.46	0.734	0.349	231	0.60
3.0	302	2.09	0.473	0.303	226	0.75
3.8	484	2.16	0.849	0.355	258	0.53
3.8	424	1.73	0.581	0.239	229	0.54
3.8	383	1.94	0.577	0.244	216	0.56
3.8	302	1.67	0.377	0.185	194	0.64
4.8	484	1.63	0.642	0.298	276	0.57
4.8	424	1.69	0.567	0.212	217	0.51
4.8	383	1.83	0.546	0.218	208	0.54
4.8	302	1.53	0.345	0.164	189	0.63

Table 5.16 MEBS /MY-750 (RT); calculation of the index of stress transfer efficiency ζ.

MUS / MY-750 (long Fibre at RT) : $\beta = 0.009$						
Applied Strain / %	*l / mm*	*$\sigma_{z,max}$ / GPa*	*$\varepsilon_{elastic}$ / MN m^{-1}*	*ε_{stored} / MN m^{-1}*	*l^* / mm*	*ζ*
1.4	501	2.40	0.861	0.666	432	0.86
1.4	1552	2.97	3.976	3.459	1379	0.89
1.5	501	2.20	0.791	0.587	422	0.84
1.5	529	2.25	0.859	0.608	432	0.82
1.5	1022	2.62	2.147	1.773	881	0.86
1.5	289	0.94	0.187	0.120	238	0.82
1.6	501	2.56	0.920	0.744	444	0.89
1.6	529	2.59	0.990	0.746	447	0.84
1.6	582	2.50	1.063	0.836	502	0.86
1.6	440	1.61	0.500	0.329	353	0.80
1.6	289	0.71	0.141	0.077	222	0.77
1.7	501	2.58	0.926	0.762	450	0.90
1.7	529	2.79	1.066	0.854	464	0.88
1.7	582	2.48	1.054	0.864	514	0.88
1.7	440	1.86	0.578	0.428	374	0.85
1.7	289	0.82	0.163	0.108	240	0.83
1.9	501	2.82	1.012	0.759	426	0.85
1.9	529	2.86	1.091	0.896	474	0.90
1.9	582	2.63	1.117	0.884	501	0.86
1.9	440	1.92	0.597	0.475	392	0.89
1.9	289	1.14	0.226	0.166	257	0.89
2.1	501	3.15	1.131	0.968	460	0.92
2.1	529	3.33	1.271	1.037	467	0.88
2.1	582	3.09	1.315	1.075	513	0.88
2.1	440	2.36	0.734	0.576	386	0.88
2.1	289	1.37	0.272	0.232	268	0.93
2.65	529	3.52	1.344	0.916	422	0.80
2.65	313	1.30	0.281	0.174	251	0.80
2.65	269	0.87	0.160	0.065	184	0.68
2.9	313	1.25	0.270	0.146	236	0.75
2.9	269	0.97	0.178	0.067	178	0.66
3.4	330	1.33	0.302	0.199	271	0.82
3.4	199	0.31	0.042	0.008	108	0.54
3.4	313	1.46	0.315	0.213	260	0.83
3.4	269	1.26	0.231	0.147	220	0.82
4.4	330	1.06	0.241	0.128	248	0.75
4.4	199	0.30	0.020	-0.004	112	0.53
4.4	313	1.05	0.227	0.072	190	0.61
4.4	269	1.01	0.185	0.077	184	0.68

Table 5.17 MUS / MY-750 (RT); calculation of the index of stress transfer efficiency ζ.

(MEBS / MY-750, long fibre coupon at room temperature)

strain/ %	ζ	*strain/ %*	ζ
1.40	0.76±0.03	*2.30*	0.77±0.06
1.50	0.76±0.02	*3.00*	0.61±0.09
1.70	0.74±0.01	*3.80*	0.57±0.05
1.90	0.79±0.05	*4.80*	0.56±0.05
2.10	0.78±0.04		

Table 5.18 MEBS / MY-750 (RT); average index of stress transfer efficiency ζ as a function of applied strain.

(MUS / MY-750, long fibre coupon at room temperature)

strain/ %	ζ	*strain/ %*	ζ
1.4	0.87±0.02	*2.1*	0.90±0.02
1.5	0.84±0.02	*2.7*	0.77±0.07
1.6	0.83±0.05	*2.9*	0.72±0.07
1.7	0.87±0.02	*3.4*	0.76±0.15
1.9	0.87±0.02	*4.4*	0.64±0.11

Table 5.19 MUS / MY-750 (RT); average index of stress transfer efficiency ζ as a function of applied strain.

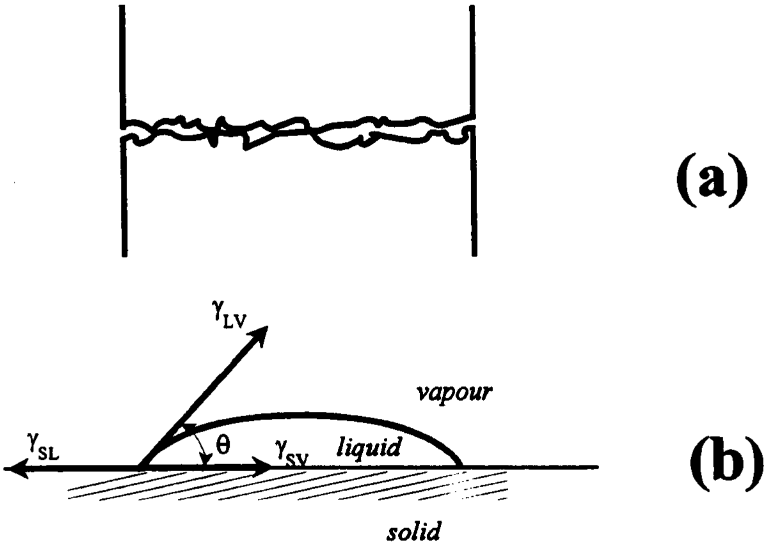

Figure 5.1 (a) Isolated contact points leading to weak adhesion between two rigid rough surfaces. (b) Contact angle θ and surface energies γ for a liquid drop on a solid surface [**Hull, 1996**].

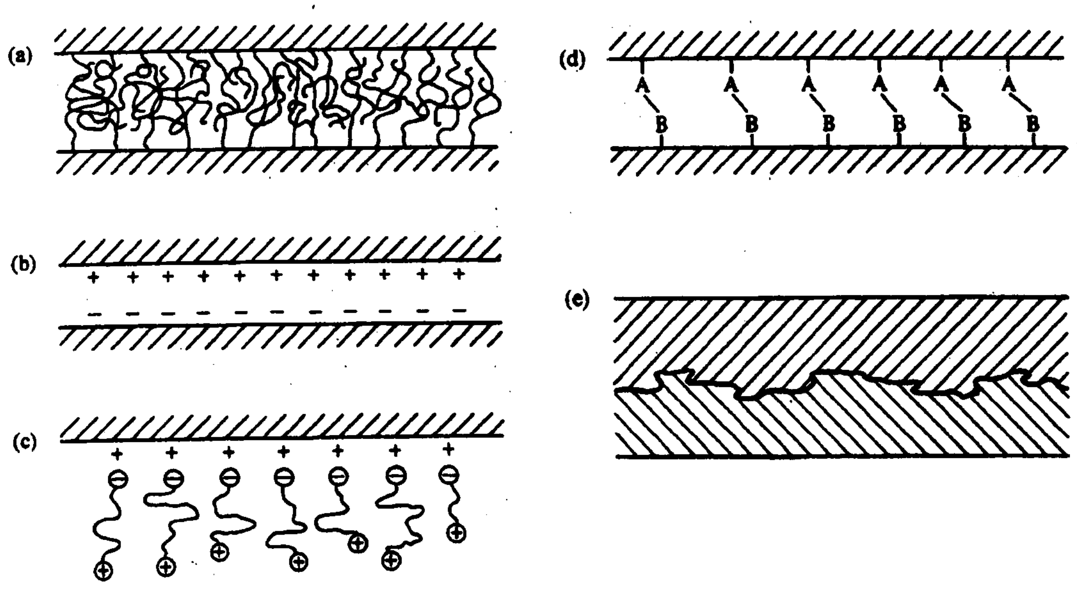

Figure 5.2 Interfacial bonds formed by (a) molecular entanglement following interdiffusion, (b) electrostatic attraction, (c) cationic groups at the end of molecules attracted to an ionic surface, resulting in polymer orientation at the surface, (d) chemical reaction, and (e) mechanical keying [**Hull, 1996**].

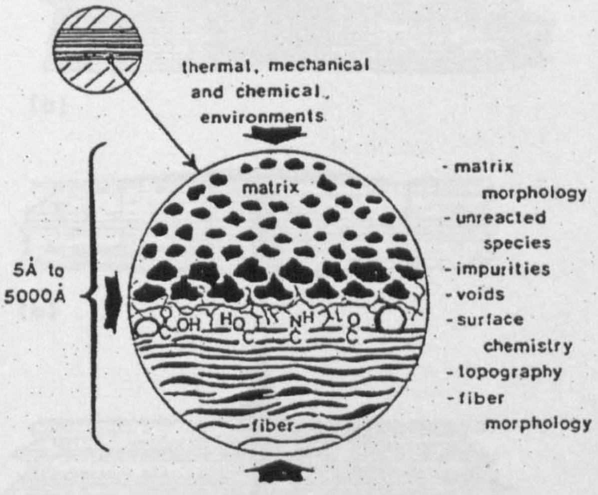

Figure 5.3 Schematic representation of the components of the three dimensional interphase between the fibre and the matrix [**Drzal, 1990**].

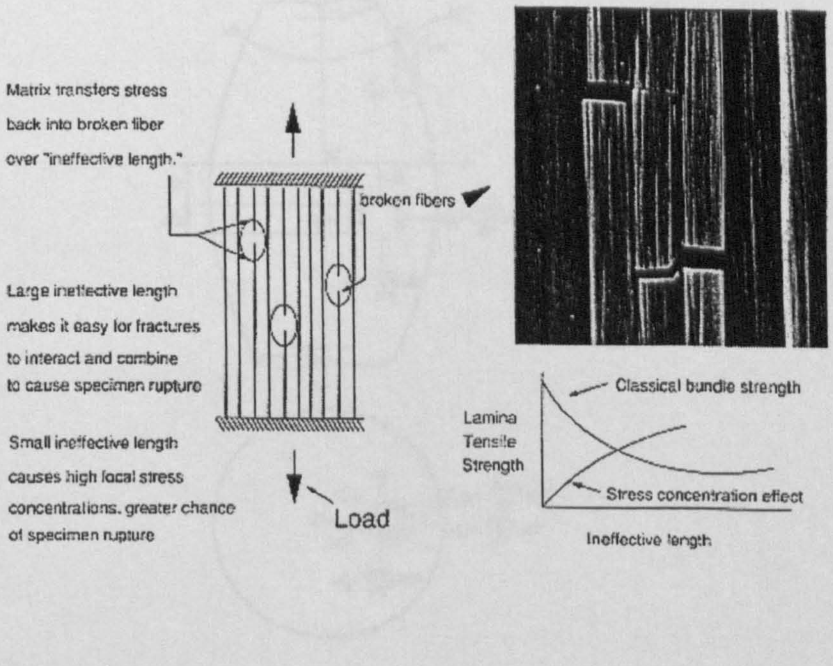

Figure 5.4 Schematic diagram of mechanisms that control the tensile strength of continuous fibre-reinforced laminae [**Reifsnider, 1994**].

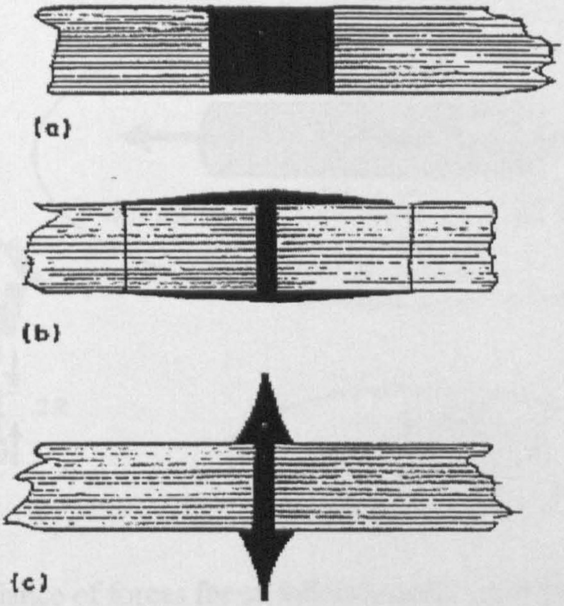

Figure 5.5 Schematic diagrams illustrating the three failure modes detected with increasing fibre-matrix adhesion for a single fibre which fractures in an epoxy matrix due to shear loading: (a) at low levels of adhesion, (b) at intermediate levels - interfacial crack growth, and (c) at the highest levels - matrix cracking perpendicular to the fibre axis **[Drzal, 1993]**.

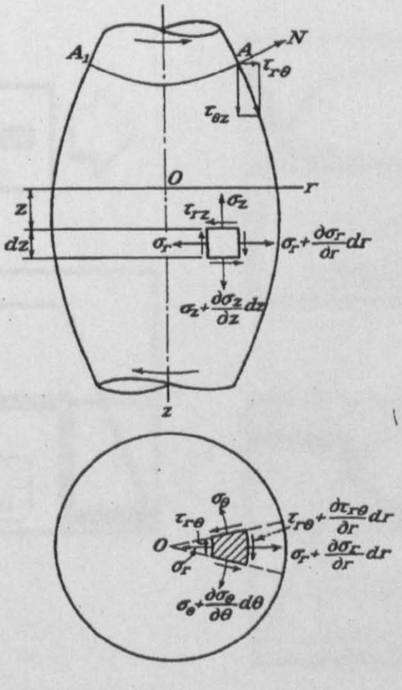

Figure 5.6 Stress components in cylindrical coordinates for axisymmetric solids **[Timoshenko, 1988]**.

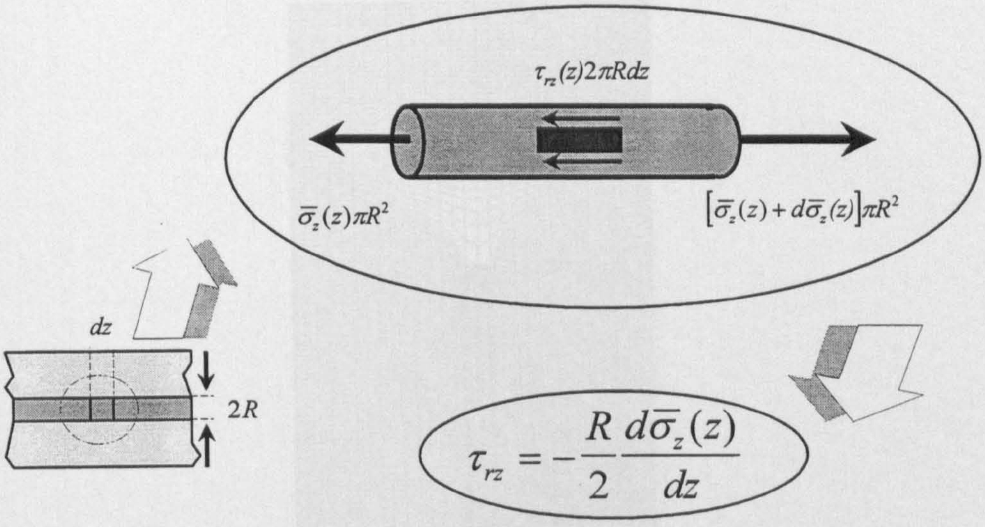

Figure 5.7 Axial balance of forces for an infinitesimally small fibre element.

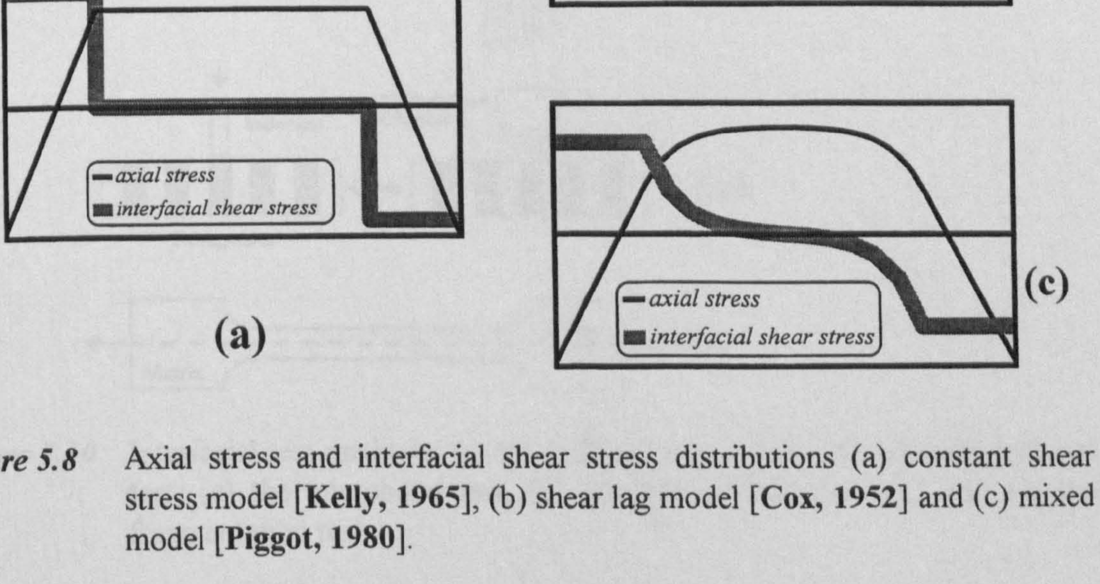

Figure 5.8 Axial stress and interfacial shear stress distributions (a) constant shear stress model [**Kelly, 1965**], (b) shear lag model [**Cox, 1952**] and (c) mixed model [**Piggot, 1980**].

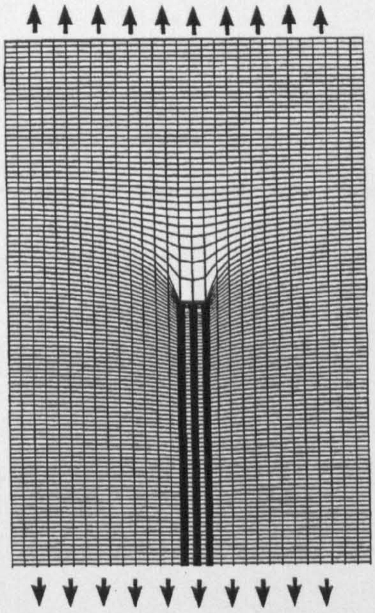

Figure 5.9 Elastic deformation of a fibre embedded in a matrix because of an axial tensile stress field for fibre / matrix stiffness ratio = 40 [**Termonia, 1987**].

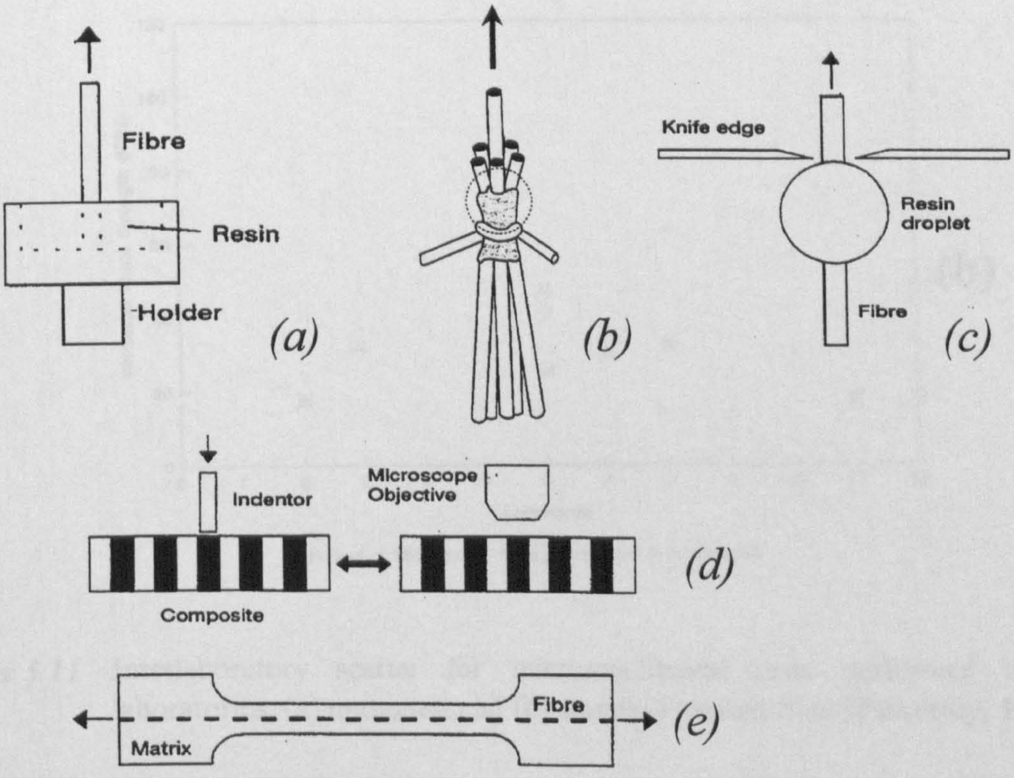

Figure 5.10 Interfacial test methods; (a) the pull-out test, (b) the microbundle pull-out test, (c) the microbond test, (d) the microindentation test, and (e) the fragmentation test.

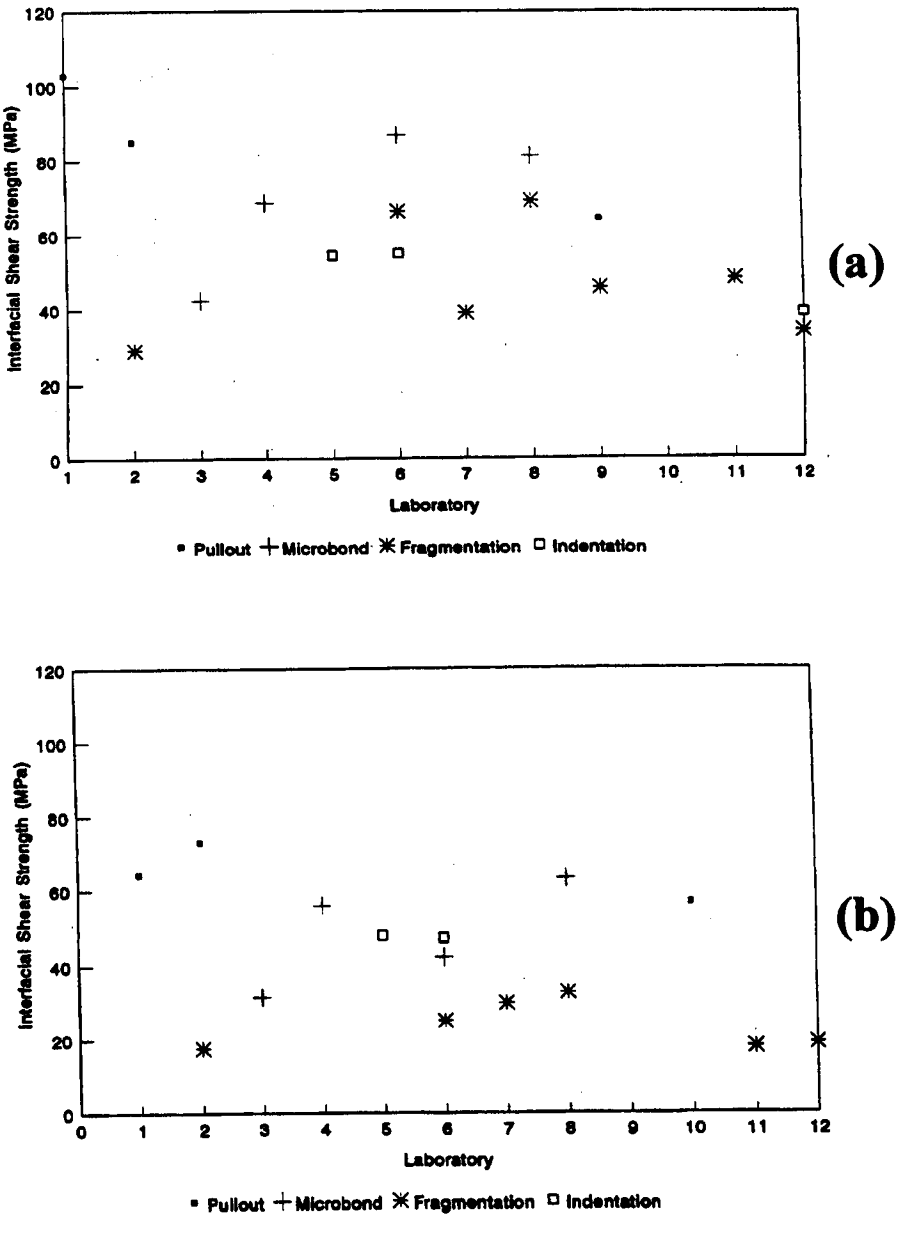

Figure 5.11 Interlaboratory scatter for micromechanical tests performed in 12 laboratories; (a) untreated and (b) standard treated fibre [**Pitkethly, 1993**].

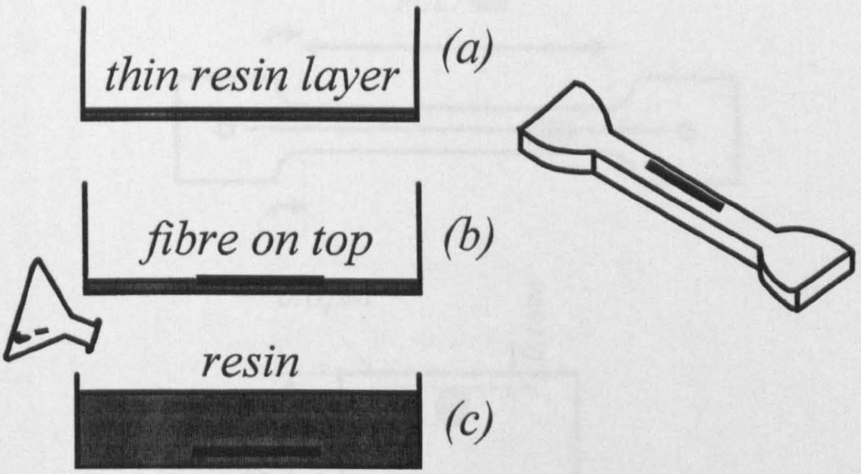

Figure 5.12 Specimen preparation for the short fibre coupon.

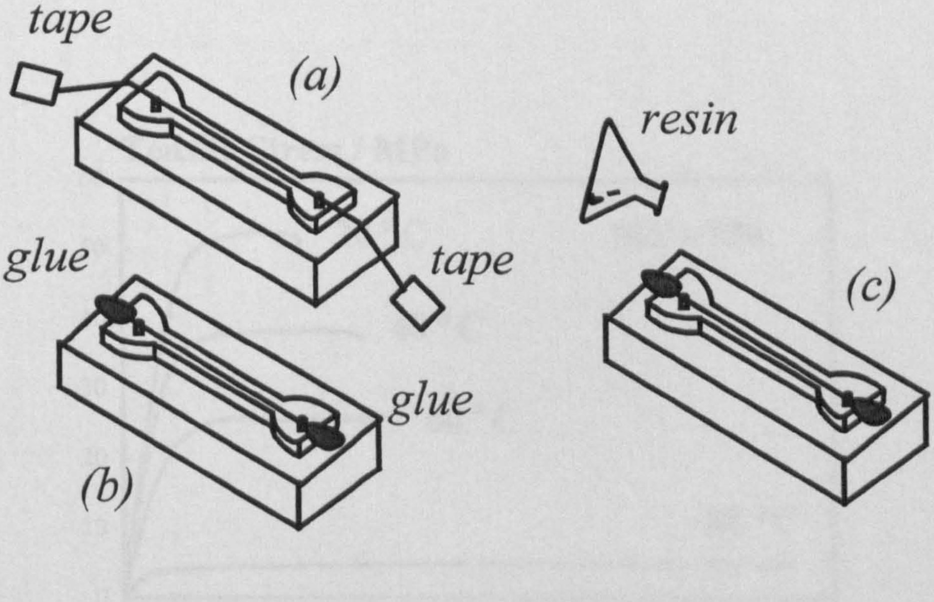

Figure 5.13 Specimen preparation for the long fibre coupon.

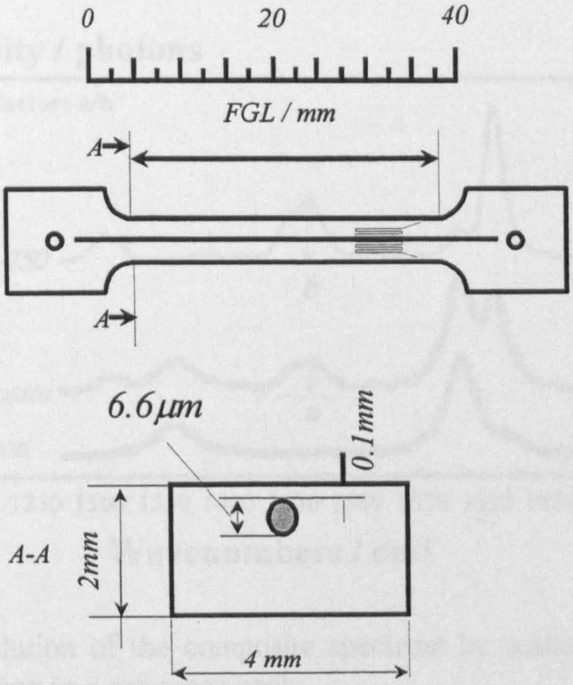

Figure 5.14 Specimen geometry used for the long fibre coupon studies; the Fragmentation Gauge Length (FGL) is 40 mm.

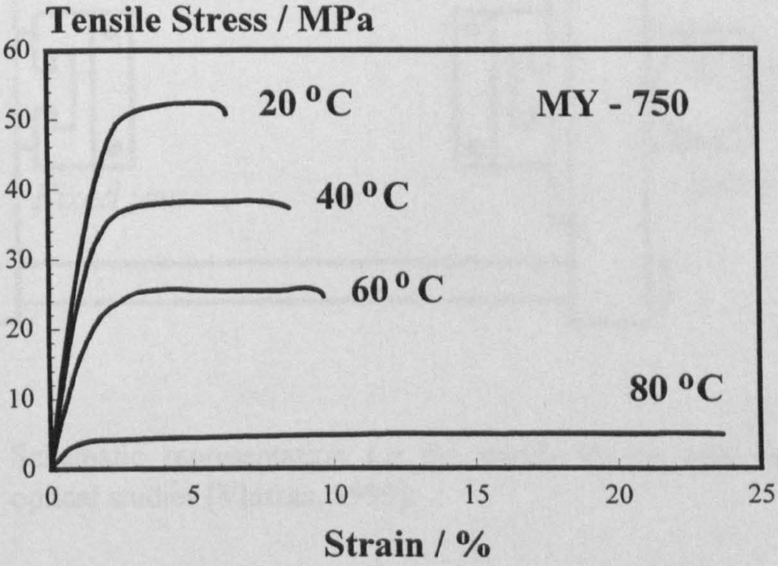

Figure 5.15 Stress - strain curves for the MY-750 matrix for different temperatures.

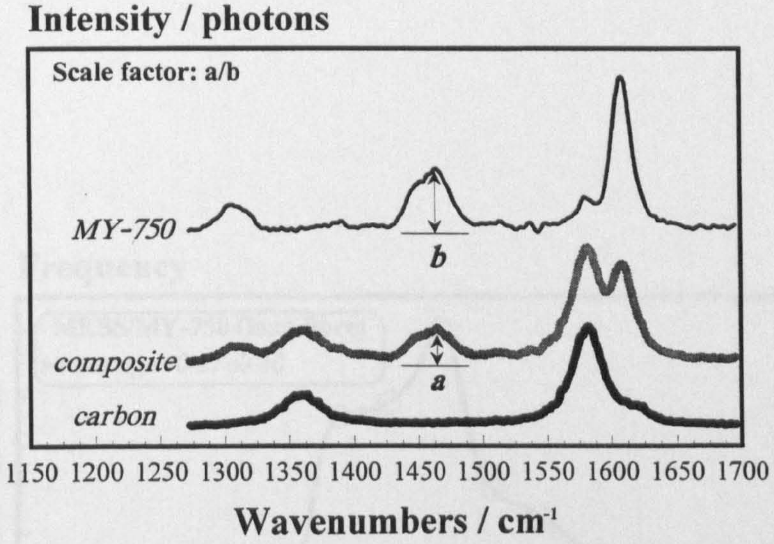

Figure 5.16 Deconvolution of the composite spectrum by scaling the resin spectrum contribution to a reference peak.

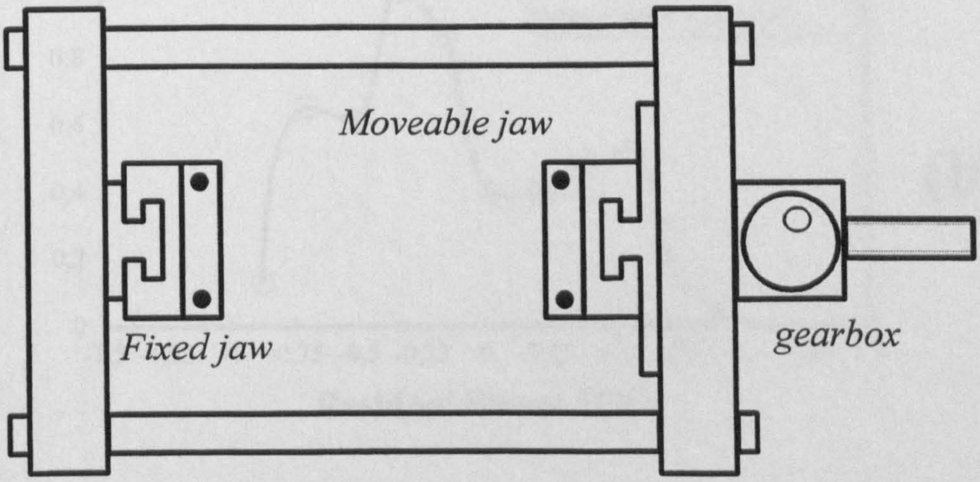

Figure 5.17 Schematic representation for the tensile device used for conventional optical studies [**Vlattas, 1995**].

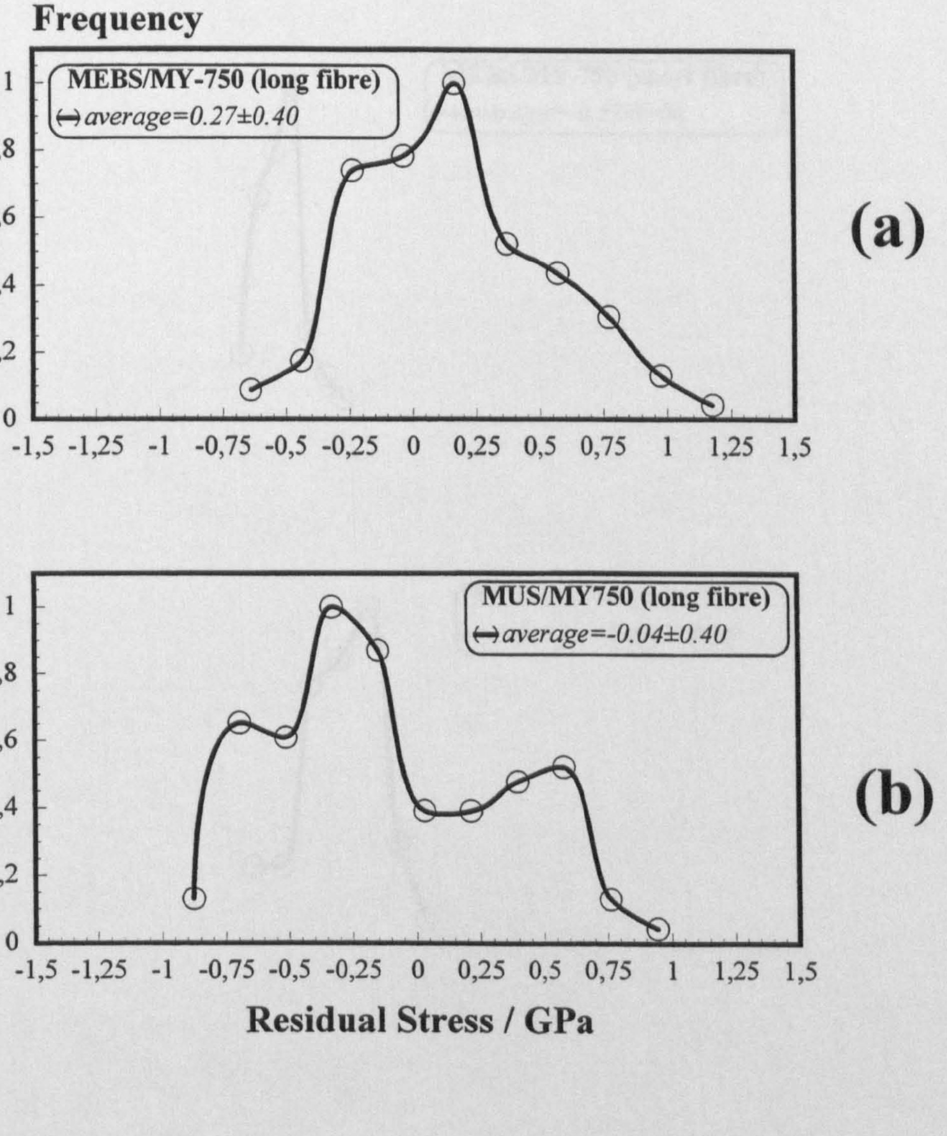

Figure 5.18 Distribution of residual stresses of the embedded fibre as compared with the fibre in air for the long fibre configuration: (a) sized (MEBS) M40 / MY-750 (six samples), and (b) unsized (MUS) M40 / MY-750 (six samples).

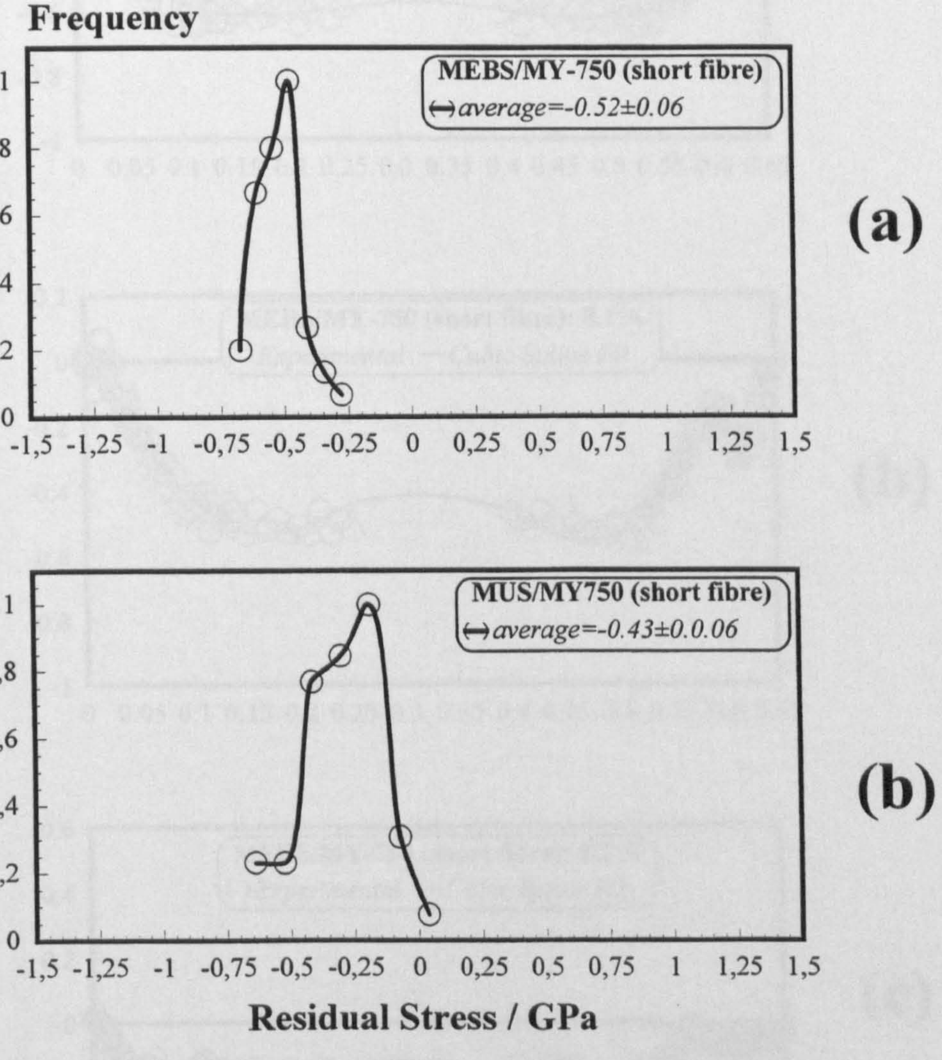

Figure 5.19 Distribution of residual stresses of the embedded fibre as compared with the fibre in air for the short fibre configuration: (a) sized (MEBS) M40 / MY-750 (six samples), and (b) unsized (MUS) M40 / MY-750 (six samples).

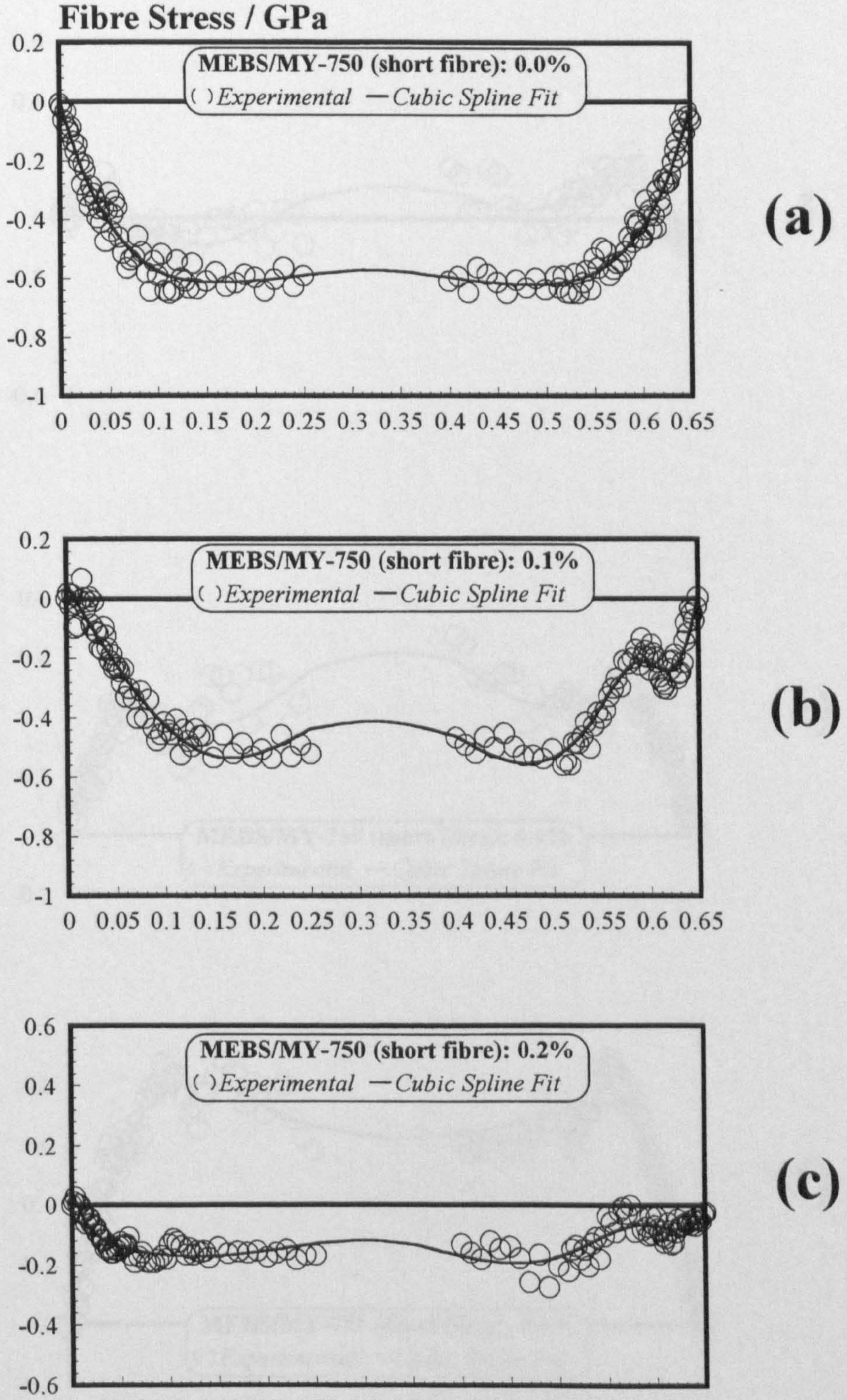

Figure 5.20 MEBS / MY-750 (short fibre coupon): (a-c) Axial stress profiles along the fibre length.

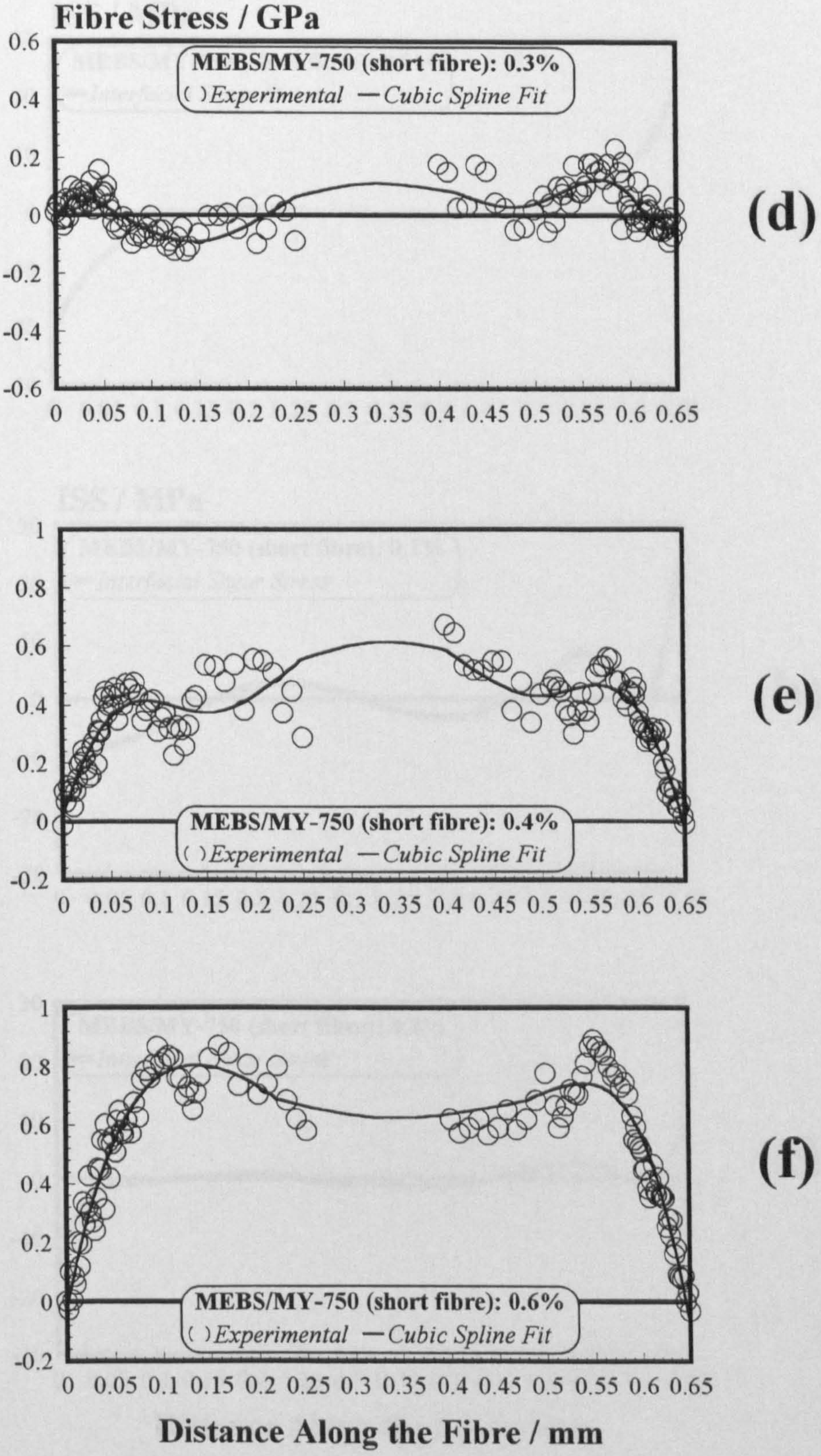

Figure 5.20 MEBS / MY-750 (short fibre coupon): (d-f) Axial stress profiles along the fibre length.

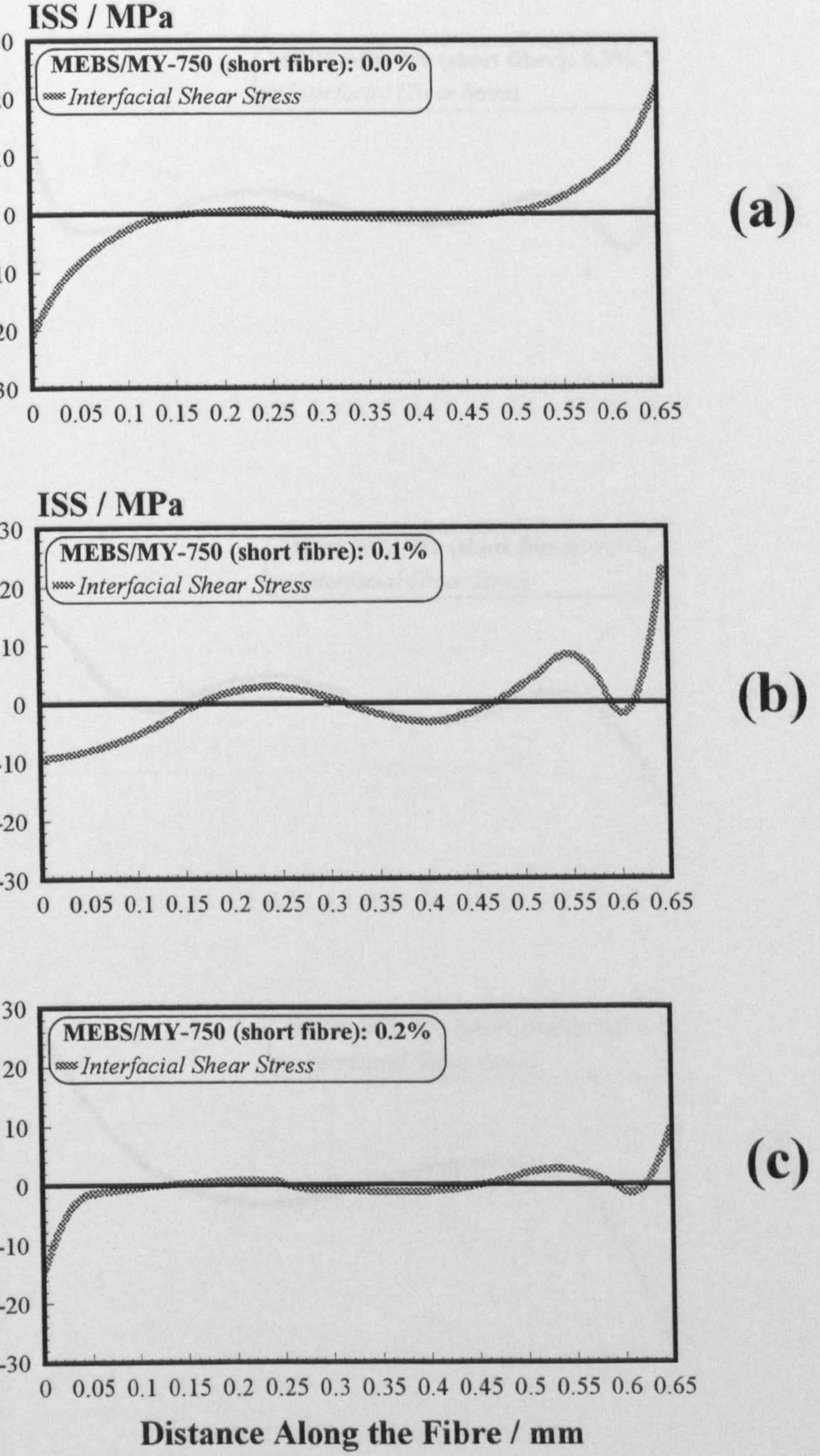

Figure 5.21 MEBS / MY-750 (short fibre coupon) (a-c): interfacial shear stress (ISS) distributions along the fibre length.

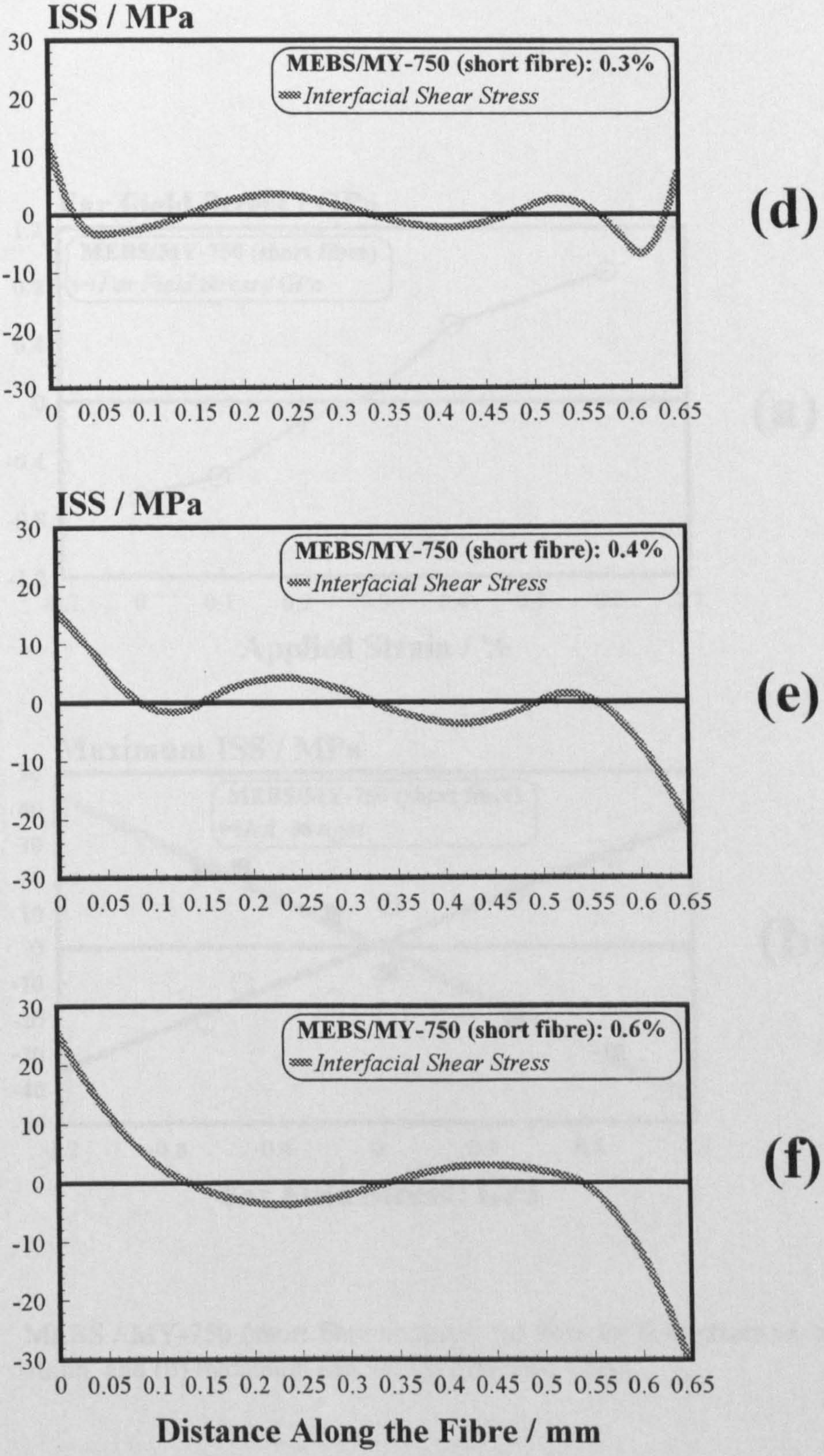

Figure 5.21 MEBS / MY-750 (short fibre coupon) (d-f): interfacial shear stress (ISS) distributions along the fibre length.

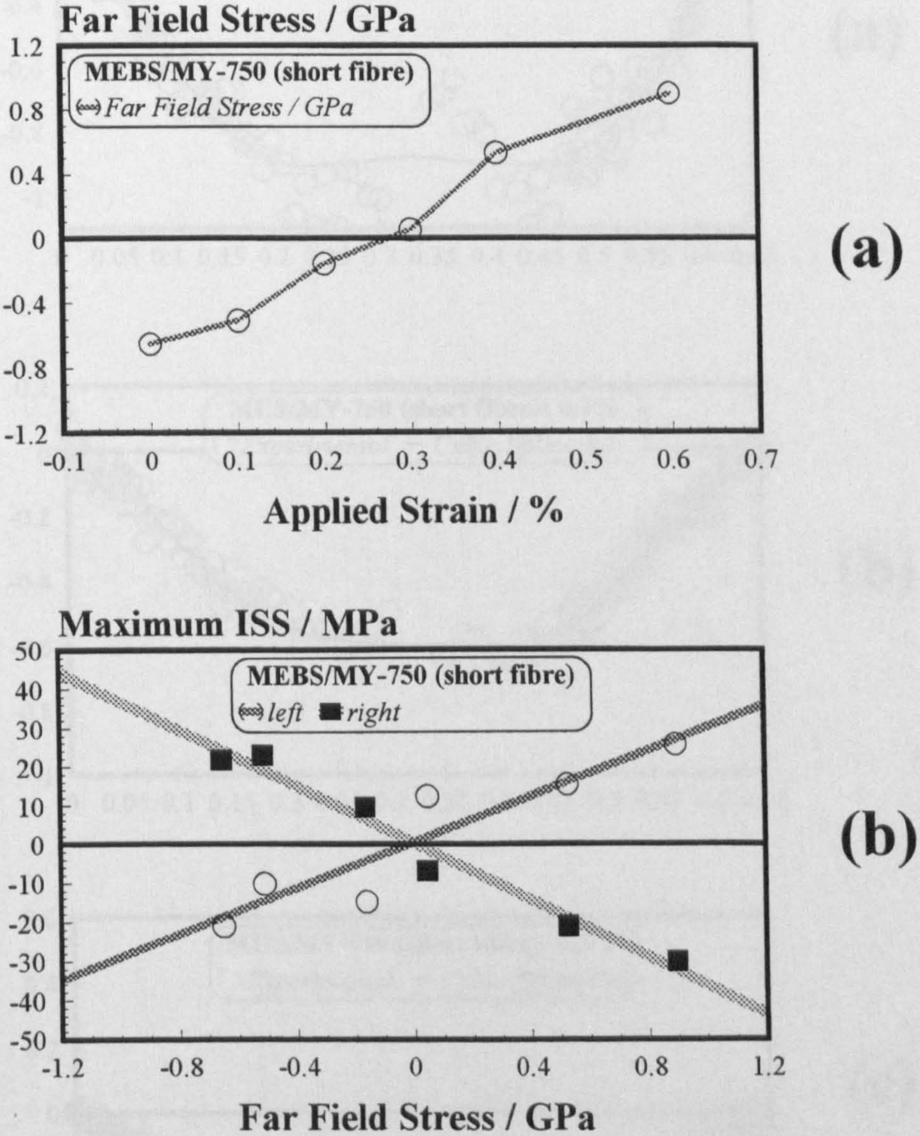

Figure 5.22 MEBS / MY-750 (short fibre coupon): (a) fibre far field stress vs. applied strain, and (b) maximum ISS vs. fibre far field stress.

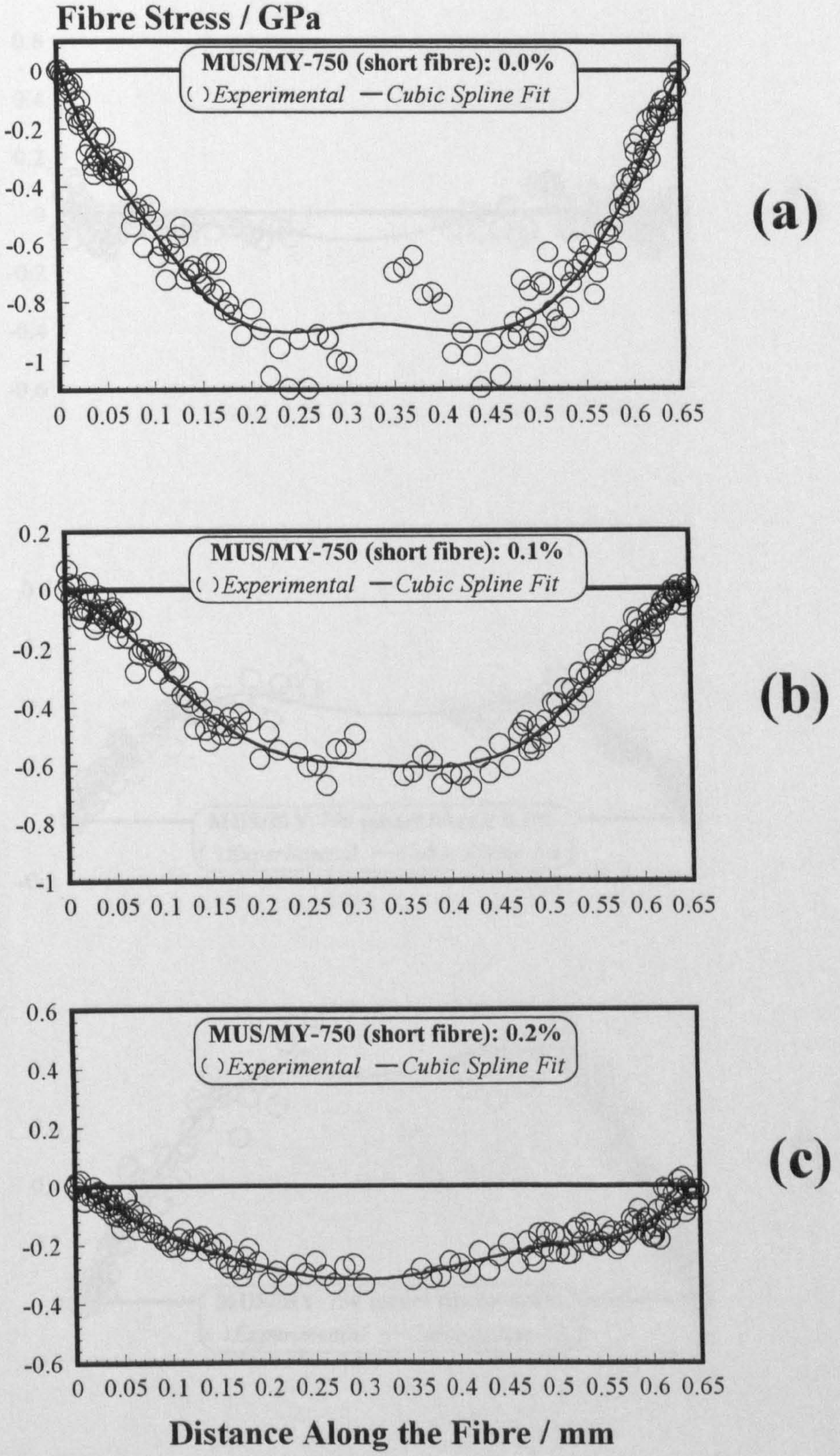

Figure 5.23 MUS / MY-750 (short fibre coupon): (a-c) Axial stress profiles along the fibre length.

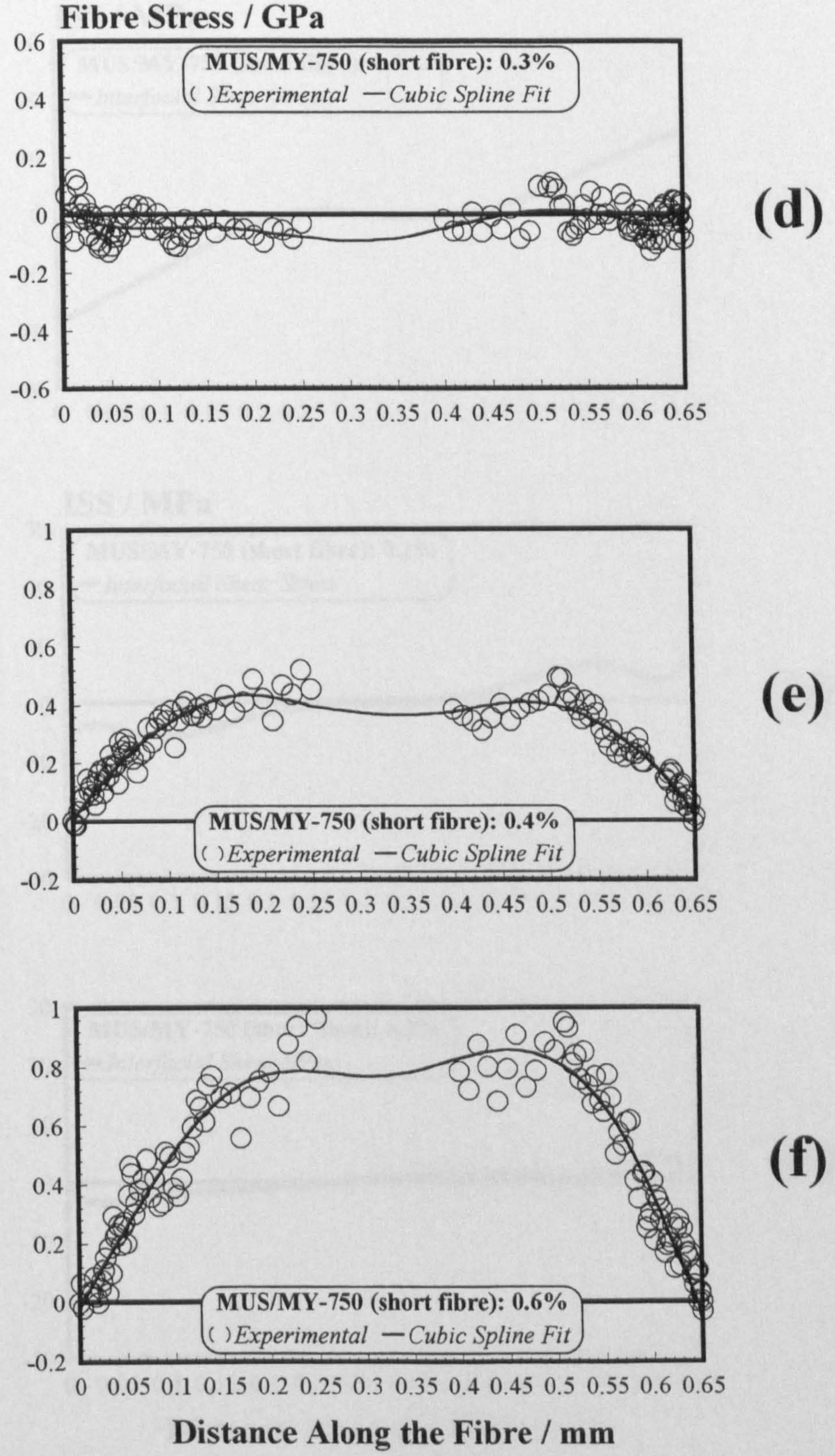

Figure 5.23 MUS / MY-750 (short fibre coupon): (d-f) Axial stress profiles along the fibre length.

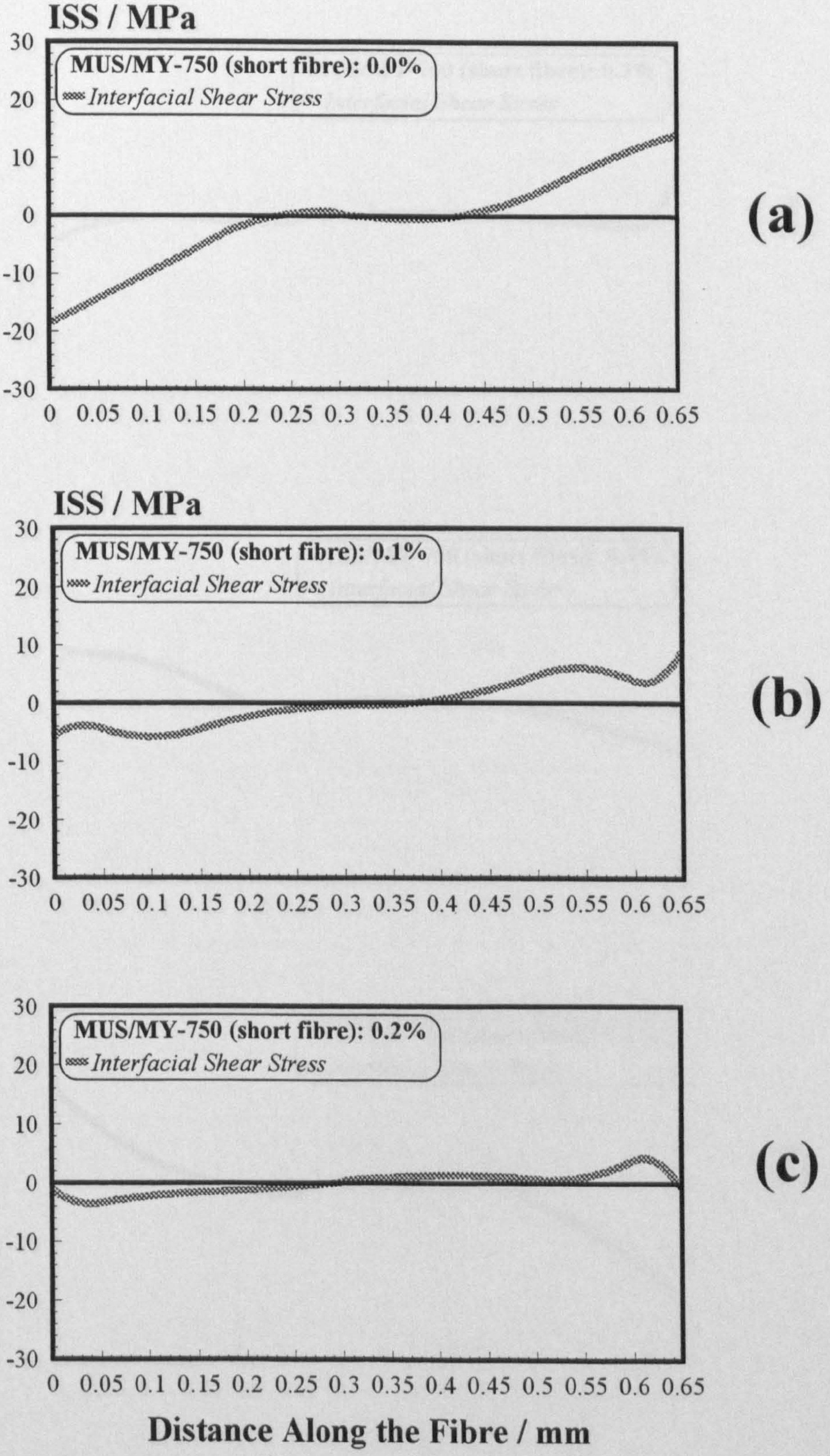

Figure 5.24 MUS / MY-750 (short fibre coupon): (a-c)(interfacial shear stress (ISS) distributions along the fibre length.

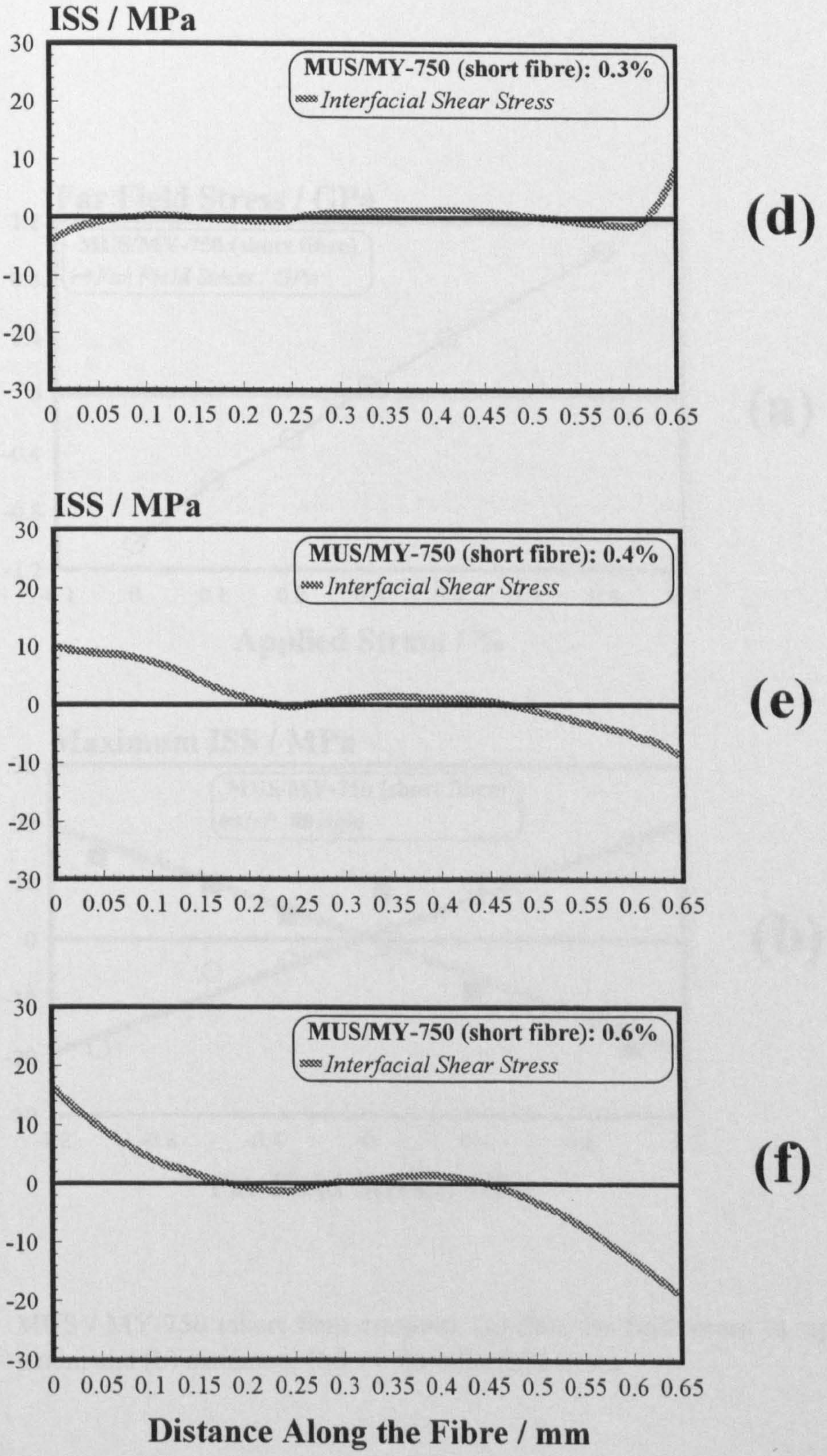

Figure 5.24 MUS / MY-750 (short fibre coupon): (d-f) interfacial shear stress (ISS) distributions along the fibre length.

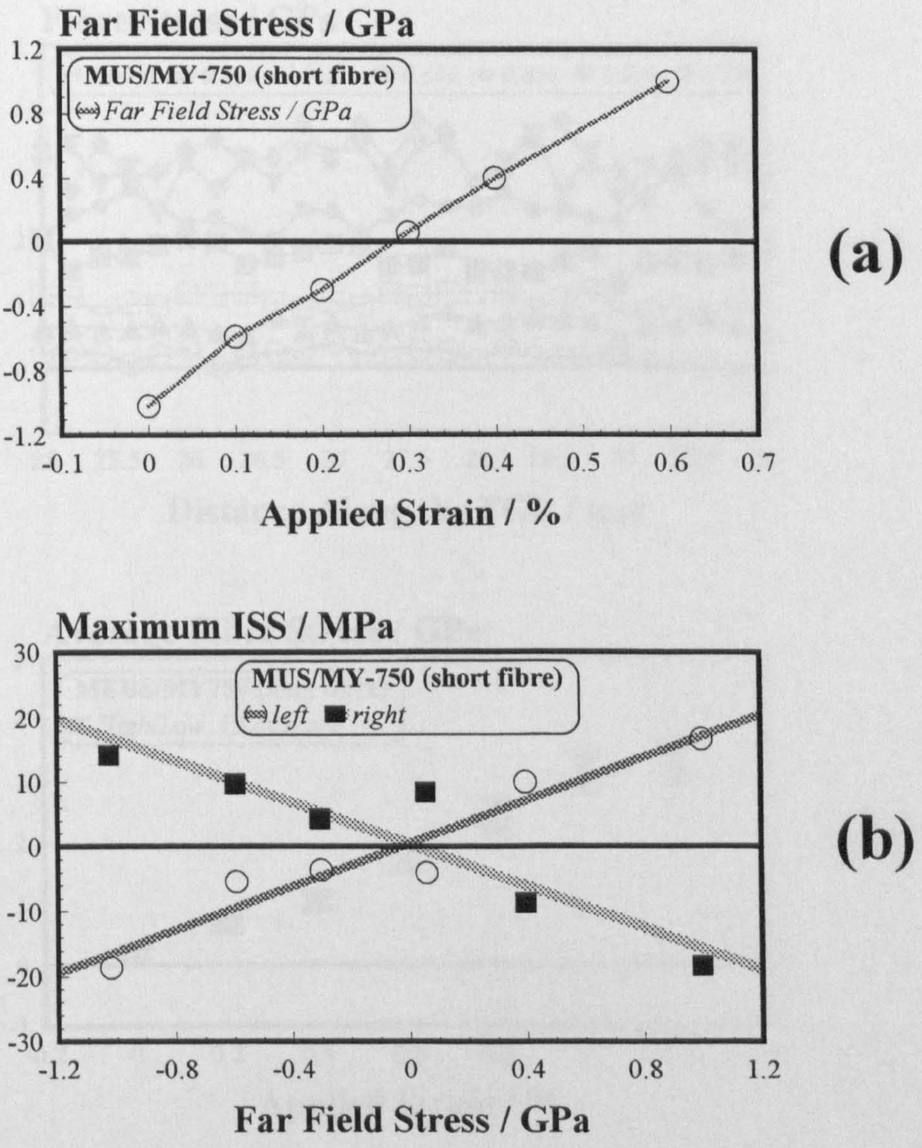

Figure 5.25 MUS / MY-750 (short fibre coupon): (a) fibre far field stress vs. applied strain, and (b) maximum ISS vs. fibre far field stress.

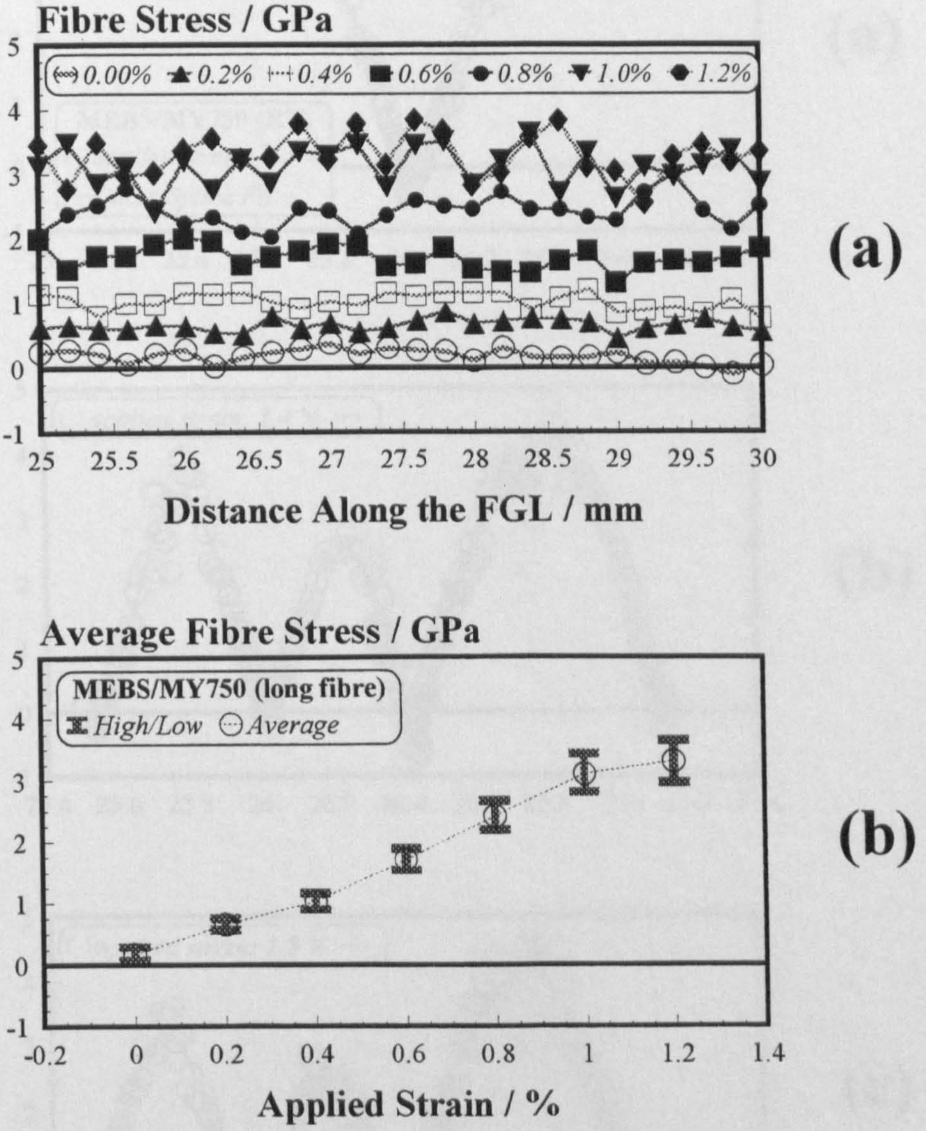

Figure 5.26 MEBS / MY-750 (long fibre coupon at RT): (a) axial stress distributions prior to fracture, (b) average stress vs. applied strain prior to fracture.

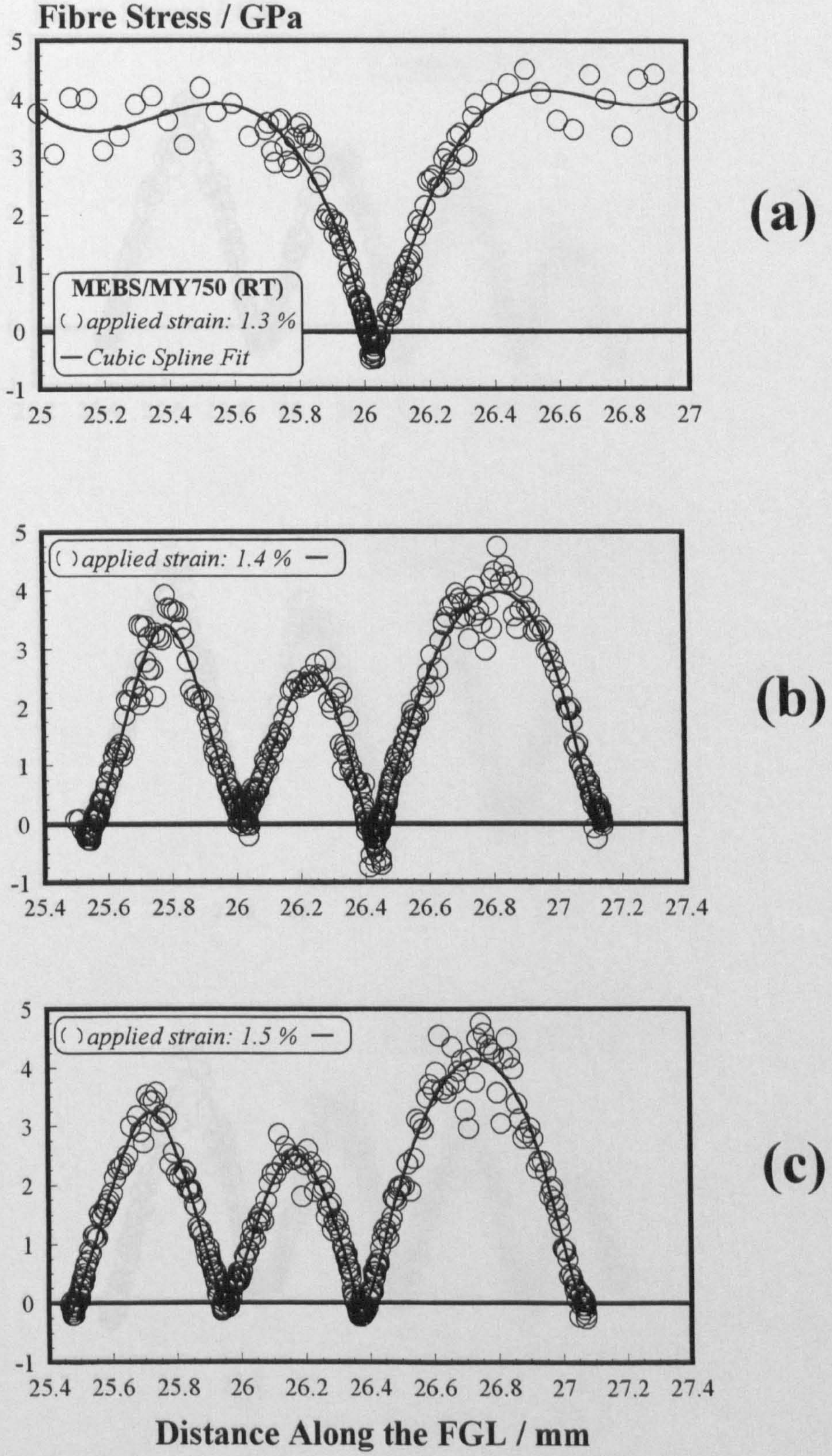

Figure 5.27 MEBS / MY-750 (long fibre coupon at RT): (a-c) axial stress profiles along the fragmentation gauge length.

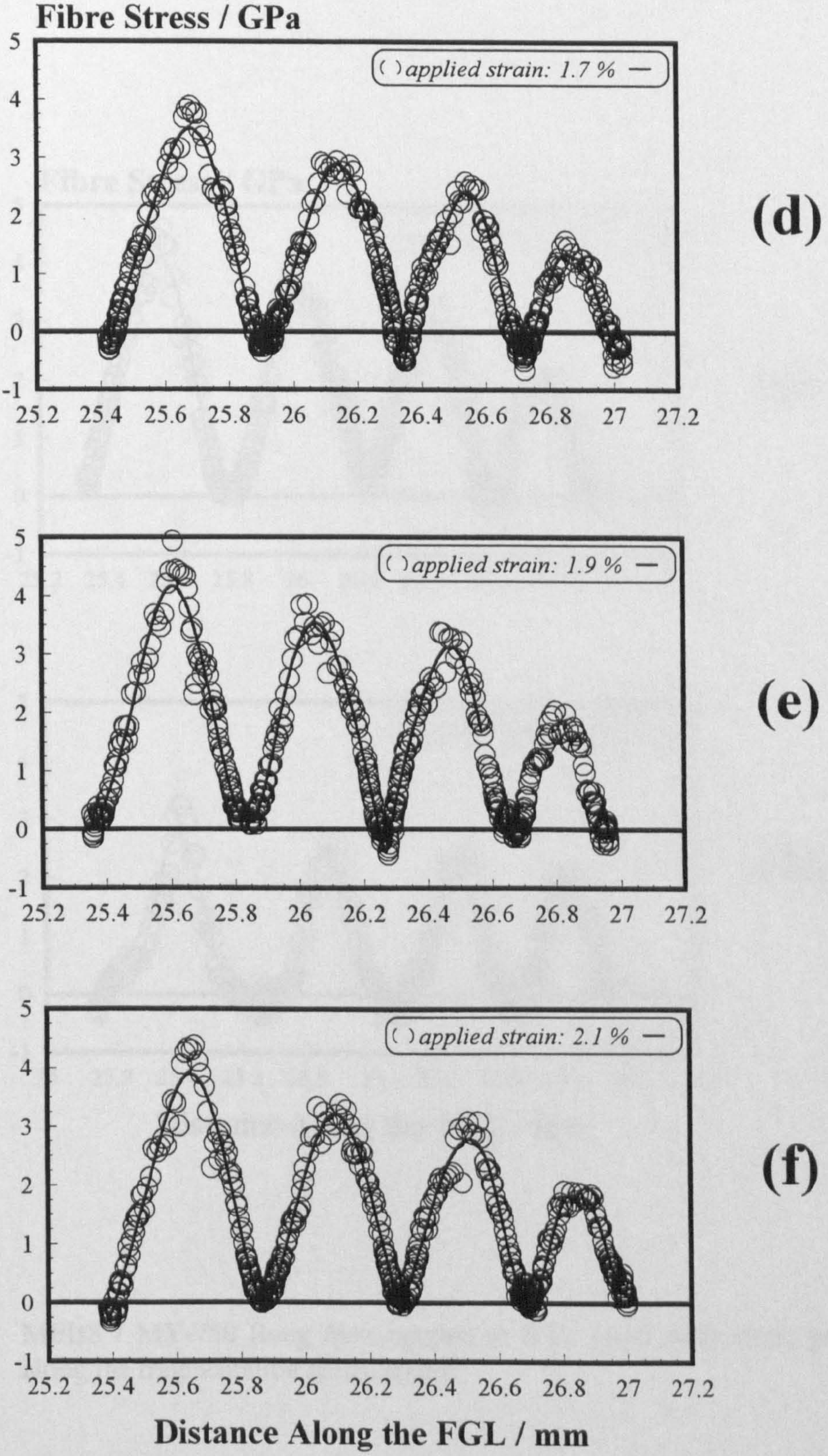

Figure 5.27 MEBS / MY-750 (long fibre coupon at RT): (d-f) axial stress profiles along the fragmentation gauge length.

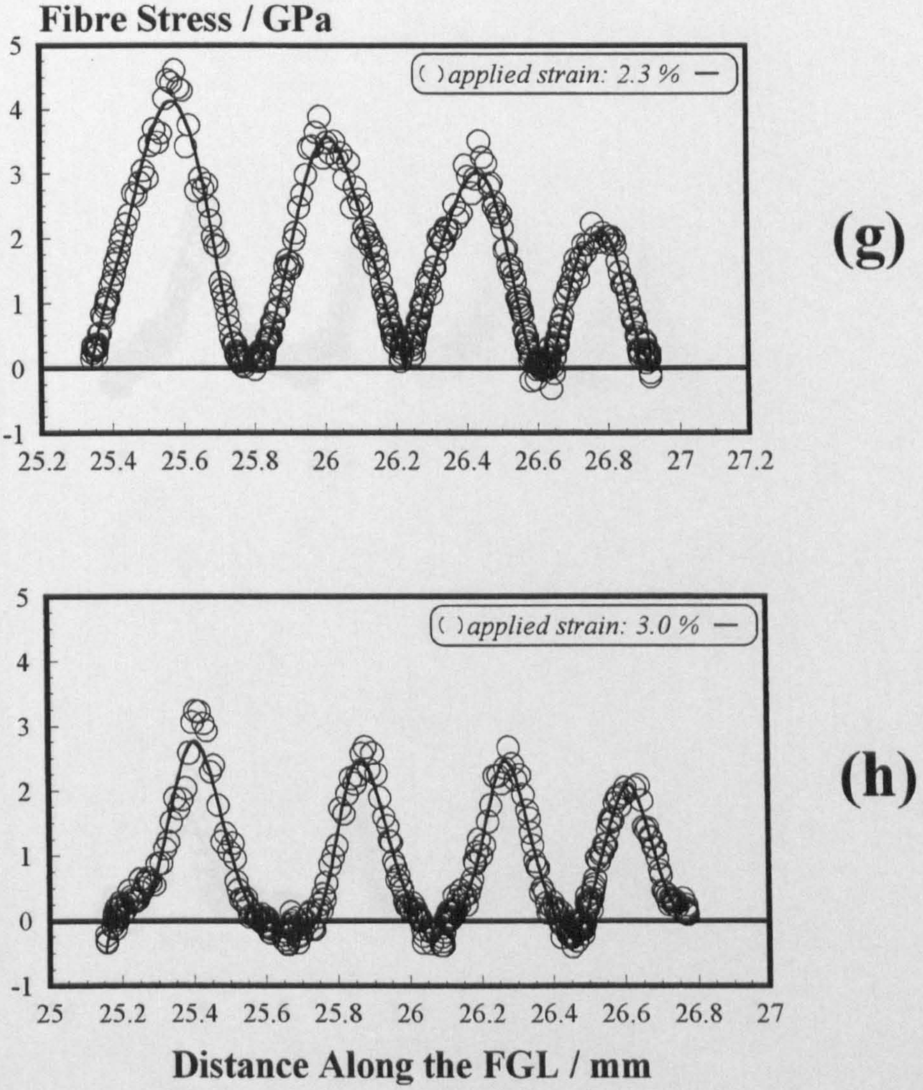

Figure 5.27 MEBS / MY-750 (long fibre coupon at RT): (g-h) axial stress profiles along the fragmentation gauge length.

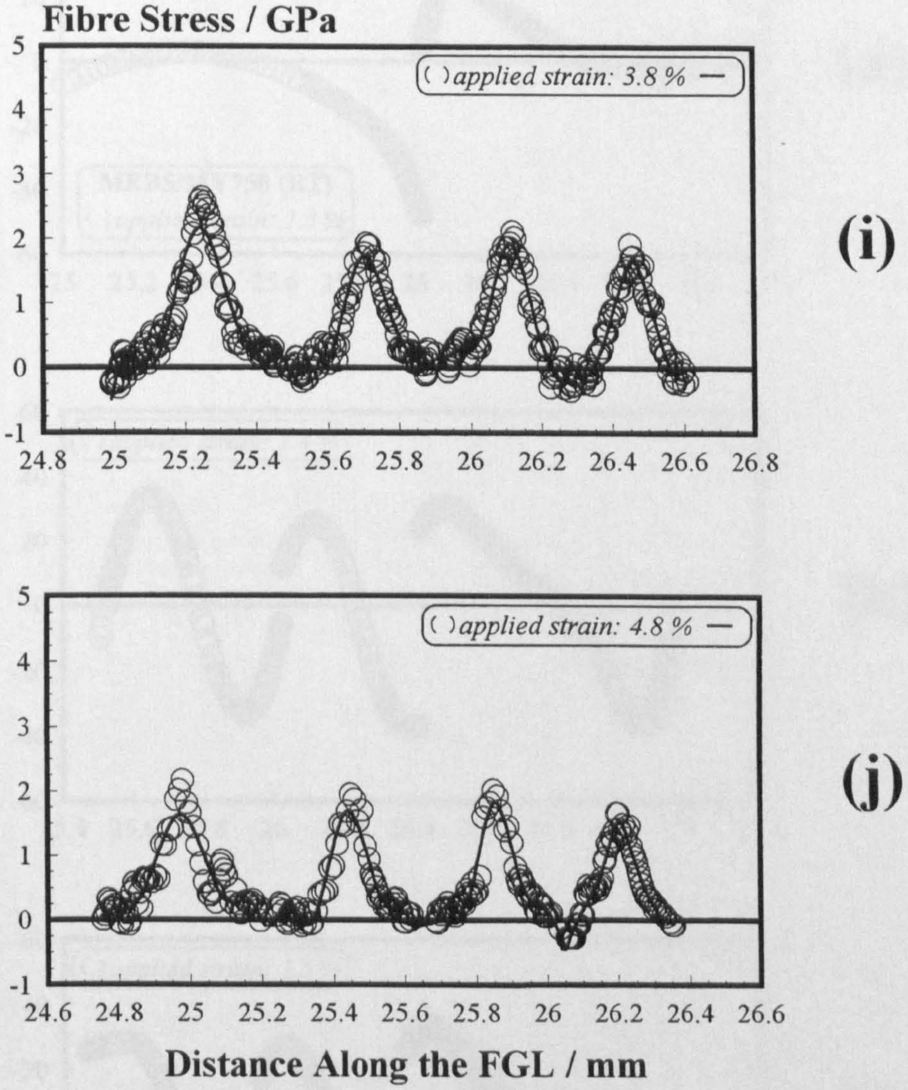

Figure 5.27 MEBS / MY-750 (long fibre coupon at RT): (i-j) axial stress profiles along the fragmentation gauge length.

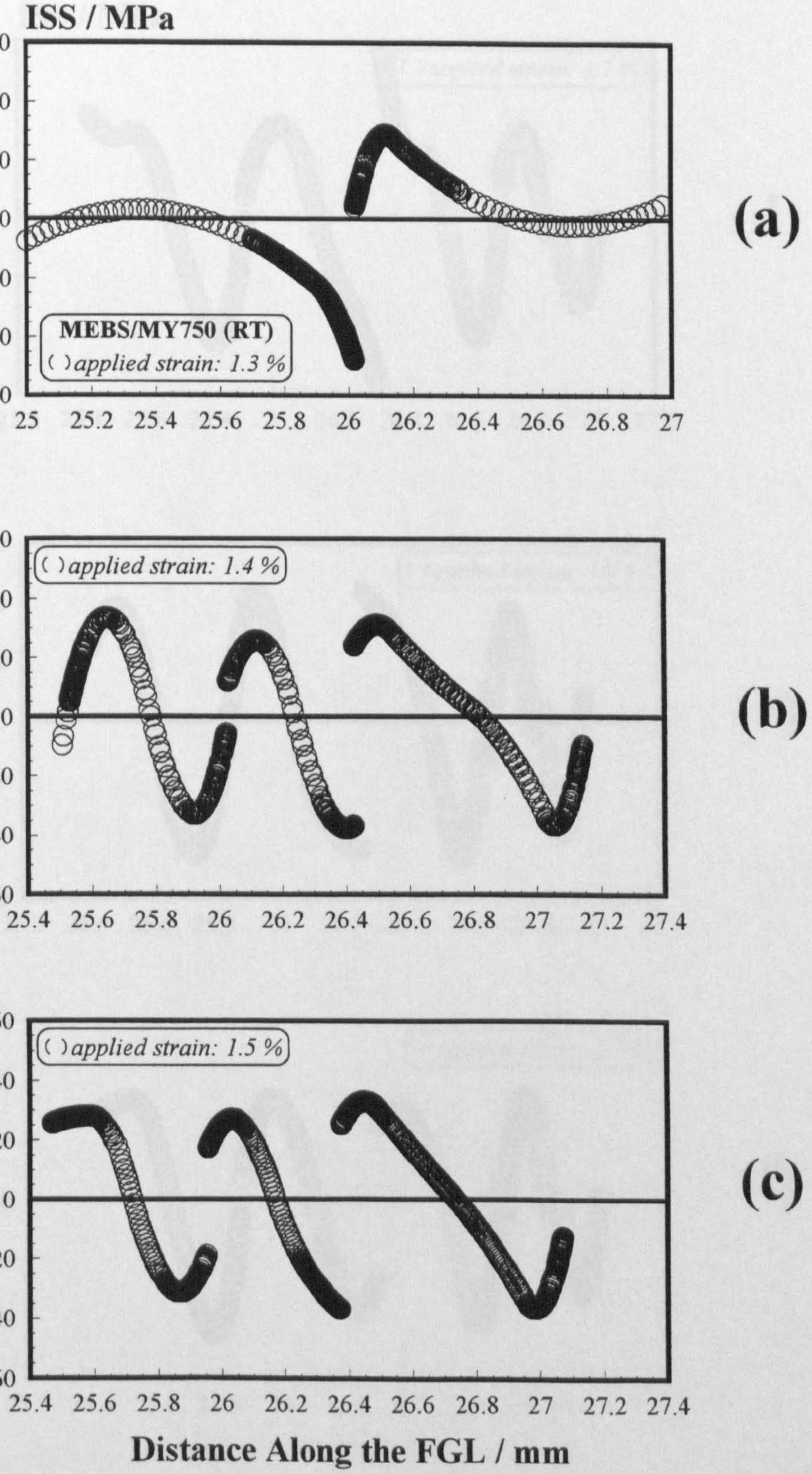

Figure 5.28 MEBS / MY-750 (long fibre coupon at RT): (a-c) interfacial shear stress (ISS) distributions along the fragmentation gauge length.

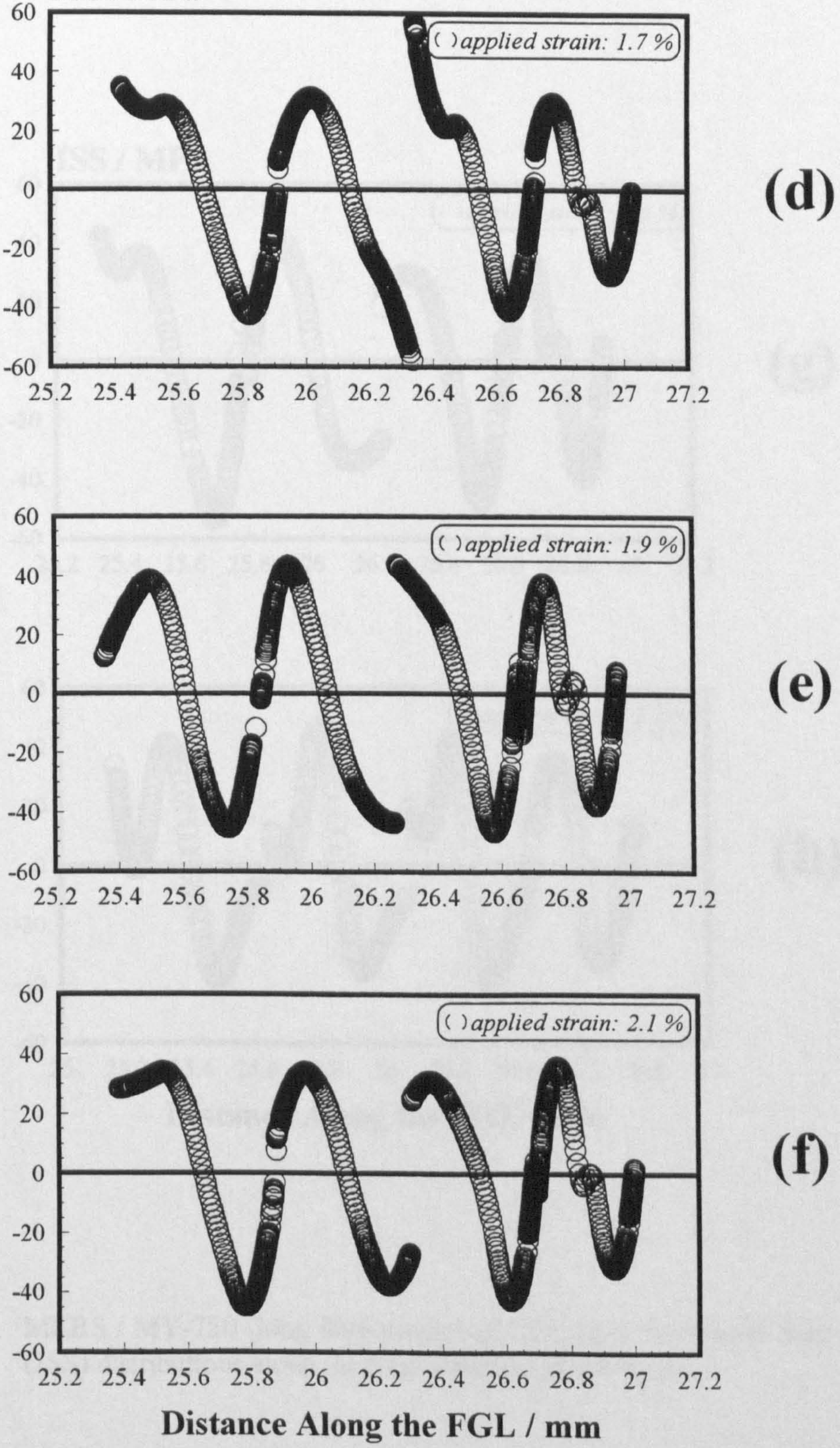

Figure 5.28 MEBS / MY-750 (long fibre coupon at RT): (d-f) interfacial shear stress (ISS) distributions along the fragmentation gauge length.

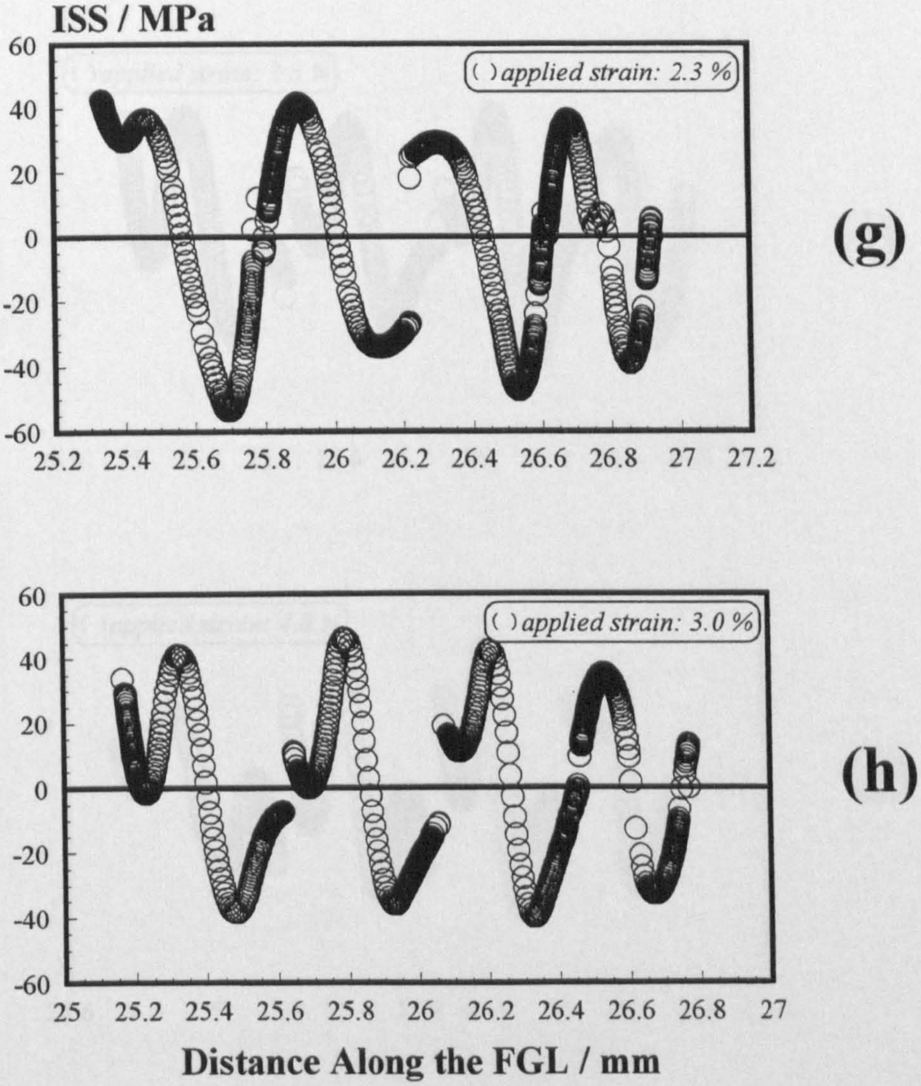

Figure 5.28 MEBS / MY-750 (long fibre coupon at RT): (g-h) interfacial shear stress (ISS) distributions along the fragmentation gauge length.

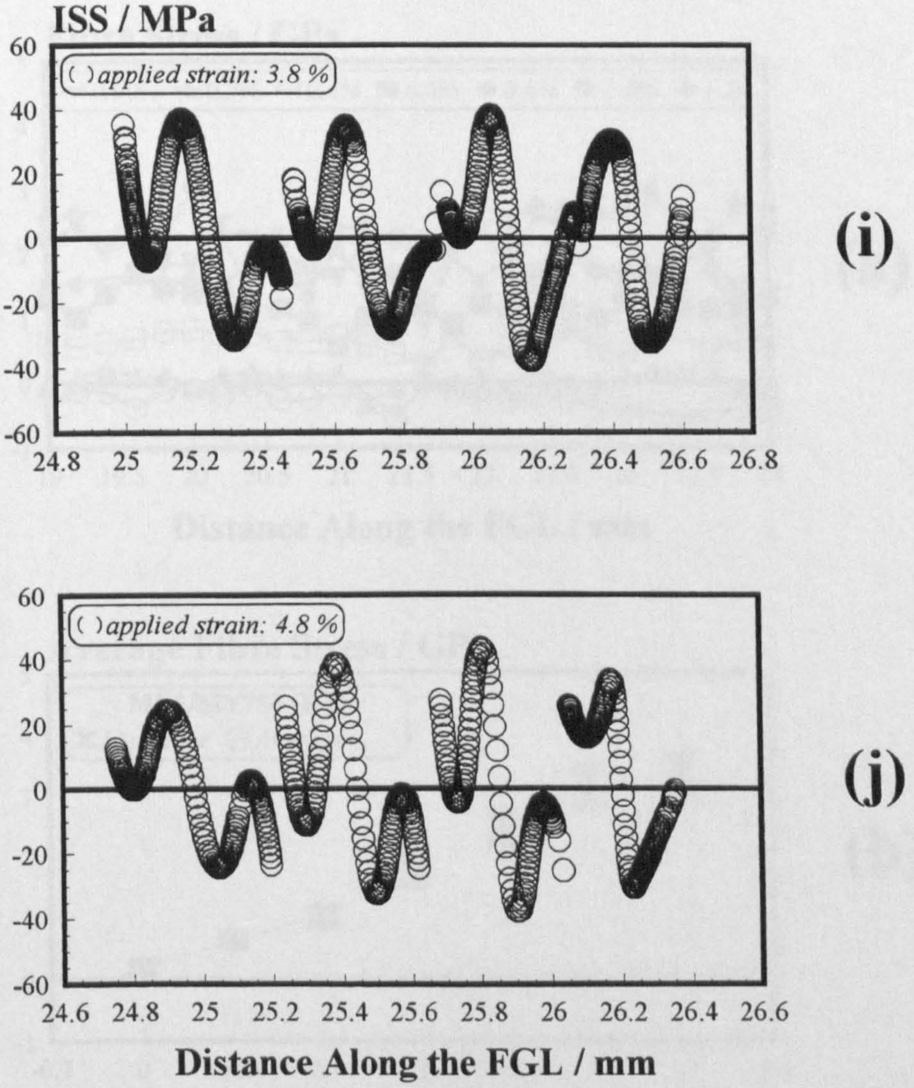

Figure 5.28 MEBS / MY-750 (long fibre coupon at RT): (i-j) interfacial shear stress (ISS) distributions along the fragmentation gauge length.

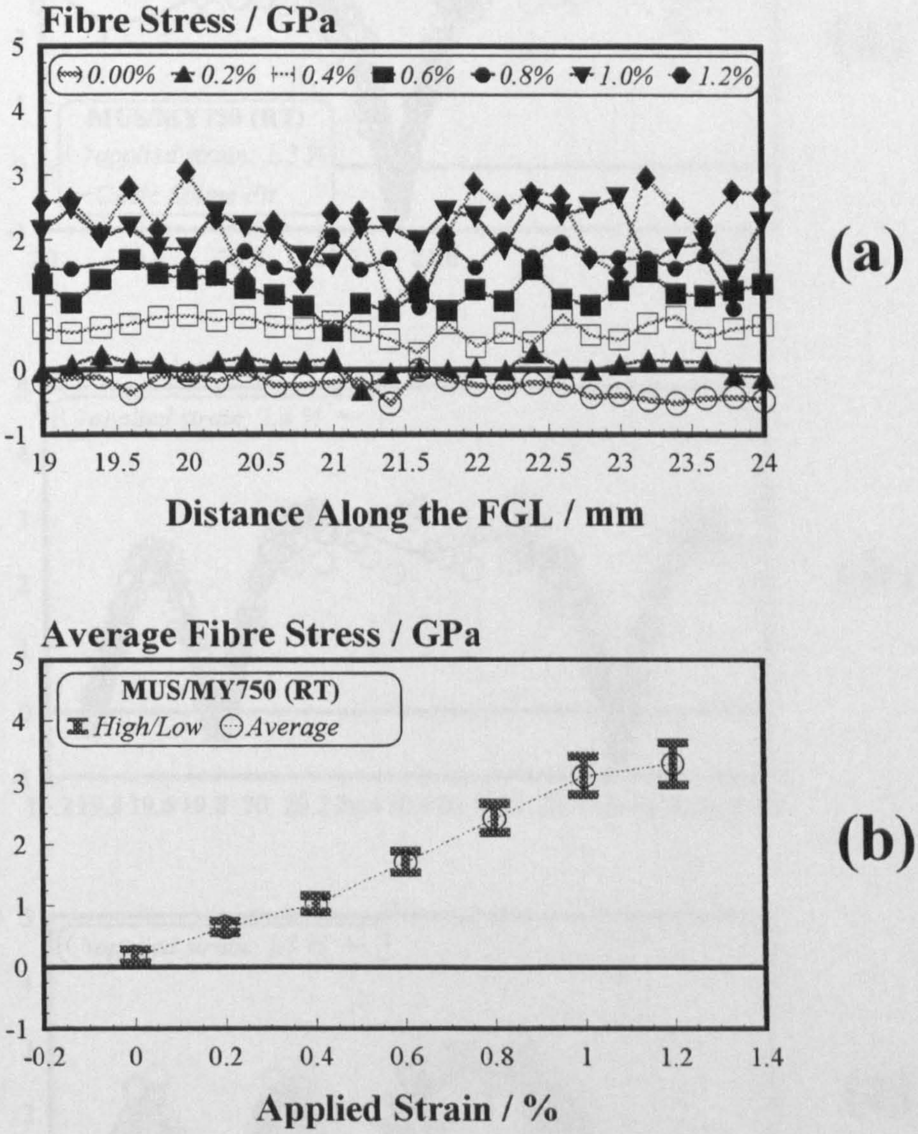

Figure 5.29 MUS / MY-750 (long fibre coupon at RT): (a) axial stress distributions prior to fracture, (b) average stress vs. applied strain prior to fracture.

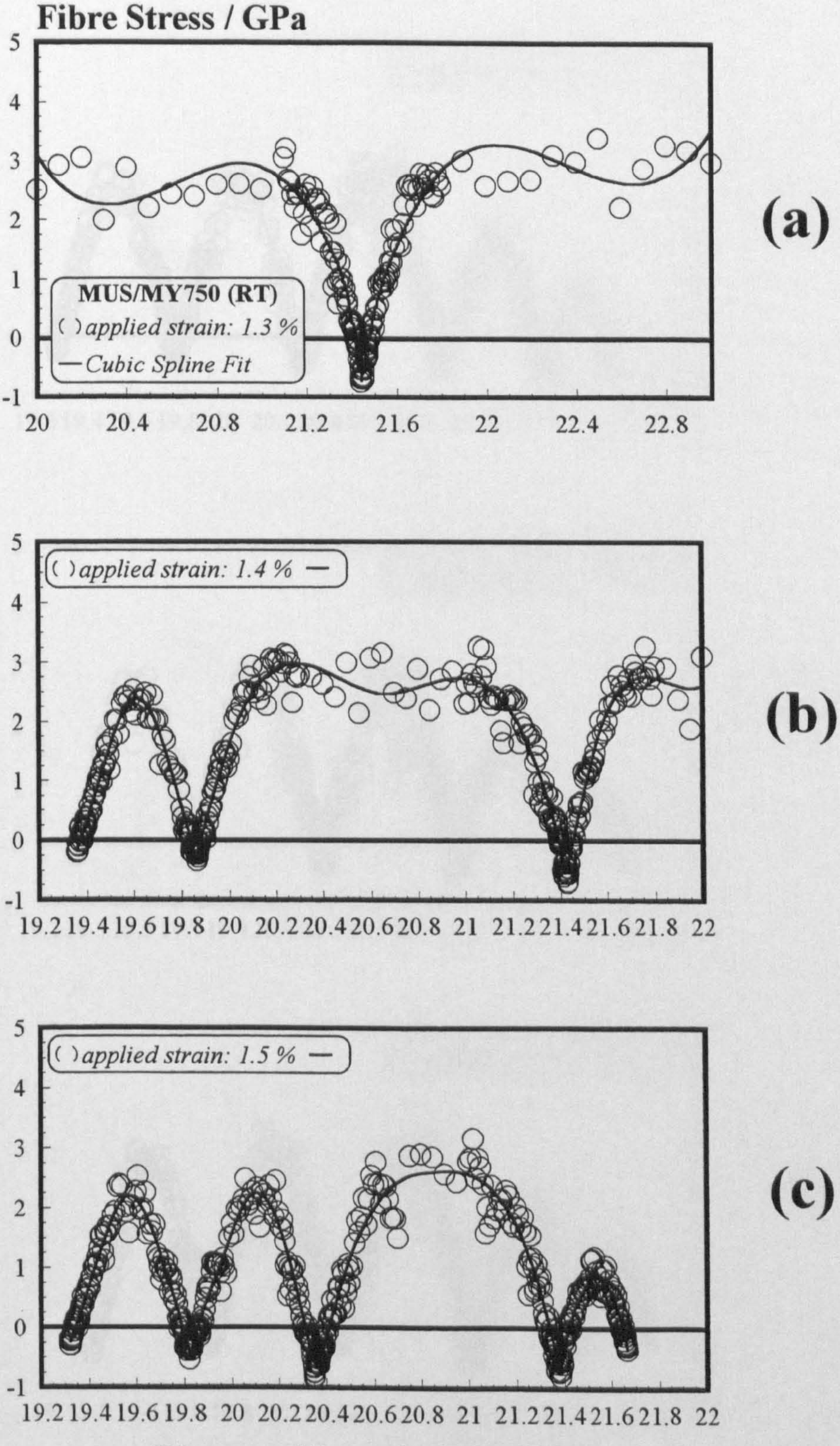

Figure 5.30 MUS / MY-750 (long fibre coupon at RT): (a-c) axial stress profiles along the fragmentation gauge length.

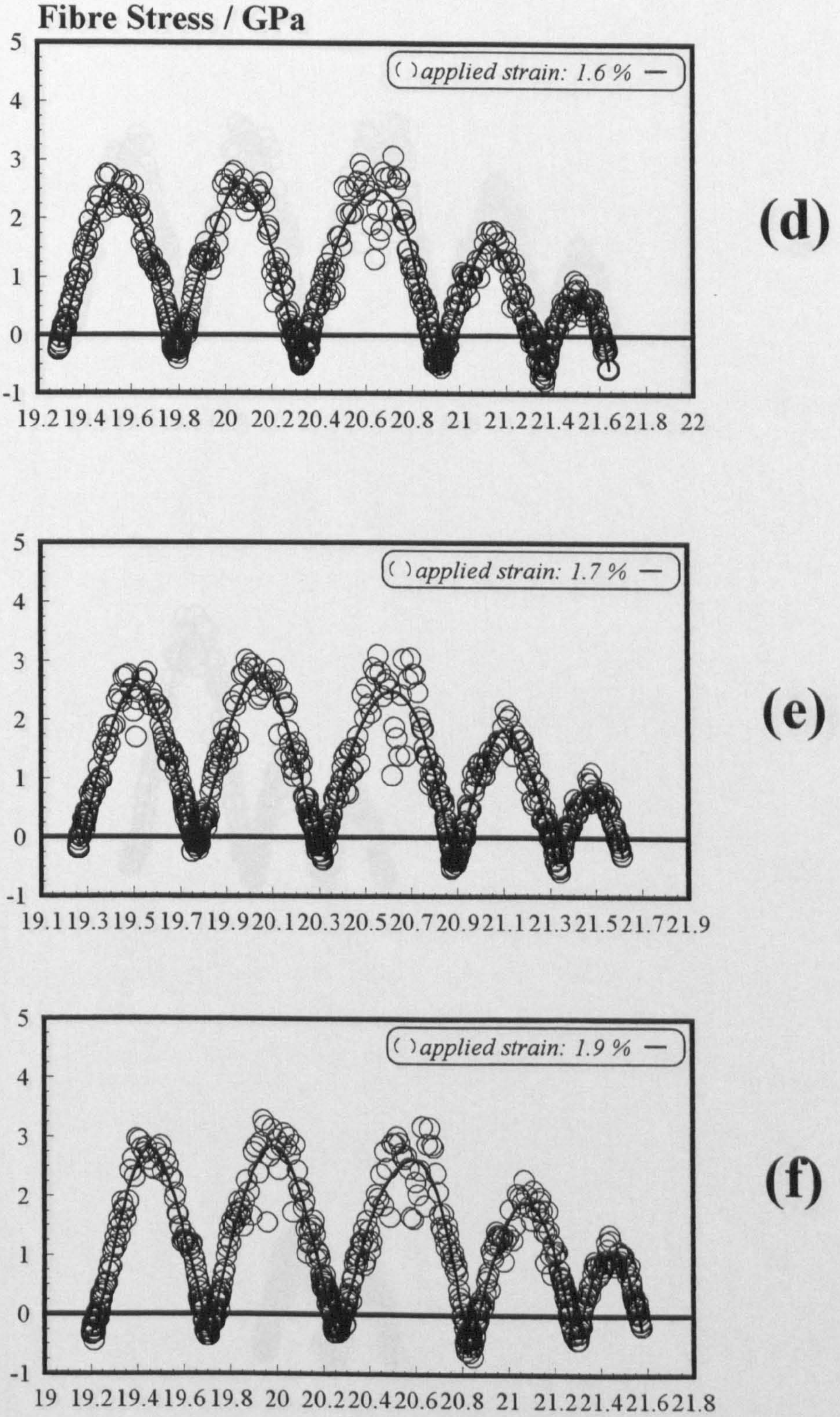

Figure 5.30 MUS / MY-750 (long fibre coupon at RT): (d-f) axial stress profiles along the fragmentation gauge length.

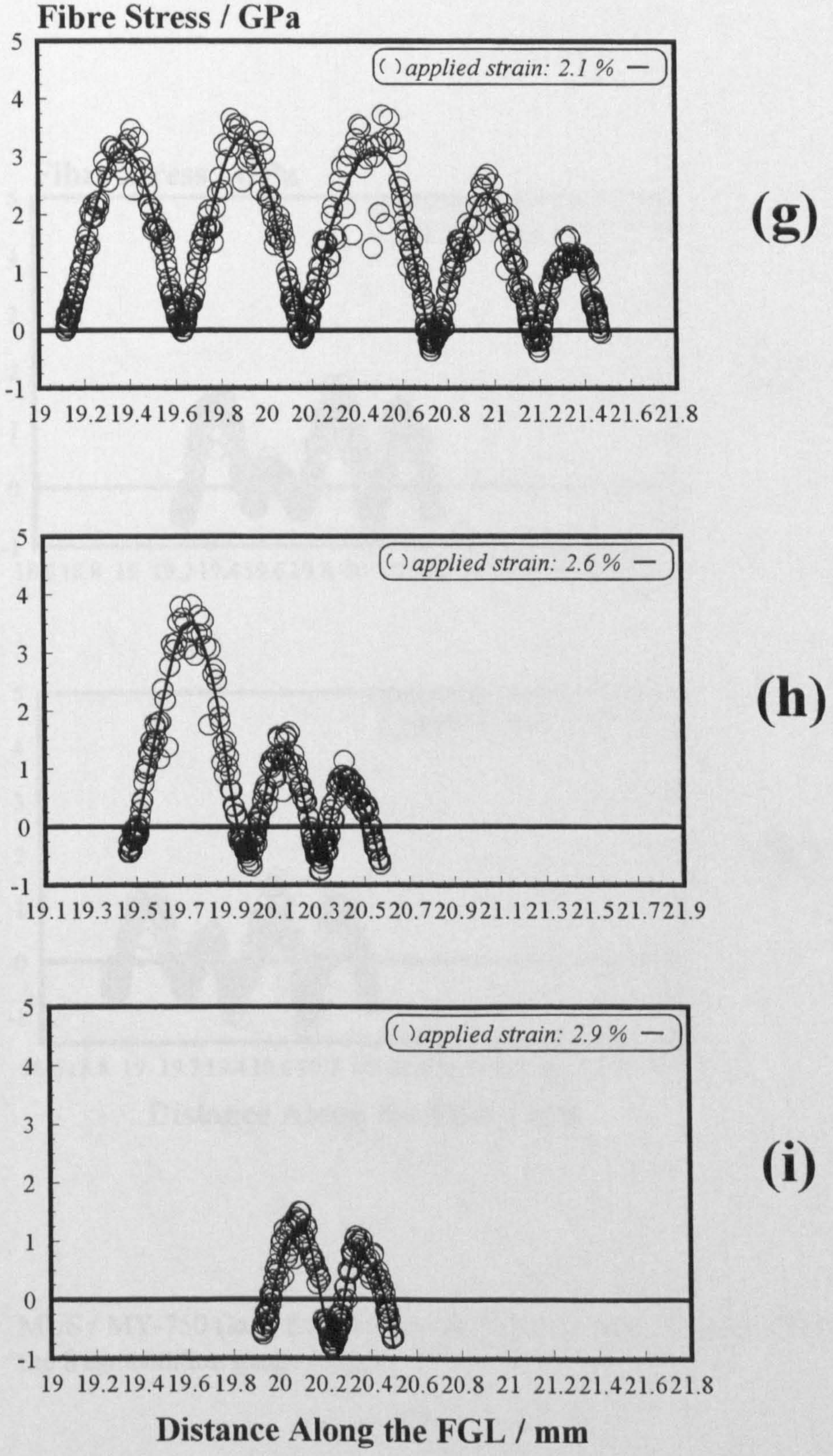

Figure 5.30 MUS / MY-750 (long fibre coupon at RT): (g-i) axial stress profiles along the fragmentation gauge length.

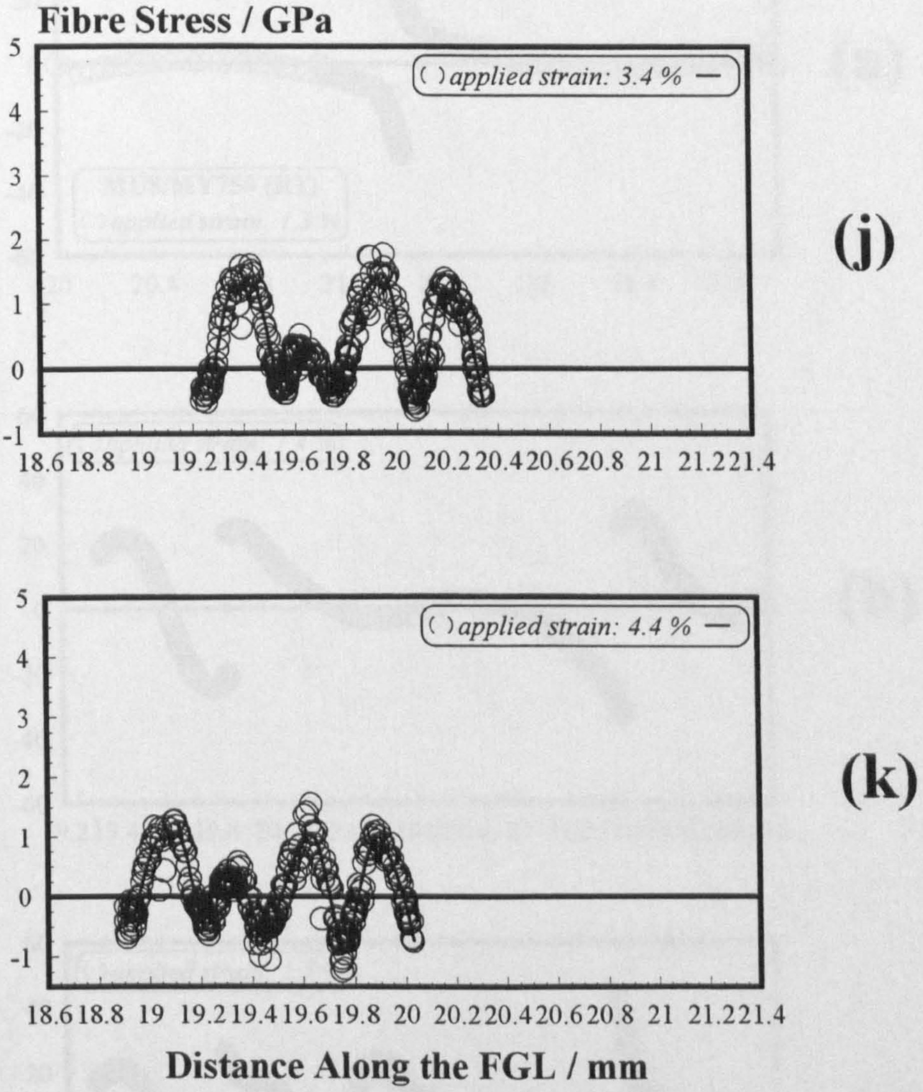

Figure 5.30 MUS / MY-750 (long fibre coupon at RT): (j-k) axial stress profiles along the fragmentation gauge length.

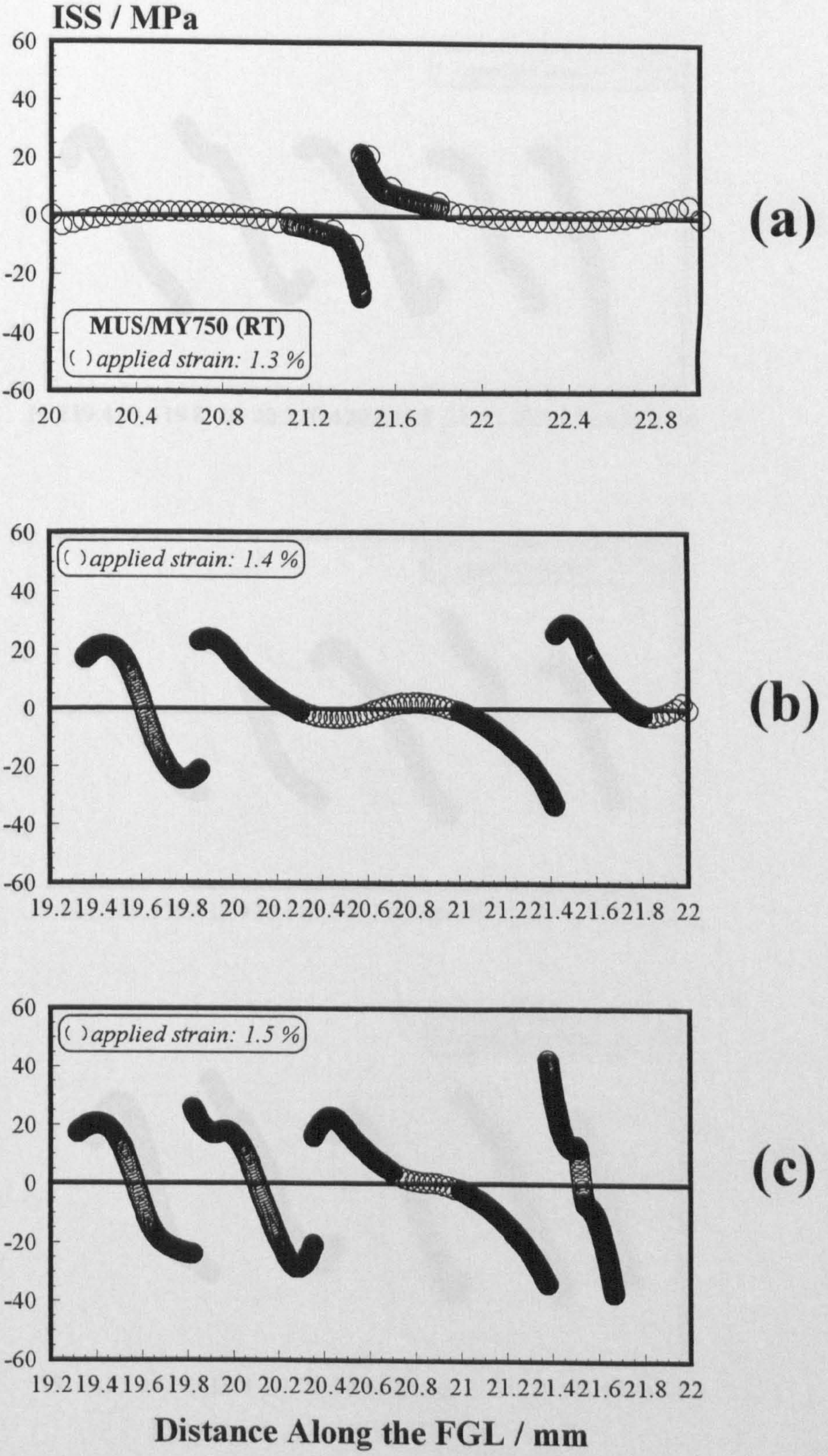

Figure 5.31 MUS / MY-750 (long fibre coupon at RT): (a-c) interfacial shear stress (ISS) distribution along the fragmentation gauge length.

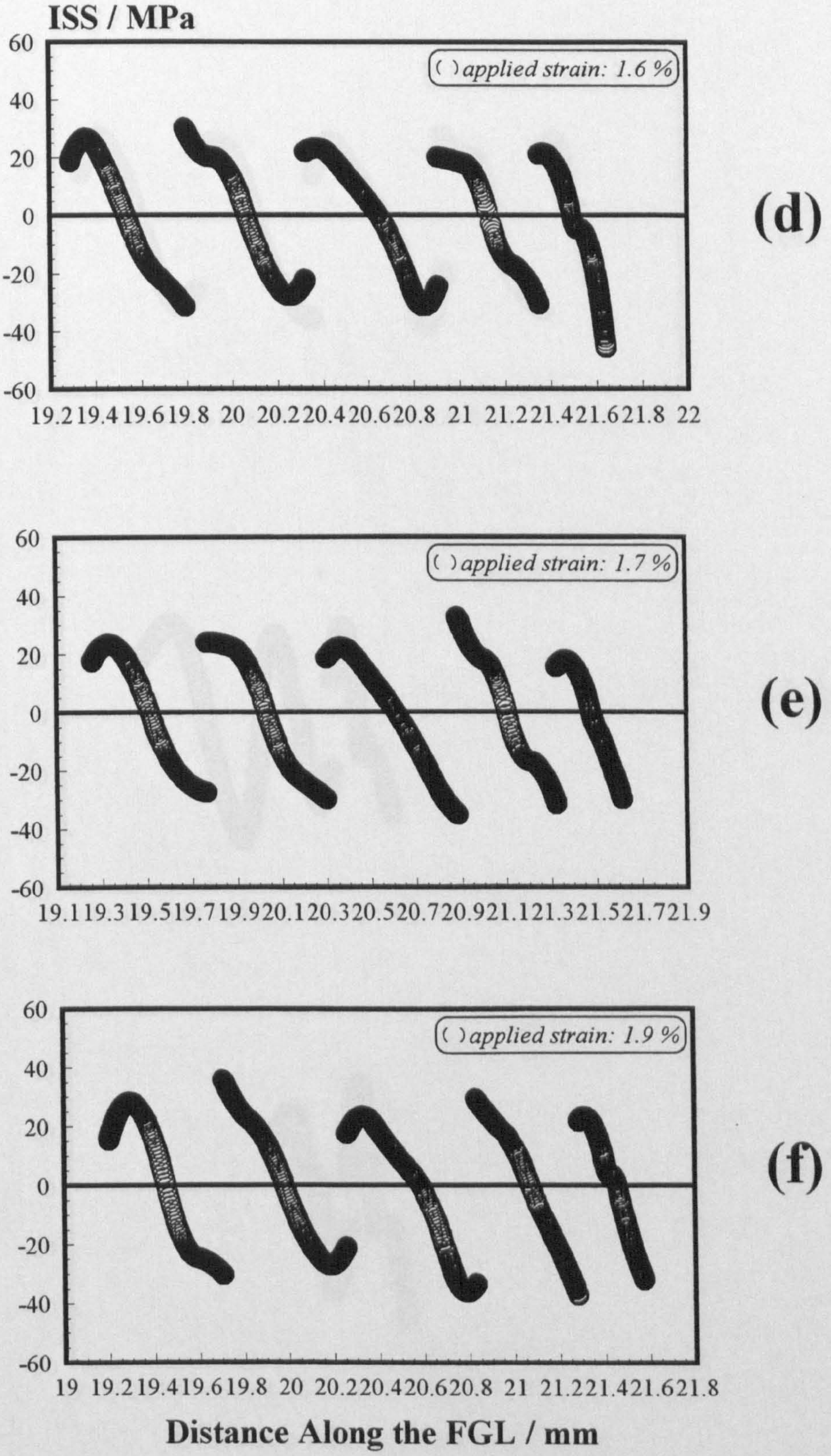

Figure 5.31 MUS / MY-750 (long fibre coupon at RT): (d-f) interfacial shear stress (ISS) distribution along the fragmentation gauge length.

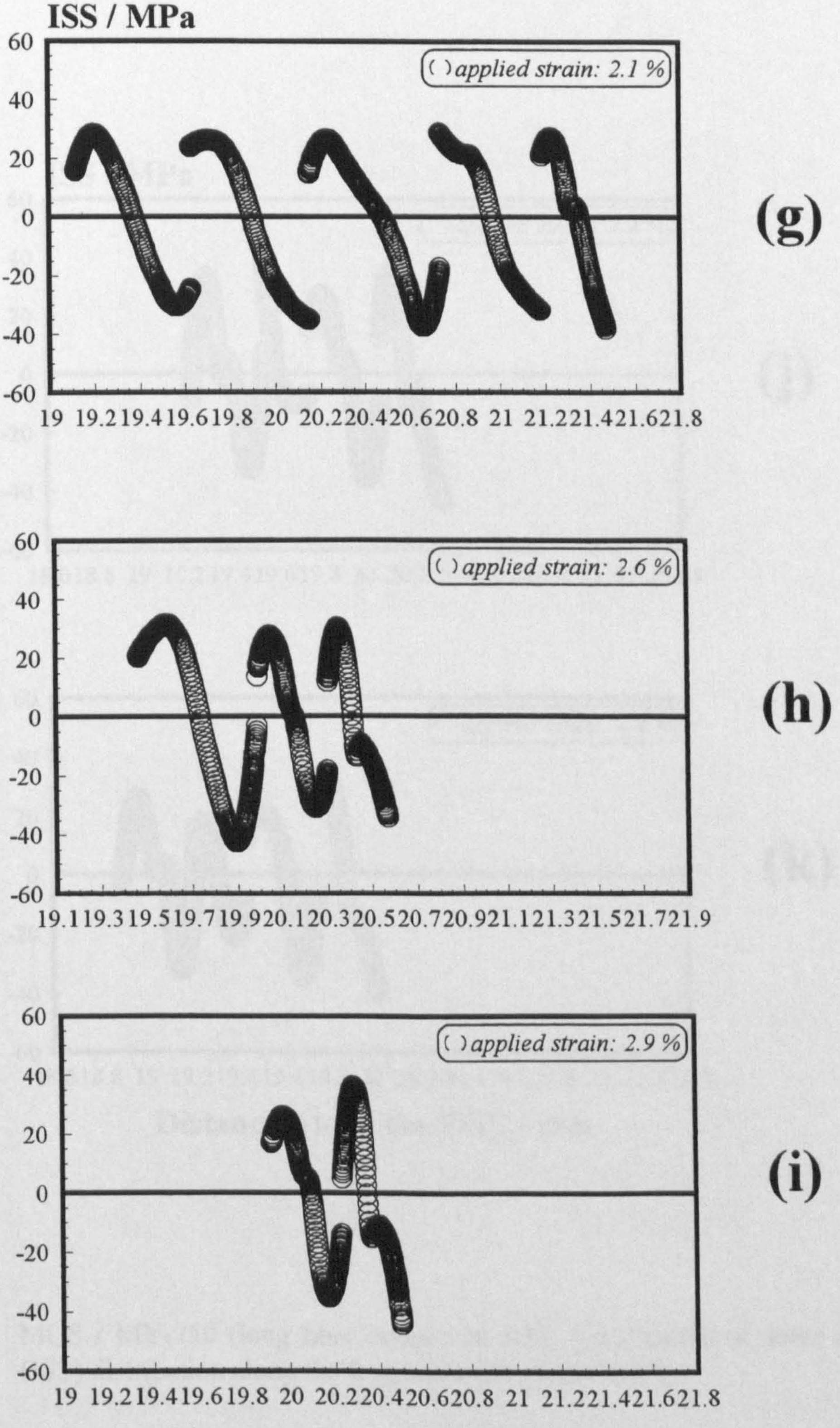

Figure 5.31 MUS / MY-750 (long fibre coupon at RT): (g-i) interfacial shear stress (ISS) distribution along the fragmentation gauge length.

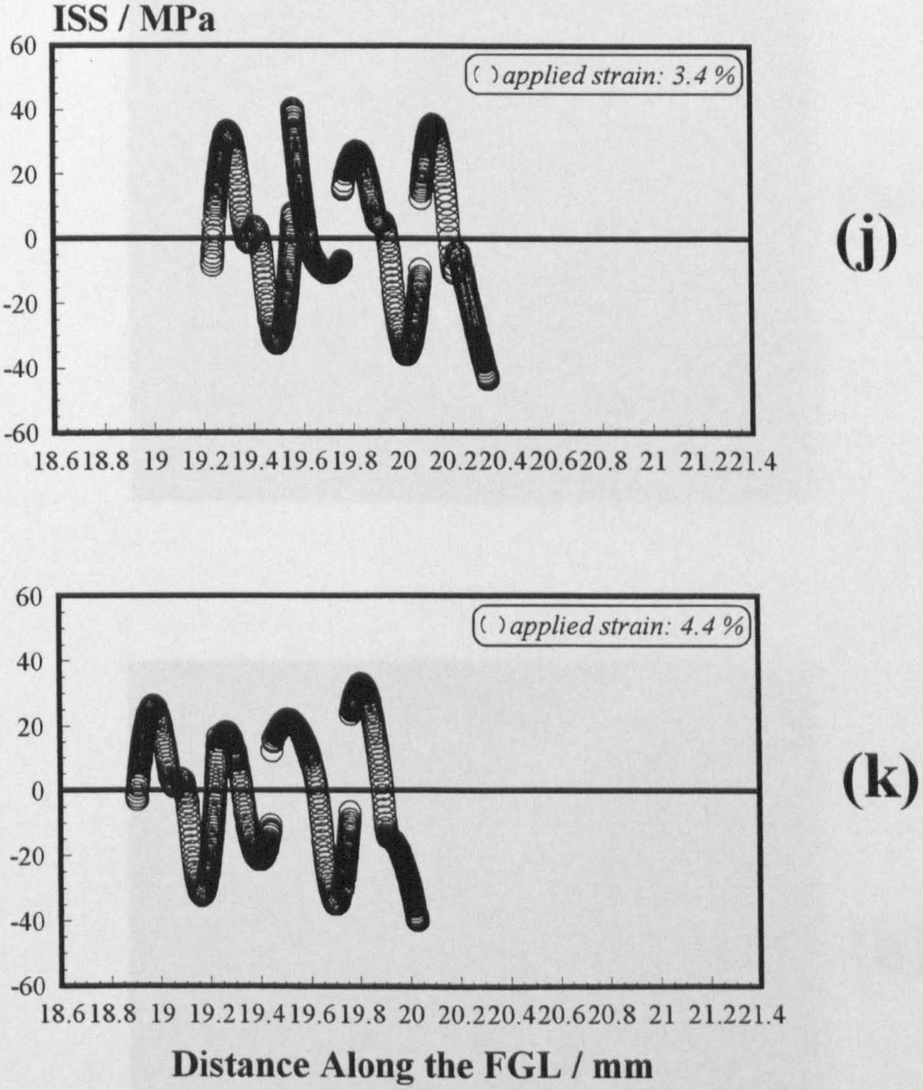

Figure 5.31 MUS / MY-750 (long fibre coupon at RT): (j-k) interfacial shear stress (ISS) distribution along the fragmentation gauge length.

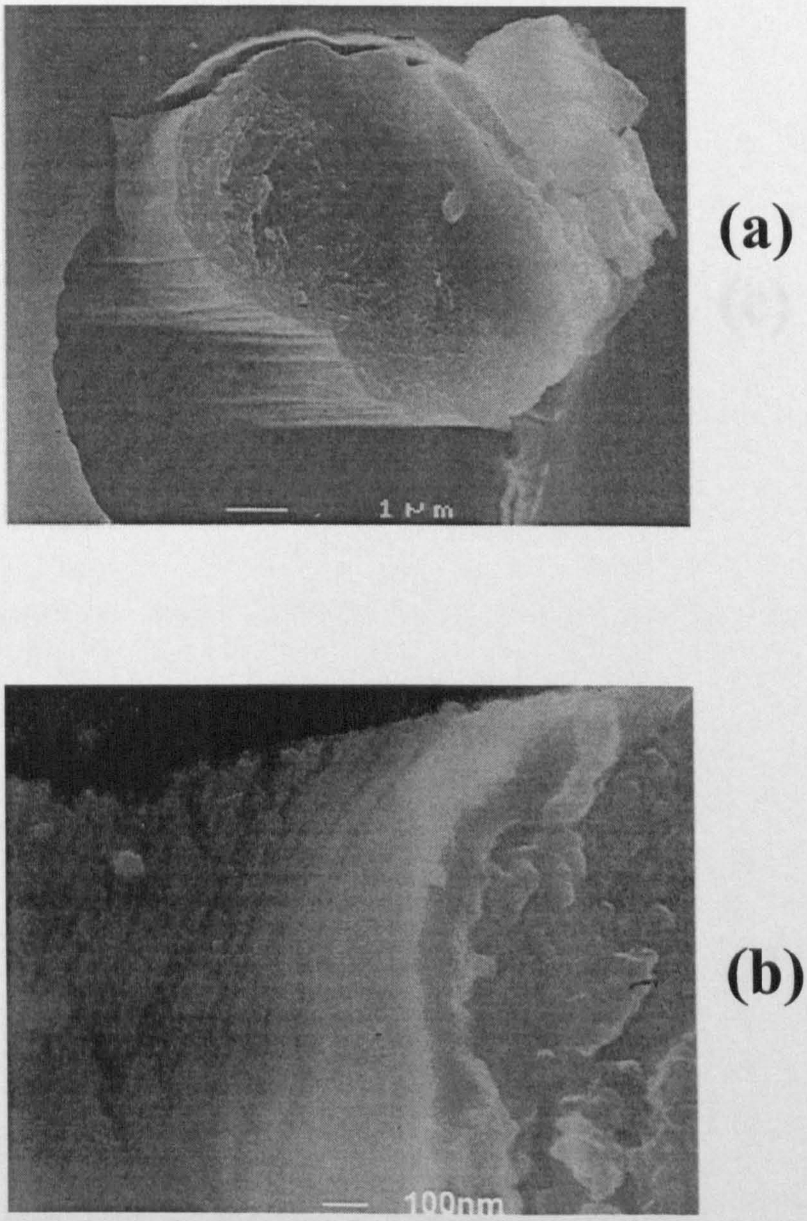

Figure 5.32 (a) SEM micrograph of the fracture surface of the sized MEBS / MY-750 system. A bright resinous layer is clearly visible surrounding the fibre, (b) characteristic ripples due to a thin resin layer on the surface of the MEBS / MY-750 system.

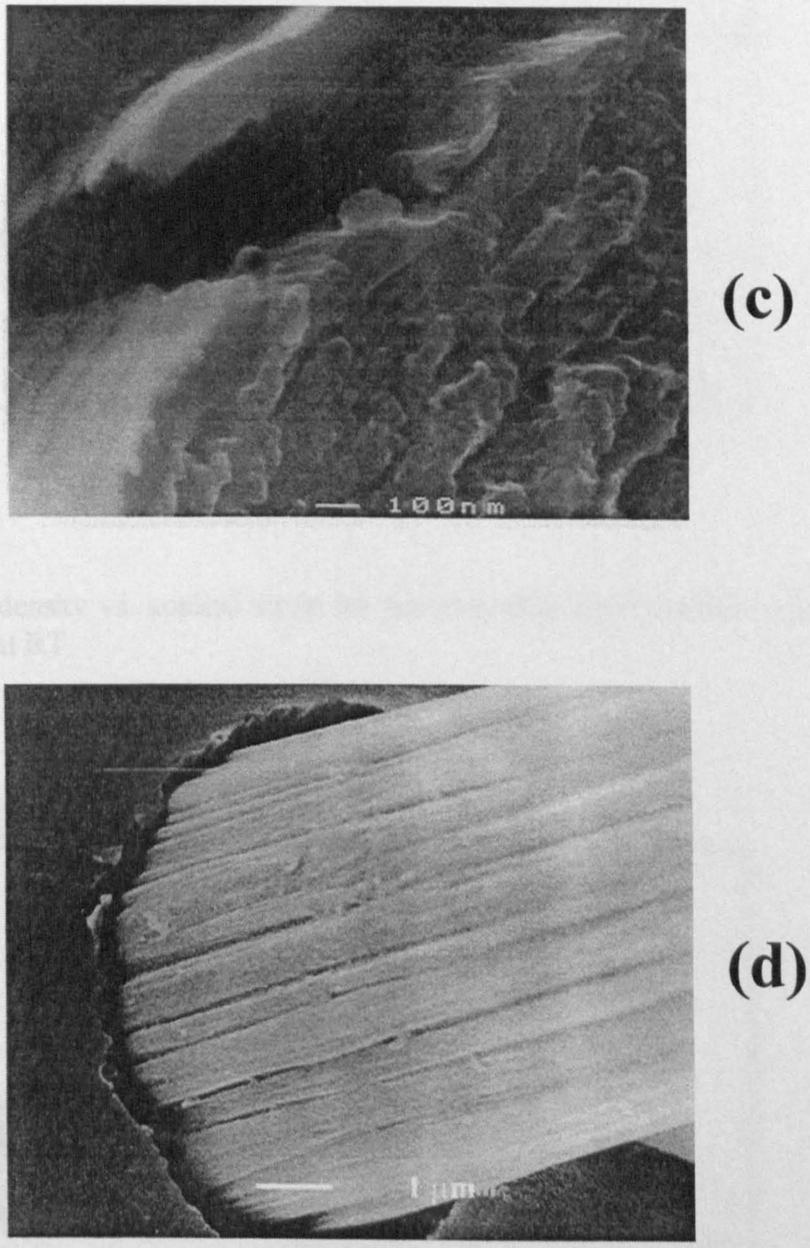

Figure 5.32 (c) Crack propagation into the interphase layer of the sized MEBS / MY-750 system, (d) clear interfacial failure for the unsized MUS / MY-750 system.

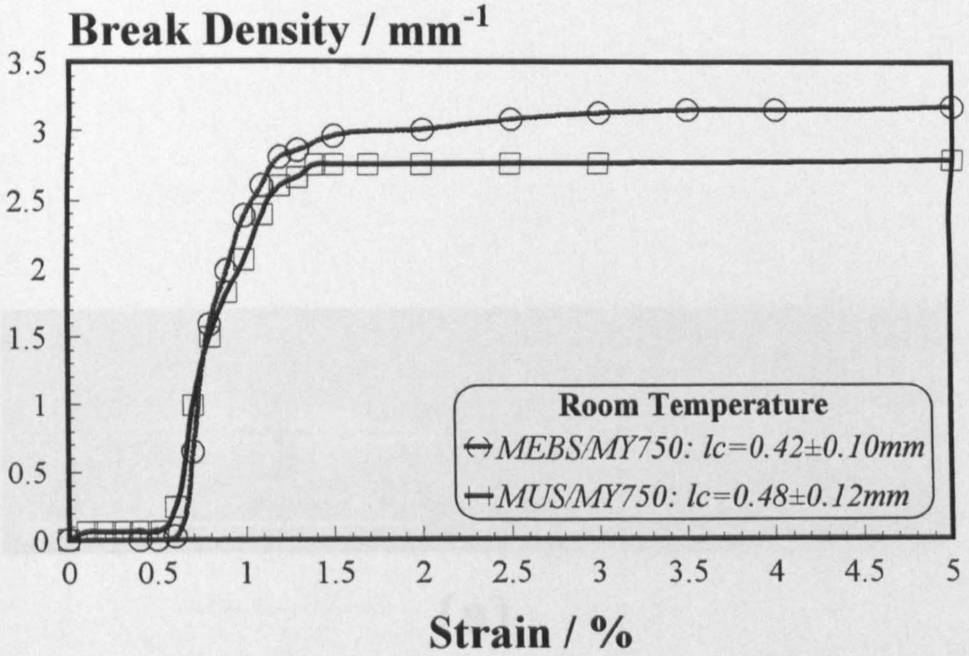

Figure 5.33 Break density vs. applied strain for the long fibre fragmentation coupons tested at RT.

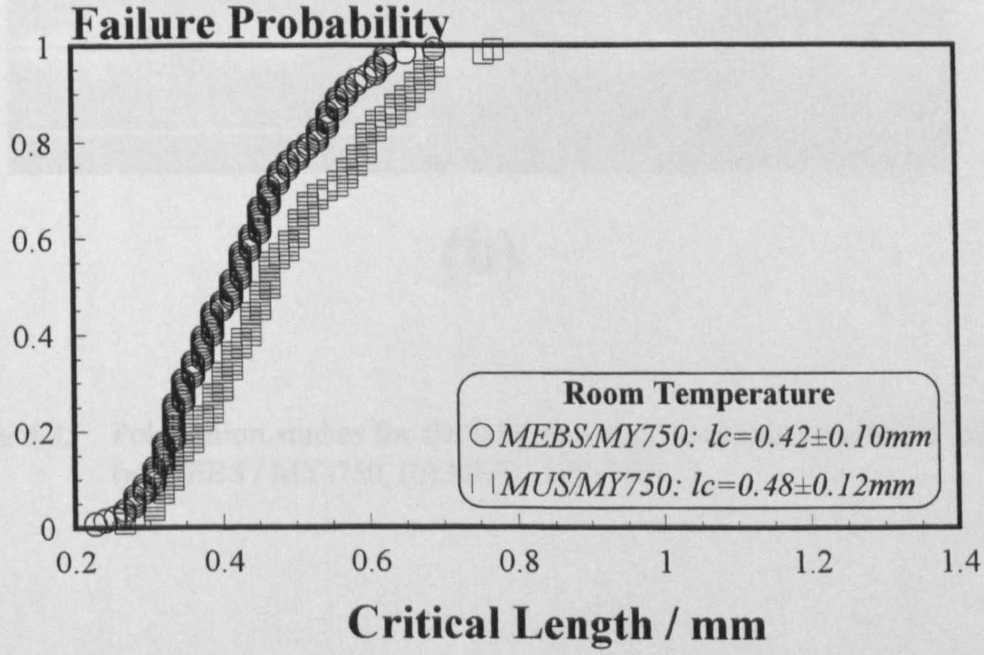

Figure 5.34 Critical length distributions vs. failure probability for the long fibre fragmentation coupons tested at RT.

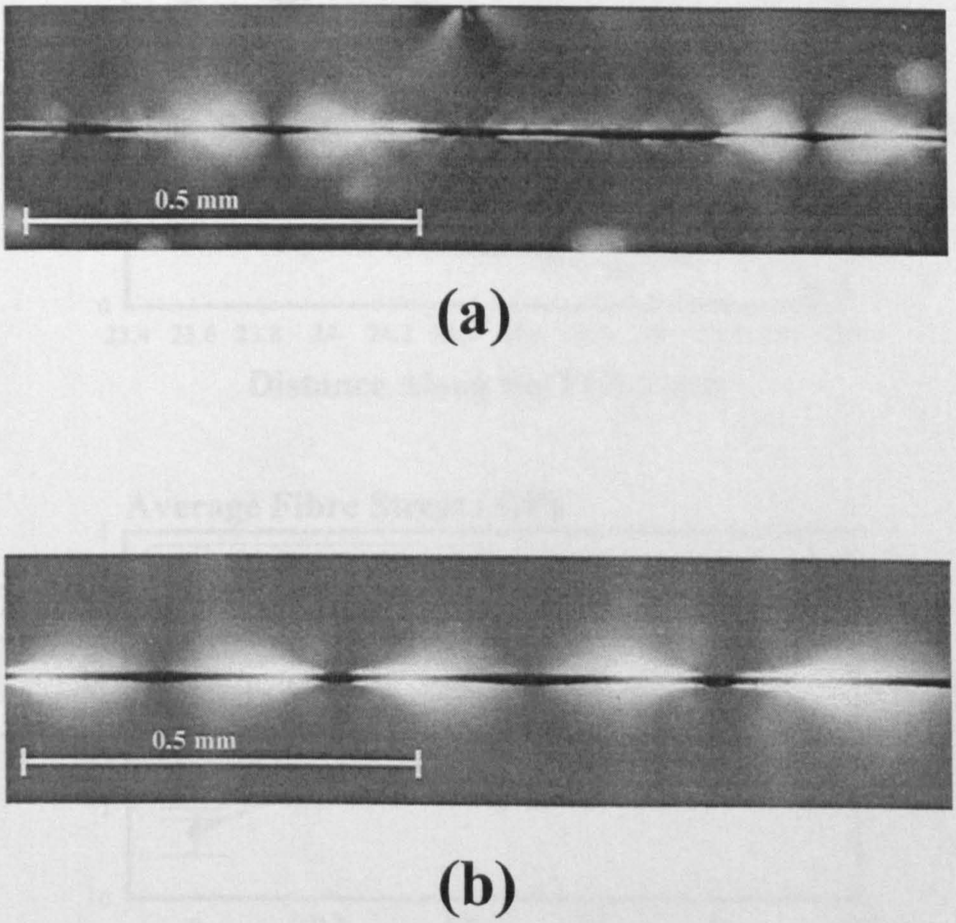

Figure 5.35 Polarisation studies for the long fibre fragmentation coupons tested at RT (a) MEBS / MY-750, (b) MUS / MY-750.

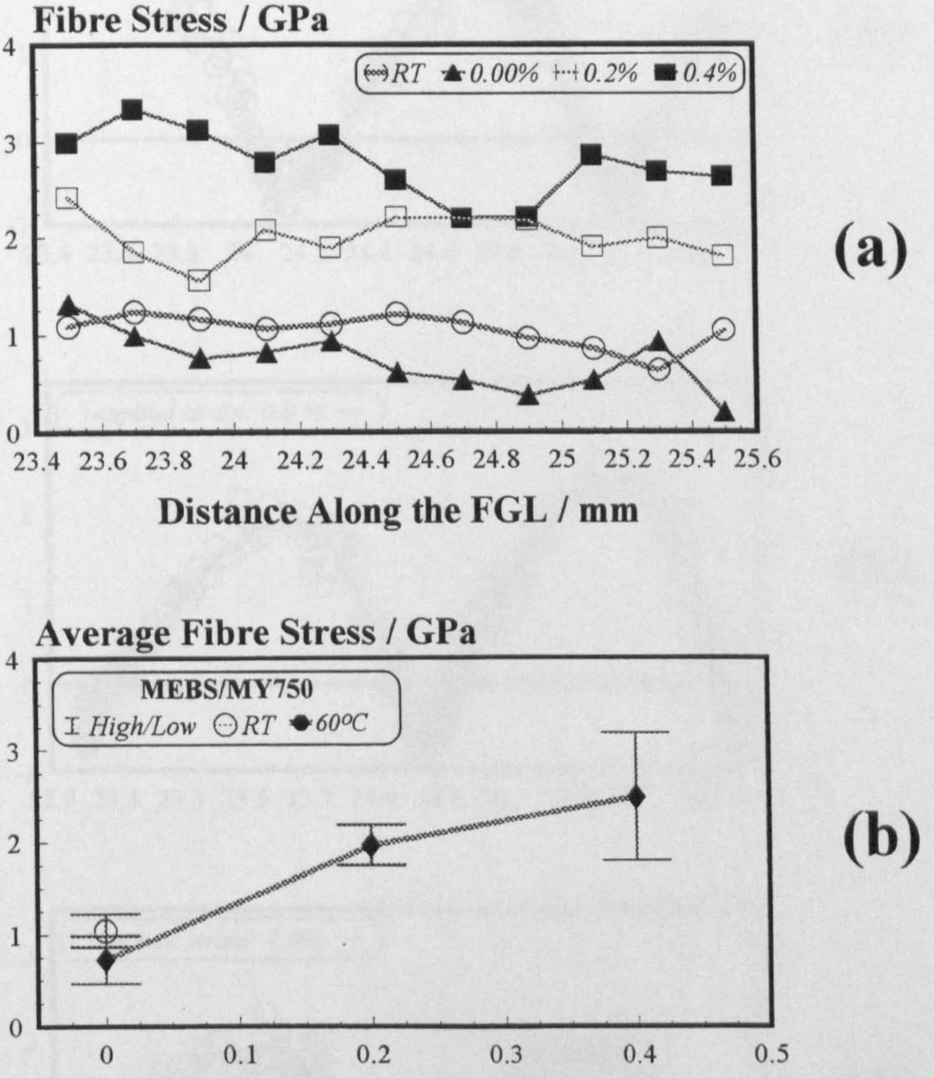

Figure 5.36 MEBS / MY-750 (long fibre coupon at 60°C): (a) axial stress distributions prior to fracture, (b) average stress vs. applied strain prior to fracture.

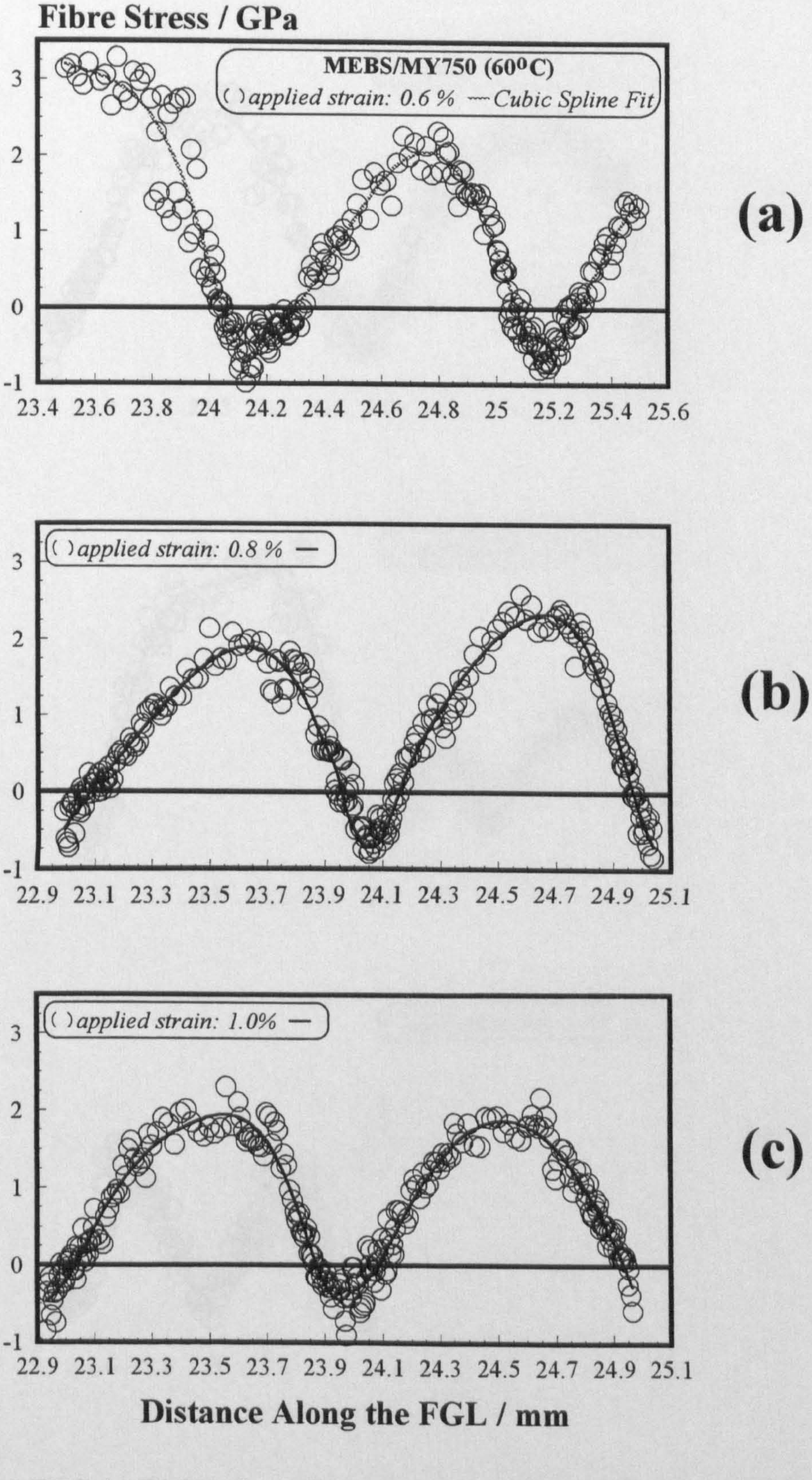

Figure 5.37 MEBS / MY-750 (long fibre coupon at 60°C): (a-c) axial stress profiles along the fragmentation gauge length.

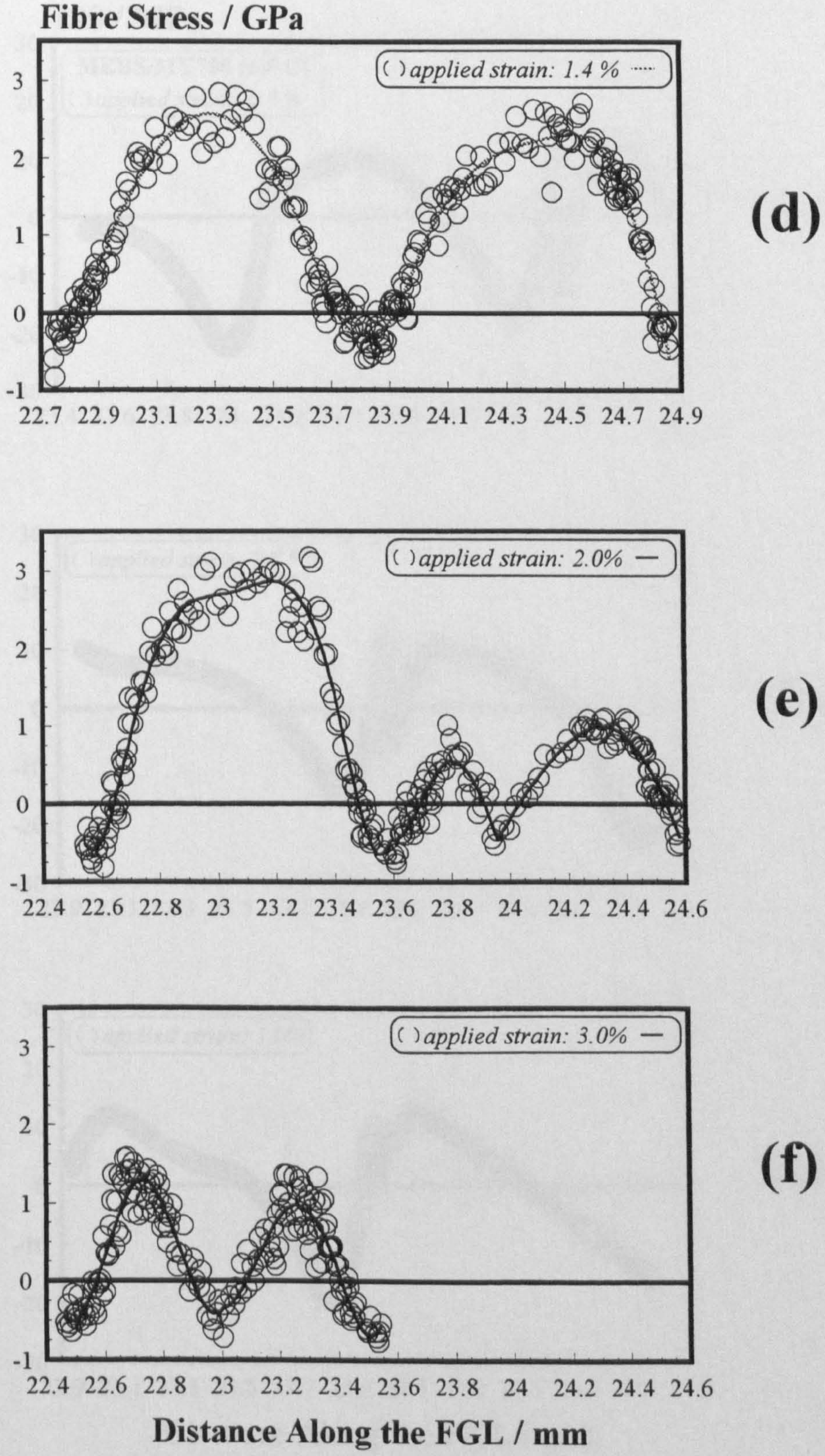

Figure 5.37 MEBS / MY-750 (long fibre coupon at 60°C): (d-f) axial stress profiles along the fragmentation gauge length.

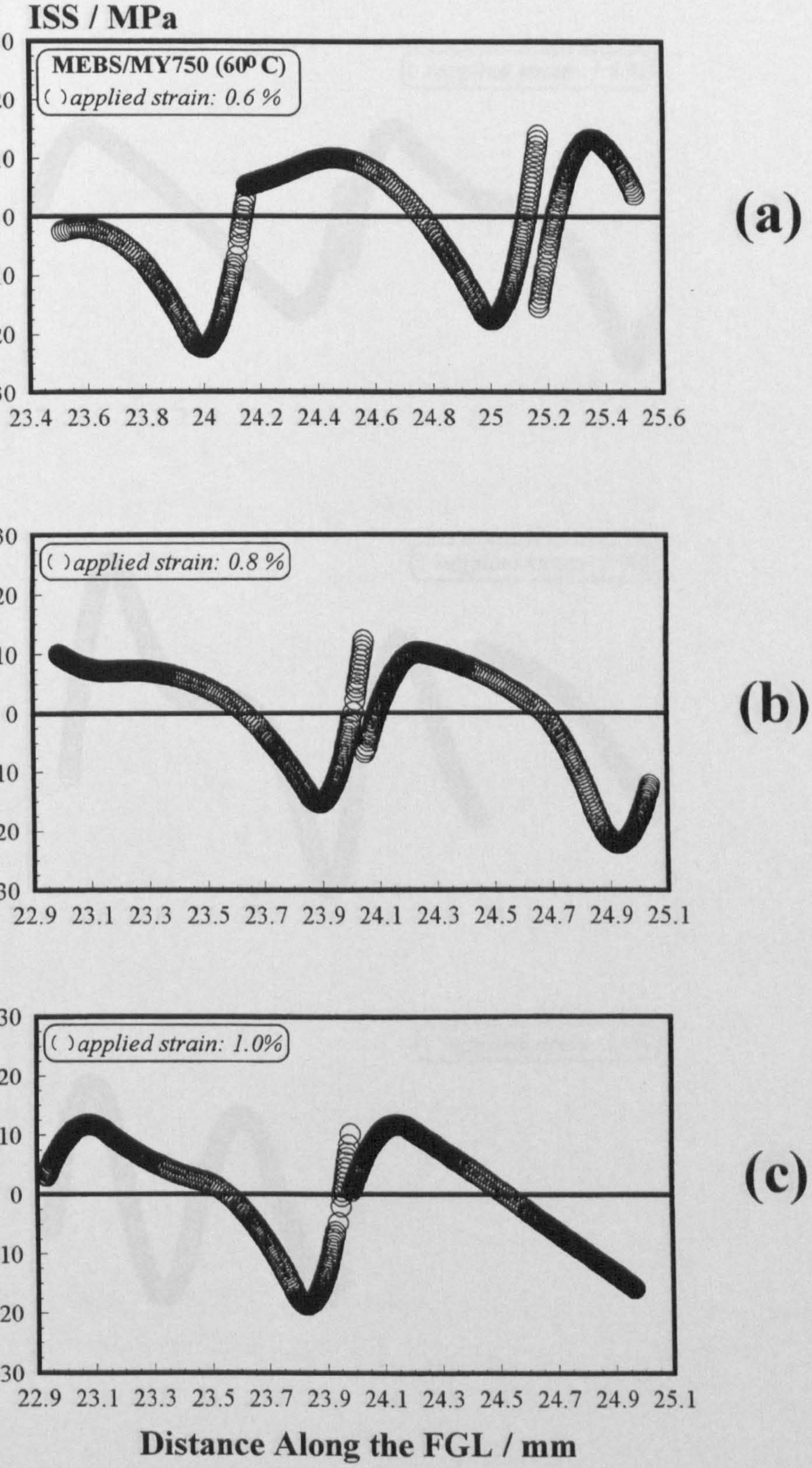

Figure 5.38 MEBS / MY-750 (long fibre coupon at 60°C): (a-c) interfacial shear stress (ISS) distribution along the fragmentation gauge length.

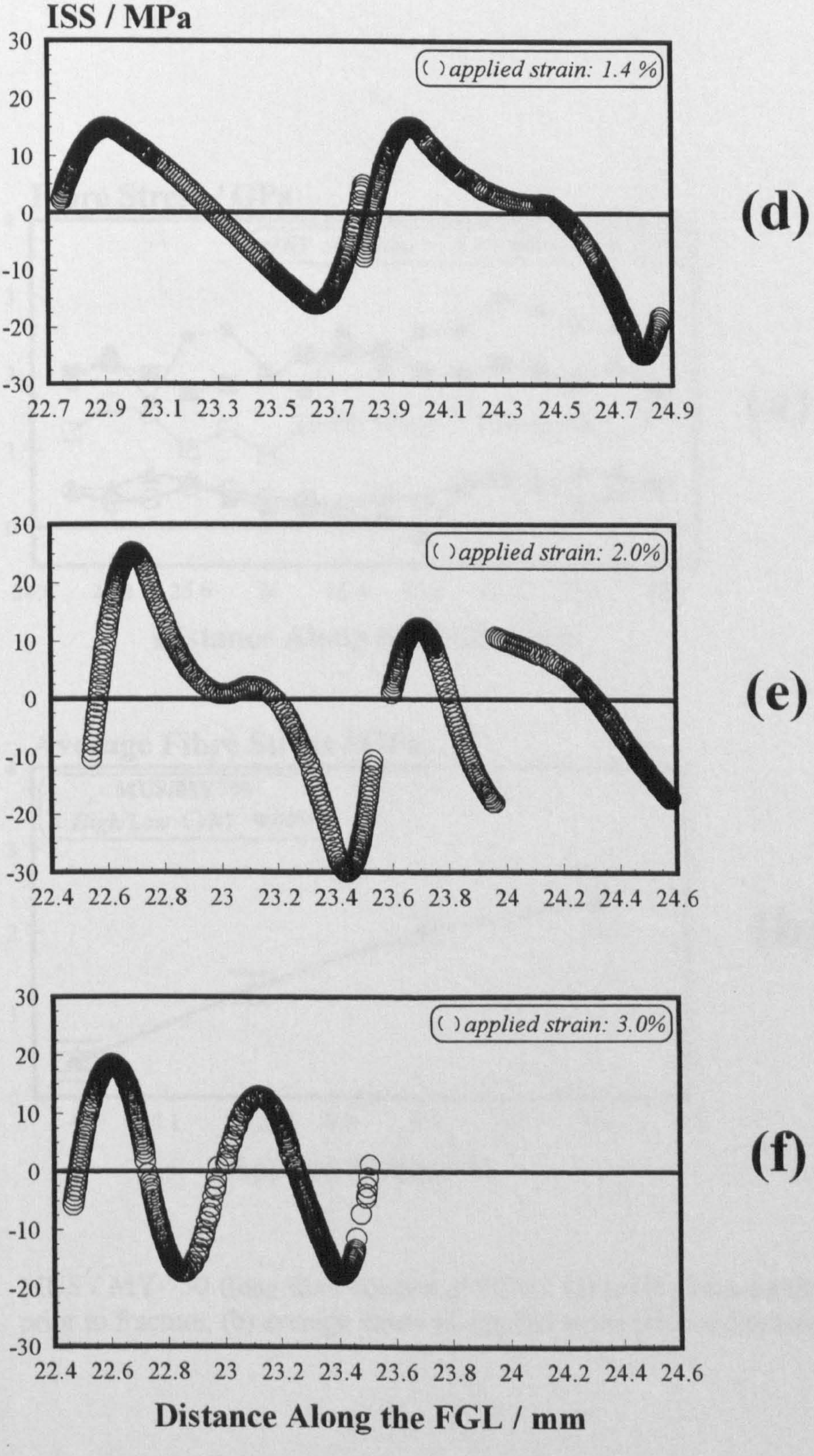

Figure 5.38 MEBS / MY-750 (long fibre coupon at 60°C): (d-f) interfacial shear stress (ISS) distribution along the fragmentation gauge length.

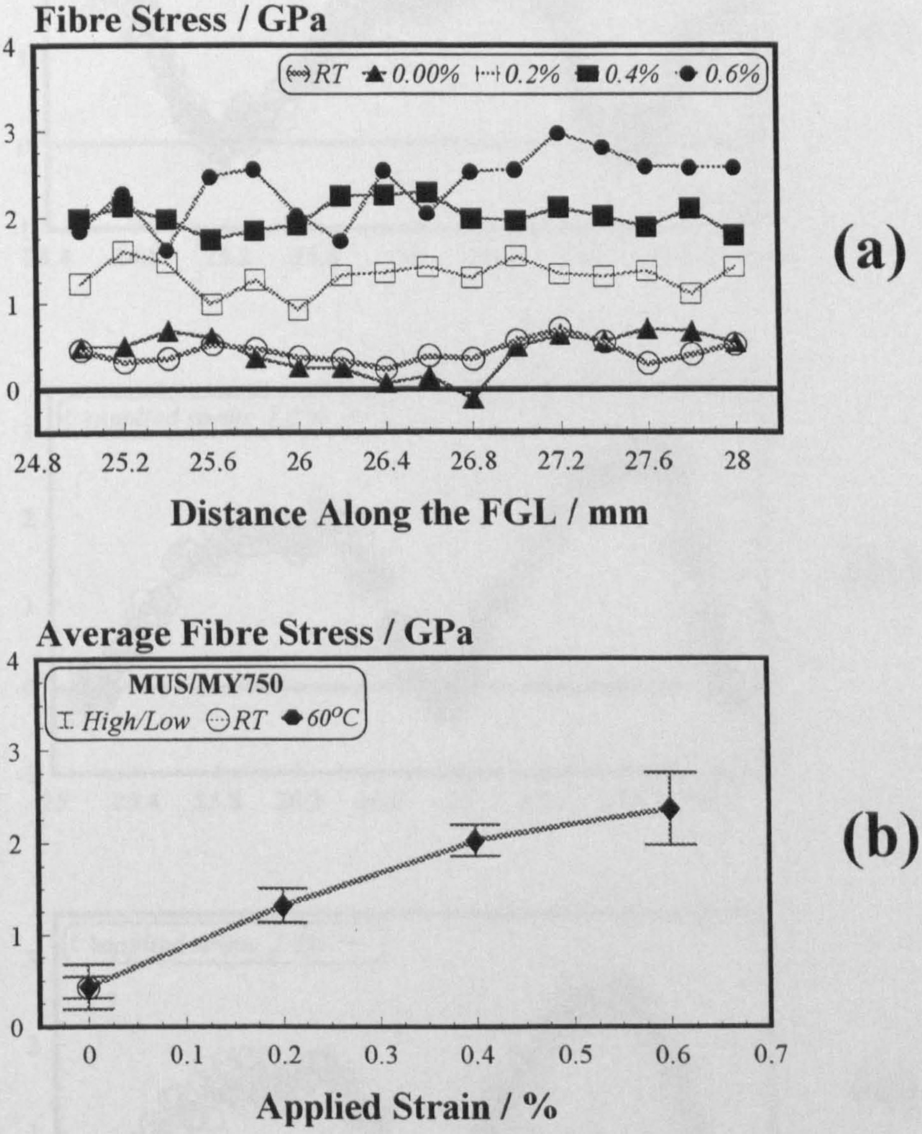

Figure 5.39 MUS / MY-750 (long fibre coupon at 60°C): (a) axial stress distributions prior to fracture, (b) average stress vs. applied strain prior to fracture.

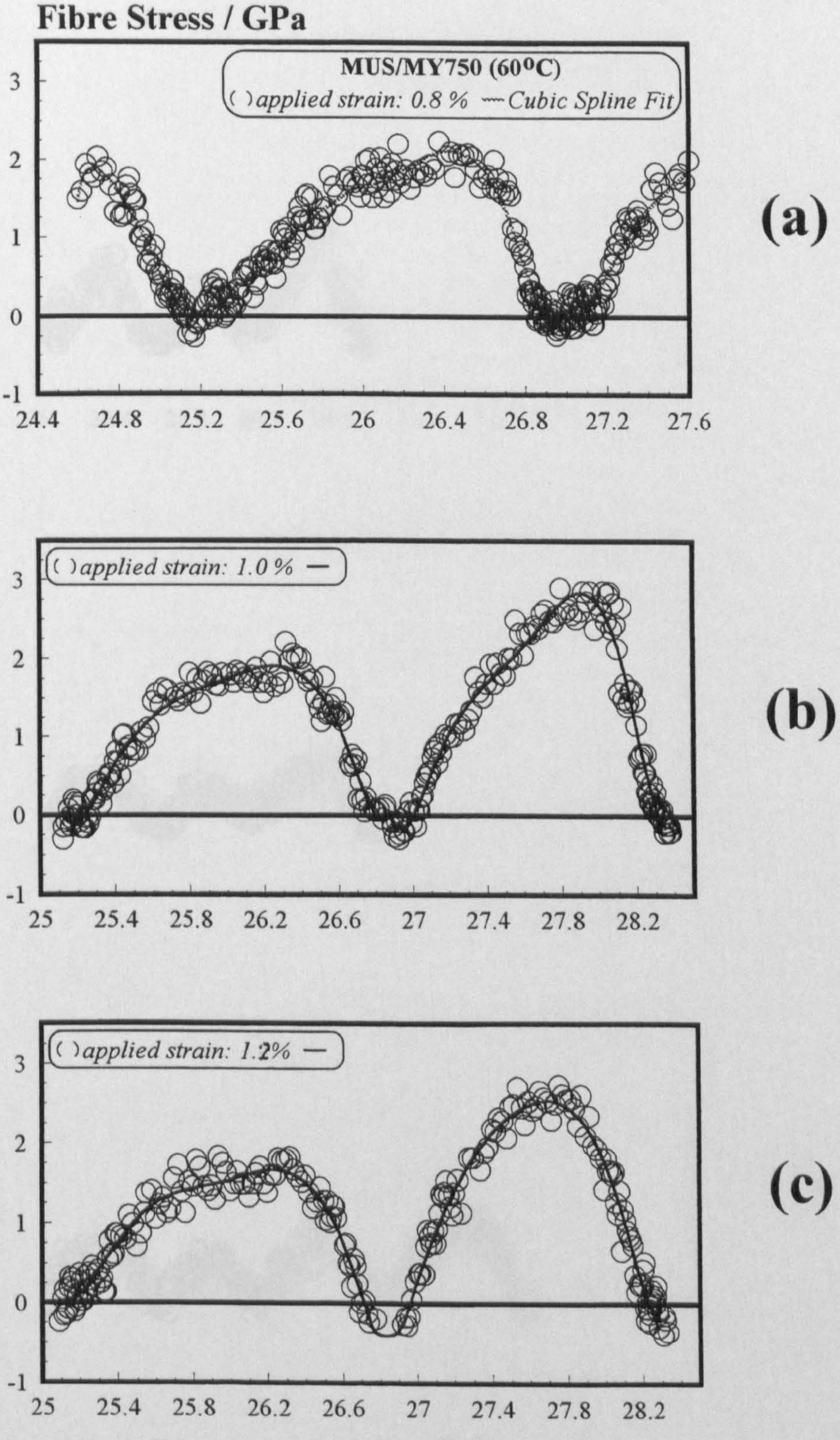

Figure 5.40 MUS / MY-750 (long fibre coupon at 60°C): (a-c) axial stress profiles along the fragmentation gauge length.

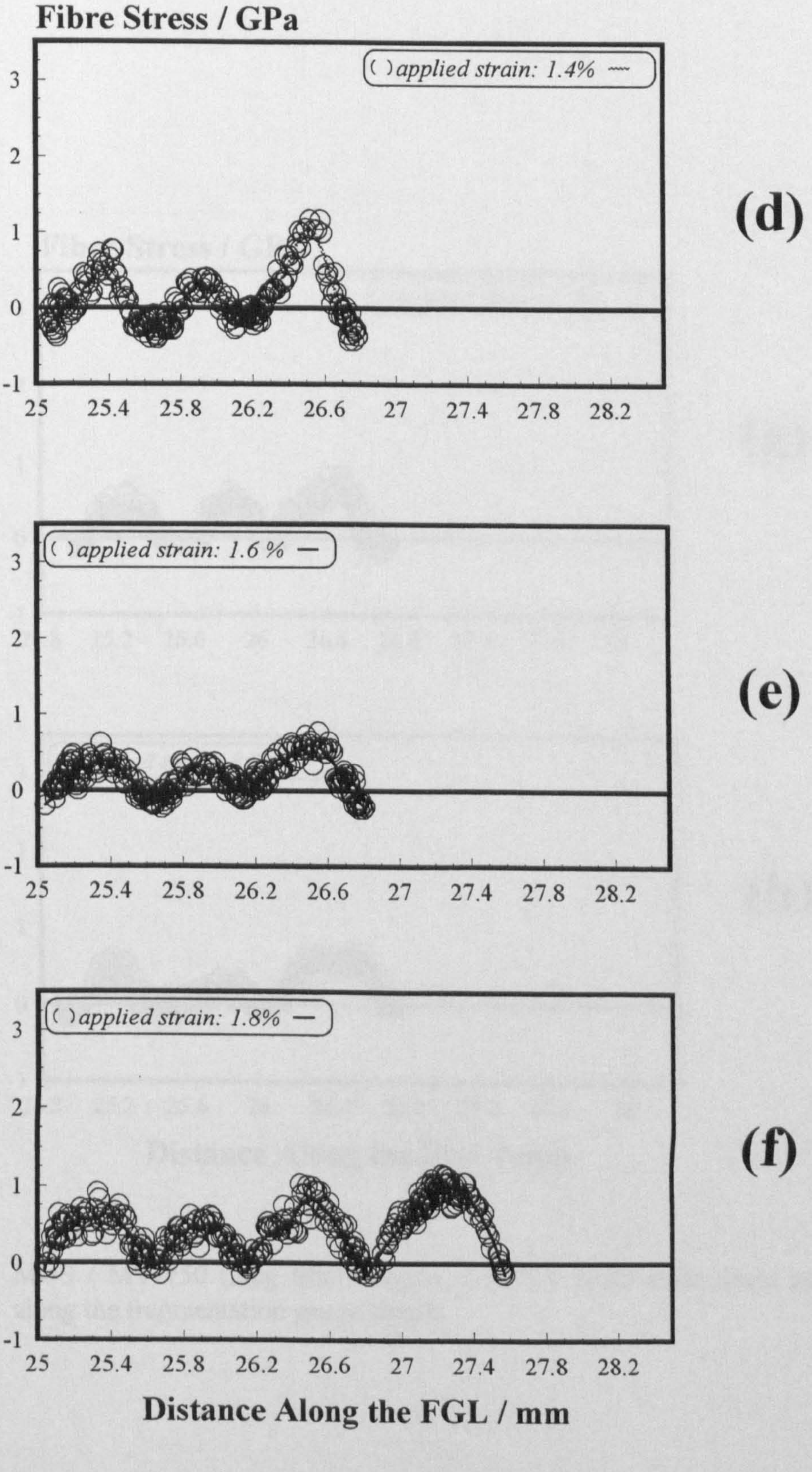

Figure 5.40 MUS / MY-750 (long fibre coupon at 60°C): (d-f) axial stress profiles along the fragmentation gauge length.

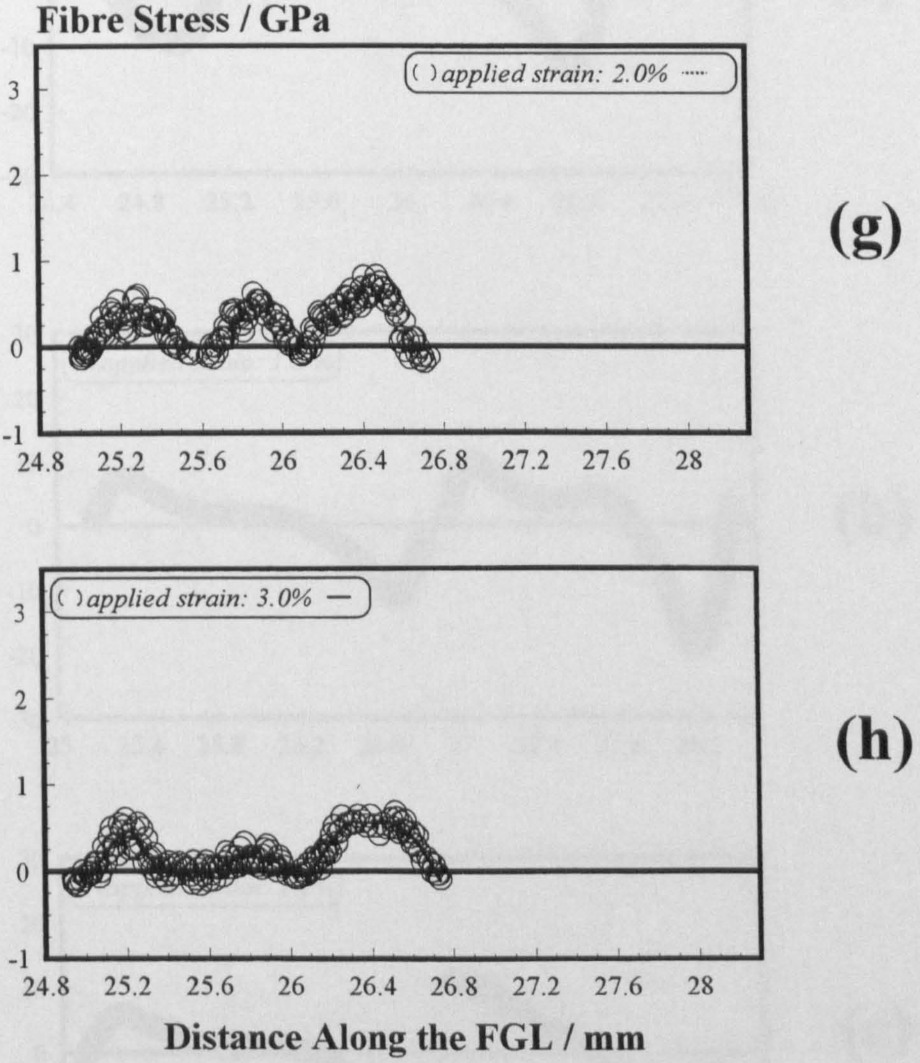

Figure 5.40 MUS / MY-750 (long fibre coupon at 60°C): (g-h) axial stress profiles along the fragmentation gauge length.

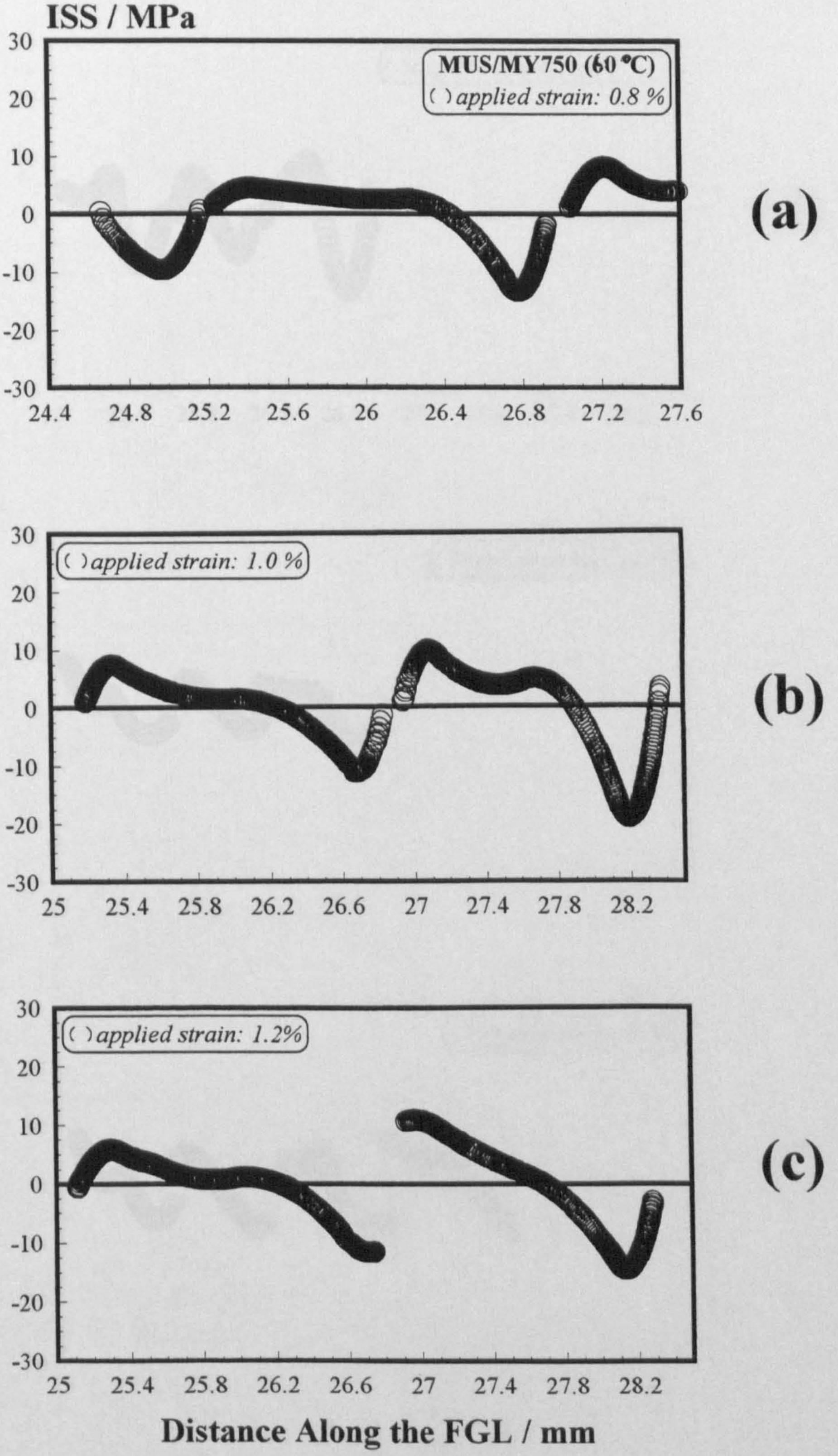

Figure 5.41 MUS / MY-750 (long fibre coupon at 60°C): (a-c) interfacial shear stress (ISS) distribution along the fragmentation gauge length

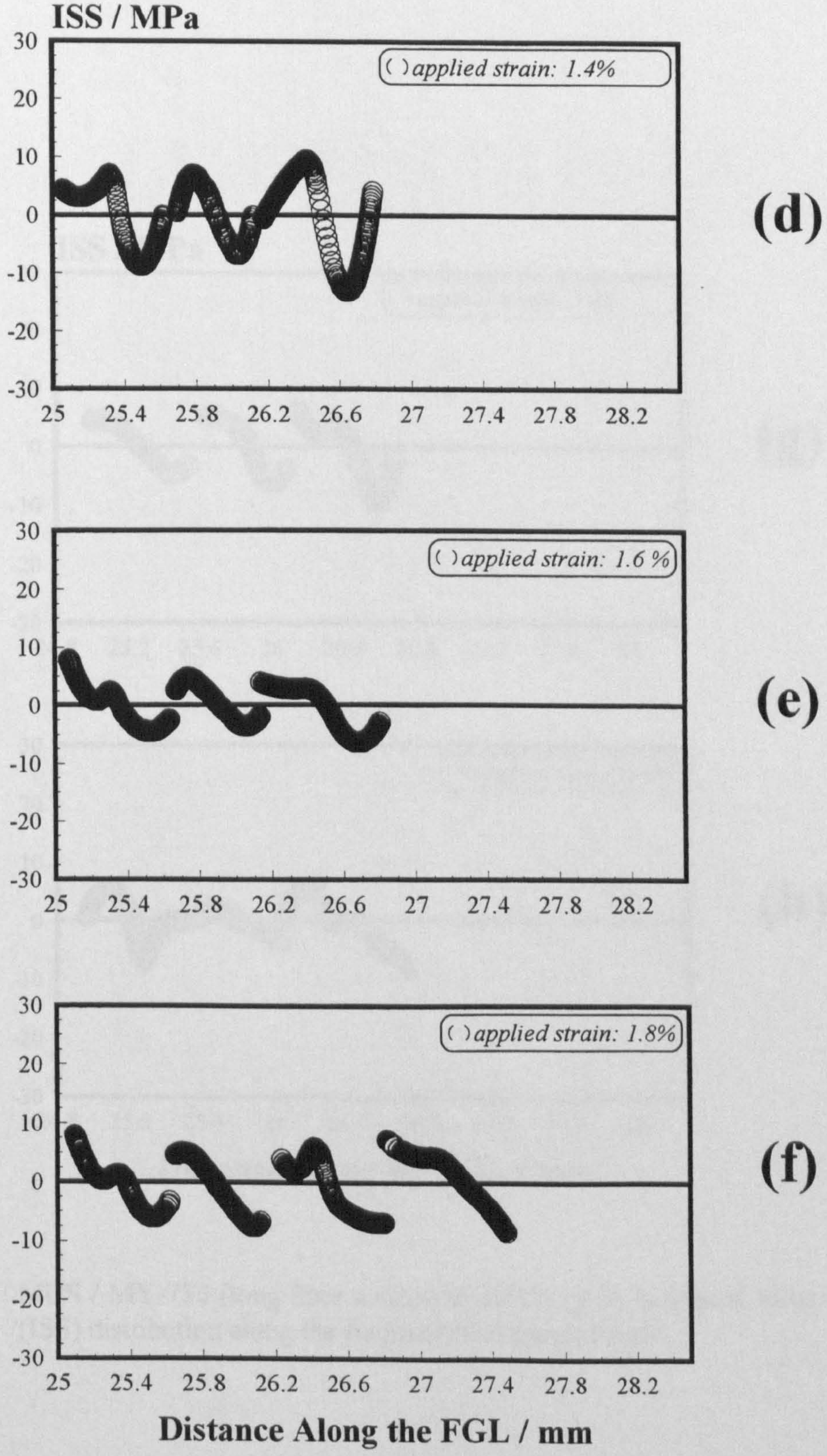

Figure 5.41 MUS / MY-750 (long fibre coupon at 60°C): (d-f) interfacial shear stress (ISS) distribution along the fragmentation gauge length

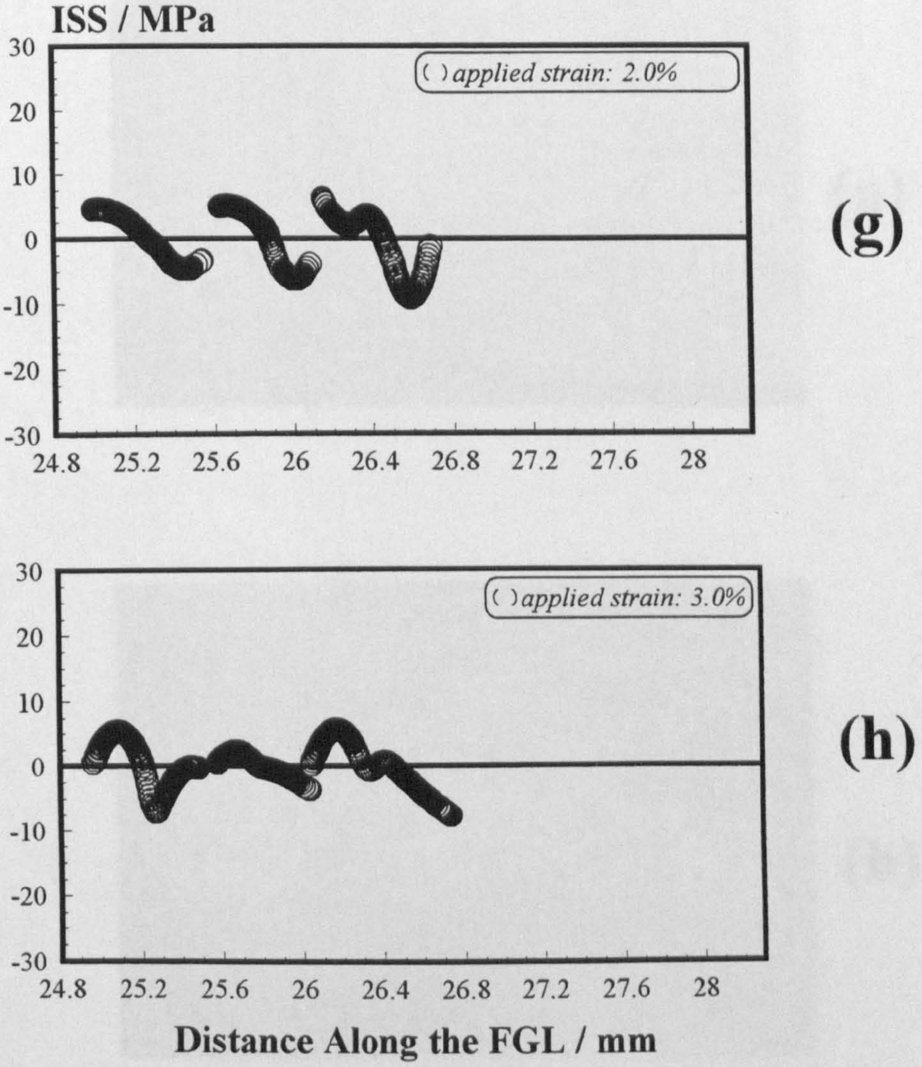

Figure 5.41 MUS / MY-750 (long fibre coupon at 60°C): (g-h) interfacial shear stress (ISS) distribution along the fragmentation gauge length

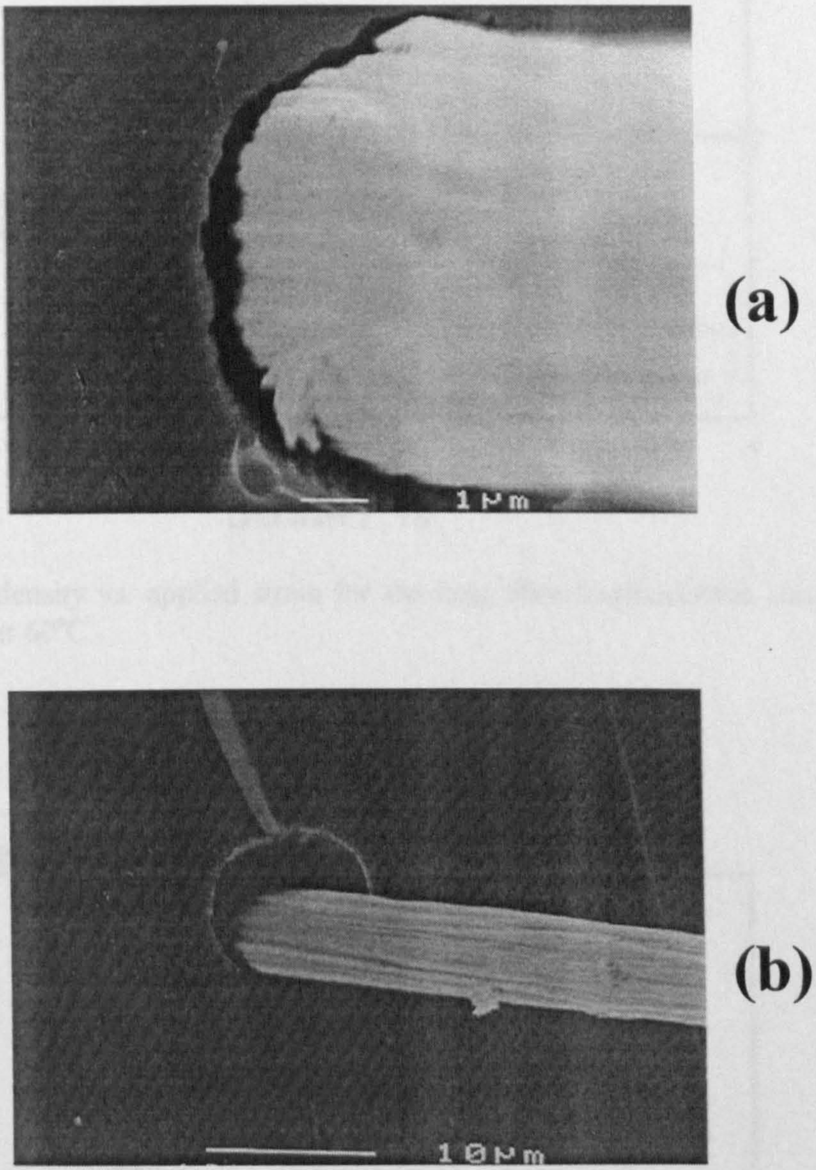

Figure 5.42 SEM micrographs of the fracture surface of the (a) sized MEBS/MY-750 and (b) the unsized MUS / MY-750 system at 60°C revealing clear interfacial failure.

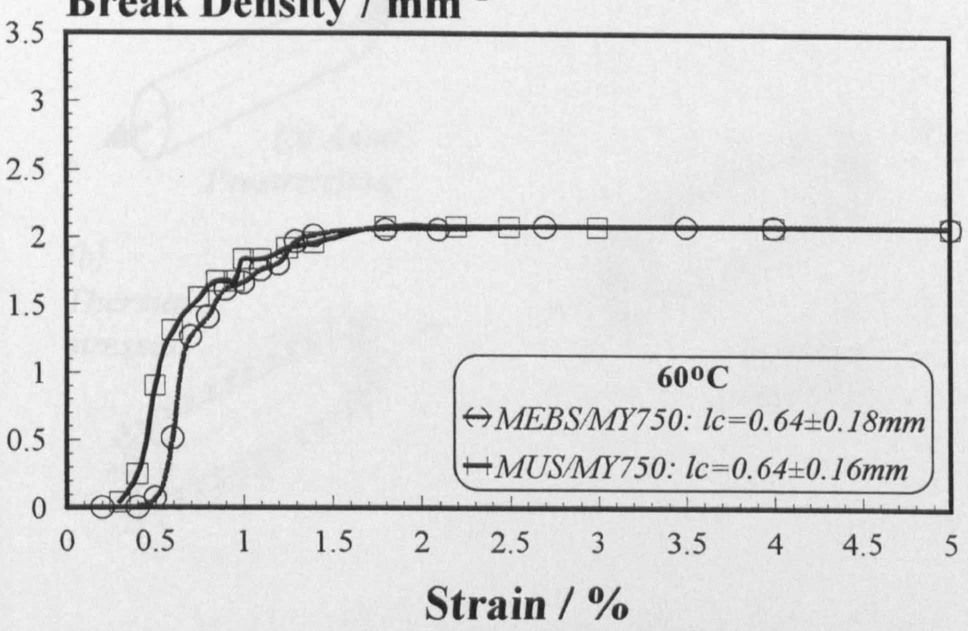

Figure 5.43 Break density vs. applied strain for the long fibre fragmentation coupons tested at 60°C.

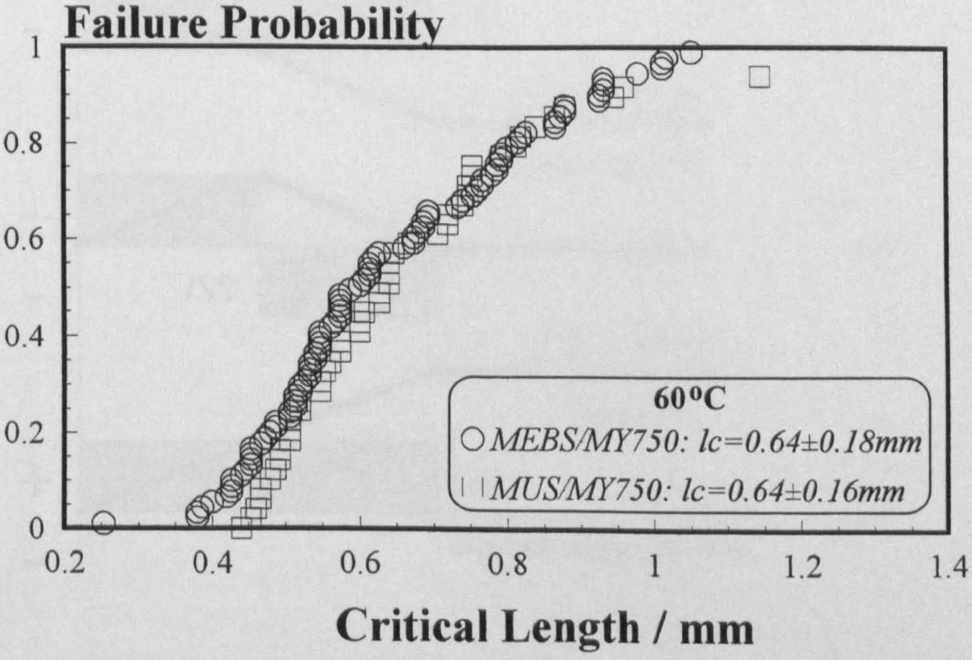

Figure 5.44 Critical length distributions vs. failure probability for the long fibre fragmentation coupons tested at 60°C.

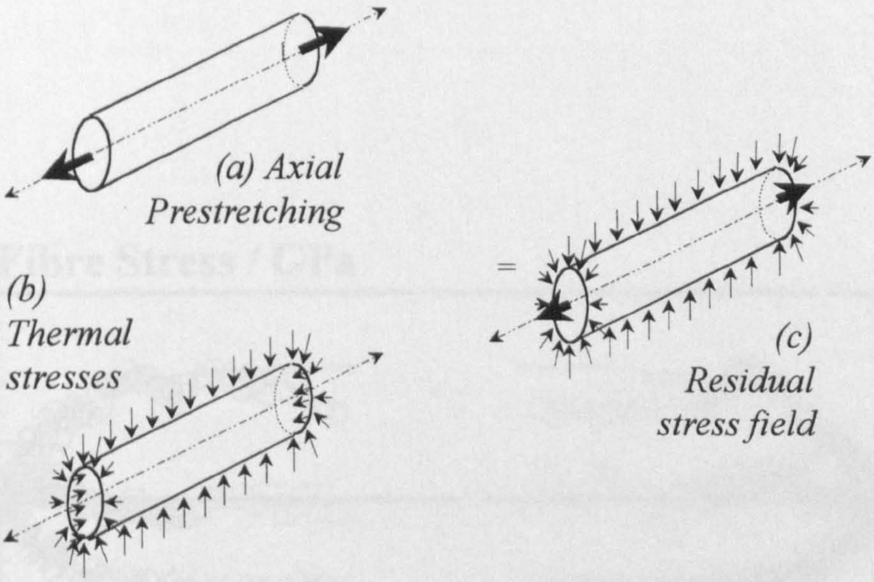

Figure 5.45 Superposition of stress fields in single fibre model composites (a) axial prestretching, (b) thermal stress field, and (c) residual stress field.

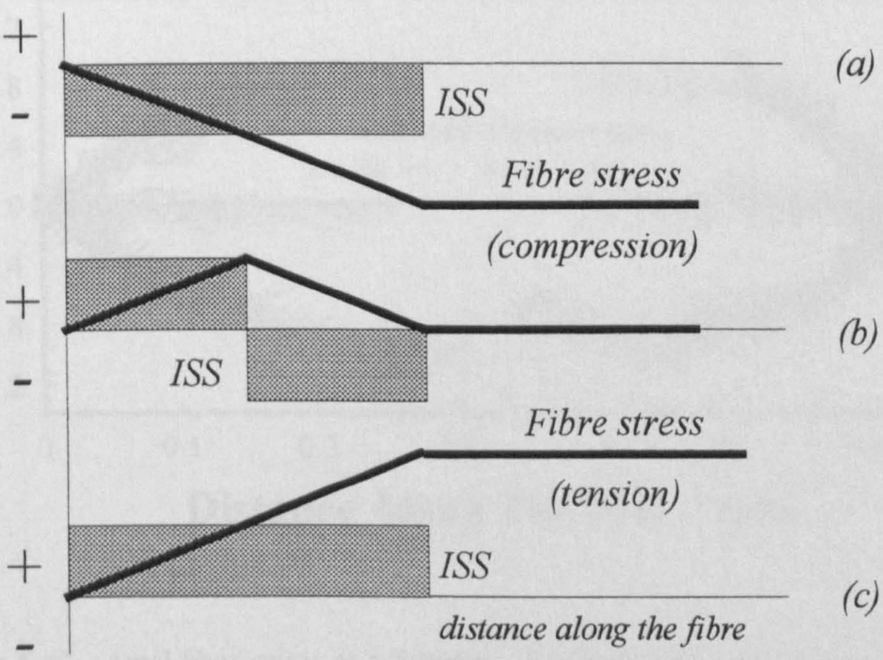

Figure 5.46 Schematic diagram of the change of sign in shear as the fibre is loaded from compression to tension [**Schadler, 1992**].

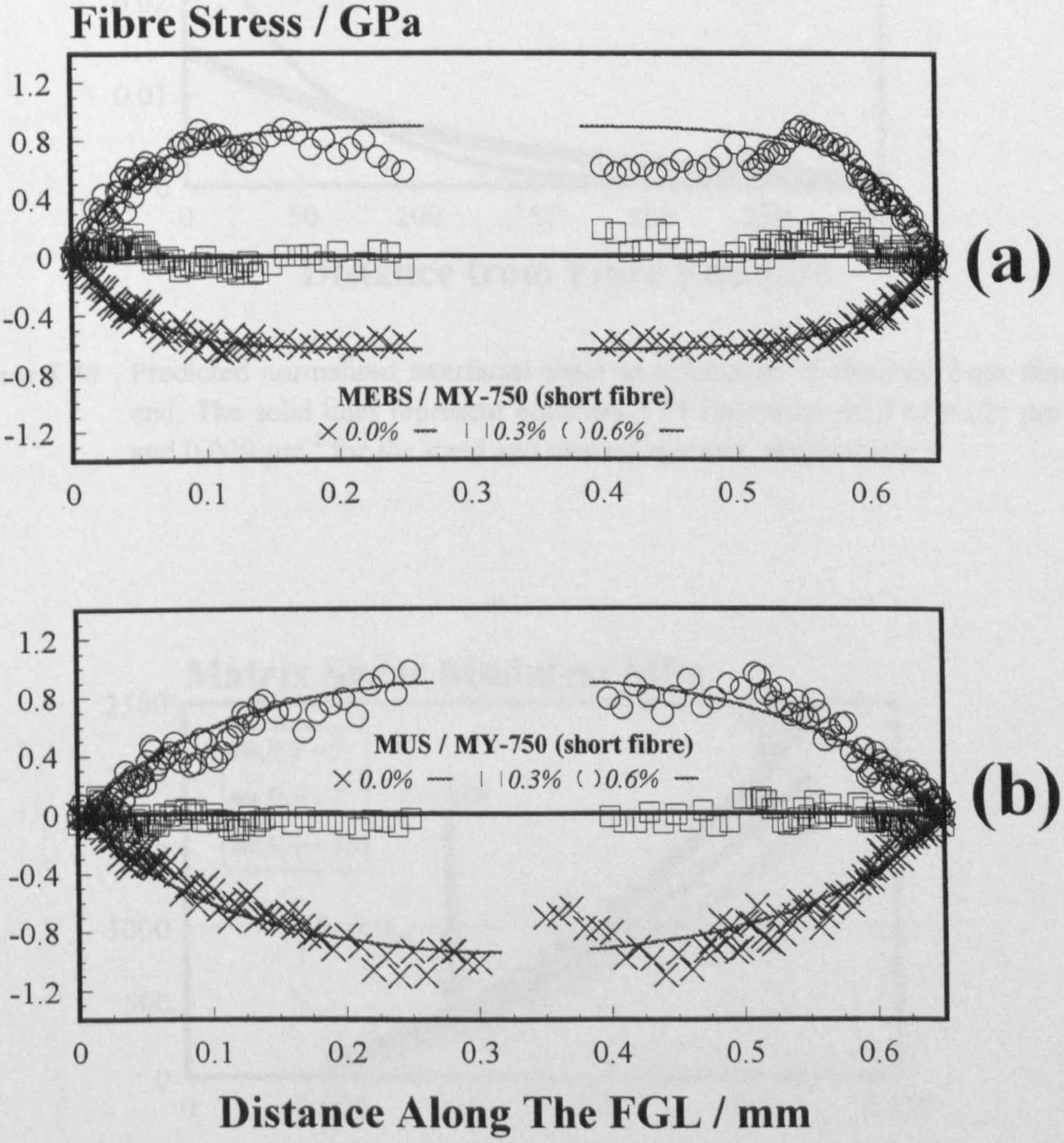

Figure 5.47 Axial fibre stress as a function of distance from the fibre end for the short fibre coupons at 0.0%, 0.3% and 0.6% applied composite strain. The solid lines at 0.3% and 0.6% strain represent best fits of equation 5.22b, through which the values of the parameter beta were derived. (a) MEBS / MY750 (sized system and (b) MUS / MY750 (unsized system).

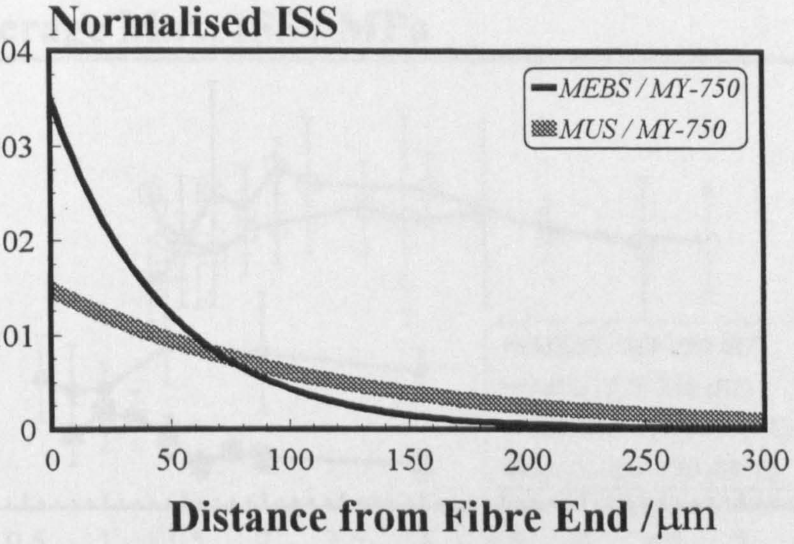

Figure 5.48 Predicted normalised interfacial shear as a function of distance from fibre end. The solid lines represent equation 5.23 for values of β of 0.02 μm^{-1} and 0.009 μm^{-1} for the sized and unsized systems, respectively.

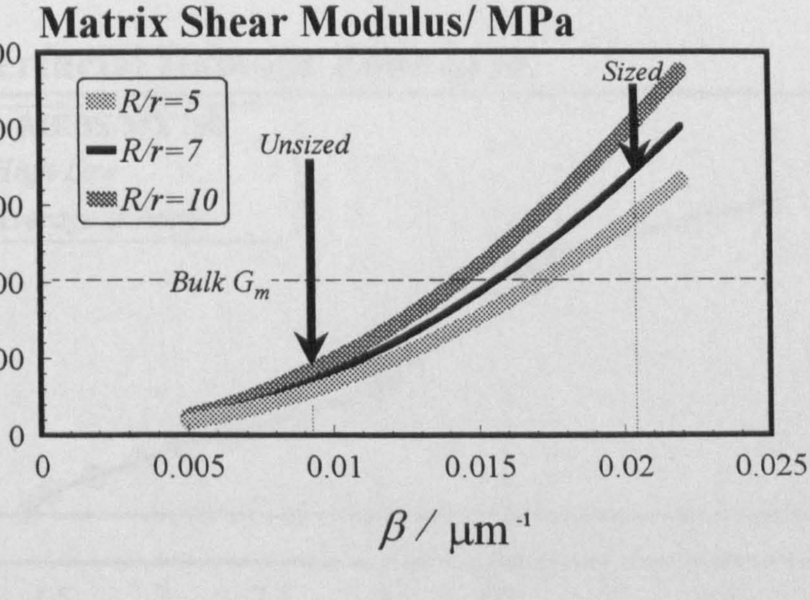

Figure 5.49 Prediction of average shear modulus of matrix cylinder of radius R_∞ as a function of β for three different R_∞/R ratios of 5, 7, and 10. The local shear moduli for the sized and unsized systems (values of β of 0.02 μm^{-1} and 0.009 μm^{-1}, respectively) are indicated.

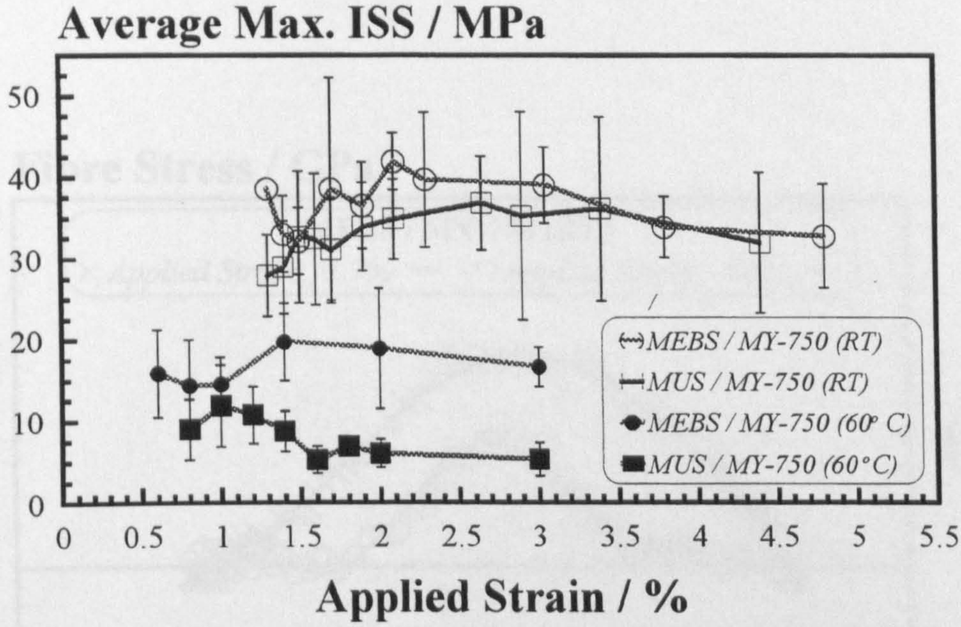

Figure 5.50 LRS interfacial shear stress (ISS) measurements for all the studied systems as a function of applied strain.

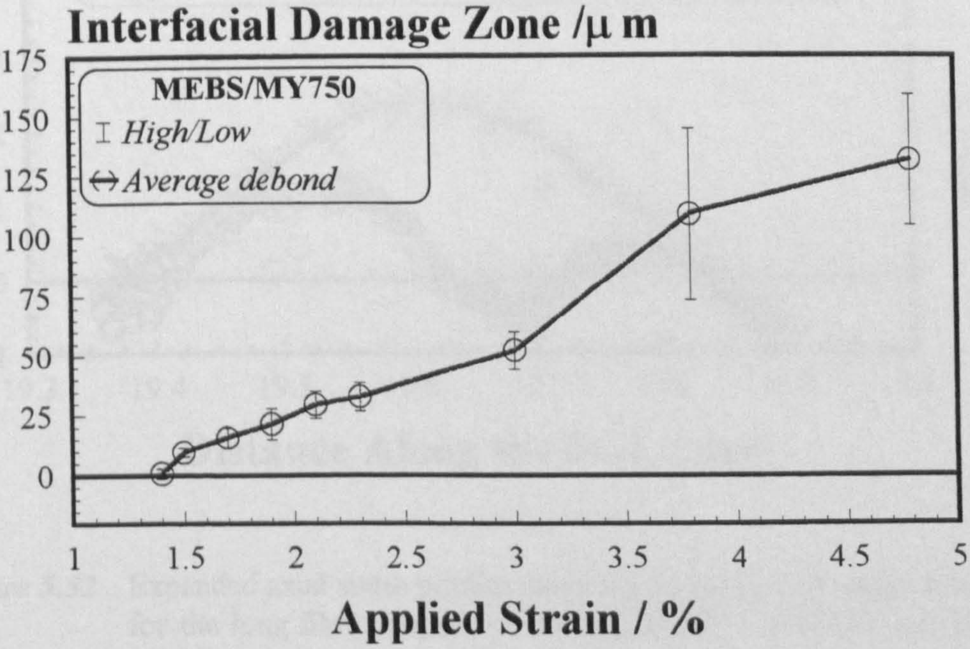

Figure 5.51 Damage zone propagation as a function of applied strain for the sized (MEBS) M40 / MY-750 system at RT.

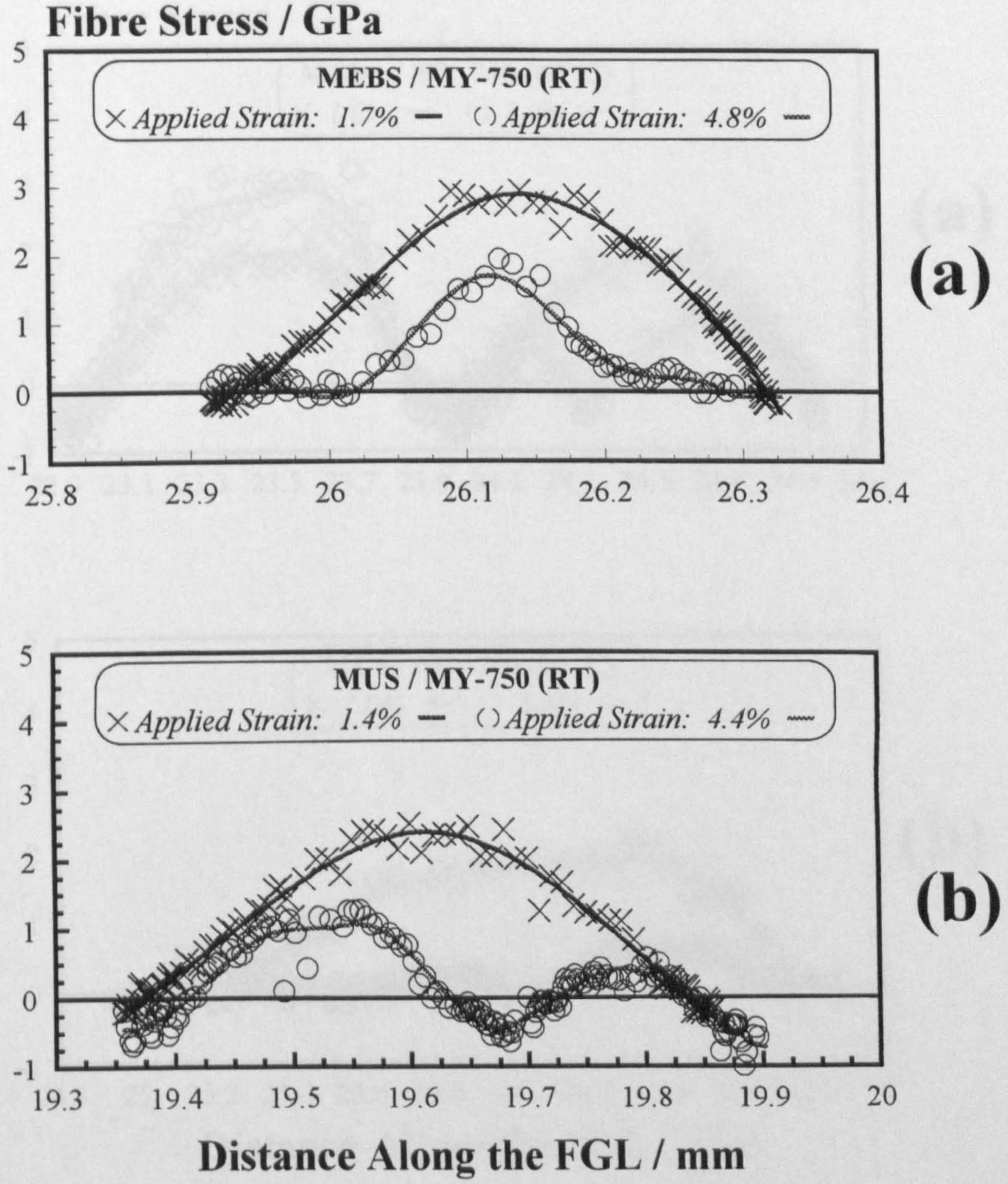

Figure 5.52 Expanded axial stress profiles along the fragmentation gauge length (FGL) for the long fibre coupons at RT: (a) MEBS / MY-750, and (b) MUS / MY-750.

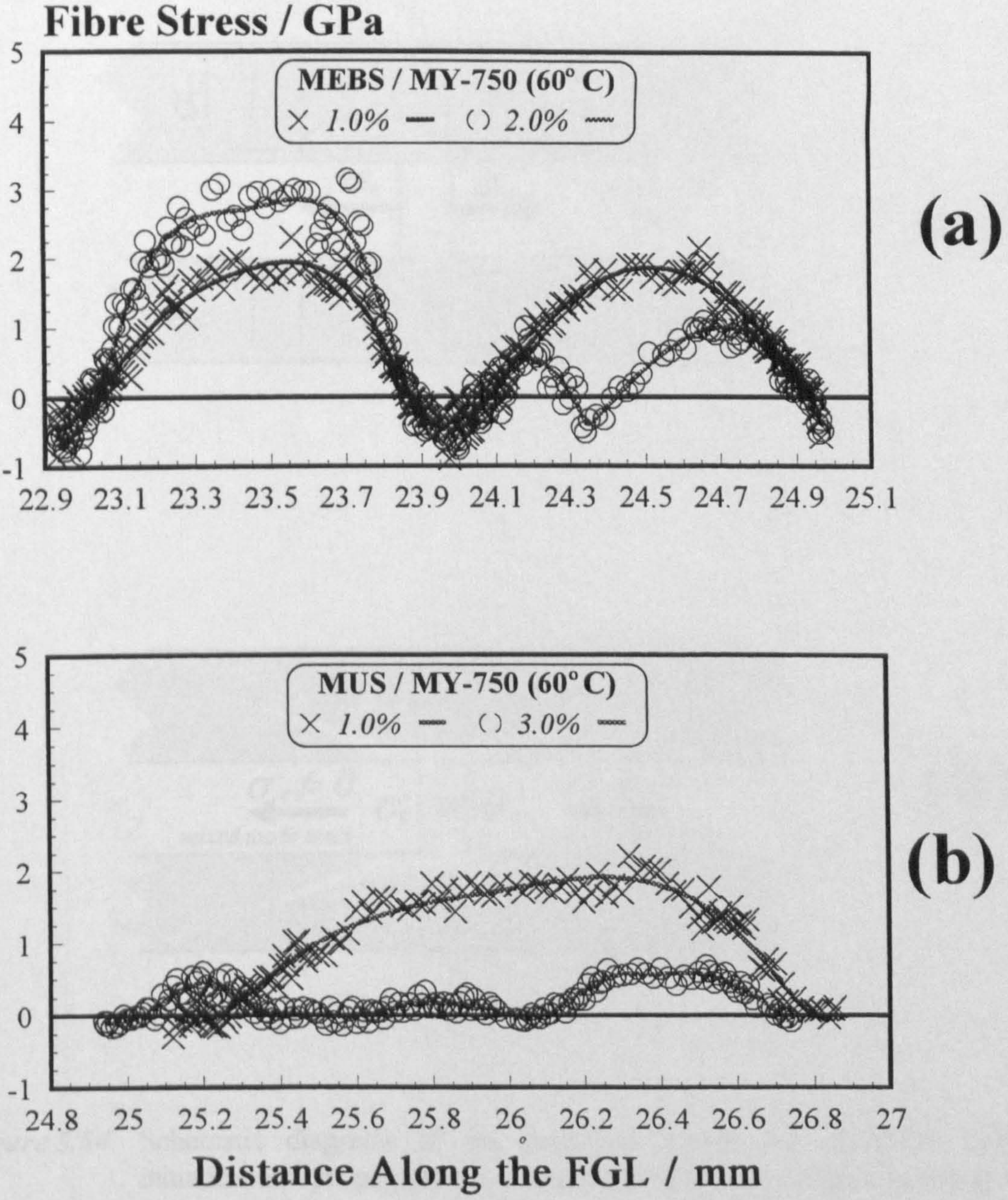

Figure 5.53 Expanded axial stress profiles along the fragmentation gauge length (FGL) for the long fibre coupons at 60°C: (a) MEBS / MY-750, and (b) MUS / MY-750.

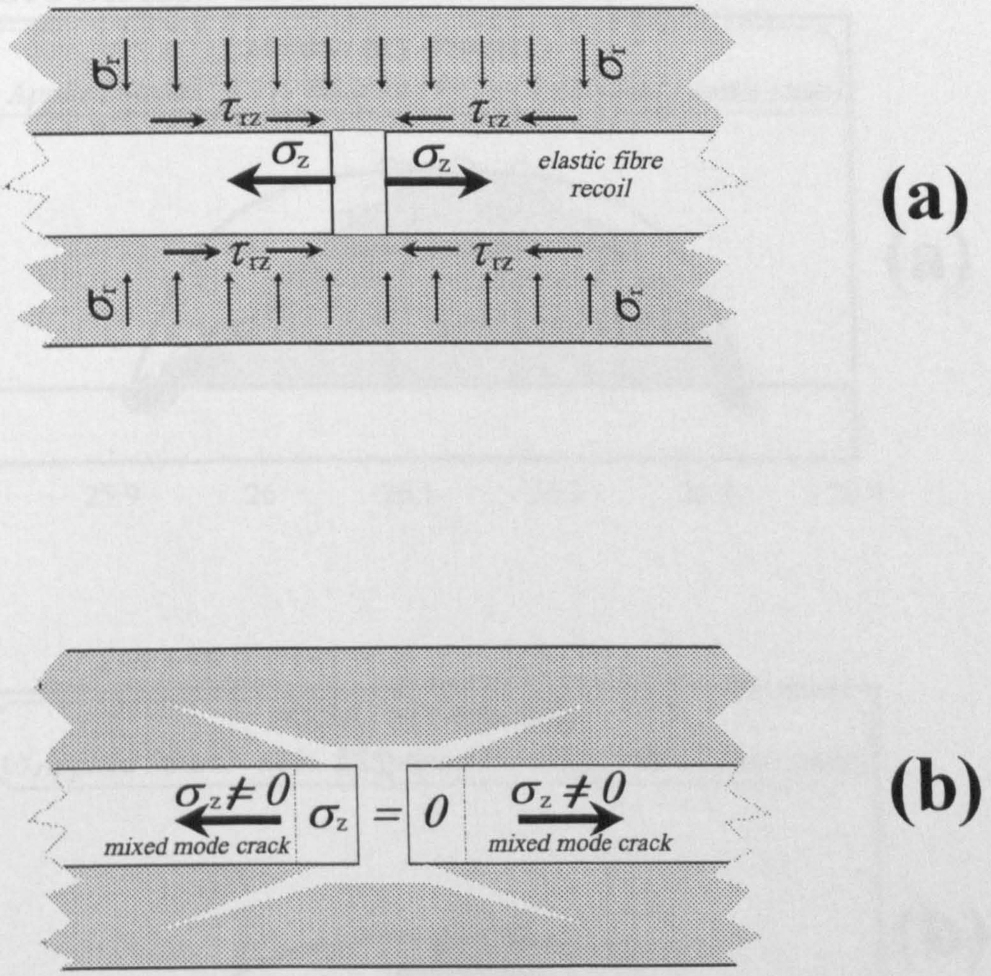

Figure 5.54 Schematic diagrams of the proposed models for interfacial damage initiation and propagation: (a) interfacial failure or mode II cracking with compressive stresses at the locus of the fibre fracture due to the elastic fibre recoil, and (b) crack deflection in the matrix or mixed mode cracking due to a brittle interphase.

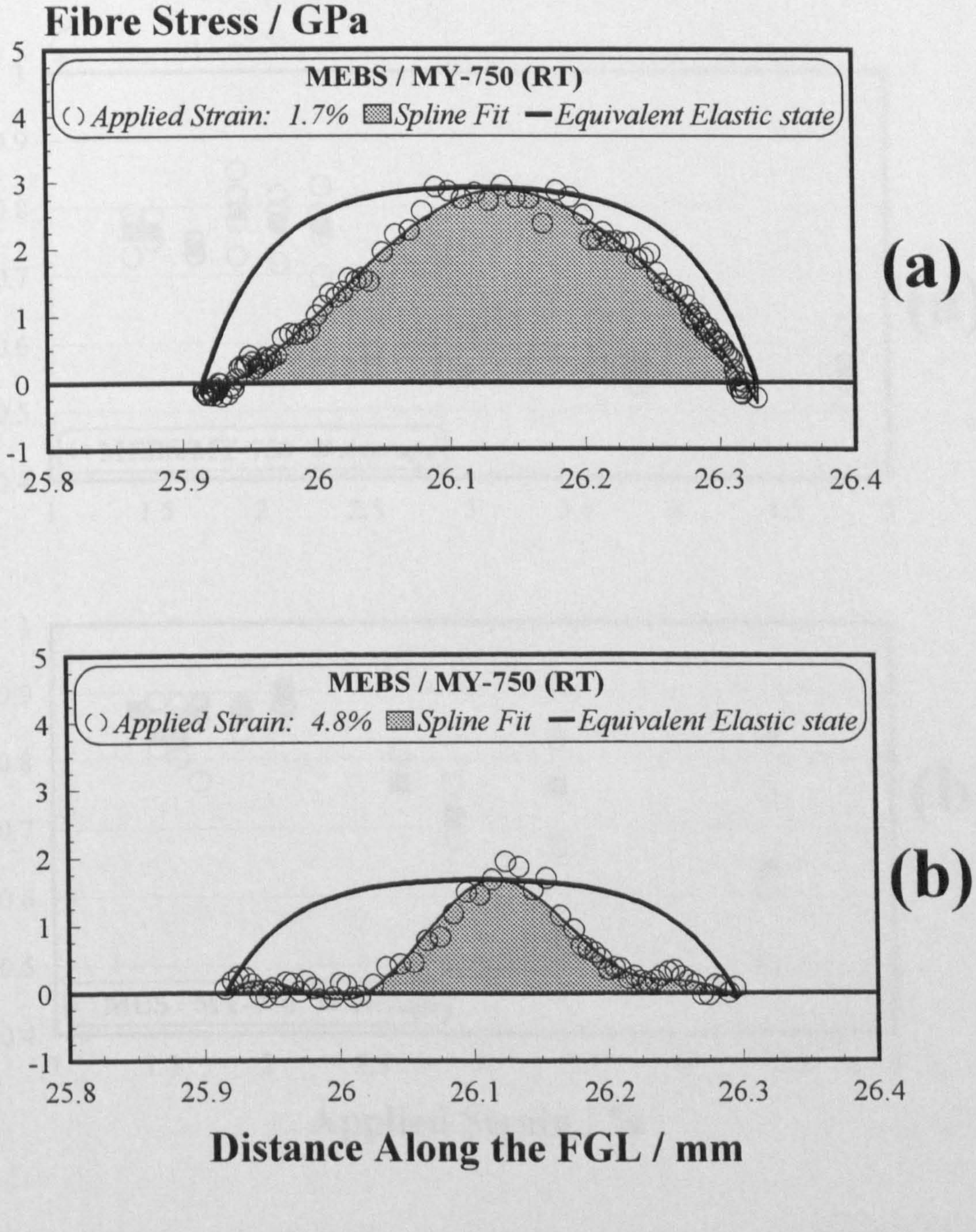

Figure 5.55 Experimental axial stress profiles and equivalent calculated profiles assuming an elastic stress state.

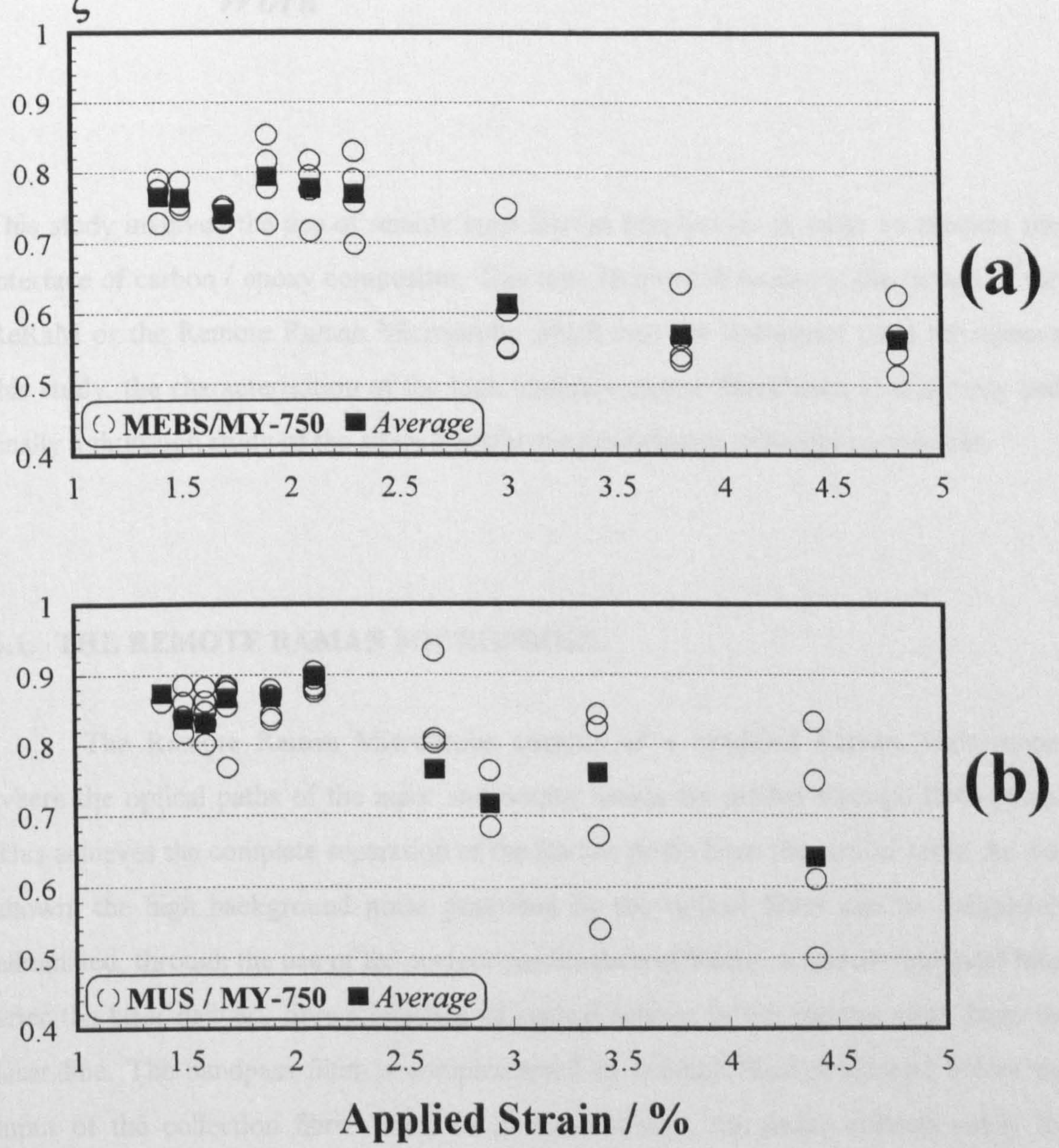

Figure 5.56 Index of stress transfer efficiency ζ as a function of applied strain; (a) MEBS / MY 750 and (b) MUS / MY 750.

Chapter 6: Conclusions and Suggestions for Further Work

This study involved the use of remote laser Raman microscopy in order to monitor the interface of carbon / epoxy composites. This task involved in sequence the design of the ReRaM or the Remote Raman Microprobe which was the instrument used throughout this study, the characterisation of the high modulus carbon fibres used in this study and finally a thorough study of the stress transfer micromechanics of model composites.

6.1. THE REMOTE RAMAN MICROPROBE

The Remote Raman Microprobe consists of a modified Raman Microscope, where the optical paths of the input and output beams are guided through fibre-optics. This achieves the complete separation of the Raman probe from the optical table. As was shown, the high background noise generated by the optical fibres can be completely eliminated, through the use of the correct combination of filters. A narrow bandpass filter after the laser delivery fibre eliminates all optical activity in the regions away from the laser line. The bandpass filter is complemented by a notch filter positioned before the input of the collection fibre. Thus, as is demonstrated, the probe collects solely the radiation which is due to the Raman activity of the material under investigation. The system design takes advantage of the use of polarisation preserving single mode fibres for laser delivery which offers the user the full potential to exploit the excellent resolution properties of a single mode laser. This is combined with the use of interchangeable optics which will match the laser beam diameter to the objective in use, no matter if this objective is a high resolution microscope objective or a tele-lens used for extra remote Raman probing.

Finally, the system design was successful in exploiting the confocal nature of the optical fibre endface. Confocal Microscopy is based on the principle that a second microscope is used to image a pinhole aperture on a single point of the specimen [**Minsky, 1988**]. This provides improved axial resolution at the expense of field of view. As was extensively described, confocality can be achieved by the use of appropriate lenses at the collection fibre endface. In other words, by changing the magnification of the projection of the optical fibre fibre tip at the sampling plane, the area of Raman signal collection is effectively controlled. This may be performed simply by changing the lens which focuses the collimated Raman signal on the collection fibre endface.

The effect of applying the confocal principles in a single fibre model composite, which was the configuration used later in this study, was demonstrated (figure 3.11). The spectrum of carbon can be successfully traced underneath the resin spectrum, and, thus, studying the carbon / epoxy interface is feasible with the remote probe. The efficiency and versatility of the probe was finally demonstrated as high quality data from diverse materials were successfully obtained. The optical design of the ReRaM was proved to offer a complete alternative to conventional Raman microscopes with the added advantage of remote probing.

The remote probe offers the feasibility of the in-situ study in various conditions. This has been demonstrated in the case of the monitoring of the modelling composite while it was strained on the loading frame, and even in an environmental chamber. The design rationale of the probe may account for all possible configurations. Thus, the same principles may be applied to make a less versatile but more compact probe, that will be dedicated to particular applications. Thus, the interchangeable optics may be withdrawn in order to account for more rigid but less versatile designs. This type of design, would allow the use of commercial optical fibre connectors in a compact system that would not need alignment, but would be dedicated to the application. As has been demonstrated (chapter 3), a similar system would have to compromise efficiency at the expense of confocality. In addition, simple designs, such as the typical confocal set-up (figure 3.8), are very attractive, due to their simplicity and minimal use of optical components. The incorporation of fibre-optics in the collection end that can be used for optical imaging is also feasible. This may be performed through the incorporation of the collection fibre in multimode bundles, such as those used for endoscopes [**Benson, 1997**]. Thus, remote sensing and imaging will be feasible at the same time. Finally, the design principles described can be used for the production of miniaturised probes optical fibre probes with a view to weight saving for additional versatility.

6.2. CARBON FIBRE CHARACTERISATION

The study of the carbon fibres involved both the conventional and the Raman characterisation of the M40 high modulus fibres with and without epoxide sizing. As expected, both sized and unsized fibres exhibited a gauge length dependence of their strength. The sized fibres showed more pronounced dependence than the unsized fibres, which was the case for epoxy sized intermediate modulus fibres. The task of testing the single fibres involved obtaining the $\ln\sigma / \ln l$ (figure 4.8) lines for both fibres. This allows the extrapolation of the fibre strength to critical length values in the single fibre fragmentation studies.

For the purposes of this study, the Raman characterisation of the fibres was confined to their first order spectrum. Both sized and unsized fibres exhibit the same features characteristic of high modulus carbon fibres. These are the E_{2g} or the peak characteristic of the graphitic structure [**Dresselhaus, 1977**], as well as the 'disorder' induced lines at 1360 cm^{-1} and 1620 cm^{-1} [**Lespade, 1984; Katagiri, 1988**]. Although the two fibres are not expected to differ in terms of structure, since they are produced and heat treated in an identical way, there are distinct differences associated with the disorder bands. In the case of the sized fibre, the intensities of the disorder induced bands are constant in relation to the intensity of the E_{2g} band. However, the unsized fibre exhibits considerable variation on the disorder bands intensities, even along a single filament. It is believed that this effect is due to abrasion during handling of the unsized fibre that affects the amount of 'crystal boundary' [**Tuinstra, 1970b**] on the fibre surface. The surface morphology of the carbon fibre is closely related to its interfacial properties when in the composite. The distinct differences in the spectrum of the two fibres are indicative of different stress transfer mechanics activated in the vicinity of the interface for each one of them.

The basic principle that allows Laser Raman spectroscopy to be used to measure stresses in composites, is the stress or strain dependence of certain vibrational modes of reinforcing fibres. This is attributed to the anharmonicity of the interatomic oscillations in the crystallite units [**Tashiro, 1990**]. The same effect is induced by other environmental parameters such as temperature or laser power *[**Bretzlaff, 1983**]. The frequency shift /* environment response can be uniquely represented through appropriate calibration curves.

All studies involving the calibration of the Raman spectrum of the carbon fibres to environmental changes were performed in relation to the E_{2g} band. The response of the Raman spectrum of the two fibres to the environment is identical within experimental error. Thus, the stress dependence of the fibres is 3.0 cm^{-1} / GPa, which is the expected magnitude for a high modulus fibre [**Melanitis, 1996**]. The cantilever beam technique revealed traces of non linear behaviour of the response of the fibre to compressive strain. This is in accordance with the behaviour of highly crystalline fibres such as carbon [**Melanitis, 1994**], or Kevlar® [**Vlattas, 1994**]. However, the behaviour of both fibres is, within experimental error, linear for compressive strains up to 0.5% (figure 4.14), and, thus, any non-linearities do not affect this study. Therefore, the linear dependence assumption is used throughout. Temperature and laser power have a less pronounced effect on the frequency shift of the E_{2g} band. As was found, 1 GPa of applied stress induces the same frequency shift as 10 mW laser power and 100°C, respectively. Thus, provided that the laser power and the temperature of the environment are relatively constant, the frequency shift is attributed to applied stress on the fibre.

6.3. INTERFACIAL STUDIES USING REMOTE LRS

The subsequent study dealt with the interfacial properties of model composites. The composite interface is known to affect considerably the properties of composites. Thus, in order to exploit fully the capabilities of the constituent materials, the mechanisms of stress transfer between the phases have to be firstly understood and subsequently controlled. Laser Raman Spectroscopy offers the unique possibility of the local measurement of axial stresses in embedded fibres. This study involved the stress monitoring of single fibre model composites with a view to identifying the mechanics of stress transfer, identify interfacial failure mechanisms and subsequently model the behaviour of the interface. The parameters studied were the fibre sizing, the coupon geometry, as well as the temperature of the environment.

The properties of the interface are generally enhanced by the presence of sizing. It is believed the sizing instigates the creation of local property variations, which are responsible for the improved stress transfer properties. The study of the elastic domain in model composites, reveals that the stress transfer efficiency is more than doubled due to the presence of sizing. The elastic domain is defined as the state where both constituents behave as linear elastic solids and no energy dissipation mechanisms are present. Thus, the interface may be studied in its intact form. The short fibre fragmentation test, where a fibre of finite length is embedded in the matrix provides the ideal geometry for the study of the elastic domain. This is due to the fact that the local discontinuity is already present, and not induced due to a fracture. The dynamic nature of the fibre fracture always induces local interfacial damage.

At low applied strains, the stress transfer in the short fibre coupon test is adequately described by the shear lag theory. All the shear lag assumptions are satisfied, as, at low applied strains, the interface is still intact and both constituents behave elastically. In addition, the stress transfer is shear dominated, as it builds from zero stress at the fibre ends to maximum stress in the middle of the fibre. The application of the shear lag theory, can provide the complete description of the interface through a single parameter β, which is experimentally derived from fitting the appropriate exponential function (§5.4.2.2). Thus, the stress field can be fully characterised. The increased interfacial properties of the sized system predict the existence of an interphase, which is almost 40% stiffer in shear than the bulk matrix. The LRS data also provide the possibility of an alternative approach, where β is calculated through the measured ISS values. Both approaches yield the same values of β within experimental error. As was demonstrated, the use of the shear-lag approach can adequately describe the stress transfer, even at the locus of the discontinuity, although the symmetry of the stress tensor demands the ISS to be zero [**McCartney, 1990; Nairn, 1992**].

During the long fibre coupon test, the dramatic differences observed in the elastic region are blunted. The sized system indicates slightly better stress transfer properties with the measured maximum interfacial shear strength (IFSS) of the sized system being approximately 15% better than the respective strength of the unsized system. This is due to different damage mechanisms present in the two systems. The presence of sizing leads to the formation of a brittle interphase [**Drzal, 1993**]. Crack formation in this interphase limits the IFSS of the system. This matrix cracking is not present in the unsized system, where compressive stresses at the fibre fracture loci bridge the axial stress transfer. The compression at the tip of the fibre is due to the 'recoil' mechanism, where, after the fracture event, the fibre recoils and freezes in compression, due to the thermal stress field of the matrix [**Netravali, 1989c**].

To our knowledge, it is the first time that LRS has been used to study the stress transfer of model composites in elevated temperatures. Elevated temperature results to a decrease in the interfacial properties of both systems. This decrease is attributed to two phenomena, that is, the obvious reduction in matrix shear modulus and the relief of the thermal stress field created by the matrix [**Ohsawa, 1978**]. The IFSS of the sized system is approximately half its room temperature value. The effect of temperature is more dramatic for the unsized system, whose interfacial shear strength is falling to less than 30% of the respective room temperature value. This is due to the combined effect of the enhanced properties of the interphase in the case of the sized system and the reduction of the thermal stress field. The thermal stress field is more important in the case of the unsized system, which is indicative of a Coulomb friction-type interface. The IFSS of such a system reaches its maximum value, just before frictional slipping occurs. The difference in IFSS between the two systems is more obvious than that observed at room temperature. This is due to the absence of damage mechanisms that were responsible for the masking of the dramatic difference observed in the elastic domain and at room temperature. The increased ductility of the interface / interphase does not allow crack formation in the matrix. The prevailing damage mechanism at 60°C is the 'recoil' mechanism, for both systems.

The efficiency of stress transfer can be modelled in relation to the equivalent elastic properties of the interface. Thus, quantitative information about its effect on stress transfer efficiency can be obtained. This is performed through a single parameter, the index of interfacial damage ζ. This parameter corresponds to the ratio of the fibre length required to transfer the same energy if the stress state were elastic, to the actual fragment length. ζ is providing accurate information about the state of the interface as a function of applied strain. The fracture events alone reduce the efficiency of stress transfer to 76% and 87% for the sized and the unsized systems, respectively. Further applied strain, leads to further reduction of ζ, to 0.56 and 0.65 for the sized and the unsized systems, respectively. The energy approach to the interfacial adhesion, takes into account the energy dissipation mechanisms, which depend on the matrix properties as well as on damage mechanisms such as the 'fibre recoil' or matrix cracking at the interface.

The complete analysis of the single fibre coupon test using LRS provides considerable insight in the area of carbon fibre / epoxy interfaces, as well as an indication of the reliability of the conventional fragmentation test. The analysis of the single fibre model composites should be extended to include the monitoring of the short fibre coupon at higher strains, and temperatures, in order to provide more insight on parameters such as the residual stress field or the energy dissipation mechanisms. In this way, a direct comparison of an existent and a fracture induced discontinuity can be simultaneously studied. In addition, phenomena like the 'frozen' shear state present in the short fibre sized system require further investigation, as the existing models are unable to predict them.

Finally, the ability of remote Raman sensing is now providing the potential for real composite testing at the locus of the discontinuity [**Galiotis, 1996; Chohan, 1997**]. Real composite Raman interrogation provides all the information needed in relation of how the interface affects composite properties. Local axial stress measurement is essential to test the validity of existing models. Although the Raman signal acquisition was until recently limited to the surface of the coupon, recent experiments show that optical waveguides embedded in laminates, can successfully transfer the information regarding the stress field in composites [**Arjyal, 1996**]. The combination of remote sensing, full scale testing as well as monitoring the through thickness properties of the material is invaluable to the researcher involved with advanced composites.

Appendix 1

The aquisition of the spectrum is performed by the Charged Coupled Device (CCD). The recording spectral window covers an area of approximately 7.5 nm, limited by the size of the CCD camera. The spectral acquisition is achieved by adding all the CCD pixel intensities (binning) on the axis perpendicular to the analysis axis. The resulting spectrum is intensity (or incident photon number) versus pixel nunber. The CCD pixels scale linearly with wavelength λ and the proportionality constant is a property of the set-up depending on the f number of the spectrometer, the dispersing element (grating) and the physical dimension of the CCD pixel. In the set-up used which is thoroughly described in chapter 3, this proportionality constant equals $K_{RERAM}=0.00231170$. The wavelength λ scales inversely with wavenumbers. The relative shift to the excitation line is expressed in Delta wavenumbers:

$$10^{-7}\left(\frac{1}{[\mathrm{nm}]_{\lambda\,\mathrm{excitation}}}-\frac{1}{[\mathrm{nm}]_{\lambda\,\mathrm{Raman}}}\right)\mathrm{nm}^{-1}=\left([\mathrm{cm}^{-1}]_{\lambda_{\mathrm{Raman}}}\right)\mathrm{cm} \qquad \text{(A1.1)}$$

Absolute values of frequency for the spectrometer are obtained either through well defined light sources (e.g. mercury or sodium lamp) or can be differentially calculated from the position of the laser line. In this study, the relative shift of the Raman bands to given reference frequencies, such as those from free fibres in air are of primary importance rather than absolute frequencies. For clarity all spectra will be presented in Delta wavenumbers as calculated from equation A1.1.

In order to define the position of the peak, a least-square 'best-fit' routine is used. The Raman bands are assumed to be symmetric distributions. The distributions may be

Lorentzian or Gaussian. Whereas the background of the distribution may be a quadratic equation. The regression formulae are:

$$\text{baseline: } Q(x) = a_0 + a_1 x + a_2 x^2 \qquad \text{A1.2)}$$

$$\text{Lorentzian: } L(x) = a_0 \frac{a_2^2}{(x - a_1)^2 + a_2{}^2} \qquad \text{(A1.3)}$$

$$\text{Gaussian: } G(x) = a_0 e^{-(\frac{x-a_1}{a_2})^2} \qquad \text{1.4)}$$

It is recommended to use a linear baseline, that is, set $a_2 = 0$ in equation A1.2, since the noise may arbitrarily affect the α_2 value and artificially alter the position of the peak position. The symmetric distributions are characterised by three constants α_0 which represents the intensity of the distribution on its symmetry axis, α_1 which is the position of its axis of symmetry and α_2 which represents the spread of the distribution. The choice of either Lorentzian or Gaussian distribution is made on an empirical basis provided that a consistency way is kept for fitting spectra from the same material. In figure A1.1 the ‘best fit’ combination used throughout this study for the first order carbon fibre Raman spectrum is shown.

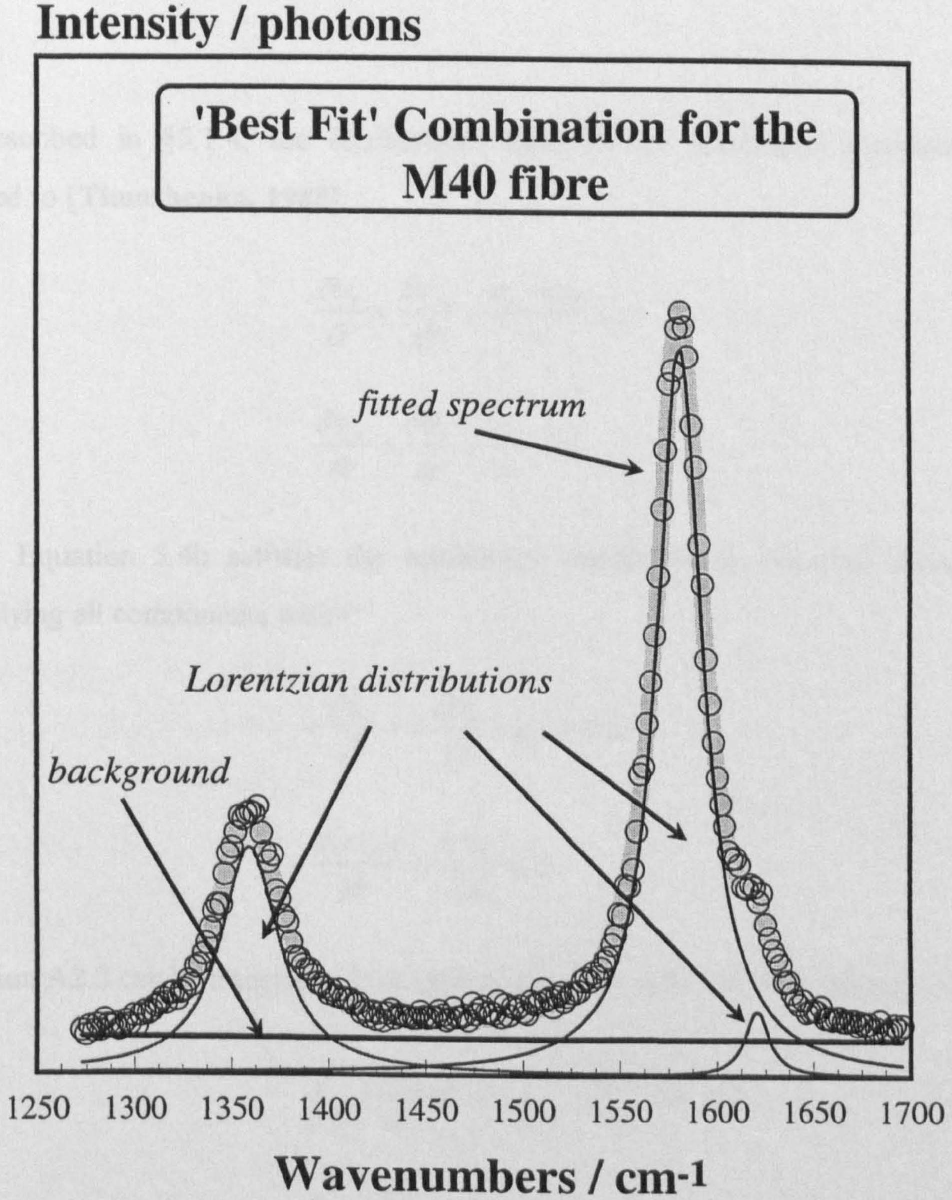

Figure A1.1 'Best fit' of the first order M40 fibre Raman spectrum.

Appendix 2

As described in §5.1.4, the equilibrium equations for torsionless axisymmetry are reduced to [**Timoshenko, 1988**]:

$$\frac{\partial\sigma_r}{\partial r}+\frac{\partial\tau_{rz}}{\partial z}+\frac{\sigma_r-\sigma_\theta}{r}=0 \tag{5.4a}$$

$$\frac{\partial\tau_{rz}}{\partial r}+\frac{\partial\sigma_z}{\partial z}+\frac{\tau_{rz}}{r}=0 \tag{5.4b}$$

Equation 5.4b satisfies the equilibrium conditions in the axial direction. By multiplying all components with r:

$$r\frac{\partial\tau_{rz}}{\partial r}+r\frac{\partial\sigma_z}{\partial z}+\tau_{rz}=0\Leftrightarrow \tag{A2.1}$$

$$\frac{\partial(r\tau_{rz})}{\partial r}+\frac{r\partial\sigma_z}{\partial z}=0 \tag{A2.2}$$

Equation A2.2 can be integrated from zero to the fibre radius R, with respect to r:

$$\int_{r=0}^{r=R}\frac{r\partial\sigma_z}{\partial z}dr=-\int_{r=0}^{r=R}\frac{\partial(r\tau_{rz})}{\partial r}dr\Rightarrow \tag{A2.3}$$

$$\int_{r=0}^{r=R}\frac{r\partial\sigma_z}{\partial z}dr=-R(\tau_{rz}|_{r=R}) \tag{A2.4}$$

The average stress $\bar{\sigma}_z$ acting on the cross-sectional area of the fibre of radius R is given by:

$$\bar{\sigma}_z = \frac{1}{\pi R^2}\int_0^{2\pi}\int_{r=0}^{r=R} r\sigma_z dr d\theta \qquad \text{(A2.5)}$$

From equation A2.5:

$$\bar{\sigma}_z = \frac{2}{R^2}\int_{r=0}^{r=R} \sigma_z dr \qquad \text{(A2.6)}$$

The differentiation of equation A2.6 with respect to *z* yields:

$$\frac{R^2}{2}\frac{\partial\bar{\sigma}_z}{\partial z} = \int_{r=0}^{r=R} \frac{r\partial\sigma_z}{\partial z} dr \qquad \text{(A2.7)}$$

By substituting equation A2.7 to equation A2.4, we obtain the balance of forces equation:

$$\tau_{rz}\Big|_{r=R} = -\frac{R}{2}\frac{\partial\bar{\sigma}_z}{\partial z} \qquad \text{(A2.8)}$$

Equation A2.8 coincides with equation 5.17 as the average stress $\bar{\sigma}_z$ is independent of *r* for a given fibre radius *R*. The assumption that the axial stress obtained through the Raman measurements is an average value over the cross-sectional area of the fibre has to be made in order to use the balance of forces model and derive ISS distributions.

Appendix 3

In order to derive ISS distributions from the axial stress profiles, the experimental data points are interpolated with a known function that can be subsequently differentiated (§5.2.6.5). Throughout this study a *cubic spline interpolation* was used [**Hayes, 1974**]. The cubic splines are series of third degree polynomials:

$$f(z) = a_0 + a_1 z + a_2 z^2 + a_3 z^3 \qquad \text{(A3.1)}$$

The algorithm of interpolating with cubic splines involves the partition of the experimental data in segments, by the use of *knots*. The knots can be single, double, or triple. This means that the third, second, or first derivative, respectively, of the interpolating polynomial is continuous at the position of the knot. Thus, the interpolation is flexible enough to allow for the fitting of the experimental data. If single polynomials were used, a compromise would be required between the quality of the fit and unnecessary oscillations of the fitted curve due to the experimental scatter.

The fitting procedure used throughout this study involved a triple knot at the locus of the fibre fracture, a single knot at the middle of each fragment and a single knot positioned at a specific position away from the fibre fracture. A considerable effort was made to minimise errors due to the interpolating procedure. This was performed by maximising the number of steps of the Raman signal acquisition (1 μm step was used near the locus of the fibre fracture). In addition, the position of intermediate single knots relative to fibre fractures was kept constant for each experiment. All interpolations were made using the Numerical Algorithms Group (NAG) B-spline routine.

A typical fit to the experimental data is shown in figure A3.1. There are three single knots positioned along the fragment length: one in the middle of the fragment and another two, each one at 0.1mm from the fibre end. The number of points in enough for the fit to be consistent, without the addition of further knots. The corresponding ISS curve is also shown. The ISS distribution was derived by differentiating the B-spline fit. The maximum ISS value is generally independent of the positioning of the knots.

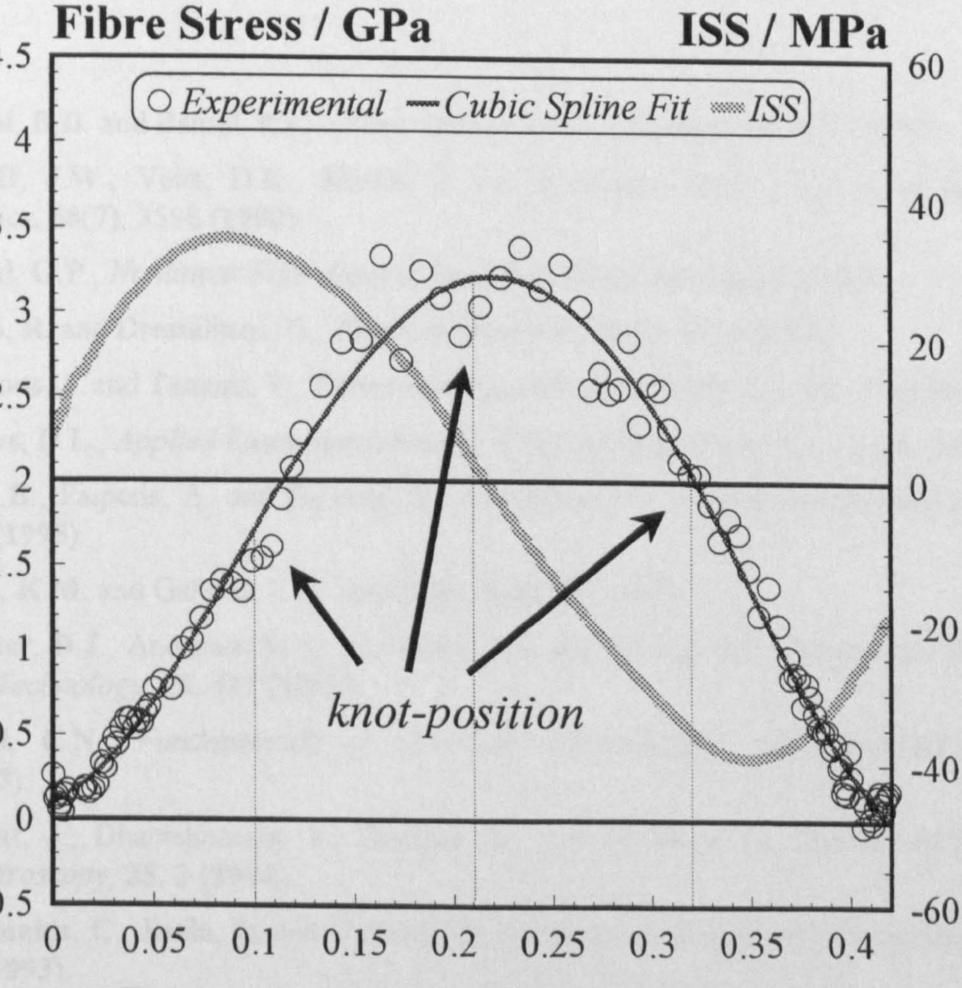

Figure A3.1 Typical cubic spline interpolation to the experimental data and derivation of the interfacial shear stress distribution.

References

Agarwal, B.D. and Bansal, R.K., *Fibre Science and Technology*, **12**, 149 **(1979)**.

Ager III, J.W., Veirs, D.K., Shamir, J. and Rosenlatt, G.M., *Journal of Applied Physics*, **68**(7), 3598 **(1990)**.

Agrawal, G.P., *Nonlinear Fiber Optics*, Academic Press, San Diego **(1989)**.

Al-Jishi, R. and Dresselhaus, G., *Physical Review B*, **26**(8), 4514 **(1982)**.

Andersons, J. and Tamuzs, V., *Composites Science and Technology*, **48**, 57 **(1993)**.

Andrews, D.L., *Applied Laser Spectroscopy*, VCH Publishers, Inc, New York **(1992)**.

Arjyal, B., Paipetis, A. and Galiotis, C., *Nondestructive Testing and Evaluation*, **12**, 355 **(1995)**.

Atallah, K.M. and Galiotis, C., *Composites*, **8**, 6325 **(1993)**.

Bannister, D.J., Andrews, M.C., Cervenka, A.J. and Young, R.J., *Composites Science and Technology*, **53**, 411 **(1995)**.

Banwell, C.N., *Fundamentals of Molecular Spectroscopy*, McGraw-Hill,London, **(1983)**.

Barbillat, J., Dhamelincourt, P., Delhaye, M. and Da Silva, E., *Journal of Raman Spectroscopy*, **25**, 3 **(1994)**.

Baxevanakis, C., Jeulin, D. and Valentin, D., *Composites Science and Technology*, **48**, 47 **(1993)**.

Bennet, S.C. and Johnson, W., in Proceedings of the fifth London Carbon and Graphite Conference, vol.1, p.377, London **(1978)**.

Benson, J., *Materials World*, **5**(9), 512 **(1997)**.

Boogh, L.C.N., Meier, R.J., Kausch, H.-H. and Kip, B.J., *Journal of Polymer Science: Part B Polymer Physics*, **30**, 325 **(1992)**.

Bretzlaff, R.F. and Wool, J., *Macromolecules*, **16**, 1907 **(1983)**.

BREU/ CT 91-9503, *Interface Contribution to the Temperature-Dependent Properties of Carbon Fibre Reinforced Bismaleimide Composites*, Mid-Term assessment Report, 47 **(1993)**.

Broutman, L.J., in *Interfaces in Composites*, ASTM STP 452, American Society for Testing and Materials, 27 (**1969**).

Broutman, L.J. and Agarwal, B.D., *Polymer Engineering and Science*, **14**(8), 581 (**1974**).

Bunsell, A.R. and Somer, A., *Plastics, Rubber and Composites Processing and Applications*, **18**, 263 (**1992**).

Buxton, A. and Baillie, C., *Composites*, **25**, 604 (**1994**).

Buxton, A. and Baillie, C., *Materials Forum*, **189-190**, 199 (**1995**).

Carraba, M., Spencer, K.M., Edmonds, R.B., Rauth, R.D. and Haas, J.W., *SPIE*, **1637**, 82 (**1992**).

Carrara, A.S. and McGarry, F.D., *Journal of Composite Materials*, **2**, 222 (**1968**).

Chamis, C.C., *Mechanics of Load Transfer at Fibre-Matrix Interface*, NASA Report TN D-5367 (**1972**).

Chang, C. and Hsu, S.L., *Polymer*, **27**, 34 (**1986**).

Cheng, T.H., Zhang, J., Yumitory, S., Jones, F.R. and Anderson, C.W., *Composites*, **25**, 661 (**1994**).

Chieu, T.C., Dresselhaus, M.S., Endo, M. and Moore, A.W., *The American Physical Society*, **26**(10), 5867 (**1982**).

Chohan, V. and Galiotis, C., *Composites Part A*, **27A**, 881 (**1996**).

Chohan, V. and Galiotis, C., *Composites Science and Technology*, in press, (**1997**).

Ciba-Geigy, *Araldite® MY-750 and MY-753 with Hardener HY-956 or HY-951*, Instruction sheet No. C.28j, (**1979**).

Colthup, N.B., *Introduction to Infrared and Raman Spectroscopy*, Academic Press Inc. Ltd., London (**1975**).

Cox, C.L., *The British Journal of Applied Physics*, **3**, 72 (**1952**).

Da Silva, E., Barbillat, J. and Geiger, R., in *Proceedings of the XIVth International Conference In Raman Spectroscopy*, edited by N.T. Yu and X.Y. Li, Dept of Chemistry, p. 800, The Hong Kong University of Science and Technology (**1994**).

Dai, S., Young, J.P., Begun, G.M., Coffield, J.E. and Mamantov, G., *Microchim. Acta*, **108**, 261 (**1992**).

Daoust, J., Vu-Khanh, T., Ahglstroim, C. and Gerard, J.F., *Composites Science and Technology*, **48**, 143 (**1993**).

Day, R.J. and Young, R.J., *Journal of Microscopy*, **169**, 155 (**1993**).

DeTeresa, S.J., Porter, R.S. and Farris, R.J., *Journal of Materials Science*, **23**, 1886 (**1988**).

Desaeger, M. and Verpoest, I., *Composites Science and Technology*, **48**, 215 (**1993**).

Detassis, M., Pegoretti, A. and Migliaresi, C., *Composites Science and Technology*, **53** 39 (**1995**).

DiBenendetto, A.T. and Jones, K.D., *Composites: Part A*, **29A**, 869 (**1996**).

Donnet, J.B. and Bansal, R.P., *Carbon Fibres*, Marcel Dekker Inc., New York (**1984**).

Dow, N.F., General Electric Co., Missiles and Space Div., Report No. R-635D61 (**1963**).

Dresselhaus, M.S., Dresselhaus, G., Eclund, P.C. and Chung, D.D.L, *Materials Science and Engineering*, **31**, 141 (**1977**).

Dresselhaus, M.S., Dresselhaus, G., Sugihara, K., Spain, I.L. and Golberg, H.A., *Graphite Fibres and Filaments*, Springer-Verlag, Berlin (**1988**).

Drzal, L.T., Rich, M.J. and Lloyd, P.F., *Journal of Adhesion*, **16**, 1 (**1983a**).

Drzal, L.T., Rich, M.J. Koenig, M.F. and Lloyd, P.F., *Journal of Adhesion*, **16**, 133 (**1983b**).

Drzal, L.T., *Materials Science and Engineering A - Structural Materials Strength Properties Microstructure and Processing*, **126**, 289 (**1990**).

Drzal, L.T. and Madhucar, M., *Journal of Materials Science*, **28**, 569 (**1993**).

Ebert, L.J. and Gadd, J.D., in *Fiber Composite Materials*, American Society for Metals, Ohio, 89 (**1965**).

Elman, B.S., Dresselhaus, M.S., Dresselhaus, G., Maby, E.W., Mazurek, H., *Physical Review B*, **24**(2), 1027 (**1981**).

Everall, D.N., Lumsdon, J. and Christopher, D.J., *Carbon*, **29**(2), 133 (**1991**).

Everall, N.J., Owen, H. and Slater, J., in *Proceedings of the XIVth International Conference In Raman Spectroscopy*, edited by N.T. Yu and X.Y. Li, Dept of Chemistry, p. 111, The Hong Kong University of Science and Technology (**1994**).

Fan, C.F. and Hsu, S.L., *Journal of Polymer Science: Part B Polymer Physics*, **30**, 603 (**1992**).

Favre, J.P. and Perrin, J., *Journal of Materials Science*, **7**, 1113 (**1972**).

Favre, J.P. and Jacques, D., *Journal of Materials Science*, **25**, 1373 (**1990**).

Favre, J.P., Sigety, P. and Jacques, D., *Journal of Materials Science*, **26**, 189 (**1991**).

Favre, J.P., Auvray, M.-H., Cheneau-Henry, P., Galiotis, C., Vlattas, C., Paipetis, A., Pegoraro, M., Severini, F., Di Landro, L. and Yuan, L., *Polymer Composites*, 17(6), 937 (**1996**).

Filon, L.N.G., *Transactions of the Royal Society (London)*, **14**, 147 (**1902**).

Fischbach, D.B. and Couzi, M., *Carbon*, **24**, 365 (**1986**).

Fitzer, E., *Carbon Fibres and Their Composites*, ed. E. Fitzer, Springer Verlag, Berlin (**1985**).

Fitzer, E., Gantner, E., Rozploch, F. and Steinert, D., *High Temperatures - High Pressures*, **19**(5), 537 (**1987**).

Fourdeux, A., Perret, R., Ruland, W., in the *Proceedings of the 1st International Conference on 'Carbon Fibres, their Composites and Applications'*, p.57, Plastics Institute, London (**1973**).

Galiotis, C., Young, R.J. and Batchelder, D.N., *J. Mat. Sci.Lett.*, **2**, 263 (**1983**).

Galiotis, C., Young, R.J., Yeung, P.H.J. and Batchelder, D.N., *Journal of Materials Science*, **19**, 3640 (**1984**).

Galiotis, C., Robinson, I.M. and Young, R.J., *Polym. Communic.*, **26**, 354 (**1985**).

Galiotis, C., and Batchelder, D.N., *Journal of Materials Science Letters*, **7**, 545 (**1988**).

Galiotis, C., Chohan, V., Paipetis, A. and Vlattas, C., in *Fiber Matrix and Interface Properties*, ASTM STP 1290, American Society for Testing and Materials, 19 (**1996**).

Galiotis, C., *Composites Science and Technology*, **42**, 125 (**1991**).

Galiotis, C., in *Phase Interaction in Composite Materials*, eds. S.A. Paipetis and C.G. Papanicolaou, p.173, (**1992**).

Galiotis, C., *Materials Technology*, **8**, 203 (**1993a**).

Galiotis, C., *Composites Science and Technology*, **48**, 15 (**1993b**).

Galiotis, C., *Proceedings of the XIVth International Conference In Raman Spectroscopy*, edited by N.T. Yu and X.Y. Li, Dept of Chemistry, p. 802, The Hong Kong University of Science and Technology (**1994**).

Gent, A.N., Chang, Y.-W., Nardin, M. and Schultz, J., *Journal of Materials Science*, **31**, 1707 (**1996**).

Gray, **J**., *Journal of Materials Science*, **19**, 861 (**1984**).

Greszczuk, **L.B**., in *Interfaces in Composites*, ASTM STP 452, American Society for Testing and Materials, 42 (**1969**).

Gu, **M.**, and Sheppard, C.J.R., *Micron*, **24**, 557 (**1993**).

Gu, **X.H**., Young, R.J. and Day, R.J., *Journal of Materials Science*, **30**, 1409 (**1995**).

Guenther, **R**., *Modern Optics*, John Wiley and Sons, New York (**1990**).

Guigon, **M**., Oberlin, A. and Desarmot, G., *Fibre Science and Technology*, **20**, 177 (**1984**).

Guigon, **M**. and Klinklin, E., *Composites*, **25**, 534 (**1994**).

Guild, **F.J**., Vlattas, C. and Galiotis, C., *Composites Science and Technology*, **50**, 319 (**1994**).

Gulino, **R**. and Phoenix, S.L., *Journal of Materials Science*, **26**, 3107 (**1991**).

Halpin, **J.C**., *Primer on Composite Materials Analysis*, 2nd ed., Technomic Publishing Company Inc., Lancaster, Pennsylvania, U.S.A. (**1992**).

Hashin, Z., *Mechanics of Materials*, **8**, 333 (**1990**).

Hayes, J.G., *Bulletin Institute of Mathematics and its Applications*, **10**, 144 (**1974**).

Hendra, P.J., Ellis, G., and Cutler, D.J., *Journal of Raman Spectroscopy*, **19**, 413 (**1988**).

Heppenstall-Butler, M., Bannister, D.J. and Young, R.J., *Composites: Part A*, **27A**, 703 (**1996**).

Herrmann, K.P., Noe, A. and Dong, M., *Composites: Part A*, **27A**, 813 (**1996**).

Hughes, J.D.H., *Carbon*, **24**, 551 (**1986**).

Hull, D. and Clyne, T.W., *An Introduction to Composite Materials*, 2nd ed., Cambridge University Press, Cambridge (**1996**).

Jahankhani, H. and Galiotis, C., *Journal of Composite Materials*, **25**, 609 (**1991**).

Jones, R.M., *Mechanics of Composite Materials*, McGraw-Hill Kogakusha, Ltd., Tokyo (**1975**).

Katagiri, G., Ishida, H. and Ishitani, A., *Carbon*, **26**, 565 (**1988**).

Kelly, A. and Tyson, W.R., *Journal of Mechanical Physics and Solids*, **13**, 329 (**1965**).

Kelly, B.T., *Carbon*, **20**, 2, (**1982**).

Kelly, A., *Strong Solids*, Clarendon Press, Oxford, (**1966**).

Kim, P.K., Xu, Y., Chang, C. and Hsu, S.L., *Polymer*, **27**, 1547 (**1986**).

Lacroix, T., Keunings, R., Desaeger, M. and Verpoest, I., *Journal of Materials Science*, **30**, 683 (**1995**).

Lekhnitski, S.G., *Theory of an Anisotropic Body*, Holden Day Inc., San Francisco, California (**1963**).

Lespade, P., Al-Jishi, R. and Dresselhaus, M.S., *Carbon*, **20**, 427 (**1982**).

Lespade, P., Marchand, A., Couzi, M. and Cruege, F., *Carbon*, **22**, 375 (**1984**).

Li, C.T. and Tiez, J.V., *Journal of Materials Science* **25**, 4694 (**1990**).

Li, J.-X., *Composites*, **25**, 558 (**1994**).

Ling, S. and Wagner, H.D., *Composites Science and Technology*, **48**, 35 (**1993**).

Loader, J., *Basic Laser Raman Spectroscopy*, Heyden & Son Ltd., London (**1970**).

Long, S. and Flower, H.M., *Composites: Part A*, **27A**, 833 (**1996**).

Lu, G.-Y. and Mai, Y.-W., *Journal of Materials Science*, **30**, 5872 (**1995**).

Mandel, J.F., Grande, D.H., Tsiang, T.H. and McGarry, F.J., in *Composite materials: testing and design*, ASTM STP 893, American Society for Testing and Materials, 87 (**1986**).

McCartney, L.N., *Proc. R. Soc. Lond.*, **A425**, 215 (**1989**).

McCrum, N.G., Buckley, C.P., Bucknall, C.B., *Principles of Polymer Engineering*, Oxford University Press, Oxford (**1990**).

Melanitis, N., PhD thesis, University of London (**1991**).

Melanitis, N., Galiotis, C., Tetlow, P.L. and Davies, C.K.L., *Journal of Composite Materials* **26**, 574 (**1992**).

Melanitis, N. and Galiotis, C., *Proc. R. Soc. Lond. A*, **440**, 379 (**1993a**).

Melanitis, N., Galiotis, C., Tetlow, P.L. and Davies, C.K.L., *Journal of Materials Science*, **28**, 1648 (**1993b**).

Melanitis, N., Tetlow, P.L., Galiotis, C. and Smith, S.B., *Journal of Materials Science*, **29**, 786 (**1994**).

Melanitis, N., Tetlow, P.L. and Galiotis, C., *Journal of Materials Science*, **31**, 851 (**1996**).

Meretz, S., Auersch, W., Marotzke, C., Schulz, E. and Hampe, A., *Composites Science and Technology*, **48**, 285 (**1993**).

Minsky, M., *Scanning*, **10**, 128 (**1988**).

Miwa, M., Takeno, A., Yamaguchi, K. and Watanabe, A., *Journal of Materials Science*, **30**, 2097 (**1995**).

Mullin, J., Berry, J.M. and Gatti, A., *Journal of Composite Materials*, **2**, 82 (**1968**).

Myrrick, M.L., and Angel, S.M., *Applied Spectroscopy*, **44**, 565 (**1990**).

Nairn, J.A., *Mechanics of Materials*, **13**, 131 (**1992**).

Nairn, J.A., Liu, Y.C., and Galiotis, C., in *Fiber Matrix and Interface Properties*, ASTM STP 1290, American Society for Testing and Materials, 47 (**1996**).

Nairn, J.A., *Mechanics of Materials*, in press, (**1997**).

Nakamizo, M., Kammereck, R., and Walker P.L.JR., *Carbon*, **12**, 259 (**1974**).

Narkis, M., Chen, J.H. and Pipes, R.B., *Polymer Composites*, **9**, 245 (**1988**).

Nath, **R.B**., Fenner, D.N. and Galiotis C., *Composites: Part A*, **27A**, 821 (**1996**).

Nayfeh, **A.H**., *Fibre Science and Technology*, **10**, 195 (**1977**).

Nemanich, **R**.J., Lucovsky, G. and Solin, S.A., *Solid State Communications*, **23**, 117 (1977).

Nemanich, **R**.J. and Solin, S.A., *Physical Review B*, **20**(2), 392 (**1979**).

Netravali, A.N., Stone, D., Ruoff, S. and Topoleski, L.T.T., *Composites Science and Technology*, **34**, 289 (**1989a**).

Netravali, A.N., Topoleski, L.T.T., Sachse, W.H. and Phoenix, S.L., *Composites Science and Technology*, **35**, 13 (**1989b**).

Netravali, A.N., Henstenburg, R.B., Phoenix, S.L. and Schwartz, P., *Polymer Composites*, **10**, 226 (**1989c**).

Ohsawa, T., Nakayama, A., Miwa, M. and Tsushima, E., *Journal of Applied Polymer Science*, **22**, 3203 (**1978**).

Paipetis, A. and Galiotis, C., *Composites: Part A*, **27A**, 755 (**1996**).

Paipetis, A., Vlattas, C. and Galiotis, C., *Journal of Raman Spectroscopy*, **27**, 519 (**1996**).

Paris, F., Cano, J.C. and Varna, J., *International Journal of Fracture*, **82**, 11 (**1996**).

Penn, L.S. and Lee S.M., *Journal of Composites Technology and Research*, **11**, 23 (**1989**).

Piggot, M.R., *Acta Metallurgica*, **14**, 1429 (**1966**).

Piggot, M.R., *Load-Bearing Fibres*, Pergamon Press, Oxford (**1980**).

Pitkethly, M.J., Favre, J.P., Gaur, U., Jakubowski, J., Mudrich, S.F., Caldwell, D.L., Drzal, L.T., Nardin, M., Wagner, H.D., Di Landro, L., Hampe, A., Armistead, J.P., Desaeger, M., Verpoest, I., *Composites Science and Technology*, **48**, 205 (**1993**).

Pitkethly, M.J., in *Fiber Matrix and Interface Properties*, ASTM STP 1290, American Society for Testing and Materials, 34 (**1996**).

Plaza, **P**., Dao, N.Q., Jouan, M., Fevrier, H. and Saisse, H., *Applied Optics*, **25**, 3448 (**1986**).

Pointer, **D**., *Laser Focus World*, **26**(3), 177 (**1990**).

Qiu, Y. and Scwartz, P., *Composites Science and Technology*, **48**, 5 (**1993**).

Raman, C.V. and Krishnan, K.S., *Nature*, **121**, 501 (**1928**).

Reifsnider, **K**.**L**., *Composites*, **25**, 461 (**1994**).

Robinson, **I**.**M**., Young, R.J., Galiotis, C. and Batchelder, D.N., *Journal of Materials Science*, **22**, 3642 (**1987a**).

Robinson, **I**.**M**., Zakhihani, M., Day, R.J., Young, R.J. and Galiotis, C., *J. Mat. Sci.Lett.*, **6**, 1212 (**1987b**).

Rosen, **B**.**W**., in *Fiber Composite Materials*, American Society for Metals, Ohio, 37 (**1965**).

Sakata, **H**., Dresselhaus, G. and Dresselhaus, M.S., *Journal of Applied Physics*, **63**(8), 2769 (**1988**).

Sastry, **A**.**M**., Phoenix, S.L. and Scwartz, P., *Composites Science and Technology*, **48**, 237 (**1993**).

Savage, **G**., *Carbon-Carbon Composites*, Chapman & Hall, London (**1993**).

Schadler, **L**.**S**., Laird, C., Melanitis, N., Galiotis, C. and Figueroa, J.C., *Journal of Materials Science*, **27**, 1663 (**1992**).

Schadler, **L**.**S**. and Galiotis, C., *International Materials Reviews*, **40**, 116 (**1995**).

Schopp, **M**., Shrotter, H.W. and Douklias, N., *Applied Spectroscopy*, **44**, 562 (**1990**).

Selvadurai, **A**.**P**.**S**. and Busschen, A. ten, *Journal of Applied Mechanics*, **62**, 98 (**1995**).

Sharonov, S., Nabiev, I., Chourpa, I., Feofanov, A., Valisa, P. and Manfait, M., *Journal of Raman Spectroscopy*, **25**, 699 (**1994**).

Shiryaeva G.V. and Andreevska, G.D., *The Plastics*, **4**, 40 (**1962**).

Smecal, A., *Naturewissenshaften*, **11**, 873 (**1923**).

Svanberg, S., *Atomic and Molecular Spectroscopy*, Springer Verlag, Berlin (**1992**).

Szymanski, **H**.A., *Raman Spectroscopy: Theory and Practice*, Plenum Press, New York (**1967**).

Tashiro, **K**., Wu, G. and Kobayashi, M., *J. Appl. Polym. Sci*., **28**, 2038 (**1990**).

ten Busschen, **A** and. Selvadurai, A.P.S., *Journal of Applied Mechanics*, **62**, 87 (**1995**).

Termonia, **Y**., *Journal of Materials Science*, **22**, 504 (**1987**).

Termonia, **Y**., *Journal of Materials Science*, **25**, 4644 (**1990**).

Timoshenko, S.**P**. and Gere, J.M., *Theory of Elastic Stability*, McGraw-Hill, New York (**1961**).

Timoshenko, S.**P**. andGoodier, J.N., *Theory of Elasticity*, McGraw-Hill, New York (**1988**).

Tripathi, **D**., Chen, F. and Jones, F.R., *Proc. R.Soc. Lond. A*, **452**, 621 (**1996**).

Tsai, **H**.**C**., Arocho, A.M. and Gause, L.W., *Materials Science and Engineering*, **A126**, 285 (**1990**).

Tsu, **R**., Gonzalez, J.H. and Hernandez, C.I., *Solid State Communications*, **27**, 507 (**1978**).

Tuinstra, **F**. and Koenig, J., *The Journal of Chemical Physics*, **53**(3), 1126 (**1970a**).

Tuinstra, **F**. and Koenig, J., *Journal of Composite Materials*, **43**, 492 (**1970b**).

Tyson, **W**.**R**. and Davies, G.J., *Brit. J. Appl. Phys*., **16**,199 (**1965**).

van den Heuvel, **P**.**W**.**J**., Hogeweg, B. and Peijs, T., *Composites Part A*, **28A**, 236 (**1997**).

Vidano, **R**.**P**., Fischbach, D.B., Willis, L.S. and Loehr, T.M., *Solid State Communications*, **39**, 341 (**1981**).

Vlattas, **C**. and Galiotis, C., in *Interface Micromechanics in Aramid/ Epoxy Model Composites in Developments in the Science and Technonogy of Composite Materials*, ECCM 5, eds. A. R. Bunsell, J. F. Jamet and A. Massiah, Bordeaux, France, 415 (**1992**).

Vlattas, **C**., and Galiotis, C., *Polymer*, **35**(11), 2335 (**1994**).

Vlattas, C., PhD thesis, University of London (**1995**).

Wagner, **H**.**D**., Nairn, J.A. and Detassis, M., *Applied Composite Materials*, **2**, 107 (**1995**).

Wagner, **H**.**D**., *Advanced Composite Letters*, **2**, 169 (**1993**).

Waterbury, M.C. and Drzal, L.T., *Journal of Composites Technology and Research*, **13**, 22 (**1991**).

Williams, K.P.J., *Journal of Raman Spectroscopy*, **21**, 147 (**1990**).

Wilson, T., *Confocal Microscopy*, Academic Press, San Diego, CA (**1990**).

Wool, R.P., *J. Polym. Sci. Polym. Phys. Ed.*, **13**, 31 (**1975**).

Ying, L., *Sampe Quarterly*, **15**, 26 (**1983**).

Young, M., *Optics and Lasers*, Spinger Verlag, New York (**1993**).

Young, R.J., *Journal of Microscopy*, **185**, 199 (**1997**).

Yumitory, S., Wang, D. and Jones, F.R., *Composites*, **25**, 698 (**1994**).

Zhang, Z. Y., *Sampe Quarterly*, **15**, 51 (**1983**).

Zhu, **Z.Y.**, and Yappert, C.M., *Applied Spectroscopy*, **46**, 912 (**1992**).

Zhu, **Z.Y.**, and Yappert, C.M., *Applied Spectroscopy*, **46**, 919 (**1992**).